technische universität dortmund

MAX PLANCK INSTITUTE OF MOLECULAR PHYSIOLOGY

IDENTIFICATION AND CHARACTERIZATION OF SMALL-MOLECULE MODULATORS THAT PROMOTE CANCER CELL ELIMINATION

Dissertation

For the achievement of the academic degree of the

Doctor in Natural Sciences

(Dr. rer. nat.)

Submitted to

Department of Chemistry and Chemical Biology

Technical University Dortmund

by

Aylin Binici

born on July 14, 1995 in Duisburg

Dortmund 2024

Die vorliegende Dissertation wurde im Zeitraum von November 2019 bis September 2024 unter der Anleitung von Prof. Dr. Dr. h.c. Herbert Waldmann und Dr. Slava Ziegler an dem Max-Planck Institut für Molekulare Physiologie und an der Fakultät für Chemie und Chemische Biologie der Technischen Universität Dortmund angefertigt.

Dekan:

Erstgutachter: Prof. Dr. Dr. h.c. Herbert Waldmann

Zweitgutachter: Prof. Dr. Carsten Watzl

Dedicated to my Grandparents

Şeyhhamit and Fatma Kavak

Sonsuza kadar size minnettar kalacağım.

‘‘As a research worker, the unforgotten moments of my life are those rare ones which come after years of plodding work, when the veil over nature's secret seems suddenly to lift and when what was dark and chaotic appears in a clear and beautiful light and pattern.’’

GERTY THERESA CORI

The results presented in this doctoral thesis contributed to the following publication:

A. Binici*, E. Hennes*, S. Koska, J. Niemann, A. Reich, C. Pfaff, S. Sievers, A. S. Kahnt, D. Thomas, S. Ziegler, C. Watzl, H. Waldmann, *"Identification of small molecule-enhancers of NK cell tumoricidal activity via a tumor microenvironment-mimicking co-culture assay", bioRxiv*, 2024.09.04.611205, https://doi.org/10.1101/2024.09.04.611205 (2024).

*Co-first authors, these authors contributed equally to the publication.

ACKNOWLEDGEMENTS

‘‘In the field of science, gratitude goes to those who illuminate paths we might never have traveled alone.’’ – ***Unkown***

This thesis would not have been possible without the support of many brilliant individuals who not only shaped me as a scientist but also contributed to my personal growth. The past years have been filled with countless challenges, and I’m thankful to have met many people who made this experience joyful and memorable.

First and foremost, I would like to express my deepest gratitude to my supervisor, Prof. Herbert Waldmann, for providing me with the opportunity to work on two incredibly exciting projects during my PhD. I am profoundly grateful for the freedom to work independently, as well as his unwavering support and patience. The insight into his thought processes and approach to chemical biology that I witnessed during these years never failed to inspire and motivate me.

I want to express my gratitude to my co-supervisor, Dr. Slava Ziegler, for consistently sharing her wisdom and providing constructive feedback during our numerous discussions. Her patience, everlasting support, valuable advice, and confidence in my abilities have significantly improved the quality of my work. Our shared enthusiasm for creating scientific figures has added an enjoyable dimension to these years.

I am very grateful to Prof. Carsten Watzl, who, as my TAC member, provided me with valuable guidance and constant scientific assistance as well as for welcoming me into his lab. His role as the second examiner for this thesis is also greatly appreciated. I also want to extend my thanks to Jens Niemann for his support of the NK cell project. I truly appreciated our time working together in the lab.

A big thank you is owed to my organic food buddy, Dr. Elisabeth Hennes, who is not just an inspiring scientist but also a wonderful friend. Her dedication and fierceness in the lab are truly admirable, and working with her on a project was a pleasure. Our shared excitement for results, frustration, countless troubleshooting sessions, and her constant creative ideas have influenced the way I approach challenges. Together with our fellow scientist friends Dr. Stefan Zimmermann, Dr. Georg Niggemeyer, and Dr. Jessica Nowacki, we have spent many hours exploring science in every aspect of our lives. Our long discussions and mutual curiosity for understanding life were great learning experiences and so much fun. Thank you!

I want to thank my highly talented master's students. I would like to thank Alisa Reich for her hard work and dedication, which greatly advanced the progress of the NK cell project. Similarly, I want to extend my thanks to Sandra Koska, for her enthusiasm for the project, reliability as well as her great contribution. We enjoyed many happy moments together, whether it was in the lab during long pipetting sessions or outside with the Fantastique 4. Additionally, I want to express my gratitude to Malte Gersch for being a part of my TAC committee and providing scientific input throughout my PhD, and to Nikolas Klink for his research compound.

The smell of Earl Grey tea and tea-time treats will always remind me of three fabulous women. My sincere thanks go to Dr. Caitlin Davies for always believing in my skills, which was a great source of motivation for me. Her adventurous nature was contagious and created a great atmosphere in the group. Her advent calendars were always a December highlight for us! My heartfelt thanks also go to Dr. Lara Dötsch. Her calm demeanor kept me grounded through many chaotic and challenging moments – truly the yin to my yang. I also would like to express my gratitude to Dr. Sarah Zinken, the artist within our tea-time pals. We shared so much laughter, and after all, every curly brunette needs her curly blonde counterpart. Thank you all for being such great friends and for your support!

I had the pleasure of working with incredible labmates in D3.32. I would like to thank Beate Schölermann for sharing years of experience, creating a fun and clean atmosphere, always having an open ear for our concerns, and for her experimental support. I extend my thanks to my two amazing mentors, Dr. Elena Reckzeh and Dr. Julian Wilke. I am also grateful to Alexandra Brause, our honorary D3.32-member, for her constant support. And, of course, my time in the lab would not have been the same without these great people: Dr. Yasemin Akbulut, Siska Führer, Dr. Belén Lucas, Celine Da Cruz Lopes Guita, and Jana Bonowski.

I am deeply thankful to the COMAS team. I want to express special gratitude to Dr. Sonja Sievers and Christiane Pfaff, whose contributions made the compound screening for my project possible. Furthermore, I would like to thank the in-house HRMS as well as the crystallography and biophysics teams, namely, I would like to mention Dr. Petra Janning, Dr. Raphael Gasper, Jens Warmers, and Malte Metz. Moreover, I would like to express my gratitude to all current and past members of department 4 who made my time there memorable. Specifically, I want to mention Eric Ogel, Georg Goebel, Cedrik Kühling, Dr. Jiming Hwang, my Yoga buddy Kim Wendrich, Kai Gallant, Dr. Rachel O'Dea, Kim Fischer, Dr. Romain Tessier, Dr. Andrei Ursu, Dr. Hélène Adihou, Dr. Tabea Lügger, Dr. Adrian Krzyzanowski, Dr. Caiming Wang, Dr. Gang Xue, Dr. Michael Grigalunas, Dr. Ruirui Zhang, Dr. Xiufen Cheng, Christine Nowak, and Sasikala Thavam.

Additionally, I want to acknowledge the contributions of Brigitte Rose and Birgit Apprecht, who are the backbone of the department.

I would like to express my gratitude to the Max Planck Research School for Living Matter and Joachim-Herz-Stiftung for their financial and scientific support. Moreover, I am sincerely grateful to Christa Hornemann and Dr. Lucia Sironi. Both of them offered consistent check-ins and tremendous support.

Most importantly, I am deeply thankful to my family and friends for their unconditional love and support, emotional reassurance, and the distractions they offered when needed. I would like to thank my grandparents, Şeyhhamit and Fatma Kavak, whose sacrifices and relentless efforts laid the foundation of my journey. I would also like to express my heartfelt appreciation to Fadime, Christian, Tyron and Dilara Materla, Gülbahar Kavak, Lemanur Kavak, Ayla and Ceyhun Binici, Ekaterina Appelhans, Denise Fellmeth and Alisa Kahler. Finally, I must express my deepest gratitude to my partner, Enis Kaan Aktan.

Thank you!

TABLE OF CONTENT

I. ABSTRACT

The devastating disease of cancer has been part of human history since ancient times. It wasn't until the early 2000s that researchers, including Hanahan, Weinberg, and Schreiber, described the fundamental differences between cancer and healthy cells and the host-protective and tumor-aiding role of the immune system in cancer development and progression. These crucial findings facilitated the development of more effective and targeted cancer treatment strategies. However, resistance mechanisms and side effects remain an accompanying phenomenon of cancer treatments, highlighting the need for the development of novel small-molecule modulators.

In this thesis, two approaches were utilized to combat cancer. The first approach focused on an indirect strategy to fight cancer *via* the immune system, namely natural killer (NK) cells, to eliminate cancer cells. In the tumor microenvironment (TME), cancer cells and the surrounding supportive tissue utilize immune inhibitory pathways, leading to the secretion of immunosuppressive factors such as kynurenine, prostaglandin E2 (PGE_2), and transforming growth factor β (TGFβ). These factors contribute to tumor progression by reducing the immunogenicity of the cancer cells, ultimately enabling them to evade immune-mediated destruction by NK cells. A co-culture-based assay system was designed to mimic the immunosuppressive nature of the TME using primary lymphocytes and a lung carcinoma cell line A549 along with immunomodulatory factors in order to screen for small molecules that restore NK cell-mediated destruction of cancer cells. A medium-throughput screening with a library of 29,502 compounds enabled the identification and validation of 11 small molecules targeting glycogen synthase kinase 3β (GSK-3β), TGFβ type I receptor (TGFβR-1), as well as inhibitors of proteins that have not been linked to NK cell activity, including phosphatidylinositol 3-kinase (VPS34), and bromodomain-containing proteins (BRD) 2, 3, and 4. The TGFβR-1 inhibitor RepSox stood out from other hits due to its ability to negate the impact of both immunosuppressive factors used in the assay, thereby significantly increasing NK cell cytotoxicity. This effect can not only be attributed to the inhibition of TGFβR-1 but also to its function as a cyclooxygenase-1 (COX-1) inhibitor, presenting a new strategy to overcome NK cell-suppressive mechanisms within TME.

The second approach aimed to target cancer cells through inhibition of the small GTPase KRas (Kirsten rat sarcoma), which is mutated in 17 % of all solid tumors. The available FDA-approved drugs that directly target KRas, are currently limited to the G12C mutant. However, patients frequently develop resistance mechanisms in the form of secondary KRas mutations during the course of treatment. The activity of KRas is intricately linked to its plasma membrane localization, and its translocation is facilitated through interaction with the prenyl group-binding chaperone

ABSTRACT

retinal rod rhodopsin-sensitive cGMP 3',5'-cyclic phosphodiesterase subunit delta (PDEδ). Thus, rather than targeting the oncoprotein itself, inhibiting PDEδ may present a more viable strategy. Previous research conducted by the Waldmann group has confirmed the feasibility of targeting PDEδ using small molecules. However, a pronounced discrepancy exists between the efficacy of these compounds *in vitro* and *in cellulo*. This difference may be associated to the ADP-ribosylation factor-like proteins 2 and 3 (Arl2/3)-mediated release of the compounds. In response to this challenge, a covalent inhibitor named Deltacovalin was developed, which is based on the structure of Deltasonamide 1. Cell-based experiments employing mammalian and murine cell lines with varying KRas mutational statuses demonstrated that the viability of KRas-dependent cells was greatly reduced or completely disrupted following sequential treatments with Deltacovalin. Deltacovalin-mediated impairment of KRas-PDEδ interaction affected KRas downstream targets. These results open new avenues for targeting KRas-dependent cancer.

II. KURZZUSAMMENFASSUNG

Die Krankheit Krebs gehört seit der Antike zur Menschheitsgeschichte. Erst zu Beginn der 2000er beschrieben Forscher, darunter Hanahan, Weinberg und Schreiber, die fundamentalen Unterschiede zwischen gesunden und Krebszellen Zellen sowie die Rolle des Immunsystems bei der Entstehung und dem Fortschreiten von Krebs, die sowohl wirtsschützend als auch tumorbegünstigend sein kann. Diese kritischen Erkenntnisse gestatteten die Entwicklung wirksamerer und gezielterer Strategien zur Behandlung von Krebserkrankungen. Jedoch sind Nebenwirkungen und Resistenzmechanismen nach wie vor eine Begleiterscheinung von Krebsbehandlungen. Dies verdeutlicht die Relevanz der Entwicklung neuartiger Substanzen.

Im Rahmen dieser Doktorarbeit wurden zwei Strategien zur Bekämpfung von Krebs verfolgt. Der Fokus der ersten Strategie war eine indirekte Strategie, welche die Verwendung von NK Zellen zur Beseitigung von Krebszellen voraussetzte. In der Tumormikroumgebung (TMU) nutzen Krebszellen und die umgebene tumorfördernde Gewebe immunmodulierende Signalwege aus, die zur Auschüttung zur Ausschüttung von immunsuppressiven Faktoren wie Kynurenin, PGE_2 und TGFβ führen. Diese Faktoren fördern die Tumorprogression, indem sie die Immunogenität der Krebszellen verringern. Somit wird Krebszellen ermöglicht, sich der immunvermittelten Zerstörung durch NK-Zellen zu entziehen. Zur Identifizierung von Substanzen, die die NK-Zell-vermittelte Zerstörung von Krebszellen fördern, wurde ein auf Co-Kulturen basierendes Testverfahren entwickelt, welches aus primären Lymphozyten, einer Lungenkarzinom-Zelllinie A549 und immunmodulatorischen Faktoren besteht. Dieses Testverfahren soll somit die immunsuppressive Natur der TMU zu imitieren.Bei einem Untersuchungsverfahren mittlerem Durchsatz wurde eine Substanzbibliothek von 29.502 chemischen Verbindungen getestest. Dies resultierte in der Identifizierung und Validierung von 11 Substanzen, darunter GSK-3β und TGFβR-1 Inhibitoren sowie Inhibitoren von VPS34 und der Proteine BRD 2, 3 und 4, die bisher nicht mit der Aktivierung der tumorzerstörenden Funktion von NK Zellen in Verbindung gebracht wurden. Der TGFβR-1-Inhibitor RepSox hob sich im Vergleich zu den anderen identifizierten Substanzen dadurch ab, dass er die Wirkung beider verwendeten immunsuppressiven Faktoren aufheben und dadurch die Zytotoxizität der NK-Zellen deutlich erhöhen konnte. Dies ist nicht nur auf die Inhibition von TGFβR-1 zurückzuführen, sondern auch auf eine gleichzeitige Inhibition von COX-1. Dieser Mechanismus stellt eine neue Strategie zur Überwindung der NK-Zell-suppressiven Prozesse im TMU dar.

KURZZUSAMMENFASSUNG

Die zweite Strategie zielt darauf ab, Krebszellen durch Hemmung der kleinen GTPase KRas zu eliminieren. Diese ist in 17 % aller soliden Tumore mutiert ist. Die bis dato, von der FDA zugelassenen Medikamente, die direkt auf KRas abzielen, sind derzeit auf die G12C-Mutante limitiert. Darüber hinaus entwickeln Patienten im Laufe der Behandlung häufig Resistenzmechanismen in Form von sekundären KRas-Mutationen. Für die Aktivität von KRas ist seine Plasmamembran-Lokalisierung essentiell. Die Translokation von KRas wird durch die Interaktion mit dem Prenylgruppen-bindenden Chaperon, PDEδ ermöglicht. Eine alternative vorgehensweise zur direkten Hemmung von KRas, könnte die Inhibition von PDEδ darstellen. Hier haben vergangene Forschungsarbeiten der Waldmann Gruppe bestätigt, dass es möglich ist, PDEδ mit Substanzen zu hemmen. Jedoch besteht eine evidente Diskrepanz zwischen der Potenz dieser chemischen Verbindungen *in vitro* und *in cellulo*. Dieser Unterschied kann auf die Arl2/3-vermittelte Freisetzung der Substanzen aus der Bindungstasche von PDEδ zurückgeführt werden. Als Lösungsansatz für diese Herausforderung wurde ein kovalenter Inhibitor namens Deltacovalin entwickelt, der auf der chemischen Struktur von Deltasonamide 1 basiert. Zellbasierte Studien mit humanen und Mäusezelllinien mit unterschiedlichem KRas-Mutationsstatus zeigten, dass das Wachstum von KRas-abhängigen Zellen nach sequentiellen Behandlungen mit Deltacovalin stark verringert oder vollständig gehemmt wurde. Ferner konnte gezeigt werden, dass die durch Deltacovalin vermittelte Beeinträchtigung der KRas-PDEδ-Interaktion sich auf nachgeschaltete KRas-Ziele auswirkte. Diese Befunde schaffen neue Optionen zur gezielten Bekämpfung von KRas-abhängigem Krebs.

1. INTRODUCTION

1.1 Cancer

Cancer has been a major cause of death globally for decades.[1] It comprises a large group of diseases that are genetically diverse but have common metabolic changes and altered signaling processes that ultimately lead to uncontrolled cell division.[1,2] In 2020 alone, there were approximately 19.3 million new cancer incidents and 9.9 million cancer-related deaths worldwide, i.e., cancer was responsible for one in six deaths.[3,4] Decades of research have aided the identification of various genetic mutations that may promote tumor development and thus enabled the improvement of therapeutic approaches.[5] Despite the progress in cancer treatment, reducing cancer mortality remains a challenge. A possible challenge in treating cancer lies in the difficulty of detecting cancer in its early stages due to the ability of cancer cells to evade the immune system. Early detection would not only enhance patient survival but also reduce the invasiveness and side effects of treatments.[4] Therefore, the development of novel strategies for early detection of cancer remains a major research focus.

The fundamental differences in functional abilities of cancer compared to healthy cells were defined by the researchers Hanahan and Weinberg in the early 2000s as hallmarks of cancer.[6] The six hallmarks that were proposed initially include sustaining proliferative signaling, evading growth suppressors, activating invasion and metastasis, enabling replicative immortality, inducing angiogenesis, and resisting cell death. In 2011, the hallmarks were extended with four more hallmarks: avoiding immune destruction, deregulating cellular energetics, genome instability and mutations as well as tumor-promoting inflammation. As cancer research progressed, four additional hallmarks and characteristics were identified and added to the existing body of knowledge in 2022: nonmutational epigenetic reprogramming, polymorphic microbiomes, senescent cells, and unlocking phenotypic plasticity.[7] This research work especially focuses on antagonizing the sustenance of proliferative signaling and the avoidance of immune destruction *via* small molecule modulators.

1.2 The role of the immune system in cancer development

More than 100 years ago, researchers discovered the immune system's ability to combat cancer.[8] In the late 19th century, William Coley treated patients with inoperable cancer by utilizing heat-inactivated bacteria.[9] However, at that time, the researcher did not understand that he was triggering an immune response to achieve cancer cell elimination. In 1909, Paul Ehrlich hypothesized that the immune system has a suppressive role for cancer growth.[10] The protective role of the immune system from malignant transforming cells also led to the proposal of the

immunosurveillance theory by Burnet and Thomas.[11,12] However, due to the lack of understanding about the intricate interactions between cancer cells and the immune system, this ability could not be harnessed. A better comprehension of tumor immunity and the dynamic interaction between cells within the tumor microenvironment (TME) led to the concept of immunoediting proposed by Schreiber *et al*.[10] This concept postulates that the interaction between cancer cells and the immune system can result in both host-protective and tumor-aiding outcomes. The process of cancer immunoediting can be divided into three distinct phases: elimination, equilibrium, and escape (Figure 1).

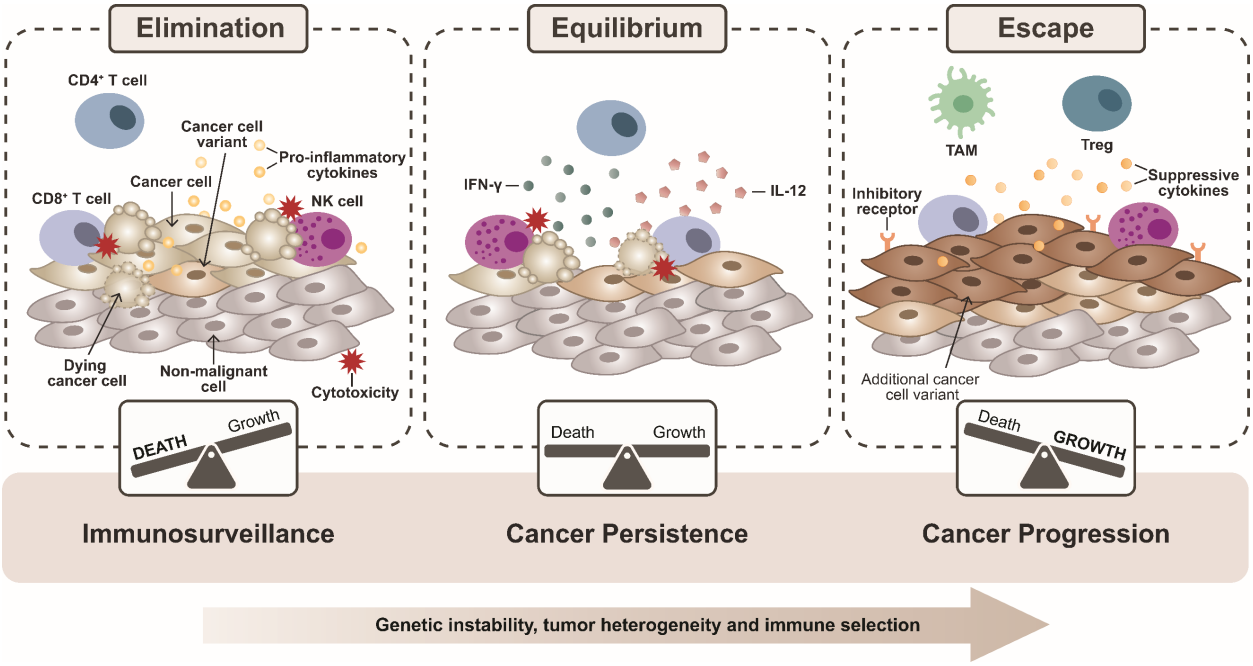

Figure 1: The three Es of cancer immunoediting. In the elimination phase, emerging cancer cells are recognized and eradicated by cytotoxic immune cells, including natural killer (NK) cells and CD8⁺ T cells. Surrounding cells such as CD4⁺ T cells support cytotoxic lymphocytes by secreting cytokines to boost immune response. In the equilibrium phase, the selective pressure driven by the immune system-mediated clearance of cancer cells leads to the development of cancer cell variants with decreased immunogenicity. This ultimately leads to the escape phase and cancer progression. IFN: interferon, IL: interleukin, TAM: tumor-associated macrophage, Treg: regulatory T cell. The figure was adapted from van der Burg *et al*.[13]

In the elimination, also known as the host-protective phase, innate and adaptive immune cells work together to recognize and eradicate emerging cancer cells through immunosurveillance.[14] The immune system can combat tumor growth through different mechanisms. This includes phenotypic changes in cancer cells, like the expression of stress-inducible ligands, presentation of tumor neoantigens, and secretion of damage-associated molecular pattern (DAMP) molecules. These changes facilitate the elimination of tumor cells by cytotoxic lymphocytes like natural killer (NK) cells and CD8⁺ T cells. Cancer cell variants with poor immunogenicity then enter the

equilibrium phase, where they remain dormant but cannot be completely eliminated. In this phase, tumor dormancy is enabled due to a balance between the tumor-promoting cytokines such as IL-10 and anti-tumor factors like IL-12 and IFN-γ.[14] While IL-10 promotes cancer progression by inhibiting the expression of major histocompatibility complex (MHC) class II and co-stimulatory molecules on cancer cells, IL-12 promotes IFN-γ production, and together, they promote cancer elimination by boosting $CD8^+$ T cell and NK cell effector functions.[9,15,16] Additionally, IFN-γ has direct antiproliferative effects on cancer cells.[9] Due to the selective pressure driven by the immune system-mediated clearance of cancer cells, some cells acquire the ability to circumvent immune control and propagate. Such cells enter the third phase, also known as the escape phase. In this phase, cell types surrounding the tumor (e.g., regulatory T cells and tumor-associated macrophages) aid in shaping the TME by promoting tumor growth and creating an immunosuppressive network.[17] Cancer cells acquire various resistance mechanisms to avoid immune destruction such as the reduced levels of antigens like MHC-I, which impedes immune recognition. Additionally, cancer cells may also increase the expression of anti-apoptotic molecules, such as Bcl2, or counteract cytotoxic lymphocytes by expressing inhibitory molecules like PD-L1.[14,18]

1.3 The tumor microenvironment (TME)

A greater understanding of tumors led to a shift from the simplistic perspective of tumors as mere accumulation of malignant cells to acknowledging the complexity of the environment surrounding them. Previously, the interactions between different cell types located in the tumor microenvironment (TME) and immunosurveillance were poorly comprehended. Today, it is widely recognized that anti-tumor immunity is tightly controlled by a balance of immune inhibitory and stimulatory pathways.[8,19] However, cancer cells in the TME create a pro-tumorigenic environment through different mechanisms aiding the decrease of the immunogenicity of cancer cells, allowing them to evade immune cell-mediated elimination.

The tumor microenvironment is an incredibly organized ecosystem harboring various acellular and cellular components, including malignant and non-cancerous cells (Figure 2). Non-cancerous cell types present in the TME include fibroblasts and immune cells such as macrophages, dendritic cells, neutrophils, and lymphocytes such as B cells, T cells, and NK cells.[2] The immune system has a dual role in the TME, where the presence of inflammatory processes determines whether immune cells are pro- or anti-tumorigenic. Immune cells such as cytotoxic T lymphocytes (CTLs), NK cells, and pro-inflammatory M1 macrophages help constrain cancer growth.

Pro-inflammatory immune cell types secrete cytokines like IL-15, IFN-γ, TNFα, and reactive oxygen species (ROS) to recruit cytotoxic lymphocytes, thereby aiding tumor cell elimination.[20,21] Persistent inflammation and the acidification of the TME caused by the preferred aerobic glycolysis metabolism of cancer cells can cause immune cells to undergo reprogramming. Together, these processes boost the activation of tumor-promoting cells, including regulatory T cells (Treg), tumor-associated macrophages (TAMs, M2 macrophages), and myeloid-derived suppressor cells (MDSCs), as well as the secretion of pro-inflammatory cytokines such as IL-6 and IL-1β, among others. Additionally, this environment inhibits the cytotoxic activity of lymphocytes, ultimately leading to an exhausted phenotype.[20,22]

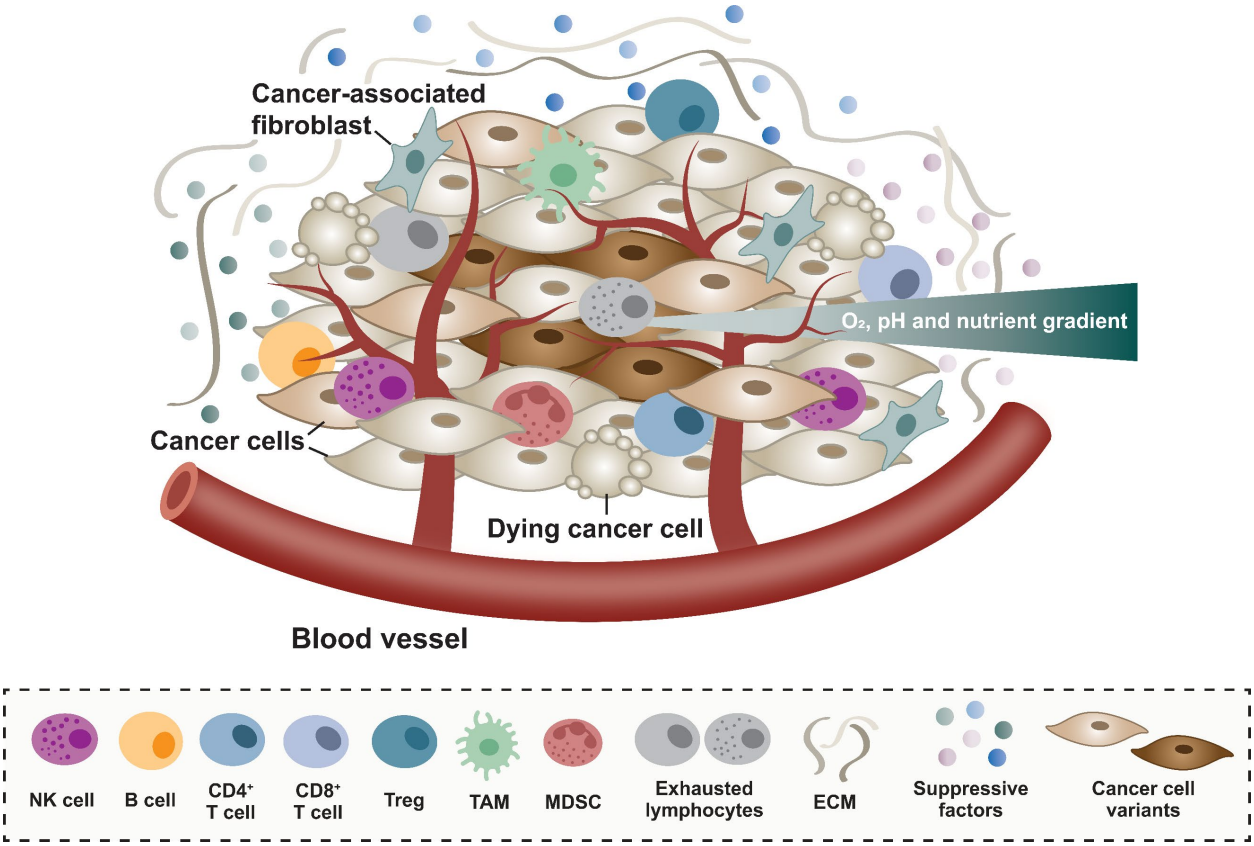

Figure 2: The tumor microenvironment (TME). The TME is a pro-tumorigenic environment harboring various acellular and cellular components. Cellular components present in the TME include different cancer cell variants, lymphocytes,i.e., B cells, NK cells, and T cells, as well as tumor-associated macrophages (TAMs) and myeloid-derived suppressor cells (MDSCs). The acellular components are the extracellular matrix (ECM) and the factors surrounding the tumor. Figure based on D.F. Quail *et al.*[2] and Tiwari *et al.*[21]

Furthermore, cancer cells hijack immune inhibitory pathways through the expression of inhibitory receptors and soluble ligands such as adenosine, vascular endothelial growth factor (VEGF), indolamine-2,3-dioxygenase 1 (IDO1), prostaglandin E2 (PGE_2), and transforming growth factor β (TGFβ), further hampering immune surveillance. Other processes that are important for catalyzing

tumor progression are remodeling the extracellular matrix (ECM) and tumor vascularization. Tumor vascularization ensures the continuous transport of oxygen and nutrients to the tumor site, and the ECM acts as storage for cytokines and growth factors.[23]

1.4 Natural killer (NK) cells

Natural killer cells are large granular cytotoxic lymphocytes that are part of the innate immune system. They were discovered by the research groups of Rolf Kiessling and Ronald Herbermann in the mid-1970s.[24,25] NK cells represent around 5-20 % of the circulating lymphocyte population and develop in the bone marrow as well as in secondary lymphoid tissues in humans.[26] Unlike cytotoxic T cells, NKs are able to sense and eliminate pathogen-infected cells as well as pre-cancerous and cancerous cells without requiring antigen exposure prior to target killing. Therefore, NK cells are indispensable for the mammalian first line of defense against pathogens and tumor development. Generally, NK cells can be divided into two subsets: $CD56^{bright}$ and $CD56^{dim}$. $CD56^{dim}$ NKs make up the majority of human peripheral blood, accounting for more than 90 %.[27] While $CD56^{bright}$ cells are strong producers of cytokines, the $CD56^{dim}$ are characterized by their strong cytolytic capabilities. However, under activating conditions, $CD56^{bright}$ NKs downregulate CD56, resulting in a gain-of-effector functions.

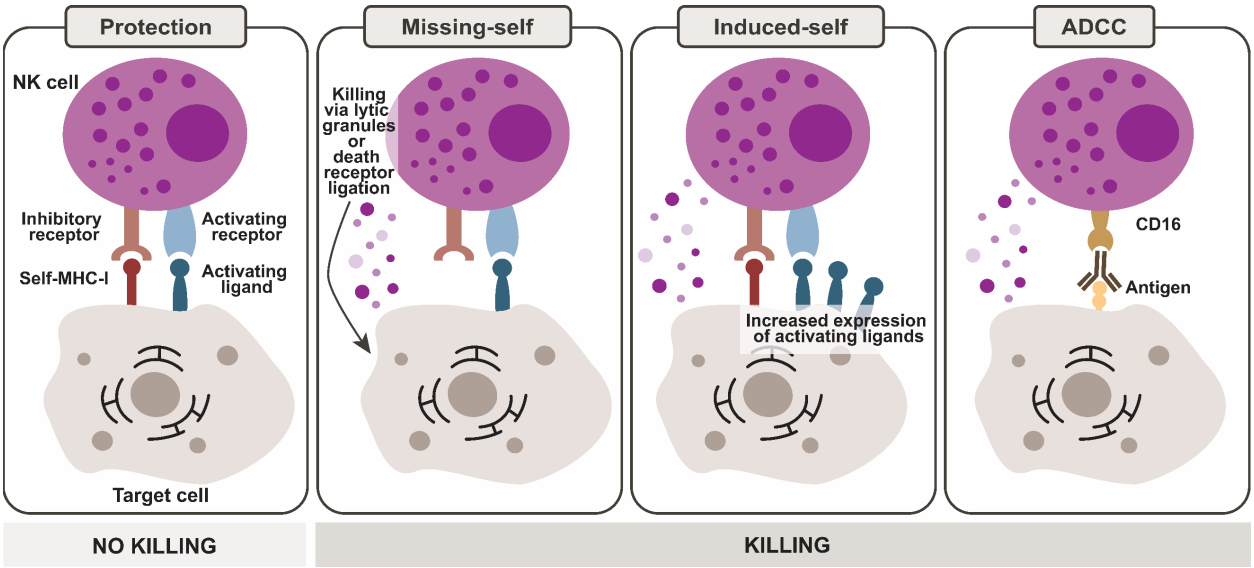

Figure 3: Mechanisms of NK cell target identification. Under normal circumstances, cells are protected from NK cell-mediated cytolysis through a balance between activating signals and inhibitory signals from self-MHC-I molecules. However, malignant transformation or pathogen infections can disrupt this balance. A reduction or the loss of self-major histocompatibility complex class-I (MHC-I) molecules (=missing-self) causes the activating signal to not be opposed and, therefore, results in NK cell-mediated target cell elimination. Pathogen infections or malignant transformations can increase the expression of NK cell-activating ligands (=induced-self), which can overcome NK inhibitory signals. Another interaction that can activate NK cell cytotoxicity is antibody-dependent cellular cytotoxicity (ADCC).

For natural killer cells to acquire functional maturation and self-tolerance, they must undergo an education process. This process involves tight interactions of self-MHC-I molecules expressed on the surface of healthy cells with inhibitory killer cell immunoglobulin-like receptors (KIRs) on NK cells.[26] In addition to inhibitory signals, activating receptors such as natural killer group 2-member D (NKG2D) and natural killer protein (NKps) can regulate NK cell function. NK cells can identify their target cells through various mechanisms (Figure 3).[26,28] Under normal physiological conditions, healthy cells are safeguarded against NK cell-mediated cytolysis through a delicate equilibrium of activating and inhibitory signals delivered from self-MHC-I molecules. However, malignant transformation or pathogenic infections perturb this balance, leading to different NK cell-activating mechanisms. NKs sense reduced or absent expression of self-MHC-I molecules ('missing-self' recognition) or are activated by an increase of NK cell-activating ligands on the surface of infected cells ('induced-self' recognition). Activating ligands for NK cell cytotoxicity include major histocompatibility complex class I chain-related sequence A or B (MICA/B) and UL16-binding protein (ULBP) proteins.[29] Tumor cells with upregulated levels of either MICA or MICB are tagged for NK cell-mediated cytotoxicity. One additional way, in which activation of NK cell cytolysis can occur, is through antibody-dependent cellular cytotoxicity (ADCC) mediated *via* the CD16 receptor on NKs.

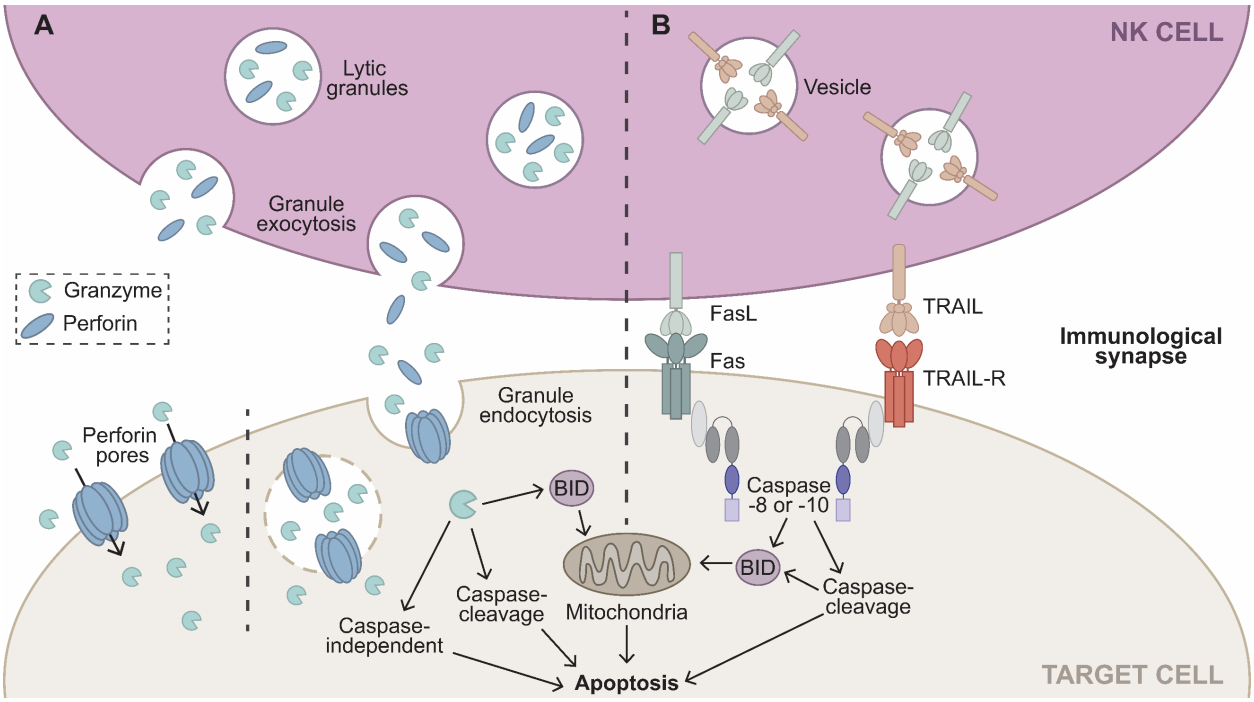

Figure 4: NK cell-mediated cellular cytolysis mechanisms. Upon activation, NK cells eliminate their target cells through two distinct mechanisms. A) Lytic granule-mediated target cell killing begins with the granule release into the immunological synapse. Perforins have the ability to create pores in the target cell membrane, enabling granzymes to enter. Alternatively, lytic granules can enter *via* endocytosis or escape

from endosomes, which is enabled by perforin pores. In the cytosol, granzymes can induce apoptosis through caspase-cleavage, mitochondrial dysfunction by BID-cleavage, and caspase-independent pathways. B) Engagement of death receptors Fas and TRAIL-R with their respective ligands FasL and TRAIL leads to apoptosis by activating a caspase cascade or inducing mitochondrial dysfunction through BID cleavage. The figure is based on I. Prager & C. Watzl.[30]

Just like cytotoxic T cells, NK cells induce apoptosis in target cells *via* exocytosis of lytic granules containing perforin and granzymes or death receptor ligation (FasL/TRAIL).[30,31] However, T cells require the engagement of a T cell receptor for activation, whereas NK cells are regulated by a balance of inhibitory and activating receptors.[32] Upon target cell recognition, NK cells form contact with the respective target cell through an immunological synapse (Figure 4). NK cells can then eliminate their targets using two mechanisms: the release of lytic granules and death receptor ligation, of which the lytic granule release is the primary mechanism.[33] Human NK cells express various granzymes (A/B/H/K/M), and the elimination of target cells is likely achieved through a combination of these granzymes, with granzyme B (GzmB) being the most well-characterized.[34,35] NK cell degranulation is facilitated by the reorganization of its cytoskeletal machinery, including the reorientation of the microtubule-organizing center (MTOC) and actin, guiding them in a controlled manner through the immunological synapse toward the target cell membrane.[26,36] At the target cell membrane, perforin molecules aggregate and form ring-shaped pores that allow GzmB to enter the target. Alternatively, cytolytic granules may be taken up through endocytosis, and their entrance into the cytosol is aided by perforin pores. Granzyme B can activate the intrinsic apoptosis program by caspase-dependent mechanisms by cleavage of caspase-3 and -8 or caspase-independent mechanisms, as well as by cytochrome c release by mitochondria induced by proteolytic cleavage of BID.[30] Death receptor-mediated killing (Fas/FasL and TRAIL-R/TRAIL) is an alternative way for target cell elimination and induces apoptosis by activation of a caspase cascade or through mitochondrial dysfunction by BID-cleavage. Interestingly, death receptor expression in target cells can be induced by NK cell-derived IFN-γ, which is secreted upon activation to support host defense.[26]

1.4.1 NK cells in the immunosuppressive TME

NK cells play a crucial role in host immune defense, controlling tumor growth as they display cytotoxic functions against pre-cancerous and cancerous cells. In order for NK cells to recognize and kill diseased cells, they must be activated. This can be achieved through stimulation with cytokines such as IL-2 or IL-15, which mediate cytotoxic NK cell functions by upregulating perforin and granzyme B levels.[37] Furthermore, tumor cells can express activating ligands such as MICA and MICB (MICA/B), which serve as ligands of the NKG2D receptor and thereby activate NK cells.[38] However, the tumor microenvironment supports cancer cell resistance to NK cell-mediated

elimination through various mechanisms leading to an exhausted phenotype. One major mechanism involves the proteolytic shedding of MICA/B molecules, which can bind to NKG2D on NKs and lead to NK cell exhaustion through persistent engagement.[38,39] Additionally, suppressive factors derived from cells within the TME, including TGFβ, PGE_2, kynurenine (kyn), reactive oxygen species (ROS), adenosine, and lactate, can inhibit the cytotoxic activity of NK cells (Figure 5A).[40-42]

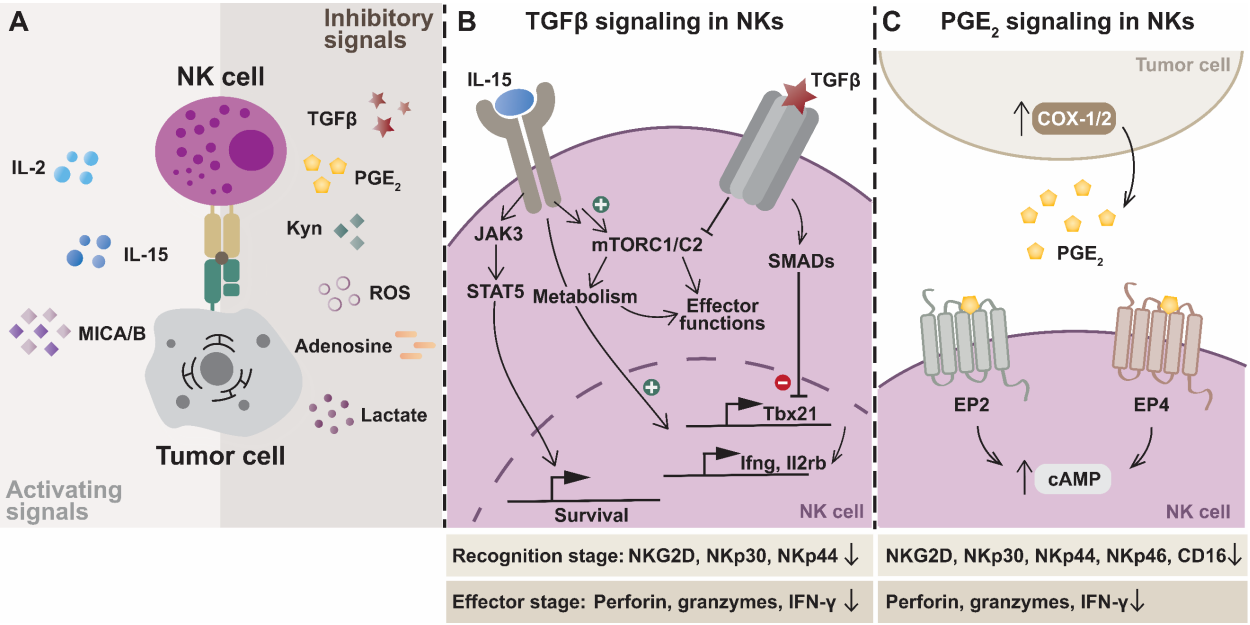

Figure 5: TME-mediated mechanisms to modulate NK cells. A) The TME is a complex ecosystem harboring different activating and inhibitory signals influencing NK cell activity. The intricate interactions between different cell types in the TME facilitate the secretion of inhibitory factors and, thus, the development of an immunosuppressive ecosystem that leads to an exhausted phenotype in NK cells. B) TGFβ signaling in natural killer cells. While IL-15 promotes NK cell effector functions through mTOR signaling and survival, TGFβ counteracts these effects. TGFβ directly represses mTOR signaling, downregulates activating receptors NKG2D, NKp30 as well as NKp44, and also downregulates effector molecules such as granzymes, perforin, and IFN-γ. C) PGE_2 suppresses NK cell cytotoxicity through prostaglandin E2 receptor EP2 and EP4. Interaction of PGE_2 with EP2/4 increases adenylate cyclase activity, upregulating the levels of cyclic adenosine monophosphate (cAMP). This, in turn, leads to a downregulation of NK cell-activating receptors and effector stage molecules.

The TGFβ signaling pathway plays a critical role in regulating numerous cellular processes, such as differentiation, proliferation, apoptosis, and immune responses.[43] Aberrant activity of this pathway can be found in various cancer types (i.e., breast, colorectal, and prostate cancer) and promotes cancer immune escape due to its powerful immunosuppressive effect (Figure 5B).[43,44] Upon binding of TGFβ ligands to its type II receptor TGFβ receptor, TβRII, the type I receptor TβRI is recruited which leads to a phosphorylation cascade. SMAD4 then forms a heterotrimeric complex with phosphorylated SMAD2 and SMAD3 that activates the transcription of its respective

target genes in the nucleus.[43] IL-15 activates NK cell metabolism and effector functions through mTOR signaling, and it promotes their survival through JAK-STAT signaling. TGFβ stimulation, on the other hand, counteracts these effects and consequently inhibits the activation of NK cells. Additionally, TGFβ signaling interferes with IL-15-induced Tbx21 transcription and thereby decreases expression levels of IFN-γ and IL-2Rβ.[44] It downregulates the levels of NK cell-activating receptors NKG2D, as well as NKp30 and NKp44, and suppresses NK cytotoxicity by downregulating the levels of granzymes and perforin.[42]

Another mechanism that aids tumor evasion and directly suppresses NK cell function is prostaglandin E2 signaling.[45] PGE_2 is produced by cyclooxygenase enzymes 1 and 2 (COX-1 and COX-2), and COX-2 is often overexpressed in various cancer types, including breast, colorectal, lung, and pancreatic cancer.[46] Active PGE_2-EP2/4 signaling induces nuclear translocation of CRE-binding protein (CREB), leading to increased COX-2 levels and PGE_2 production in cancer cells.[47,48] In the TME, pro-inflammatory PGE_2 molecules modulate NK cell cytotoxicity through prostaglandin receptor E2 subtypes EP2 and EP4.[49] Stimulation of EP2 and/or EP4 by PGE_2 results in increased adenylate cyclase activity. This leads to an increase in intracellular cAMP levels and downregulation of NK cell-activating receptors such as NKG2D, NKp30, NKp44, NKp46, and CD16, as well as effector molecules like IFN-γ, granzymes, and perforin.[42,47] It also leads to an upregulation of NK cell inhibitory receptors like NKG2A.[50]

1.4.2 Cancer immunotherapies: NK cells on the frontline

A better comprehension of the architecture of the TME enabled the development of numerous successful immunotherapeutic approaches. Many therapies aim to inhibit the immunosuppressive interactions between immune and cancer or antigen-presenting cells.[51] One successful immunotherapeutic approach to treat cancer is the use of monoclonal antibodies that block inhibitory immune checkpoints. The interactions with inhibitory checkpoints are usually crucial for regulating the immune system anf thereby preventing autoimmunity and maintaining peripheral tolerance. Cancer cells hijack these pathways to escape cytotoxic T and NK cell-mediated eliminiation. Immune checkpoint inhibitors reverse the negative regulation of cytotoxic T-cell function.[52] Two of the most commonly targeted checkpoints are CTLA-4 (e.g., ipilimumab, approved 2011 by the U.S. Food and Drug Administration (FDA)) and programmed cell death protein 1 (PD-1) or ligand 1 ((PD-L1) e.g., pembrolizumab and nivolumab, FDA approved in 2014). These were able to restore T-cell function and showed encouraging results in clinical trials against certain malignancies (e.g., advanced melanomas, lung and kidney cancer).[51-53] These findings revolutionized the field of immuno-oncology, and therefore, the researchers J. P. Allison and

T. Honjo received the Nobel Prize in Physiology or Medicine in 2018 for their significant contribution to these novel therapy approaches.[54] Another clinically successful immunotherapeutic approach to treat cancer uses engineered cytotoxic T cells with a chimeric antigen receptor (CAR). In 2017, Kymriah® became the first FDA-approved CAR T cell therapy for B-lymphoid malignancies treatment.[55] Although immunotherapeutic approaches have achieved great success, numerous challenges remain. Immune checkpoint inhibitor-based therapies only have a patient response rate of 20-30 %, and CAR T cell therapies cause life-threatening adverse effects, such as cytokine release syndrome. Additionally, CAR T cell-based drugs are ineffective in treating solid tumors, which represent 90 % of human tumors, due to immunosuppressive interactions in the TME that cause exhaustion.[55,56]

Many immunotherapeutic strategies focus on utilizing cytotoxic T cells, however, NK cells possess numerous advantageous properties as well, making them suitable for immunotherapy.[57] Therefore, various approaches to harness their full anti-tumor activity are currently being investigated. One of the biggest advantages is that, unlike T cell-based therapies, strategies using NKs do not require personalization for each patient through the use of autologous cells, as there is a remote likelihood of graft-versus-host disease (GVHD).[58] This is particularly beneficial for the manufacturing process as it would be less time-consuming (21-35 days for CAR T cell generation) and costly (up to 500,000 $ for CAR T cell therapies) and would allow the production of an ''off-the-shelf'' product.[55,58] However, initial strategies utilizing the adoptive transfer of NK cells focused on promoting tumor recognition and cytotoxic capacities, i.e., by *ex-vivo* conditioning using activating cytokines such as IL-2 or IL-15, had mixed outcomes.[58,59] One of the main obstacles to using NK cell-based therapies to treat solid tumors is that when NK cells reach the tumor site, their cytotoxicity is inhibited through suppressive factors in the TME, leading to an exhausted phenotype.[60] Therefore, novel strategies to preserve NK cell tumoricidal activity within the TME, e.g., by engineering them with CARs or T cell receptors (TCRs) or using monoclonal antibody-based therapies targeting tumor-specific antigens, were explored and showed encouraging results.[58] Despite the fact that monoclonal antibodies-based checkpoint inhibitors have shown promising results in clinics, they have limitations, such as the requirement for infusion and the possibility of immune-related adverse effects.[61] Small molecules have several advantageous attributes justifying their use as drugs, including their oral availability, short half-lives, and reversible action, which reduces the chance of lasting adverse effects.. Additionally, small molecules could be utilized to modulate pathways within tumor cells that are involved in the suppression of the immune system or by directly targeting NKs, thereby enhancing their tumoricidal activity.[61,62] Immunomodulatory drugs (IMiDs) and proteasome inhibitors enhance NK

cell cytotoxicity by upregulating the levels of NK cell receptors DNAX accessory molecule-1 (DNAM-1) and NKG2D activating ligands (such as MICA or poliovirus receptor (PVR)).[60] Other relevant targets for boosting NK cell cytolytic activity are TGFβ, IDO1, glycogen synthase kinase 3 (GSK3), and arginase inhibitors, as well as Toll-like receptor (TLR) agonists.[60,63-65] Utilizing such small molecules for combinational immunotherapies may effectively preserve anti-tumor immunity and simultaneously enhance the efficacy of existing immunotherapies.

1.5 Oncogenic KRas signaling and the role of its chaperone PDEδ

The rat sarcoma (Ras) superfamily consists of small GTPases of over 150 human members, including its most prominent members HRas (Harvey Ras), KRas (Kirsten Ras), and NRas (Neuroblastoma Ras).[66-70] The three *RAS* genes encode four proteins: HRas, KRas4a, KRas4b, and NRas. Ras proteins consist of two main domains: a G domain that facilitates GTP hydrolysis through a conformational change of the switch I and II motifs and a C-terminal hypervariable region (HVR) including the CAAX (C: cysteine, A: aliphatic amino acid, X: any amino acid) motif. The CAAX motif is crucial for posttranslational modifications (PTMs) such as carboxymethylation, farnesylation, and palmitoylation, which are essential for Ras function and membrane localization.[70,71] While KRas4a, NRas, and HRas are farnesylated and palmitoylated, KRas4b is only farnesylated and has additional positively charged lysine side chains that enable stable membrane anchoring.[72,73]

Ras proteins are commonly mutated in human cancers.[70,74] KRas is one of the most frequently mutated oncogenes in several fatal cancer types (approx. 86 % of Ras-driven cancers), such as colorectal, pancreatic, and non-small cell lung cancer (NSCLC).[74-76] Tumor-associated KRas mutations are predominantly single-nucleotide missense mutations, with G12 mutations being most prevalent in cancers (85 % lung, 91 % pancreatic ductal, and 68 % colorectal adenocarcinoma), followed by G13 and Q61 mutations.[76-78] In healthy cells, activation of KRas can occur through stimulation of receptor tyrosine kinases (RTKs) by extracellular growth factors (i.e., epidermal growth factor (EGF)).[75] Within cells, Ras proteins act as molecular switches that transduce these extracellular stimuli intracellularly. The activity of Ras proteins is balanced through cycling between the GTP-bound active state and GDP-bound inactive state mediated by guanine nucleotide exchange factors (GEFs, e.g., son of sevenless (SOS)) and GTPase-activating proteins (GAPs), respectively.[75] Active KRas can stimulate downstream pathways such as the RAF-MEK-ERK and PI3K-Akt-mTOR pathways. This leads to the transcription of its target genes (e.g., ELK, MYC, and JUN) in the nucleus, which regulate various cellular processes, including adhesion, migration, differentiation, proliferation, and survival.[70,77] Activating mutations

in Ras result in a constant GTP-bound active state (Figure 6A). This process occurs early in tumor development and is accompanied by the loss of tumor suppressor proteins (i.e., tumor protein 53 (TP53) or adenomatous polyposis coli (APC)), leading to amplified oncogenic signaling and tumor progression.[76]

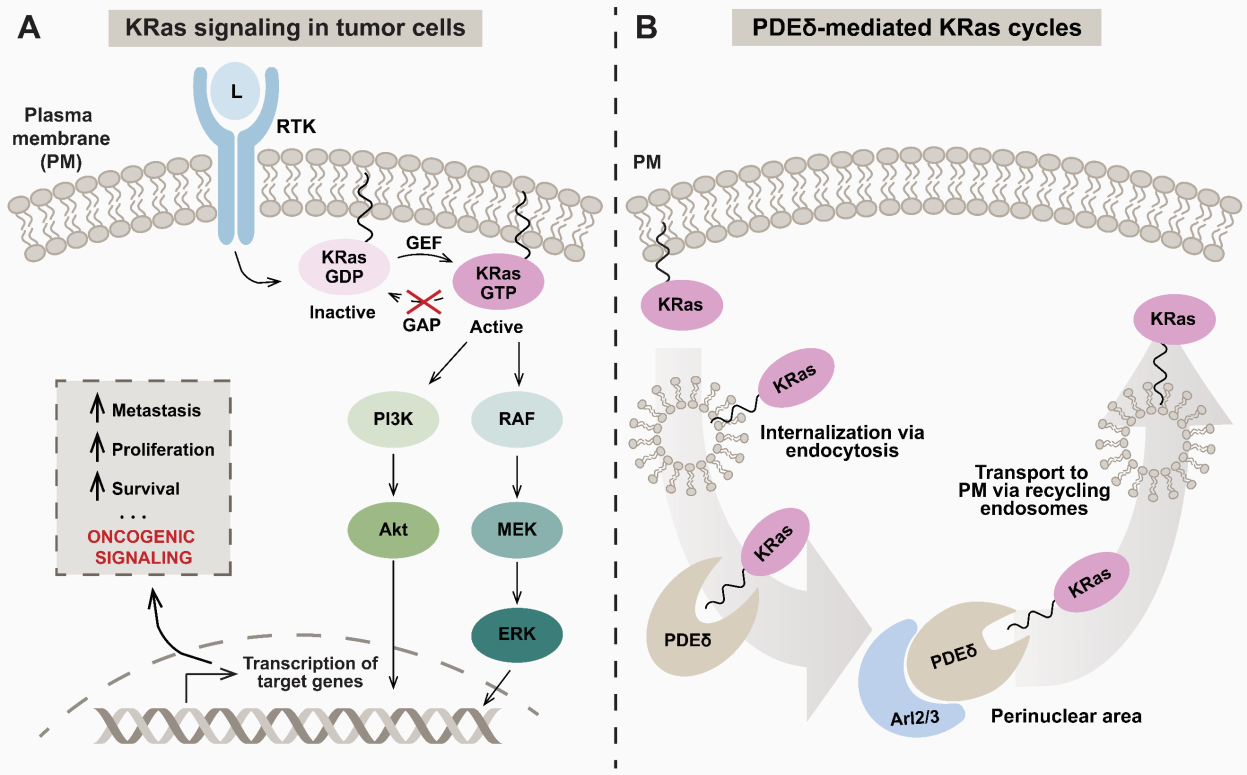

Figure 6: Cellular KRas signaling activity and PDEδ-mediated trafficking cycle. A) KRas-mediated oncogenic signal transduction cascade. Upon binding of an extracellular growth factor (L) to its receptor tyrosine kinase (RTK), a signaling cascade that activates KRas is initiated. Activated KRas can stimulate various signaling pathways, such as RAF-MEK-ERK and PI3K-Akt-mTOR, leading to the transcription of target genes involved in metastasis, proliferation, and survival. B) Spontaneous dissociation of KRas from the plasma membrane into the cytosol results in uptake through endocytosis. The positively charged stretch of KRas enables its anchoring at negatively charged phospholipid membranes (e.g., PM or endocytic vesicles). KRas is transported through the cytosol by forming a complex with PDEδ, which enables its solubilization. Arl2 and/or Arl3 (Arl2/3) bind to the KRas-PDEδ complex in the perinuclear region, assisting in KRas dissociation. Finally, KRas binds to negatively charged recycling endosomes and is transported back to the plasma membrane.

A critical factor for proper KRas-mediated signal transduction is its localization at the plasma membrane. A key aspect of KRas enrichment at the plasma membrane during its trafficking cycles involves its solubilization within the cytosol, enabled by the protein retinal rod rhodopsin-sensitive cGMP 3',5'-cyclic phosphodiesterase subunit delta (PDEδ).[79,80] The PDEδ protein was initially found as the fourth subunit of rod cGMP phosphodiesterase 6 (PDE6) in retinal cells.[81] PDE6 is a membrane-associated prenylated protein consisting of two catalytic α- and β- subunits and two

inhibitory γ-subunits.[82] PDEδ acts as a solubilizing factor for PDE6, reducing phototransduction and light-activated cGMP hydrolysis without disrupting its catalytic function.[82] While PDE6 is exclusively expressed in the retina, PDEδ is expressed throughout all mammalian cell types, indicating that its function goes beyond solubilizing PDE6.[83] Indeed, through its β-sandwich fold-like structure, PDEδ has a hydrophobic pocket that allows engagement with various prenylated proteins, including Ras, Rab13, Rab28 Rheb, Rho6, RhoB, Rap1a, and Rap2b.[83,84] Additionally, the ADP-ribosylation factor-like proteins 2 and 3 (Arl2/-3) can bind to PDEδ in an allosteric fashion, stabilizing a conformation that facilitates the release of PDEδ's cargos. Throughout its trafficking cycles, KRas is internalized *via* endocytosis, followed by its dissociation from endocytic vesicles into the cytosol or local endomembranes (Figure 6B). The affinity of KRas towards uncharged endomembranes is lower compared to negatively charged plasma membranes. Consequently, the trapping of KRas by prenyl-binding PDEδ within the cytosol is enabled. PDEδ is essential for solubilizing and enabling free diffusion of KRas in the cytoplasm. In the perinuclear region, Arl2/3 mediate the allosteric release of the farnesylated cargo in a GTP-dependent manner.[85,86] The locally increased levels of KRas lead to its accumulation at recycling endosomes, triggering the transport back to the plasma membrane.

1.5.1 Strategies for targeting KRas signaling and the potential of PDEδ inhibition

The high prevalence of Ras mutations, particularly KRas, in aggressive cancer types, along with evidence indicating a reliance on sustained oncoprotein expression for tumor survival, underlines the relevance of developing KRas inhibitors.[87] Sequencing studies showed that approximately 17 % of all solid tumors have KRas mutations.[88] These include 86 % pancreatic, 41 % colorectal, and 32 % lung adenocarcinomas.[78] Moreover, aberrantly active KRas mutants have an immunosuppressive effect on the TME and are implicated in tumor immune evasion.[89] The KRas signaling pathway increases the levels of pro-inflammatory factors in the TME, including IL-6, IL-8 and IL1α, which are essential for the initiation and progression of tumors.[90-92] The oncoprotein promotes tumor immune escape by promoting the secretion of immunosuppressive cytokines such as TGFβ and IL-10 (i.e., leading to the conversion of $CD4^+$ T cells into Tregs) and the expression of inhibitory ligand PD-L1.[74,93] This highlights the importance of abrogating KRas activity to target KRas dependent cancer cells and to simultaneously enhance anti-tumor immunity and thereby reduce cancer immune evasion.[93]

For numerous years, the direct targeting of Ras oncoproteins has posed great challenges, leading to the widespread belief that Ras proteins are "undruggable" due to a lack of pharmacologically targetable pockets.[88] Attempts to develop GTP-competitive inhibitors to replicate the approach of

ATP-competitive kinase inhibitors failed because Ras proteins have a picomolar affinity to GTP, whereas kinases have a micromolar affinity to ATP.[76] The discovery of a new pocket within the switch-II region, crucial for the conformational change of Ras proteins during activation cycles along with switch I, paved the way for the successful development of mutant-specific Ras inhibitors.[94] The first effective $KRas^{G12C}$ inhibitor, sotorasib (LUMAKRAS®), was FDA-approved in 2021 for the second line of treatment of NSCLC.[95] Sotorasib binds irreversibly to a cysteine close to the switch II pocket of GDP-bound $KRAS^{G12C}$ in a covalent fashion.[96] Adagrasib (KRAZATI®) is a second irreversible $KRAS^{G12C}$ inhibitor approved by the FDA in 2022, with a longer half-life (24 h compared to sotorasib with 5.5 h).[97,98] Several other G12C-specific inhibitors are currently being investigated in clinical trials, including LY3537982, divarasib, and opnurasib.[99] However, a great challenge for these $KRas^{G12C}$-specific inhibitors is the resistance mechanisms patients acquire during treatments. These include on-target resistance during sotorasib or adagrasib treatments in the form of secondary KRas mutations leading to disruptions of drug binding, whereas off-target resistance mechanisms involve mutations of the other Ras isoforms HRas and NRas, which compensate for the suppressed G12C KRas activity.[99]

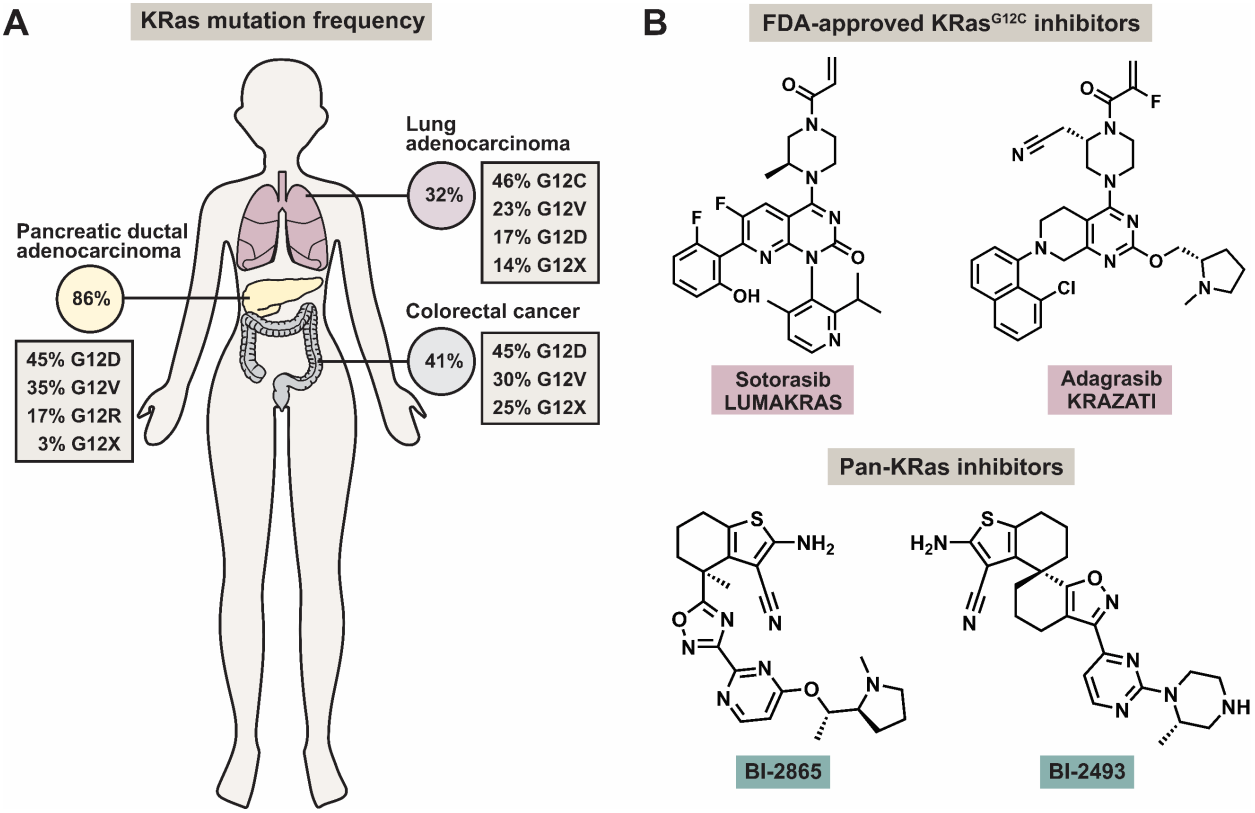

Figure 7: Combating aberrantly active mutant KRas. A) Among different tissues, 86 % of pancreatic ductal adenocarcinoma (PDAC), 41 % of colorectal adenocarcinoma (CRC), and 32 % of lung adenocarcinoma (LAC) mutations can be attributed to KRas. The majority of these KRas mutations are

single-nucleotide missense mutations of codon 12, with PDAC having 91 %, LAC 85 % and CRC 68 % G12 mutations. The mutations at codon 12 involve substitutions of glycine with another amino acid which are either specified or denoted as X. X = A, C, D, F, L, R, S, V or Y. Figure modified according to A. R. Moore *et al.*[78] B) Chemical structures of FDA-approved KRas^{G12C} inhibitors sotorasib (LUMAKRAS®) and adagrasib (KRAZATI®) as well as pan-KRas inhibitors BI-2865 and BI-2493.

Boehringer Ingelheim developed the pan-KRas inhibitor, BI-2865, by removing the warhead of the parental covalent inhibitor, BI-0474. BI-2865 reduces the growth of cells bearing G12C, G12D, or G12V KRas mutations.[100] Its derivative BI-2493 was optimized for *in vivo* administration and attenuated tumor growth in mice bearing different KRas mutations. However, treating wild-type cells with the pan-KRas inhibitor led to the upregulation of NRas and HRas protein levels, suggesting possible resistance mechanisms.[100]

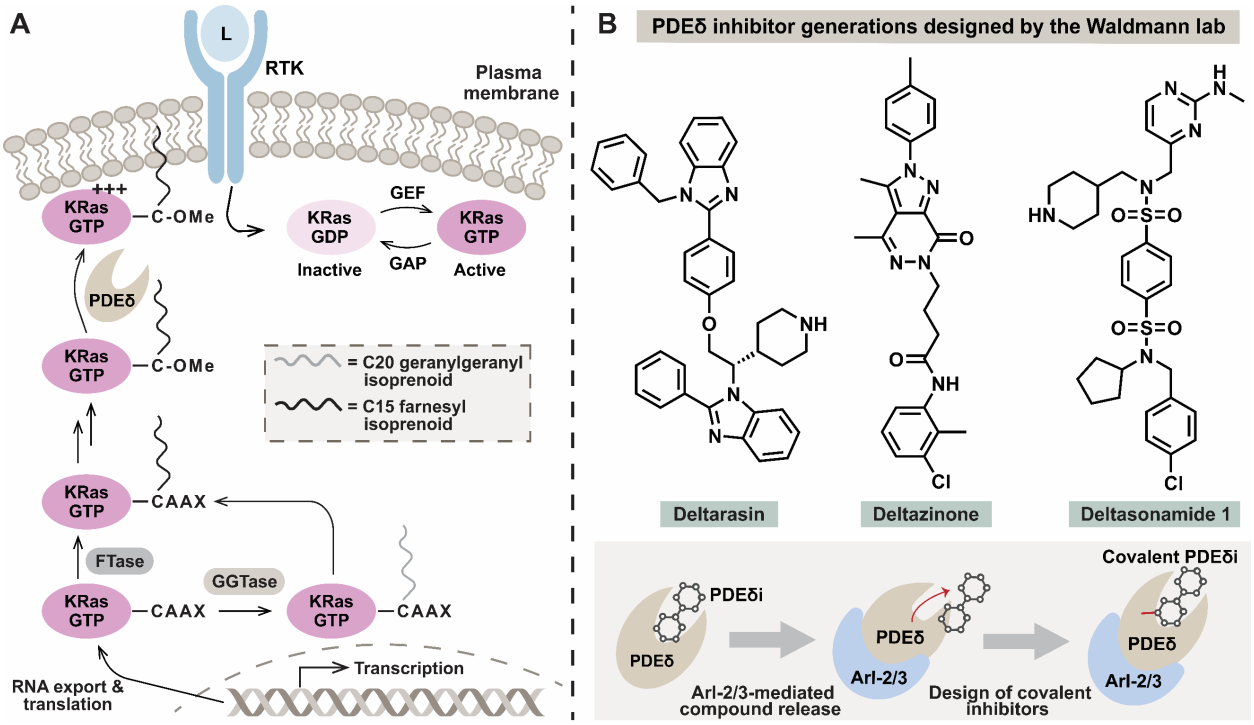

Figure 8: Strategies for displacing mutant KRas from the plasma membrane. A) Mechanisms involved in the post-translational modification, namely prenylation, proteolysis, and carboxymethylation, of KRas proteins. These are essential to ensure plasma membrane localization of KRas and, thus, proper signal propagation. GGTase-mediated prenylation of KRas occurs in the event of FTase activity inhibition. FTase: farnesyltransferase, GGTase: geranylgeranyltransferase. Figure modified according to L. Huang *et al.*[75] B) Chemical structures of PDEδ inhibitors (PDEδi) Deltarasin, Deltazinone, and Deltasonamide 1, along with a schematic illustration of the challenge of Arl2/3-mediated inhibitor release, which results in dampened efficacy of KRas dislocation.

Alternative strategies to inhibit oncogenic KRas activity aim to displace it from its plasma membrane location, which is essential for its activity and proper signal propagation (Figure 8A). Therefore, research efforts focused on developing inhibitors of the enzymes directly involved in the prenylation of KRas CAAX motif, such as farnesyltransferase inhibitors (FTIs). FTIs hinder

KRas membrane association by preventing the introduction of the prenyl group.[75] However, despite FTIs such as Tiffany and Ionafarnib entering phase III clinical trials, the drugs ultimately failed to treat KRas-driven cancers due to lacking anticancer effects.[101]

The Waldmann lab has successfully developed multiple generations of PDEδ inhibitors that bind directly to the prenyl-binding pocket, thereby blocking the interaction with KRas (Figure 8B).[102-104] The development of the first nanomolar PDEδ inhibitor, Deltarasin, began with identifying hits sharing a benzimidazole structure utilizing an Alpha screen technology-based high-throughput screening (HTS).[102] Due to unspecific cytotoxicity, a second generation was developed guided by structure-based compound design, yielding the pyrazolopyridazinone structure-based compound Deltazinone.[103] Although Deltarasin and Deltazinone are strong binders *in vitro*, their ability to reduce the growth of KRas-dependent cell lines requires micromolar compound concentrations. This discrepancy between *in vitro* and *in cellulo* activity can be attributed to the rapid release of these inhibitors mediated by Arl2/3 proteins. To address this challenge, a second Alpha screening technology-based HTS was performed, which led to the discovery of the bis-sulfonamide-based compound Deltasonamide 1.[104] Deltasonamide 1 is a picomolar inhibitor that can form up to seven hydrogen bonds with PDEδ. However, the Deltasonamides exhibit an activity gap as well, requiring micromolar concentrations to inhibit the growth of KRas-dependent cell lines. Current efforts are focused on developing efficient covalent inhibitors to bypass Arl2/3 displacement. The first covalent PDEδ inhibitor was designed utilizing a Woodward's reagent K (WRK)-based warhead to target glutamic acids in the binding pocket of PDEδ, as it lacks targetable cysteine or lysine residues.[105] The WRK-based covalent inhibitor displayed instability, however, it served as a promising starting point for advancing covalent PDEδ inhibitors.

1.6 Development and identification of bioactive small molecules

1.6.1 Strategies for the generation of bioactive small molecules

The field of chemical biology aims to develop and employ small molecules as tool compounds to explore and understand biological phenomena. This involves the study of specific biological pathways or proteins and their interactions.[106] Small molecules can have various intracellular and extracellular targets such as RNA, enzymes, or receptors.[107,108] They also have diverse functionalities as they can act as inhibitors, activators, allosteric binders, protein-protein-interaction (PPI) stabilizers or destabilizers, and protein degraders.[108-112]

The core of chemical biology revolves around generating bioactive small molecules to study and potentially reverse disease-related phenotypes. A valuable source of inspiration for identifying bioactive small molecules often derived from natural products (NPs) such as alkaloids, i.e., morphine, from opium poppy plants.[113] Their structures have been selected and optimized by evolution for thousands of years, resulting in higher selectivity towards biological targets.[114] Regardless of their benefits, the synthesis or isolation of NPs is very demanding, leading to a decreased interest in their discovery. However, the number of small molecules exhibiting drug-like properties is estimated to be approximately 10^{60}, making it unfeasible to explore them individually.[115] For this reason, there was the need to establish efficient approaches enabling the exploration of novel biologically meaningful chemical space. One approach aiding the discovery of bioactive small molecules is the biology-oriented synthesis (BIOS) developed by the Waldmann group.[116,117] The BIOS strategy aims to reduce the structural complexity of guiding NPs to core scaffolds which allows the maintenance of biological relevance and simplification of their chemical synthesis and modification. Structurally-related natural products Nigalin B and lamellarin D are marine NPs displaying different biological activities, such as anticancer activity and HIV-1 (human immunodeficiency virus 1) integrase inhibition. Reduction to their guiding structure and modification following the BIOS principles resulted in Pyrcoumin, an inhibitor of canonical Wnt signaling.[118] Another strategy to utilize the inherited biological activity of NPs is to deconstruct them into their core fragments using cheminformatic tools. The resulting NP-derived fragments are assayed for their binding capabilities to specific proteins of interest and then combined and modified to enhance their binding affinities. The relevance of this strategy was validated by discovering various phosphatase inhibitors and stabilizers of the inactive conformation of p38α MAP kinase.[119] While the outlined principles directed the discovery of novel small molecule modulators, several restrictions exist. For example, BIOS-derived compounds often display similar bioactivities to their guiding NP as they occupy comparable chemical space. To tackle these challenges and explore uncharted biological and chemical space, the principles of BIOS and NP-derived fragment strategies were merged to result in the pseudo-natural product concept. Pseudo NPs are generated through the *de novo* combination of biosynthetically unrelated NP fragments.[120] One of the initial exemplary cases of the pseudo-NP strategy involves chromopynones, which are generated from combining chromane and tetrahydropyrimidone NP fragments. Chromopynones are dual inhibitors of glucose transporters GLUT-1 and 3. Another relevant pseudo-NP class is the apoxidoles, resulting from merging indole and tetrahydropyridine fragments. Investigations in several cell-based assays revealed that Apoxidole-1 reduces kynurenine levels and is an inhibitor of apo-IDO1.[121]

1.6.2 Biological characterization of small molecules using chemical genetics

To gain insights into the biological activity of small molecules, the chemical genetics approach can be utilized. Chemical genetics can be categorized into two approaches: a phenotype-based approach known as forward chemical genetics and a target-based approach known as reverse chemical genetics (Figure 9). Both approaches aim to characterize a specific biological system, such as a protein associated with a disease or a disease-related phenotype, through intervention with small molecules.[122]

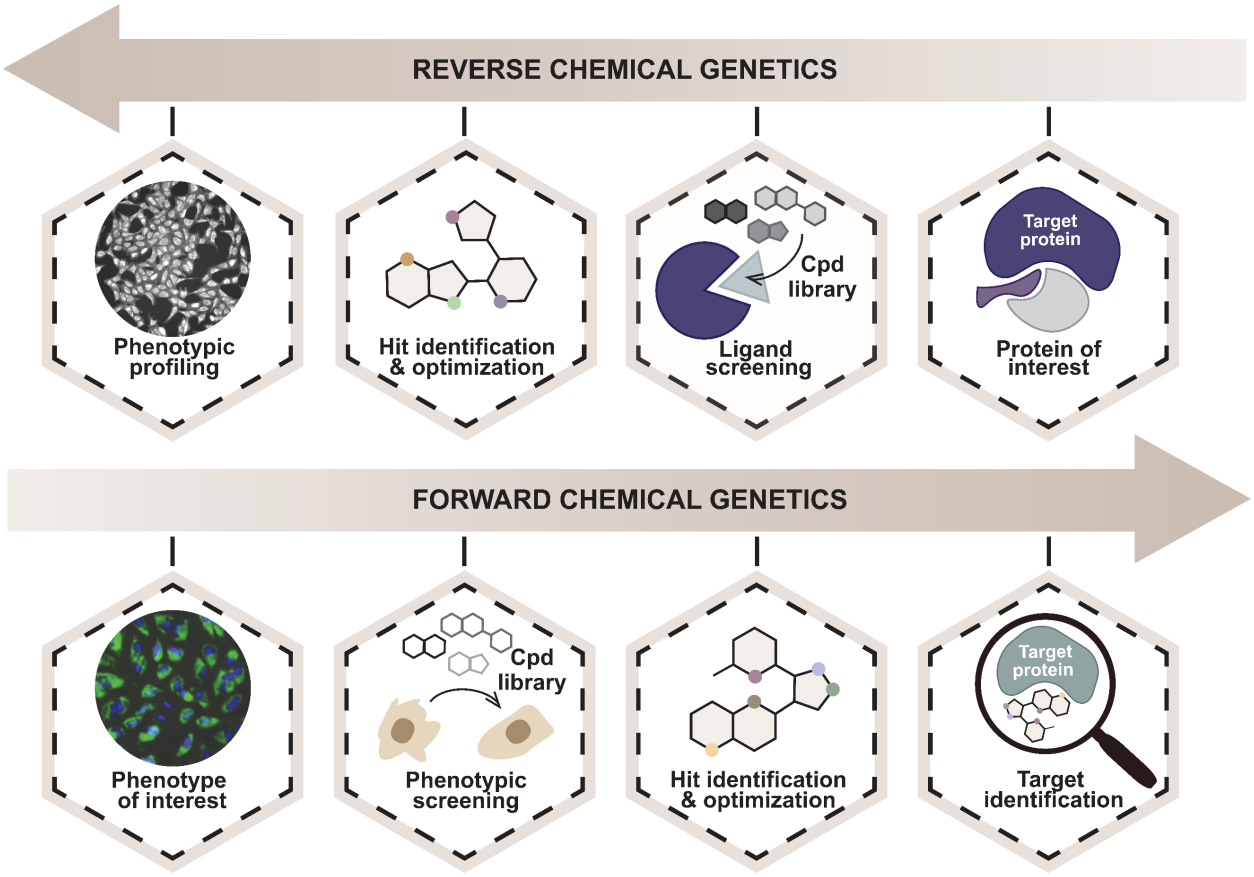

Figure 9: Chemical genetics concept: reverse vs. forward chemical genetics. Reverse chemical genetics aims to identify a small molecule that can modulate the activity of a specific protein of interest. In contrast, forward chemical biology involves discovering small molecules to generate a desired phenotype. Cpd: compound.

Reverse chemical genetics entails commencing with a specific protein of interest, usually related to a disease, to gain a deeper understanding of the disease and potentially develop therapeutics. To this end, a suitable biological *in vitro* assay is set up to detect the binding of a ligand, i.e., by enhancing or suppressing the functionality of the target protein. This can involve the protein's ability to convert metabolites, such as converting ATP to ADP through kinase-substrate phosphorylation.[123] Hit compounds undergo structure-relationship (SAR) studies (i.e.,

methodically swapping substituents or extending the structure) to optimize their selectivity and potency. These optimized ligands undergo investigations in cells or intact organisms to assess their effects on the phenotype.[124] Target-based approaches yielded a great number of FDA-approved drugs.[125] However, the RCG approach presents challenges, as the *in vitro* assays used for ligand screening do not adequately reflect the complexity of cellular biological systems, and key factors such as compound half-life and permeability are not accurately represented.

Forward chemical genetics encapsulates the complexity of biological systems, allowing the identification of novel targets and disease mechanisms, unlike RCG-based strategies, which are limited to known targets.[125,126] The starting point of FCG involves identifying a desired phenotype of interest by exposing cells to compound libraries. After identifying hit compounds, the next steps involve SAR studies for hit optimization, followed by target identification experiments. There are several strategies to identify targets, including omics approaches such as genomics, transcriptomics, proteomics, and metabolomics.[127] One of the leading technologies for target identification is chemoproteomics. It can not only facilitate target identification but also offers insights into potential off-targets and the mode of action (MoA). For a significant period of time, the prevailing approach in drug discovery research was the "one drug, one target" paradigm. Presently, it is widely recognized that diseases are complex, multifaceted conditions, and polypharmacology, i.e., addressing multiple targets simultaneously, is more likely to lead to effective treatment.[125] Therefore, utilizing FCG along with chemoproteomics methods, e.g., affinity-based proteomics or thermal proteome profiling (TPP), may be beneficial for discovering multi-target drugs.[128,129]

Affinity-based proteomics is a reliable method for identifying targets of bioactive small molecules. For this purpose, an activity-based probe that serves as ‘fishing bait’ for the target proteins is designed. This is achieved by attaching a reporter group (e.g., biotin) or a biorthogonal clickable handle (e.g., azide or alkyne groups) to the small molecule through a suitable space-creating linker.[130] This probe is typically incubated with live cells or cell lysates. Subsequently, the labeled proteins undergo enrichment (e.g., *via* streptavidin-biotin interactions) and are processed for mass spectrometry-based analysis (LC-MS/MS) to identify the enriched proteins.[131,132] One significant limitation of activity-based protein profiling (ABPP) approaches is the need to conduct extensive structure-activity relationship (SAR) studies on the parental small molecule to identify sites that can be altered to create a probe. This process can be challenging due to the potential loss of affinity for the target protein(s). Additionally, the introduced linker or reporter groups (e.g., biotin) may cause non-specific binding of proteins to these modifications.[133] An alternative

proteomics method that does not require probe generation is thermal proteome profiling.[133] TPP experiments focus on monitoring changes in the thermal stability of proteins induced by the small molecule compared to the control.[134] TPP can be performed with cell lysates or live cells and allows unbiased melting behavior analysis of over 7000 human soluble and membrane proteins. The extent of thermal shifts is influenced by three factors: compound concentration and affinity, as well as the target protein structure. This presents a challenge of false negatives as small molecule binding to multidomain proteins can result in insignificant changes in thermal stability.[133] For this reason, an advanced protocol called 2D-TPP has been recently developed, which considers both temperature-dependent and concentration-dependent changes in the thermal stability of proteins.

1.6.3 Target validation strategies

Small molecules can often interact with multiple cellular targets. For this reason, it is essential to validate that the modulation of the identified target is responsible for the phenotype observed during phenotypic screening. Several target validation strategies are available, as multiple aspects require validation, including confirmation of target binding and chemical and genetic validation. To ensure direct binding of a small molecule to a protein of interest, it is advisable to use an orthogonal setup, for example, employing biophysical methods such as isothermal titration calorimetry (ITC) or differential scanning fluorimetry (DSF).[135] Another widely employed technique to prove small molecule target engagement in cells is the cellular thermal shift assay (CETSA). Generally, a strong indicator of target-specific effects is the correlation between the SAR observed in phenotypic assays and a target-specific assay.[135,136] Chemical validation entails testing established small molecule modulators with different chemotypes that are selective for the target of interest and display the same phenotype.[137] It can also involve chemical knockdowns of the protein of interest *via* proteolysis-targeting chimeras (PROTACs) to confirm the target.[138] Genetic target validation methods involve the depletion or overexpression of the target protein. Target gene knockdown *via* RNA interference or deletion using CRISPR-Cas9 can mimic the phenotype achieved with pharmacological target inhibition, whereas reduced target protein expression may result in increased potency of the small molecule.[135-137] Protein overexpression experiments can confer resistance to small molecules and reduce their potency, thereby rescue the phenotype.[136] Altogether, small molecules can be excellent as tool compounds for elucidating biological pathways or for drug development. However, it is crucial to thoroughly investigate a compound's pharmacology and mode of action to properly validate the on-target activity, thus avoiding wasting time and resources with faultily characterized small molecules.

2. AIM OF THE THESIS

Due to its high incidence and heterogeneity, developing effective therapeutic strategies to combat cancer is a relentless challenge. Cancer is a multifaceted disease with various attributes, as researchers Hanahan and Weinberg have described in recent years. This research work addressed two hallmarks of cancer: 1. inhibiting proliferative signaling and 2. evading immune destruction using small-molecule modulators through two distinct approaches. (Figure 10).

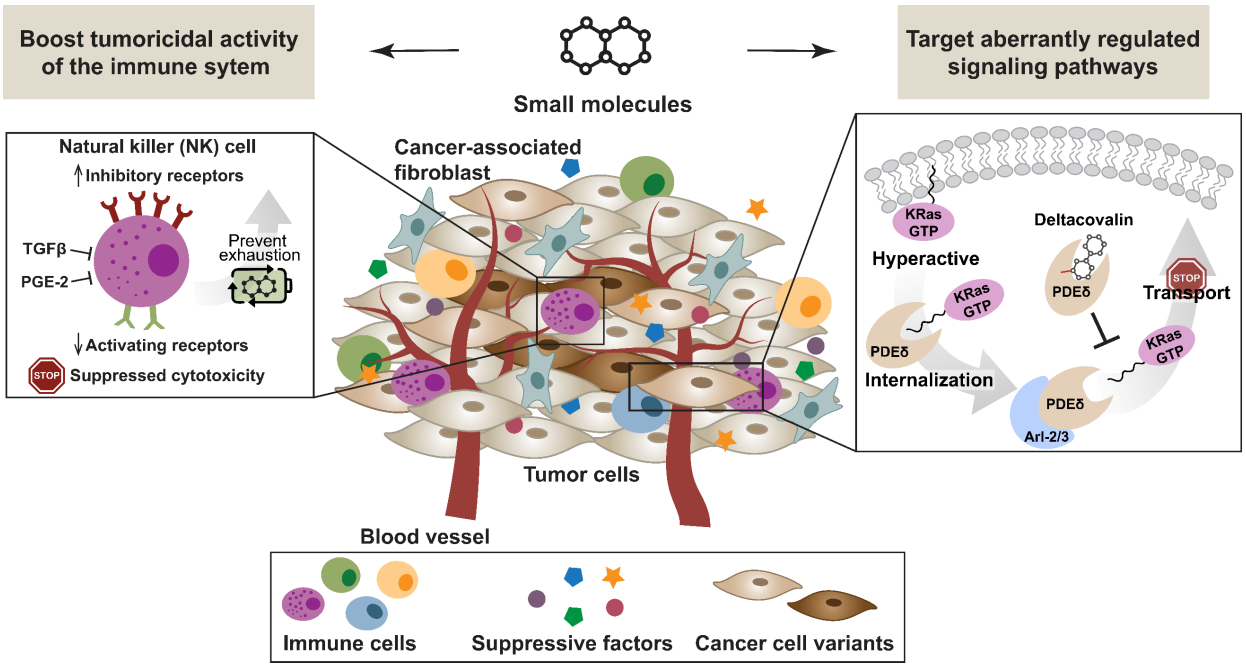

Figure 10: Schematic presentation of the project objectives.

The first project was centered around utilizing small molecules to boost the cancer-eliminating activity of NK cells. NK cells exhibit many beneficial anti-cancer properties. They have the unique ability to detect malignant changes in cells and eradicate them without prior sensitization. Therefore, a phenotypic assay was established to identify small molecules that modulate cancer or NK cells and thereby strengthen NK cell-mediated recognition and eradication of cancer cells. The assay setup involved a co-culture assay of cancer cells and lymphocytes and inhibitory factors to mimic the immunosuppressive nature of the TME. The assay was miniaturized and subjected to a medium-throughput screening campaign performed by the Compound Management and Screening Center (COMAS) in Dortmund. In this research work, hit compounds that induce the desired phenotype were (de)validated employing the NK cell-mediated cytolysis assay and investigating IFN-γ and granzyme B levels. Additionally, respective targets and mechanisms involved in preserving NK cell tumoricidal activity were elucidated.

In the second project, small molecules were employed to antagonize the abnormal regulation of the proliferative KRas signaling pathway. Oncogenic KRas proteins play a critical role in cancer proliferation, and previous research efforts aimed at directly targeting them showed limitations. Instead of targeting the oncoprotein itself, the Waldmann group successfully synthesized different classes of inhibitors that target its chaperone PDEδ, which impaired the enrichment of KRas molecules at the plasma membrane. However, there is a significant gap between the effectiveness of PDEδ inhibitors *in vitro* and *in cellulo*. This discrepancy might be caused by an Arl2/3-mediated release of the small molecules in cells. To address this issue, a new generation of Deltasonamide scaffold-based inhibitors was designed that covalently bind to PDEδ. Previous investigations showed that one derivative, Deltacovalin, displayed great stability, solubility, and covalent binding to PDEδ *in vitro* as well as efficacy in initial cell-based experiments. In this research work, cell-based target engagement studies of Deltacovalin to PDEδ were conducted. The sensitivity towards the displacement of KRas from PDEδ by Deltacovalin of various cancer cell lines was explored. The consequence of impairing KRas-PDEδ interaction on respective downstream targets was analyzed. Finally, studies were performed to elucidate the mechanisms responsible for the potency gap of PDEδ inhibitors *in vitro* and *in cellulo*.

3. MATERIAL AND METHODS

3.1 Material

3.1.1 Chemicals and reagents

Compounds used in this research study were obtained from the Compound Management and Screening Center (COMAS), official suppliers, or synthesized by chemists from the Waldmann group at the Max-Planck-Institute of Molecular Physiology in Dortmund. The compounds that have been purchased will be listed in the table below.

Reagent	Supplier	Catalog No.
2-chloroacetamide (CAA)	Sigma-Aldrich Chemie GmbH	C0267
2,2,2-Trifluoroethanol (TFE)	Thermo Fisher Scientific	10051560
2-(4-(2- hydroxyethyl)-1-piperazine ethane sulfonic acid (HEPES)	GERBU Biotechnik GmbH	1009.0250
7-AAD	BioLegend Inc.	420404
Acetonitrile (ACN), HPLC grade	VWR International GmbH	83640.290
Acrylamide / Bisacrylamide (30 %) solution	AppliChem GmbH	A1672
AH6809	MedChemExpress LLC	HY-10418
Ammonia solution (25 %)	Merck KGaA	533003
Ammonium chloride potassium (ACK) lysis buffer	Gibco®, Thermo Fisher Scientific	A1049201
Ammonium persulfate (APS)	SERVA Electrophoresis GmbH	13375
Ampicillin	GERBU Biotechnik GmbH	10416.0050
Anti-FLAG® M2 Magnetic Beads	Millipore	M8823
BD Horizon™ Brilliant Stain Buffer	BD Biosciences	566349
Bovine albumin fraction V (BSA)	SERVA Electrophoresis GmbH	11945.03
Bromophenol blue	Sigma-Aldrich Chemie GmbH	A512.1
CellEvent™ Caspase-3/7 Green	Thermo Fisher Scientific	R37111
cOmplete™, EDTA-free protease inhibitor cocktail	Roche Diagnostics GmbH	4693132001
D-Glucose	Carl Roth GmbH	6887.1
Dimethyl sulfoxide (DMSO)	Sigma-Aldrich Chemie GmbH	41639
Dithioerythritol (DTE)	GERBU Biotechnik GmbH	1007.0025
Dulbecco’s modified eagle medium (DMEM)	PAN™ Biotech GmbH	P04-03550
E7046	MedChemExpress LLC	HY-103088
EGF, human recombinant	STEMCELL Technologies Inc.	78006
Ethanol (EtOH), absolute	Fisher Scientific GmbH	UN1170

Reagent	Supplier	Catalog No.
Ethylene diamine tetra acetic acid (EDTA)	GERBU Biotechnik GmbH	1034
Fetal bovine serum (FBS)	Gibco®, Thermo Fisher Scientific	10270-106
FuGENE® HD	Promega Corporation	E2311
Geneticin (G418) disulfate salt solution	Sigma-Aldrich Chemie GmbH	G8168
Glu-C, sequencing grade	Promega Corporation	V1651
Glycerol	Carl Roth GmbH	783.1
Glycine	Carl Roth GmbH	3790.2
Glycolic acid	Merck KGaA	104106
Grapiprant	MedChemExpress LLC	HY-16781
Guanidine hydrochloride	VWR International GmbH	M110
Hoechst-33342	Invitrogen™ Thermo Fisher Scientific	H1399
Hydrochloric acid (HCl)	VWR International GmbH	30024.29
IL-15, human recombinant	STEMCELL Technologies Inc.	78031
IMR-1	Sigma-Aldrich Chemie GmbH	SML1812
Intercept® (PBS) Blocking Buffer	LI-COR Biosciences	927-70001
Iscove's modified Dulbecco's medium (IMDM)	PAN™ Biotech GmbH	P04-20150
Lipofectamine® 2000	Thermo Fisher Scientific	11668019
Lymphocyte Separating Medium, Pancoll human, Density: 1,077 g/L	PAN™ Biotech GmbH	P04-60125
Magnesium chloride hexahydrate	AppliChem GmbH	A3618
MagReSyn TiO_2 microparticles	ReSyn Biosciences	MR-TID005
McCoy's 5A medium (modified)	PAN™ Biotech GmbH	P04-05500
Methanol (MeOH)	Honeywell	32213
Non-essential amino acid solution (MEM NEAA), 100X	PAN™ Biotech GmbH	P08-32100
Nonidet P-40 (NP40) alternative	Merck KGaA	492016
Odyssey® PBS-based blocking buffer	LI-COR Biosciences	927-40000
Opti-MEM™ reduced serum medium	Thermo Fisher Scientific	31985062
PAGE Ruler™ plus prestained protein ladder	Thermo Fisher Scientific	26620
Passive Lysis 5X Buffer (PLB)	Promega Corporation	E1941
PBS tablets	Jena Bioscience	AK-102P-L
PF-04418948	MedChemExpress LLC	HY-18966

Reagent	Supplier	Catalog No.
PhosSTOP™ phosphatase inhibitor tablets	Sigma-Aldrich Chemie GmbH	4906845001
Potassium chloride (KCl)	J.T. Baker	0509
Potassium dihydrogen phosphate (KH_2PO_4)	J.T. Baker	0240
Prostaglandin E2 (PGE_2)	TCI Deutschland GmbH	P1884
Radioimmunoprecipitation assay (RIPA) buffer 10x	Cell Signaling Technology	9806
RepSox	Selleckchem	S7223
Rosewell Park Memorial Institute (RPMI) 1640 medium	PAN™ Biotech GmbH	P04-18047
RPMI1640	PAN™ Biotech GmbH	P04-16500
RPMI1640 phenol red-free	PAN™ Biotech GmbH	P04-16515
RT-PCR grade water	Thermo Fisher Scientific	AM9935
SAR405	Selleckchem	S7682
Soluble delta-like ligand (sDLL-4), human recombinant	PeproTech	140-07-100
Sera-MagTM SpeedBeadTM Carboxylate-Modified Magnetic Particles (Hydrophilic)	GE Healthcare	45152105050250
Sera-MagTM SpeedBeadTM Carboxylate-Modified Magnetic Particles (Hydrophobic)	GE Healthcare	65152105050250
Sodium chloride (NaCl)	VWR International GmbH	27810.295
Sodium dodecyl sulfate (SDS) pellets	Carl Roth GmbH	CN30.2
Sodium hydroxide (NaOH)	J.T. Baker	7036
Sodium hydrogen carbonate ($NaHCO_3$)	J.T. Baker	0263
Sodium hydrogen phosphate (Na_2HPO_4)	Merck KGaA	1.06580.0500
Sodium pyruvate, 100 mM	PAN™ Biotech GmbH	P04-43100
Sulfuric acid	Sigma-Aldrich Chemie GmbH	100731
Tetramethylethylenediamine (TEMED)	Carl Roth GmbH	2367.3
Tris(2-carboxyethyl)phosphine (TCEP·HCl)	Thermo Fisher Scientific	20491
Triethylammonium bicarbonate (TEAB) buffer, 1M	Sigma-Aldrich Chemie GmbH	T7408
TGFβ-1	STEMCELL Technologies Inc.	78067
TMB substrate	BioLegend Inc.	421101

Reagent	Supplier	Catalog No.
TRIS	Carl Roth GmbH	4855,2
Trypan blue, 0.4 % (w/v)	Invitrogen™ Thermo Fisher Scientific	T10282
Trypsin, 0.05 % (w/v), EDTA, 0.02 % (w/v)	PAN™ Biotech GmbH	P10-023100
Trypsin/Lys-C mix, mass spec grade	Promega Corporation	V5073
Tween® 20	Sigma-Aldrich Chemie GmbH	P2287

3.1.2 Buffers

Name	Composition
Bacterial lysis buffer	30 mM TRIS 150 mM NaCl 1 mM DTE 1mM phenylmethylsulfonylfluoride 10 µg/mL DNase I pH = 7.5
CETSA lysis buffer	PBS supplemented with 0.4 % (v/v) NP-40 alternative
FACS buffer 1	PBS supplemented with FBS 2 % (v/v)
FACS buffer 2	FACS buffer 1 supplemented with 50 % (v/v) BD Horizon™ Brilliant Stain Buffer
IFN-γ ELISA assay diluent	PBS supplemented with: 5 % (w/v) BSA 0.1 % (v/v) Tween® 20
IFN-γ ELISA coating buffer	Carbonate-bicarbonate buffer 100 mM $NaHCO_3$ 33.6 mM Na_2CO_3
IFN-γ ELISA wash buffer	PBS supplemented with: 0.2 % (v/v) Tween® 20
IFN-γ ELISA stop solution	2 N H_2SO_4
Lysogeny broth (LB) medium	1 % (w/v) Bacto tryptone 0.5 % (w/v) Bacto yeast extract 171 mM NaCl pH = 7.4
LB agar plates	LB Medium with 1.5 % Bacto agar
NP-40 lysis buffer	150 mM NaCl 50 mM TRIS-HCl 1 % NP-40 alternative pH = 8 cOmplete™ protease inhibitor cocktail 1 tablet / 10 mL PhosSTOP™ phosphatase inhibitor 1 tablet / 10 mL

Name	Composition
Phosphate-buffered saline (PBS)	2.7 mM KCl 1.5 mM KH_2PO_4 136.9 mM NaCl 8.1 mM Na_2HPO_4 pH = 7.4
PBS-T	PBS supplemented with 0.1 % (v/v) Tween® 20
Phosphoproteomics digestion buffer	1 M TEAB 10 % (v/v) TFE Trypsin/Lys-C Mix (add 40 µg/sample)
Phosphoproteomics elution buffer	1 % (v/v) ammonia solution
Phosphoproteomics loading buffer	80 % (v/v) ACN 1 M glycolic acid 5 % (v/v) TFA)
Phosphoproteomics lysis buffer	6 M guanidine hydrochloride, 10 mM TCEP, 40 mM CAA 100 mM TRIS-HCl pH = 8.5
Phosphoproteomics stage tip buffer A (equilibration)	30 % (v/v) MeOH 0.2 % (v/v) TFA
Phosphoproteomics stage tip buffer B (wash)	0.2 % (v/v) TFA
Phosphoproteomics stage tip buffer C (elution)	80 % (v/v) ACN 5 % (v/v) ammonia solution
Phosphoproteomics wash buffer 1	80 % (v/v) ACN 1 % (v/v) TFA
Phosphoproteomics wash buffer 2	10 % (v/v) ACN 0.2 % (v/v) TFA
Proteomics lysis buffer	PBS supplemented with 0.4 % (v/v) NP-40 alternative
RIPA lysis buffer	1x RIPA buffer cOmplete™ protease inhibitor cocktail 1 tablet / 10 mL PhosSTOP™ phosphatase inhibitor 1 tablet / 10 mL
SDS running buffer (10X)	2.5 M glycine 35 mM SDS 250 mM TRIS
SDS sample buffer (5X)	400 mM DTE 277 mM SDS 0.5 M TRIS-HCl, 0.3 mM bromophenol blue 40 % (v/v) glycerol pH = 6.8
SDS separating gel buffer	1.5 M TRIS-HCl, pH = 8.8

Name	Composition
SDS stacking gel buffer	1.0 M TRIS-HCl, pH = 6.8
Stage-tip buffer A (wash buffer)	80 % (v/v) ACN 0.1 % (v/v) formic acid
Super optimal broth with catabolite repression (SOC)	2 % (w/v) Bacto tryptone 0.5 % (w/v) Bacto yeast extract 10 mM NaCl 2 mM NaCl 10 mM $MgCl_2$ 10 mM $MgSO_4$ 20 mM D-glucose
Stage-tip buffer B (elution buffer)	0.1 % (v/v) Formic acid
Terrific broth (TB)	1.2 % (w/v) Bacto tryptone 2.4 % (w/v) Bacto yeast extract 0.4 % (v/v) glycerol 72 mM K_2HPO_4 17 mM KH_2PO_4 pH = 7
Transfer buffer	25 mM TRIS 188 mM glycine 10 % (v/v) MeOH
TRIS-buffered saline (TBS)	150 mM NaCl 50 mM TRIS-HCl pH = 7.5
TBS-T	TBS supplemented with 0.1 % (v/v) Tween® 20

3.1.3 Cell lines

3.1.3.1 Mammalian cells

Cell line	Specification	Supplier	Catalog No.
A549	Human lung carcinoma	DSMZ, Germany	ACC107
$A549^{Green}$	A549 stably transfected with H2Bj-eGFP construct	-	-
BxPC-3	Human pancreatic adeno-carcinoma	DSMZ, Germany	ACC760
HEK293T	Human embryonic kidney	ATCC, USA	CRL-1268
HeLa	Human cervix carcinoma	DSMZ, Germany	DSMZ#57
HCT116	Human colorectal adenocarcinoma	DSMZ, Germany	ACC581
HT-29	Human colorectal adeno-carcinoma	ATCC, USA	HTB-38
Jurkat	Human T cell leukemia	DSMZ, Germany	ACC282

Cell line	Specification	Supplier	Catalog No.
LS-174T	Human colorectal adeno-carcinoma	DSMZ, Germany	ACC759
MIA PaCa-2	Human pancreatic adenocarcinoma	ATCC, USA	CRM-CRL-1420
NCI-H358	Human bronchioalveolar carcinoma	LGC Standards, Germany	ATCC-CRL-5807
NCI-H358	Human lung adenocarcinoma	LGC Standards, Germany	ATCC-CRM-HTB-174
PANC-1	Human pancreatic carcinoma	ATCC, USA	CRL-1469
PA-TU-9802	Human pancreatic carcinoma	DSMZ, Germany	ACC179
PBMCs	Peripheral blood mono-nuclear cells, primary cells	DRK Hagen, Germany	-
SK-LU-1	Human lung adenocarcinoma	CLS GmbH, Germany	300335
SW480	Human colorectal adeno-carcinoma	ATCC, USA	CCL-228
U-2OS	Human osteosarcoma	CLS GmbH, Germany	300364

DRK = Deutsches Rotes Kreuz, DSMZ = Deutsche Sammlung von Mikroorganismen und Zellkulturen, ATCC = American Type Culture Collection, CLS = Cell Lines Service.

3.1.3.2 Murine cell lines

Cell line	Specification	Supplier
KP1035 KPACK135-1 KPACK135-10	Murine lung adenocarcinoma ($KRas^{G12D}/TP53^{fl/fl}$)	Generated and supplied by the Reinhardt Lab[139], University Hospital Essen, Germany

3.1.4 Growth and assay media

Description	Medium composition
A549, BxPC-3, HEK293T, HeLa, HCT116, KP1035, KPACK135-1, KPACK135-10, LS-174T, MIA PaCa-2, PANC-1, PA-TU-8902, U-2OS	DMEM supplemented with: 10 % FBS (v/v), 1 % MEM NEAA (v/v) 1 mM sodium pyruvate
HEK293T reporter gene assay medium	DMEM supplemented with: 2 % FBS (hi (v/v)), 1 % MEM NEAA (v/v) 1 mM sodium pyruvate

Description	Medium composition
PA-TU-8902 starvation medium	DMEM supplemented with: 2 % FBS (v/v), 1 % MEM NEAA (v/v) 1 mM sodium pyruvate
PBMCs	IMDM supplemented with: 10 % FBS (hi (v/v))
HT-29	McCoy's 5A supplemented with: 10 % FBS (v/v) 1 % MEM NEAA (v/v)
SK-LU-1	MEM Eagle supplemented with 10 % FBS (v/v), 1 % MEM NEAA (v/v) 1 mM sodium pyruvate
A549^{Green}	RPMI1640 (P04-16500) supplemented with: 10 % FBS (hi (v/v)), 1 % MEM NEAA (v/v) 1 mM sodium pyruvate 0.7 mg/mL G418
A549^{Green} and lymphocyte or NK cell co-culture assay media	RPMI1640 (P04-16515) supplemented with: 10 % FBS (hi (v/v)), 1 % MEM NEAA (v/v), 1 mM sodium pyruvate 2.5 g/L D-glucose
Jurkat, LS-174T, NCI-H358, NCI-H441, SW480	RPMI1640 (P04-18047) supplemented with: 10 % FBS (v/v) 1 % MEM NEAA (v/v) 1 mM sodium pyruvate

3.1.5 Commercial kits

Description	Supplier	Catalog No.
DC™ Protein Assay Kit II	Bio-Rad Laboratories, Inc.	000112
Dual-Glo® Luciferase Assay System	Promega Corporation	E2940
Dynabeads™ Untouched™ Human NK Cells Kit	Invitrogen™ Thermo Fisher Scientific	11349D
ELISA MAX™ Human IFN-γ	BioLegend Inc.	430101
EndoFree Plasmid Maxi Kit	Qiagen N.V.	12163
Pierce™ 660 nm Protein Assay and Ionic Detergent Compatibility Reagant	Thermo Fisher Scienitific	22660 22663
Phusion High-Fidelity PCR Kit	NEW ENGLAND BioLabs GmbH	E0553S
QIAquick PCR Purification Kit (50)	Qiagen N.V.	28104

3.1.6 Antibodies

3.1.6.1 Antibodies for immunoblotting

Antibody	Host, clonality	Dilution	Buffer	Supplier, catalog no.
Primary antibodies				
COX-2 (D5H5)	Rabbit, monoclonal	1:500-1:1000	Intercept® PBS Blocking Buffer	Cell Signaling Technologies 12282S
EP2	Rabbit, monoclonal	1:1000	Intercept® PBS Blocking Buffer	Abcam, ab167171
EP4 (C-4)	Mouse, monoclonal	1:500	Intercept® PBS Blocking Buffer	Santa Cruz Biotechnology, sc-55596
Flag Tag M2	Mouse, monoclonal	1:1000	Intercept® PBS Blocking Buffer	Sigma Aldrich F3165
GAPDH (14C10)	Rabbit, monoclonal	1:1000	Intercept® PBS Blocking Buffer	Cell Signaling Technologies 2118S
Granzyme B	Rabbit, monoclonal	1:1000	Intercept® PBS Blocking Buffer	Abcam, ab134933
Notch1 (D1E11)	Rabbit, monoclonal	1:1000	Intercept® PBS Blocking Buffer	Cell Signaling Technologies 3608s
PDEδ	Rabbit, polyclonal	1:500	Intercept® PBS Blocking Buffer	Thermo Fischer Scientific PA5-22008
Vinculin (HVIN-1)	Mouse, monoclonal	1:2500-1:5000	Intercept® PBS Blocking Buffer	Merck KGaA V9131
Secondary antibodies				
Mouse 680RD	Donkey	1:2500-1:5000	Intercept® PBS Blocking Buffer	LI-COR Biosciences, 926-68074
Mouse 800CW	Goat	1:2500-1:5000	Intercept® PBS Blocking Buffer	LI-COR Biosciences, 926-32210
Rabbit 800 CW	Donkey	1:2500-1:5000	Intercept® PBS Blocking Buffer	LI-COR Biosciences, 926-32213

3.1.6.2 FACS antibodies

Antibody, clone	Host, clonality	Conjugate	Dilution	Buffer	Supplier, catalog no.
Determination of NK cell proportion					
CD3 (HIT3a)	Mouse, monoclonal	PE	1:100	FACS buffer 1	BioLegend Inc., 300308
CD56 (NCAM-16.2)	Mouse, monoclonal	BV421	1:100		BD Biosciences, 562751

Antibody, clone	Host, clonality	Conjugate	Dilution	Buffer	Supplier, catalog no.
NK mixed receptor panel					
4-1BB (4B4-1)	Mouse, monoclonal	BV421	1:50	FACS buffer 2	BioLegend Inc., 309820
CD11a (HI111)	Mouse, monoclonal	AF488	1:800		BioLegend Inc., 301216
CD161 (HP-3G10)	Mouse, monoclonal	BUV661	1:100		BD Biosciences, 750596
CD18 (TS1/18)	Mouse, monoclonal	AF700	1:800		BioLegend Inc., 302124
CD27 (M-T271)	Mouse, monoclonal	PerCP-Cy5.5	1:50		BD Biosciences, 560612
CD3 (UCHT1)	Mouse, monoclonal	BUV563	1:200		BD Biosciences, 748569
CD38 (HB7)	Mouse, monoclonal	BUV395	1:100		BD Biosciences, 563811
CD56 (NCAM16.2)	Mouse, monoclonal	BUV805	1:500		BD Biosciences, 749086
CD8a (RPA-T8)	Mouse, monoclonal	AF532	1:200		Thermo Fischer Scientific 58-0088-42
CTLA-4 (BNI3)	Mouse, monoclonal	PE-Dazzle	1:100		BioLegend Inc., 369616
FasL (NOK-1)	Mouse, monoclonal	BV650	1:100		BD Biosciences, 744100
HLA-DR (L243)	Mouse, monoclonal	BV605	1:50		BioLegend Inc., 307640
KLRG1 (2F1)	Syrian Hamster, monoclonal	BV510	1:50		BioLegend Inc., 138421
NKG2A (Z199)	Mouse, monoclonal	PE	1:100		Beckman Coulter, IM3291U
NKG2C (134591)	Mouse, monoclonal	BUV496	1:50		BD Biosciences, 749844
PD-1 (EH12.1)	Mouse, monoclonal	AF647	1:100		BD Biosciences, 329910
TIGIT (741182)	Mouse, monoclonal	BV786	1:100		BD Biosciences, 747838
TIM-3 (F38-2E2)	Mouse, monoclonal	APC-Fire 750	1:50		BioLegend Inc., 345044
TRAIL (N2B2)	Mouse, monoclonal	PE-Cy7	1:50		BioLegend Inc., 308210
NK cell activating receptor panel					
2B4 (C1.7)	Mouse, monoclonal	FITC	1:200	FACS buffer 2	BioLegend Inc., 329506
CD16 (3G8)	Mouse, monoclonal	PE-Dazzle	1:100		BioLegend Inc., 302054

Antibody, clone	Host, clonality	Conjugate	Dilution	Buffer	Supplier, catalog no.
NK cell activating receptor panel					
DNAM-1 (DX11)	Mouse, monoclonal	AF647	1:100	FACS buffer 2	BD Biosciences, 564797
NKG2D (149810)	Mouse, monoclonal	AF700	1:100		R&D Systems FAB139N
NKp30 (P30-15)	Mouse, monoclonal	APC-Fire750	1:100		BioLegend Inc., 325226
NKp44 (P44-8)	Mouse, monoclonal	PerCP-Cy5.5	1:100		BioLegend Inc., 325114
NKp46 (9E2)	Mouse, monoclonal	BV421	1:50		BioLegend Inc., 331914

AF = Alexa Fluor®, APC = Allophycocyanin, BV = Brilliant Violet™, BUV = Brilliant Ultra Violet™, FITC = Fluorescein-5-isothiocyanate, PE = Phycoerythrin, PerCP = Peridinin-Chlorophyll-Protein.

3.1.7 Plasmids

Plasmid	Vector backbone	Insert	Catalog No	Supplier
pRluc-TK	pRL	*Renilla* luciferase	E2241	Promega Corporation
SBE4-Luc	pBV-Luc	*SBE4*-Fluc luciferase	16495	Addgene[140]
Flag-PDEδ	pcDNA3	Flag-PDEδ	Plasmids were kindly provided by A. Wittinghofer, MPI Dortmund.	
His-PDEδ	pET28a	His-PDEδ		
His-Arl2	pET20B	His-Arl2		

3.1.8 Consumables

Consumable	Supplier	Catalog No.
6-well plate, clear, flat bottom	Sarstedt AG & Co. KG	83.3920
12-well plate, clear, flat bottom	Sarstedt AG & Co. KG	83.3921
24-well plate, clear, flat bottom	Sarstedt AG & Co. KG	83.3922
96-well plate, clear, flat bottom	Corning Inc.	353075
96-well plate with conical bottom	Sarstedt AG & Co. KG	82.1583001
96-well plate half area white flat bottom	Corning Inc	3693
Breathe-Easy® sealing membrane	Diversified Biotech	BEM-1
Cell scraper 25 cm, 20 mm	VWR Brand	734-2602
Countess™ Cell Counting Chamber Slides	Thermo Fisher Scientific	C10283
CryoPure, cryogenic vials	Sarstedt AG & Co. KG	72.379.992
CytoOne® dishes, 100 x 20 mm, non-treated	STARLAB Group	CC7672-3394

Consumable	Supplier	Catalog No.
EmporeTM High-Performance Extraction Disks, C18 (Octadecyl), 20 disks/pack, 47 mm diameter	3M BIOANALYTICAL TECHNOLOGIES	2215
FACS tubes with cell strainer	Corning Inc	352235
Falcon tubes, 15 mL	Sarstedt AG & Co. KG	62.554.502
Falcon tubes, 50 mL	Sarstedt AG & Co. KG	62.547.254
Gel-loading tips	Corning Inc	10078930
Immobilion-FL PVDF membrane	Merck KGaA	IPF00010
Microcentrifuge tube, Eppendorf, 5 mL	Kisker Bio	G05-ML
Nunc™ MaxiSorp™ ELISA plates, Uncoated	BioLegend Inc.	423501
Parafilm®	Bemis Company, Inc.	PM-996
PCR Tubes, 0.2 mL, flat cap	Thermo Fisher Scientific	AB0622
Reaction tube, Protein LoBind 0.5 mL	Eppendorf AG	0030108094
Reaction tube, Protein LoBind 1.5 mL		0030108116
Reaction tube, Protein LoBind 2.0 mL		0030108132
Reaction tube, SafeSeal 0.5 mL	Sarstedt AG & Co. KG	72.704
Reaction tube, SafeSeal 1.5 mL		72.706
Reaction tube, SafeSeal 2.0 mL		72.695.500
SafeSeal tips premium, 10 µL	Biozym Scientific GmbH	693010
SafeSeal tips premium, 100 µL		690101
SafeSeal tips premium, 200 µL		692069
SafeSeal tips premium, 1250 µL		692089
SDB-RPS Empore® Extraction Disks, 20 disks/pack, 47 mm diameter	3M BIOANALYTICAL TECHNOLOGIES	AH0-4048
Serological pipette, 1 mL	Sarstedt AG & Co.	86.1251.001
Serological pipette, 5 mL		86.1253.001
Serological pipette, 10 mL		86.1254.001
Serological pipette, 25 mL		86.1685.001
Serological pipette, 50 mL		86.1256.001
Syringe filter: Filtropur S 0.2 µM	Thermo Fisher Scientific	83.1826.001
Tissue culture flask T25		83.3910.002
Tissue culture flask T75		83.3912.002
Tissue culture flask T175		83.3911.002
Ultracentrifuge polycarbonate tubes, thick walls, 0.5 mL	Beckman Coulter	343776
Whatman® gel blotting paper	Sarstedt AG & Co. KG	WHA10426994

3.1.9 Laboratory devices

Device and description	Supplier
Automated Cell Counter: Countess™ II	Thermo Fisher Scientific
Biological safety cabinets	
MSC Adventage™ 1.2	Thermo Fisher Scientific
NU437-600E	NuAire
Centrifuges	
Optima™5415 MAX-XP Ultracentrifuge	Beckman Coulter
5417R	Eppendorf AG
5430	
5702	
5810R	
MiniSpin	
SpeedVac Concentrator 5301 plus	
Chromatography column and system	
ÄKTAprime Plus	GE Healthcare Life Sciences GmbH
GSTTrap HP	Cytiva
HiLoad™ 16/600 Superdex™ 200 pg	
Flow cytometers	
Cytek® Aurora 5L	Cytek Bioscience Inc., Fremont
FACS LSRII Flow Cytometry System	BD Biosciences
Incubators	
MCO-230AICUV-PE IncuSafe CO2 incubator	PHCbi
INE400	Memmert GmbH and Co. KG
Imaging device: ChemiDoc™ MP system	Bio-Rad Laboratories, Inc.
Live-cell imaging and analysis systems	
IncuCyte® S3	Sartorius AG
IncuCyte® ZOOM	
Spectrometer	
Mass spectrometer: Q Exactive! HF Plus Hybrid Quadrupole-Orbitrap	Thermo Fisher Scientific
Microscopes	
Axiovert 200M automated microscope	Zeiss
Primo Vert light microscope	
Plate reader: Tecan Spark® multimode microplate reader	Tecan Trading AG
PCR cycler: Mastercycler epgradientS	Eppendorf AG

Device and description	Supplier
pH-Meter: FiveEasy PlusTM (FEP20)	Mettler Toledo
Pipettes	
Eppendorf Pipette Xplorer® (15-300 µL)	Eppendorf AG
Multi-channel pipettes: Eppendorf Research® plus (10 µL, 100 µL and 300 µL)	
Single-channel pipettes: Eppendorf Research® plus (2.5 µL, 10 µL, 20 µL, 100 µL, 200 µL and 1000 µL)	
Pipetting aid: Pipetboy acu2	INTEGRA GmbH, Brand GmbH
Power supply: PowerPac™ Basic	Bio-Rad Laboratories, Inc.
Protein electrophoresis equipment: Mini-PROTEAN® tetra electrode assembly	Bio-Rad Laboratories, Inc.
Protein wet blotting system: 2-gel tetra and blotting module	Bio-Rad Laboratories, Inc.
Sonicator	
Sonoplus HD2080	Bandelin
ThermoMixer® C	Eppendorf AG
Water bath	Memmert GmbH and Co. KG

3.1.10 Software

Description	Supplier
Chemical illustration and analysis: ChemDraw	PerkinElmer, Inc.
Data analysis	
Excel	Microsoft
GraphPad Prism 9.0	GraphPad Software
Electrophoresis gel and blot analysis: Image Lab	Bio-Rad Laboratories, Inc., USA
FACS analysis: FlowJo™ v10	BD Biosciences
Image analysis: Fiji	Open source
Live cell imaging analysis	
IncuCyte® S3 2019B software	Sartorius AG
IncuCyte® ZOOM 2018A software	
Proteomics analysis tool: MaxQuant[141]	Free download
Tool for scientific figures: Adobe Illustrator	Adobe Inc.

3.2 Methods

3.2.1 Cell biology methods

All cell culture work was carried out under sterile conditions using suitable equipment and a laminar flow hood.

3.2.1.1 Sub-cultivation of cell lines

All cell lines were cultivated in the corresponding culture media (see 3.1.4) in tissue culture flasks (25 cm², 75 cm², or 175 cm²) in a humidified atmosphere at 37 °C and 5 % CO_2. The cells were passaged as soon as they reached a confluence of 80 to 90 %. For passaging adherent cells, medium was removed, cells were washed using sterile and pre-warmed PBS and then detached from the surface using a trypsin/EDTA solution. During trypsinization, cells were incubated for 5-10 min at 37 °C and 5 % CO_2. Next, cells were suspended using the pre-warmed culture medium, separated, diluted accordingly, and placed into a new tissue culture flask. Suspension cells were passaged upon reaching the distributor's recommended maximal growth density (e.g., Jurkat 2 x 10^6 cells/mL). For this purpose, cells were transferred into a 50 mL tube and collected at 300 x g for 5 min. Subsequently, cells were resuspended in fresh growth medium with an appropriate cell density (e.g., Jurkat 0.2 x 10^6 cells/mL) and transferred into a new tissue culture flask.

3.2.1.2 Mycoplasma detection assay

Cell cultures were tested monthly and prior to cell cryopreservation for mycoplasma contamination using Lonza's MycoAlert™ Mycoplasma Detection Kit. The detection assay was conducted in accordance with the manufacturer's instructions.

3.2.1.3 Heat inactivation of FBS

For heat inactivation, FBS was divided into 50 mL aliquots. Each aliquot was placed in a 56 °C water bath with a sufficient volume of water to fully immerse the tubes. Aliquots were incubated for 30 min and then cooled to room temperature before being stored at -20 °C until further use.

3.2.1.4 Cell count determination and cell seeding

Cell cultures were dissociated (adherent cells), suspended (see 3.2.1.1), and the obtained cell suspension was centrifuged at 300 x g for 4 min. Next, the cell pellet was resuspended in an appropriate amount of pre-heated medium. To assess the cell count, the cell suspension was mixed with Trypan blue in a 1:1 ratio to enable differentiation of living from dead cells. 10 µL of the resulting mixture was placed into a disposable cell counting slide to determine the cell count using the Countess™ Cell Counting Chamber. The percentage of cells that were alive was

determined and utilized for required calculations. Finally, the cell suspension was diluted using the appropriate assay medium and then seeded into the appropriate cell culture plate. To reduce edge effects due to excessive medium evaporation in experiments, wells on the border of multi-well plates were excluded, and plates were sealed with a gas-permeable membrane in case of long incubation times (i.e., 48 h or longer).

3.2.1.5 Cryopreservation of cells

For cryopreservation of cell lines, cells were detached, washed, and pelleted by a centrifugation step at 300 x g for 5 min and then resuspended in DMSO-supplemented media (5-10 % v/v) to the desired cell density. Peripheral blood mononuclear cells (PBMCs) were cryopreserved in heat-inactivated (hi) FBS supplemented with 10 % (v/v) DMSO at a cell density ranging between 5×10^6 and 2×10^7 cells/mL. After preparing the cell suspension, cells were transferred to cryogenic vials (1 mL cell suspension per vial), placed into a Mr. Frosty™ freezing container to ensure a slow and even temperature decrease, and moved into a -80 °C freezer overnight. Finally, cells were transferred to a liquid nitrogen tank and stored in the vapor phase for future usage.

3.2.1.6 Thawing of cryopreserved cells

Cryopreserved cells were removed from the liquid nitrogen tank and thawed in a 37 °C water bath. Next, the cell suspension was placed into a 15 mL tube containing 9 mL of fresh, pre-warmed growth medium. After centrifuging the tube at 300 x g for 5 min to remove possible cell debris and DMSO, the cell pellet was resuspended in 12 mL medium before being transferred to a tissue culture flask. Cells were then cultured in a humidified atmosphere at 37°C and with 5 % CO_2.

3.2.1.7 Compound treatment

All compounds used in this research work were dissolved in either DMSO or water and stored in aliquots at -20 °C to minimize freeze-thaw cycles. Stock concentrations varied from 2 mM to 10 mM based on the compound solubility. For biological assays involving compound treatment, it was necessary to include a control condition using the same concentration of the solvent in which the compound was dissolved. In case the compound of interest was dissolved in DMSO, the maximal concentration used was 0.5 % (v/v) for cellular and 2 % (v/v) for biochemical assays. For dose-response analysis, compounds were diluted in a three-step procedure. Compounds were diluted in DMSO through a serial dilution method in the first step. Afterwards, the diluted compounds were mixed with the assay medium. Finally, compounds were added to cells or purified protein to obtain the required final concentration. For the determination of an IC_{50} or EC_{50}, a minimum of at least five concentrations of compound was used.

3.2.1.8 Isolation of PBMCs from buffy coats

The peripheral blood mononuclear cells utilized for this research work were obtained from healthy donors through the Deutsches Rotes Kreuz (DRK) Hagen. To isolate PBMCs, the buffy coats were diluted with sterile PBS (1:2 dilution ratio) and gently layered over Pancoll-containing Lymphocyte Separating Medium tubes. Next, density gradient centrifugation was conducted by spinning the samples at 800 x g for 25 min at room temperature. It was crucial for this step to switch the centrifuge brake off to prevent the breakage of the individual layers. Subsequently, the plasma layer was removed, and then the PBMC layer was collected, transferred to a fresh tube, and washed with PBS. For the removal of remaining red blood cell residues, donor samples were treated with 5 mL ACK lysis buffer for 5 min at room temperature. After two additional washing steps using PBS, cells were resuspended in (hi) FBS, cryopreserved (see 3.2.1.5), and stored in the vapor phase of a liquid nitrogen tank.

3.2.1.9 Isolation of NK cells

NK cells utilized in this research study were isolated from PBMCs. For this purpose, cryopreserved PBMCs were thawed (see 4.2.1.4) and cultivated in a tissue culture flask overnight at a density of 1 x 10^6 cells/mL. This process facilitated the separation of adherent cell types from the lymphocyte fraction. Following the manufacturer's instructions, the lymphocyte fraction was further processed to purify NK cells *via* negative selection isolation using Dynabeads® Untouched™ Human NK Cells Kit.

3.2.1.10 Manual NK cell-mediated cancer cell cytolysis assay

The NK cell-mediated cancer cell cytolysis assay is a phenotypic co-culture-based approach that was designed to identify small molecules that restore NK cytotoxicity within an artificial TME. The assay was optimized and developed by Dr. Elisabeth Hennes (Waldmann lab, MPI Dortmund).

$A549^{Green}$ cells (3 x 10^3 cells/well) were seeded in RPMI1640 growth medium in transparent 96-well tissue culture plates. Subsequently, cryopreserved PBMCs (1 x 10^6 cells/mL) were thawed in IMDM to separate the lymphocyte fraction from the adherent monocytes. Cells were then incubated overnight in a humidified atmosphere at 37 °C and 5 % CO_2. The next day, the lymphocyte fraction was collected and resuspended in co-culture assay medium (see 3.1.4). Subsequently, immunomodulating factors were added: IL-15 (30 ng/mL for lymphocytes and 7.5 ng/mL for NKs), TGFβ-1 (30 ng/mL for lymphocytes and 7.5 ng/mL for NKs), and PGE_2 (200 ng/mL). The effector-to-target (E:T) ratios required for each donor were immediately assessed after purifying the PBMCs. To conduct experiments using purified NK cells, the isolation procedure described in 3.2.1.9 was followed, and an E:T of 10:1 was used. Next, lymphocytes or

NK cells were added to A549^{Green} cells, followed by the addition of compounds or DMSO as control to samples that were treated with the cytokine mix (IL-15, TGFβ-1, and PGE_2). Co-cultures were monitored for up to 144 h in 4 h intervals at 10X magnification using kinetic live-cell imaging *via* the IncuCyte® S3 device. Data analysis was conducted using the IncuCyte® S3 2019B Rev software. The cytolysis rate was determined using the area under the curve (AUC) utilizing GraphPad Prism 9, and the obtained data was then normalized to the IL-15 condition, which was considered 100 % NK cytolysis, and the cytokine mix, which was considered 0 % NK cytolysis. EC_{50} values were determined using non-linear regression with a four-parameter fit.

3.2.1.11 Automated NK cell-mediated cancer cell cytolysis assay

The Compound Management and Screening Center (COMAS) in Dortmund, miniaturized the NK cell-mediated cancer cell cytolysis for medium-throughput screening. A total of 29,502 compounds were included, of which 19,396 were selected commercial compounds from several sources, including ChemDiv, the Edelris library (Keymical Collections™), the LOPAC® library, the Prestwick Chemical Library® of FDA-approved and EMA-approved drugs, and 10,106 compounds of the unique in-house library.

A549^{Green} cells were seeded in black, clear bottom tissue culture plates (500 cells/well for 384 and 400 cells/well for 1536 well plates) using phenol red-free high glucose RPMI1640 medium using the Multidrop Combi device (Thermo Fischer Scientific). The plates were incubated at 37 °C and 5 % CO_2 overnight in a humidified atmosphere. Prior to the screening, donor lymphocytes underwent testing to determine the optimal E:T ratio for achieving optimal signal-to-background (S/B) ratios. Compound addition was performed using an Echo550 dispenser (Labcyte) at a final concentration of 11 µM for the initial screening and a serial dilution for EC_{50} determination. Next, immunomodulating factors IL-15 (30 ng/mL), TGFβ-1 (30 ng/mL), and PGE_2 (200 ng/mL) were added to the lymphocyte suspension, and the treated cells were added to the screening plates using the Multidrop Combi device (Thermo Fisher Scientific). Three sets of samples were used as controls: untreated lymphocytes and lymphocytes treated with the activating factor IL-15 or the cytokine mix. Imaging was conducted using the ImageXpress Micro XL device (Molecular Devices) at 10X magnification. A549^{Green} cells were detected using excitation st 465/40 nm and emission at 525/30 nm. The Cell Proliferation HT module of MetaXpress was utilized to perform image analysis. The A549^{Green} count was measured in comparison to the co-culture treated with cytokine mix as well as DMSO.

3.2.1.12 FACS-based characterization of lymphocytes

In order to determine NK cell proportion within donor lymphocytes or the purity of isolated NKs (see 3.2.1.9), CD56 and CD3 were stained, which are specific surface markers for NK cells and T cells, respectively (see Figure 11).

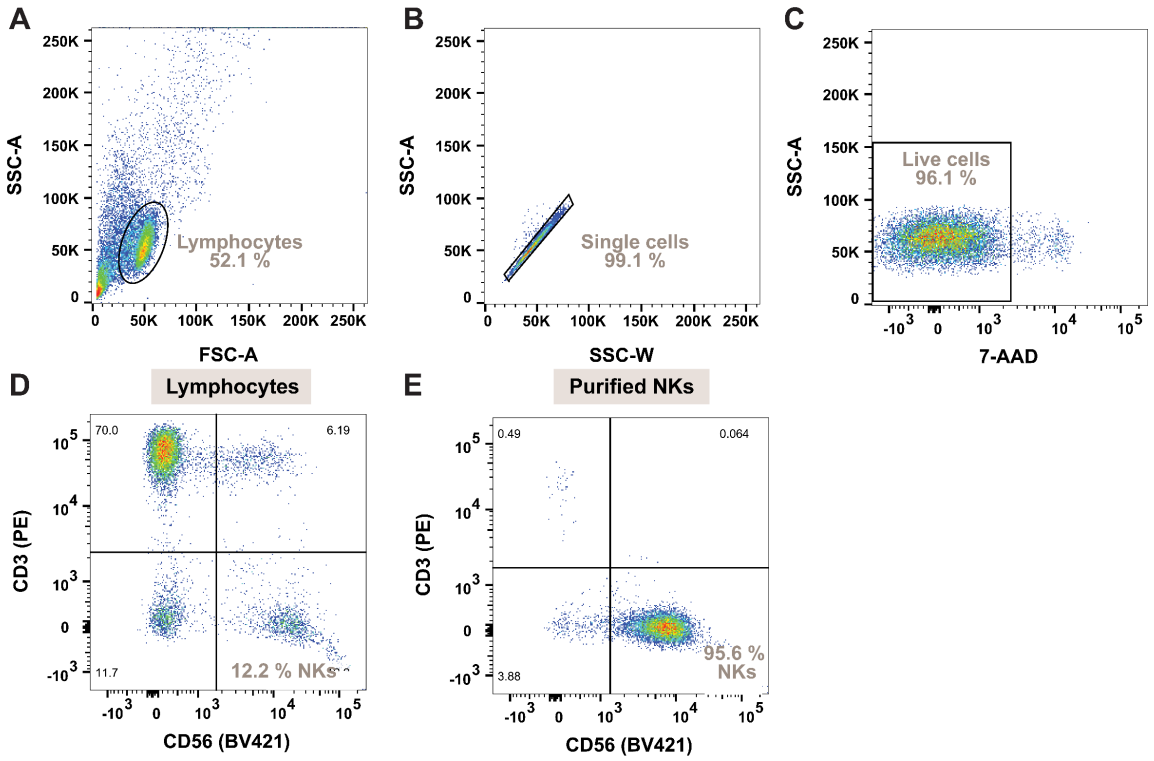

Figure 11: FACS gating strategy to determine the proportion of NK cells. Following the selection of the lymphocyte population (A), single cells (B), and live cells (C), the NK cell proportion was assessed (D and E) through analysis of CD3 and CD56 expression.

Lymphocytes or purified NK cells were suspended in FACS buffer 1, and then stained with fluorescently labeled anti-CD3-PE and anti-CD56-BV421 antibodies. After 20 min of antibody incubation on ice, cells were washed twice using FACS buffer 1, and 7-AAD (1:50) was added for live-dead discrimination. Samples were then analyzed using flow cytometry with the BD LSR II device using 405 nm and 488 nm for excitation and emission conducted using the following filters: 450/50, 575/26, and 695/40 nm. Fluorescence compensation was applied by analyzing the utilized fluorophores individually prior to sample analysis. Finally, data analysis was performed using FlowJo™ version 10.8.2 software.

3.2.1.13 FACS-based analysis of NK cell surface receptor expression

The following experiment was performed in collaboration with Jens Niemann (Watzl lab, Leibniz Research Centre for Working Environment and Human Factors (IfADo) Dortmund).

Two panels of antibodies against various NK cell surface receptors were used to evaluate the effect of IL-15 or the cytokine mix, individually or combined with RepSox, on the expression of NK cell surface receptors (see 4.1.4.2.). The surface receptors that were studied are crucial for various aspects of NK cell function, such as adhesion, cytotoxicity, identification, and inhibition. The first step was to isolate the lymphocyte fraction of PBMCs (see 3.2.1.8). Subsequently, the lymphocyte fraction (8 x 10^6 cells/mL) was seeded in non-treated CytoOne® dishes and treated with IL-15 (30 ng/mL) individually or in combination with TGFβ-1 (30 ng/mL) and PGE_2 (200 ng/mL), with or without 1 µM RepSox. Samples were then incubated for 48 h in a humidified atmosphere at 37 °C and 5 % CO_2. Next, cells were harvested, washed, and resuspended in FACS buffer 1. This was followed by determining the cell count using the CASY Cell Counter & Analyzer (OLS® OMNI Life Science) and adjusting the cell numbers. Lymphocytes were stained using Zombie NIR (1:700 in PBS) for live-dead discrimination and then washed using FACS buffer 1. Cells were stained after diluting antibodies for the mixed and activator panel in FACS buffer 2 (see 3.1.6.2). After two wash steps with FACS buffer 1, lymphocyte samples were analyzed *via* a Cytek® Aurora device (5L, Cytek Bioscience Inc.) utilizing the SpectroFlo® 3.1 software. Data analysis was conducted using FlowJo™ version 10.8.2 with the FlowAI 2.3.1 plug-in at default settings to clean up the obtained experimental data. Manual gating was performed to analyze NK populations, followed by an analysis of percent positive cells or geometric mean fluorescence intensity (gMFI) to best fit the populations. For dimensionality reduction, an equal number of NK cells per donor and stimulation condition was concatenated, and lastly, the default settings of the FlowJo software inbuilt t-distributed stochastic neighbor embedding (tSNE) algorithm were utilized. Cluster analysis was performed utilizing the FlowJo PhenoGraph clustering algorithm plugin.

3.2.1.14 Generation of cell lysates

In order to evaluate changes in cellular protein levels, it was necessary to lyse cells before conducting further analysis. Depending on the protein of interest, different cell lysis methods were utilized. In the first step of generating cell lysates, cells were collected either immediately (suspension cells) or detached using trypsin/EDTA or a cell scraper (adherent cells) and then transferred into reaction tubes. Next, cells were washed using ice-cold PBS, pelleted, and then lysed using the conditions described in Table 1. For cell lysis *via* RIPA or NP-40 lysis buffers,

cells were resuspended in an appropriate volume of the respective buffer and incubated for 30 min on ice. Samples were centrifuged for 25 min at 14,000 x g and 4 °C. Next, the supernatants were collected in fresh tubes. To prepare cell lysates for CETSA experiments, cells were harvested, washed, pelleted and resuspended in CETSA lysis buffer. Samples were lysed through five consecutive freeze-thaw cycles. After snap-freezing the samples in liquid nitrogen, they were immediately thawed on ice until 60-80 % of the sample was defrosted. After five repetitions, samples were centrifuged at 20,000 x g and 4°C for 25 min. Finally, supernatants containing the soluble protein fraction were collected in fresh tubes. The protein concentration was determined, and in case samples were prepared for immunoblotting, 5X SDS sample buffer was added in a 5:1 ratio, and samples were boiled at 95 °C for 5 min.

Table 1: List of utilized lysis methods required for assessment of protein levels.

Protein of interest	Cell type	Adherence type	Lysis buffer
COX-2	BxPC-3	Adherent	RIPA lysis buffer
EP2	PBMCs	Suspension	RIPA lysis buffer
EP4	PBMCs	Suspension	RIPA lysis buffer
Granzyme B	PBMCs	Suspension	NP-40 lysis buffer
NOTCH-1	PBMCs	Adherent	RIPA lysis buffer
PDEδ	Jurkat	Suspension	NP-40 lysis buffer
			CETSA lysis buffer
Phosphoproteins	PA-TU-8902	Adherent	Phosphoproteomics lysis buffer

To prepare cell lysates for phosphoproteomics experiments, cells were washed twice using pre-warmed PBS, followed by a wash step using TBS. Next, Phosphoproteomics lysis buffer was added to the cells, which were then collected using a cell scraper and transferred to a fresh tube. The cell lysates were boiled for 5 minutes at 96 °C using the thermomixer and then sonicated (4 x 30 sec cycles at 60 % power). Subsequently, samples were centrifuged at 16,000 x g for 30 minutes at room temperature, and the supernatants were collected in fresh tubes. Finally, the protein concentration was measured using Pierce 660 nm protein assay following the manufacturer's instructions.

3.2.1.15 SBE4-dependent reporter gene assay

To evaluate the effect of compounds on the activity of the TGFβ pathway, the *SBE4*-dependent reporter gene assay was utilized. The pBV-SBE4-Fluc plasmid contains four consecutive copies of the Smad-binding element (SBE) and regulates the expression of a firefly luciferase (FLuc) reporter that is inducible upon pathway activation.[140] The pRL-TK- plasmid, on the other hand, directs the expression of the constitutively expressed *Renilla* luciferase (Rluc). HEK293T cells were transiently transfected with Fluc and Rluc-expressing plasmids *via* a reverse transfection protocol. For this purpose, 0.6 µg Fluc and 0.5 µg Rluc plasmids were mixed with Lipofectamine™ 2000 in a 1:3 ratio in serum-free Opti-MEM medium and incubated for 20 min to form the DNA-lipid complex. At the same time, 12 mL of HEK293T cell suspension with a density of 4.44 x 10^5 cells/mL was prepared in DMEM medium with 2 % FBS (hi). Next, the complex was introduced into the HEK293T suspension. Following this, cells were seeded at a concentration of 4.0 x 10^4 cells per well 90 µL in a transparent 96-well plate. The plate was then incubated for 6 h in a humidified atmosphere at 37 °C and 5 % CO_2. To induce the expression of firefly luciferase, cells were treated with 20 ng/mL TGFβ-1, and compounds or DMSO were added simultaneously using serum-reduced DMEM medium (2 % FBS (hi)) for 24 h. A control without TGFβ-1 stimulation was included. After the incubation, cells were lysed using 25 µL of 1X PLB, and the firefly and *Renilla* luciferase activities were assessed using the Dual-Glo® Luciferase Assay System according to the manufacturer's instructions. The signals were measured using the Tecan Spark® multimode microplate reader. The *SBE4* promoter activity was determined by normalizing the obtained Fluc to their corresponding Rluc values, and the values obtained for cells treated with TGFβ-1 and DMSO were set to 100 %. Finally, IC_{50} values were determined using GraphPad Prism 9.0 *via* a non-linear regression using a four-parameter curve fit.

3.2.1.16 Firefly luciferase activity assay

The Fluc activity assay was conducted to exclude the possibility of the investigated compounds to directly modulate the firefly luciferase in the reporter gene assay. For this, HEK293T cells were transfected as described in 3.2.1.14 and stimulated with 20 ng/mL TGFβ-1 for 24 h. A control without TGFβ-1-stimulation was included as well. Next, cells were lysed using 1X PLB, collected in tubes, snap-frozen, and stored at -80 °C. To perform the assay, 9 µL cell lysate was transferred into the wells of a white 96-half-well microplate, and 1 µL in 1X PLB pre-diluted compound, firefly luciferase inhibitor (Figure 12) or DMSO was added to the respective wells. The plate was incubated on a microplate shaker at 400 rpm for 1 h at 25°C. Subsequently, the firefly luciferase activity was assessed using the Dual-Glo® Luciferase Assay System, and the respective signals were measured using the Tecan Spark® multimode microplate reader. The obtained values were

normalized to the lysates treated with DMSO and TGFβ-1 and finally, analyzed using GraphPad Prism 9.0 software.

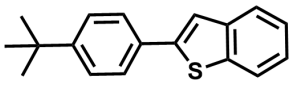

Firefly luciferase inhibitor

Figure 12: Chemical structure of the firefly luciferase control inhibitor

3.2.1.17 Cellular Thermal Shift Assay (CETSA)

The cellular thermal shift assay is a valuable method to assess the target engagement of ligands to the protein of interest. This label-free technique detects changes in the thermal stability of proteins induced upon ligand binding and can even provide insights into downstream effects.[142] There are different variations for the CETSA assay, and in this study, the focus is on CETSA performed with intact cells (i.e., in-cell CETSA) and cell-lysates (i.e., lysate-based CETSA) to evaluate small molecule binding to the respective protein of interest.

I. Lysate-based CETSA

Jurkat cells were seeded in two T175 flasks (2.5 x 10^7 cells/flask) in 50 mL RPMI1640 media and incubated overnight in a humidified atmosphere at 37 °C and 5 % CO_2. Next, cells were collected, washed with PBS three times, pelleted, and lysed in CETSA lysis buffer following procedure 3.2.1.14. Samples were centrifuged for 25 min at 100,000 x g and 4 °C (Beckman Optima MAX-TL), and the soluble protein fractions were collected. Subsequently, the protein concentration was determined using the DC™ Protein Assay Kit II according to 3.2.2.1. Lysates were diluted to a concentration of 2.5 g/L and treated with 10 µM Deltacovalin or DMSO for 10 min at room temperature. The compound and vehicle-treated samples were equally divided into ten aliquots and subjected to individual heat treatment with an Eppendorf Mastercycler ep Gradient S or MasterCycler X50s device.

Table 2: Temperature gradient used for PDEδ lysate-based CETSA.

Cycler 1 /°C	37.0	40.6	45.5	53.2	57.2
Cycler 2 /°C	60.1	65.6	70.9	76.0	79.9

Next, denatured proteins were separated by ultracentrifugation centrifugation at 20,000 x g and 4 °C for 25 min, and the supernatants of the individual samples were transferred into fresh tubes. After combining the samples with 5X SDS sample buffer at a 5:1 ratio, they were boiled at 95 °C

for 5 min. Finally, samples were subjected to immunoblotting according to 3.2.2.2 and underwent densitometric analysis using the Image Lab software. Purified His-PDEδ (1 pg) was used as a positive control to confirm PDEδ identity. The resulting protein abundance was normalized to the protein level of the lowest temperature (37 °C) for each condition. The melting temperature was determined using a non-linear regression curve fit using GraphPad Prism 9.0.

II. In-cell CETSA

Jurkat (9 x 10^6 cells/flask) or BxPC-3 (6.5 x 10^6 cells/flask) cells were seeded into two T75 tissue culture flasks in 10 mL RPMI1640 media. While Jurkat cells were treated immediately after seeding, BxPC-3 cells were incubated overnight at 37 °C and 5 % CO_2 in a humidified atmosphere. For the treatment, either compound or DMSO was added to the cells, followed by an incubation step at 37 °C and 5 % CO_2 for 20 min (for COX-2) to 2 h (for PDEδ). Subsequently, cells were harvested, washed twice with PBS, and resuspended in 0.6 mL PBS. The cell suspensions were then divided into ten aliquots and underwent heat treatment with an Eppendorf Mastercycler ep Gradient S or MasterCycler X50s device.

Table 3: Temperature gradients used for in-cell CETSA.

PDEδ							
Cycler 1 /°C	37.0	45.5	53.2	56.5			
Cycler 2 /°C	64.6	68.2	73.2	78.5	82.9	84.8	
COX-2							
Cycler 1 /°C	36.9	48.2	57.3				
Cycler 2 /°C	62.5	64.3	68.6	71.2	73.9	79	82.8

Next, either PBS with 4.4 % NP40 alternative (0.4 % final concentration) in case of PDEδ or 5x RIPA lysis buffer in case of COX-2 was added to each aliquot, and the cells were lysed *via* free-thaw cycles following procedure 3.2.1.14. This was followed by a centrifugation step at 100,000 x g and 4 °C for 25 min (Beckman Optima MAX-TL). The supernatants were transferred into fresh tubes, 5X SDS loading buffer was added, and the samples were boiled at 95 °C for 5 min. The samples were then analyzed *via* immunoblotting. Purified His-PDEδ (1 pg) was used as a positive control to confirm PDEδ identity. Band intensities were quantified using the Image Lab software. The protein abundance was normalized to the protein level at 37 °C for each condition, and the melting temperature was determined using a non-linear regression curve fit with GraphPad Prism 9.0.

3.2.1.18 Viability assay

To assess the effect of a compound on cell viability, kinetic live-cell analysis was utilized. For this, $A549^{Green}$ cells (3 x 10^4/well) were seeded in transparent 96-well tissue culture plates (see 3.2.1.4) and incubated overnight at 37 °C and 5 % CO_2. The following day, cells were treated with a serial dilution of the compound of interest (see 3.2.1.7), and cell growth was monitored by tracking the cell count using the IncuCyte® S3 or ZOOM devices. Cells were imaged in 2 h or 4 h intervals for 96 h and 10X magnification, capturing phase contrast and green fluorescent images. Data analysis was performed using the IncuCyte® S3 2019B Rev or IncuCyte® ZOOM 2018A software. The obtained values were plotted using the GraphPad Prism 9.0 software.

3.2.1.19 Washout and sequential treatment assays

To validate the covalent binding of Deltacovalin *in cellulo*, washout and sequential treatment experiments were conducted. In these experiments, cells were exposed to both Deltacovalin and the noncovalent control Deltasonamide 1 for a specific time period, which was followed by a washout step. The cell growth rates of various mammalian and murine cell lines (see Tables 4 and 5) were investigated. For washout experiments, cells were seeded in a transparent 96-well tissue culture plate and incubated overnight in a humidified atmosphere at 37 °C and 5 % CO_2. The next day, the plate was imaged prior to compound treatment using the phase contrast channel with IncuCyte® ZOOM devices at 10X magnification. Next, cells were treated with the compound or DMSO for 4, 5, or 6 h. This was followed by washing the cells with the appropriate culture media three times, and phase-contrast imaging was performed at 1-h intervals for a total of 96 h. For sequential treatment experiments, cells were seeded and treated similarly to the washout experiments. Cell lines were treated with compounds or DMSO for 4 h, followed by a triple PBS wash and a 20-h compound-free incubation. This process was repeated for a total of four treatment days. For sequential treatment experiments, phase contrast imaging continued in 1-h intervals during and after the compound treatments for a total of 120 h.

Table 4: Seeding densities for mammalian cell lines used for wash-out or sequential treatment experiments.

Cell line	Seeding density [cells/well]
A549	5.0×10^3
BxPC-3	5.0×10^3
HCT116	5.0×10^3
HT-29	8.0×10^3
LS-174T	1.2×10^4
MIA PaCa-2	5.0×10^3
NCI-H358	5.0×10^3
NCI-H441	7.0×10^3
PANC-1	5.0×10^3
PA-TU-8902	5.0×10^3
SK-LU-1	4.0×10^3
SW480	5.0×10^3

For sequential treatment experiments using the murine cell lines KP1035, KPACK135-1, and KPACK135-10, the treatment protocol was modified to include the fluorescent dye CellEvent™ Caspase-3/7 Green (90 µL/mL) to detect apoptotic cells. The dyes were added to the cells after the PBS-based compound washout. They were left on the cells during the first three treatments for 20 h, and during the last treatment, they remained in the wells. For both experiments, analysis of data was performed using the IncuCyte® S3 2019B Rev or IncuCyte® ZOOM 2018A softwares. The obtained values were represented utilizing the GraphPad Prism 9.0.

Table 4: Seeding densities for murine cell lines used for sequential treatment experiments.

Cell line	Seeding density [cells/well]
KP1035	6.5×10^3
KPACK135-1	4.0×10^3
KPACK135-10	4.0×10^3

3.2.1.20 Lysosomotropism assay

The lysosomotropism assay was conducted to examine whether compounds accumulate in the lysosomes. For this purpose, the red fluorescent dye LysoTracker® Red DND-99 was used. This dye is a weak base that accumulates in acidic lysosomes. Lysosomotropic small molecules cause an increase in lysosomal pH, which in turn decreases the levels of the dye in the lysosomes. For this experiment, U-2OS cells (7.0 x 10^3 cells/well) were seeded into black, clear bottom tissue culture plates and incubated overnight at 37°C and 5 % CO_2. The next day, cells were treated with compounds and incubated for 1 h. Medium containing the fluorescent dyes LysoTracker® Red DND-99 (1 µM) and Hoechst-33342 (10 µg/µL) was added, and cells were incubated for 30 min at 37 °C and 5 % CO_2. Subsequently, the U-2OS cells were washed three times with PBS and fixated by adding a 3.7 % paraformaldehyde solution, then incubated for 10 min in the dark at room temperature. Finally, after washing the cells twice with PBS, imaging was conducted utilizing an Axiovert 200 M automated screening microscope (Zeiss) at 10x magnification. The analysis of the images was conducted using the open-source image analysis software CellProfiler.[143] The resulting data were normalized to DMSO (representing 100 % LysoTracker Red intensity) and Chloroquine (representing 0 % LysoTracker Red intensity). The normalized data were then presented and plotted using GraphPad Prism 9.0.

3.2.1.21 Phospholipidosis assay

The following experiment was performed by Dr. Belén Lucas (Waldmann lab, MPI Dortmund).

For the phospholipidosis assay, the detection reagent HCS LipidTOX™ Red was utilized. Therefore, U-2OS cells (5.0 x 10^3 cells/well) were seeded into black, clear-bottom 96-well tissue culture plates and incubated overnight at 37 °C and 5 % CO_2. The cells were then treated with medium containing the compound of interest, sertraline (4 µM), as a positive control and DMSO as a negative control for 4 h at 37 °C and 5 % CO_2. Afterwards, cells were washed with PBS thrice, and then medium containing HCS LipidTOX™ Red was added to the wells, or the wash step was skipped, and the dye was immediately added. This was followed by a 24-h incubation in a humidified atmosphere at 37 °C and 5 % CO_2. Next, Hoechst-33342 (5 µg/mL) was added to the cells for 30 min at 37 °C and 5 % CO_2. Finally, cells were fixated using a paraformaldehyde solution (3.7 %), washed, and imaging was conducted using the ImageXpress Micro XL device (Molecular Devices) at 20X magnification.

3.2.2 *In vivo* studies using a KRas^{G12D} andTP53$^{fl/fl}$ (KP) mouse line

The following experiment was performed in collaboration with Maxim Huetzen (Jachimowicz lab, MPI for Biology of Ageing, Cologne).

The previously described KP mouse line was employed for *in vivo* studies.[144] For induction of lung tumors, mice were anesthetized using ketamine (100 mg/kg) and xylazine (10 mg/kg) through intraperitoneal administration (IP). Subsequently, a replication-deficient adenovirus that expressed the Cre-recombinase (Adeno-Cre, 2.5 x 10^6 PFU) was intratracheally instilled. The formation and growth of tumors was consistently monitored through computed tomography (CT) imaging *via* the Skyscan 1176 (Bruker, Massachusetts, USA). For CT imaging, mice underwent 2.5 % isoflurane-based anesthesia and tumor identification was achieved utilizing the Bruker Dataviewer software. Deltacovalin was dissolved in 30 % (v/v) 2-Hydroxypropyl-β-cyclodextrin (HP-β-CD) and 0.5 % (v/v) Hydroxypropyl-methylcellulose (HPMC) in water, resulting in a final concentration of 1.5 mg/mL. The compound was administered daily for 21 days through IP injections using a concentration of 15 mg/kg (i.e., 0.1 mL/10 g body weight). The GV-SOLAS guidelines for substance administration in experimental animals were followed throughout the experiment. Preliminary PK/PD studies conducted in non-tumor bearing mice indicated that administering 15 mg/kg of Deltacovalin daily for 21 days via IP injections was the most effective dosage and application method for *in vivo* use of the covalent inhibitor. This approach has been approved by the veterinary office of Saarland (file number C1_2.4.2.2 14-2020). For the first compound treatment days, the mice displayed drowsiness and a pilorection post-treatment for about 4 h. The behavior normalized after a few days. The body weights of the mice remained unchanged throughout the in vivo study, and no signs necessitating termination of the study were observed. The lung tumor volumes were assessed using the sum of the product of means (SPD) as a metric. For this purpose, width and length of tumors were measured in the transverse plane. Quantification of CT images of mouse lungs were performed utilizing the HOROS software.

3.2.3 Molecular biology, biochemical and biophysical methods

3.2.3.1 Determination of protein concentrations

Protein concentrations were assessed using DC™ Protein Assay Kit II. The colorimetric assay was performed in accordance with the manufacturer's instructions. The readout was conducted using the Spark® multimode microplate reader, measuring the absorbance at 750 nm. The protein concentration was determined using a BSA protein standard curve.

For the phosphoproteomics experiment, the protein concentration was determined using the Pierce™ 660 nm Protein Assay kit, which is compatible with detergents and reducing agents.

3.2.3.2 Immunoblotting

Immunoblotting experiments were performed to evaluate the influence of compounds or other stimulants on a specific protein in cell lysates. For this purpose, cell lysates were generated (see 3.2.1.14), the protein concentration was determined, and samples were denatured by mixing them with 5X SDS loading buffer and boiling them at 95 °C for 5 min. Proteins were separated based on their molecular weight using 10-12 % SDS polyacrylamide gels in a TRIS/glycine buffer system under reducing and denaturing conditions. Protein samples (10-40 µg) and the size control PageRuler™ pre-stained protein ladder were loaded onto the gel. Next, proteins were stacked at 80 V current for 5-10 min, followed by protein separation at 100-120 V in 1X SDS running buffer. The proteins were transferred from the gel to the polyvinylidene difluoride (PVDF) membrane *via* wet tank transfer using a transfer buffer. For this purpose, the PVDF membrane was treated with 100 % methanol for 30 s, and the transfer cassette was assembled in the following order: fiber pad, blotting paper, PVDF membrane, gel, blotting paper, and fiber pad. Next, air bubbles were removed, the transfer cassette was placed into the tank, and a 100 V current was applied for 1 h. Subsequently, the membrane was blocked for 1 h at room temperature, and then primary antibodies diluted in blocking buffer (see 3.1.6.1) were added and incubated either overnight at 4 °C or 1 h at room temperature. Afterwards, the membrane was washed three times using PBS or TBS and then incubated with secondary antibodies diluted in blocking buffer containing 0.1 % Tween® 20 for 1 h at room temperature in the dark. The utilized secondary antibodies were coupled to LI-COR infrared (IR) dyes, which enable direct visualization of protein band. After incubation with the secondary antibodies, membranes were washed, and imaging was conducted using the ChemiDoc MP Imaging System. Quantification of protein band intensities was performed using the ImageLab software.

3.2.3.3 IFN-γ Enzyme-linked Immunosorbent Assay (ELISA)

The levels of secreted IFN-γ were quantified for an orthogonal validation of NK cell cytotoxic activity. Therefore, the supernatants of the NK cell-mediated cancer cell cytolysis assay samples were collected and subjected to the human IFN-γ ELISA MAX™ kit. The day before the assay, the Nunc™ MaxiSorp™ ELISA 96-well plate was treated with IFN-γ ELISA coating buffer containing capture antibody (1:200) and incubated overnight at 4 °C. All washing steps were carried out using IFN-γ ELISA wash buffer, and incubation steps were conducted at room temperature. On the next day, the plate was washed and blocked using IFN-γ ELISA assay diluent for 1 h. In the meantime, the samples and the IFN-γ standard were diluted and prepared for testing. Subsequently, the plate was washed and treated with the samples for 2 h. After an additional wash step, the detection antibody solution was added to the plate and incubated for

1 h, followed by another wash step. Next, the plate was treated with Avidin-HRP (horse radish peroxidase) solution and then incubated for 30 min. The plate was thoroughly washed, and then the TMB substrate solution was added for 10 min in the dark. The reaction was stopped by adding IFN-γ stop solution. Finally, the absorbance was measured on the Spark® multimode microplate reader at 450 nm for the background and 570 nm to measure the absorbance of the diimine resulting from the HRP/TMB reaction. Finally, the background absorbance A_{450} was substracted, and the IFN-γ concentration was determined using the IFN-γ standard curve. The obtained data was represented utilizing GraphPad Prism 9.0.

3.2.3.4 Prostaglandin formation assay

The following experiment was performed in collaboration with Dr. Astrid Kahnt (Goethe University, Frankfurt).

The secretion levels of prostaglandins and thromboxane were evaluated to assess the impact of compounds on prostanoid biosynthesis. A549 cells (1.5 x 10^6 cells/10 cm dish) were seeded in DMEM medium and allowed to attach for 24 h in a humidified atmosphere at 37 °C and 5 % CO_2. Next, the cells were simultaneously treated with IL-1β (1 ng/mL) and compounds or DMSO in serum-reduced DMEM (2 % (v/v) FBS) and incubated for 16 h at 37 °C and 5 % CO_2. The supernatants were then collected and submitted to LC-MS/MS-based analysis.

3.2.3.5 Enzymatic COX-1 and COX-2 assay

The enzymatic assays for analysis of COX-1 and COX-2 were performed by Eurofins Discovery.

For assessment of human recombinant COX-1 activity, a mixture containing 3 µM arachidonic acid (AA), 25 µM 10-acetyl-3,7-dihydroxyphenoxazine (ADHP), and 20 µM RepSox was prepared and incubated for 3 min at room temperature. To assay the activity of human recombinant COX-2, 1.2 µM AA, 25 µM ADHP, and 20 µM RepSox were incubated for 5 min at room temperature. For both proteins, an oxidation reaction *via* the addition of HRP was induced. The fluorescence of the resulting resorufin was measured to determine the enzymatic activity.

3.2.3.6 Plasmid isolation

After the amplification of plasmids using chemically competent *E. coli* strains, they were isolated utilizing the QIAGEN® Maxi Kit in accordance with the manufacturer's protocol. Bacteria containing the respective plasmid were grown overnight at 37 °C in LB medium supplemented with an appropriate antibiotic (Ampicillin, 100 µg/mL). Next, the bacterial suspension was pelleted, followed by alkaline lysis, centrifugation, and transfer of the supernatant to a column, allowing the plasmid DNA to bind to a solid phase. The DNA was then washed to remove impurities, e.g.,

salts, and eluted in sterile water. Finally, the plasmid DNA concentration was determined using the NanoDrop™ 2000 spectrophotometer, measuring the absorbance at 260 nm.

3.2.3.8 PDEδ protein purification

The expression and purification of PDEδ proteins were performed by Christine Nowak (Waldmann lab, MPI Dortmund).

Recombinant His-PDEδ and GST-PDEδ were expressed in E.coli Rosetta cells. A single colony was used to inoculate the preculture in |TB medium, supplemented with 100 ug/mL ampicillin and 30 µg/mL chloramphenicol, before overnight incubation at 37 °C with simultaneous shaking. The next day, 5,000 mL of TB medium was inoculated with 50 mL of the Rosetta suspension. Expression of His-PDEδ and GST-PDEδ was induced by adding 100 or 300 µM of β-D-1-thiogalactopyranoside (IPTG), respectively, followed by a 7-h incubation at 25°C. Next, cells were pelleted, resuspended in bacterial lysis buffer, homogenized via sonication, and lysed through mechanical lysis. The soluble fraction of the lysate was then separated via centrifugation for 35 min at 10 °C and 13,000 x g and further processed for protein purification.

For the purification of His-PDEδ, lysate was first loaded onto a Ni-NTA column, washed, and then eluted using an imidazole containing elution buffer (30 mM TRIS-HCl, 150 mM NaCl, 1 mM β-mercaptoethanol and 250 mM imidazole, pH 7.5). Next, the sample was further purified using the size exclusion column HiLoad 26/600 Superdex 75 pg column, the elution buffer without. imidazole. For purification of GST-PDEδ, lysate was loaded onto a GSTrap HP-column, washed, and proteins were eluted with elution buffer (30 mM TRIS-HCl, 150 mM NaCl, 1 mM β-mercaptoethanol and 20 mM glutathione, pH 7.5). Proteins were subsequently separated from the GST tag using thrombin protease for proteolytic cleavage, followed by further purification through size exclusion on a HiLoad 26/600 Superdex 75 pg column using elution buffer without glutathione. Protein purity was confirmed by SDS-PAGE.

3.2.3.9 Arl2 protein purification and nucleotide exchange

The expression, purification, and nucleotide exchange of Arl2 proteins were performed together with Christine Nowak (Waldmann lab, MPI Dortmund).

Recombinant human His-Arl2 was expressed in *E.coli* Rosetta cells. Expression of His-Arl2 was induced by adding 100 µM of IPTG followed by an overnight incubation at 25°C. Next, cells were pelleted, resuspended in bacterial lysis buffer, homogenized via sonication, and lysed through mechanical lysis. The soluble fraction of the lysate was then separated *via* centrifugation for 35 min at 10 °C and 13,000 x g and further processed for protein purification. For the purification of

His-Arl2, lysate was first loaded onto a Ni-NTA column, washed, and then eluted using an imidazole containing elution buffer (30 mM TRIS-HCl, 150 mM NaCl, 1 mM β-mercaptoethanol and 250 mM imidazole, pH 7.5). Next, the sample was further purified using the size exclusion column HiLoad 26/600 Superdex 75 pg column, the elution buffer without. imidazole. SDS-PAGE confirmed protein purity.

Purified Arl2 proteins are bound to GDP and, therefore, nucleotide exchange was performed. For this purpose, 4 U/mg alkaline phosphatase and 2X molar excess of the non-hydrolyzable GTP analogue GppNHp were added to Arl2 overnight incubation at 4 °C. Nucleotide exchange was confirmed *via* reversed-phase HPLC using a Prontosil 120-5-C18 column in potassium phosphate buffer with 10 mM tetrabutylammonium bromide and 8 % (v/v) ACN pH 6.6 (Figure 13).

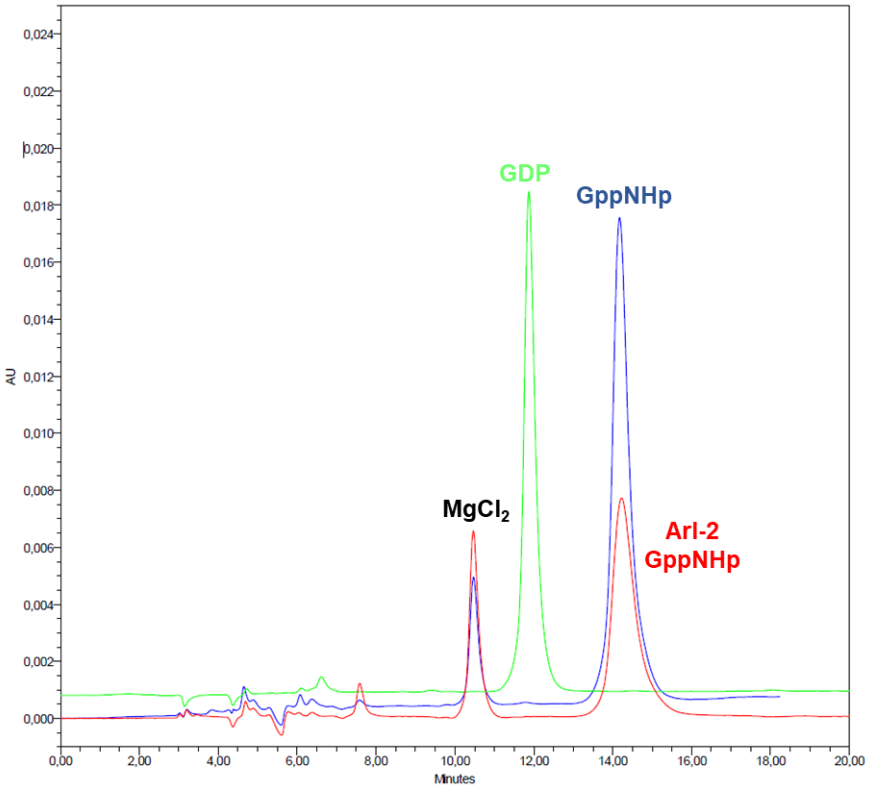

Figure 13: Overlayed chromatogram to confirm Arl2 nucleotide exchange.

3.2.3.10 Crystallization of PDEδ

Recombinant human GST-PDEδ was expressed in *E. coli*, purified, and the protein tag was removed as described in 3.2.2.8. Four equivalents of Deltacovalin (2.5 % (v/v) DMSO) were combined with PDEδ protein in 25 mM TRIS-HCl, pH 7.5, 150 mM NaCl, and 3 mM DTE, and then incubated at 37 °C for 48 hours shaking at 400 rpm. Subsequently, precipitates were removed *via* centrifugation at 20,000 x g and 4 °C for 5 min. The sitting drop approach (iQ plates, SPT Labtech) was utilized to crystallize PDEδ. For this purpose, 100 nL of the reservoir buffer (20 % (w/v) PEG3350 and 0.2 M potassium formate) was mixed with 100 nL protein-compound complex and incubated at 20 °C. After 10 days, PDEδ crystals were harvested. For this, 20 % (w/v) PEG400 solution was added as a cryoprotectant to the drop before fishing out the crystals and plunging them in liquid nitrogen. A resolution of 1.9 Å was obtained from the Synchrotron X-ray diffraction data using the X10SA beamline at the Swiss Light Source at the Paul Scherrer Institute. Data processing and scaling were performed using XDS and XSCALE.[145] Subsequently, the protein structure was solved using a homology model of PDEδ from PDB 5ML3 using the software Phaser from the Phenix suite.[146,147] This was followed by structure refinement cycles using phenix.refine and Coot.[148,149] Finally, figures were created utilizing the PyMOL molecular visualization system (Schrödinger).

3.2.3.10 Arl2 competitive PDEδ fluorescence polarization (FP) assay

The FP assay was performed by Dr. Ruirui Zhang (Waldmann lab, MPI Dortmund).

For fluorescence polarization assays, the tag of GST-tagged PDEδ was removed as described in 3.2.3.8. PDEδ (40 nM) was mixed with fluorescein-labeled atorvastatin probe (24 nM) and ranging compound concentration in the presence or absence of Arl2·GppNHp (40 nM) in PBS (containing 0.05 % (w/v) CHAPS and 1 % (v/v) DMSO). This was followed by an overnight incubation at room temperature. The fluorescence polarization was measured on the Spark® multimode microplate reader using an excitation wavelength of 450 nm and an emission wavelength of 535 nm.

3.2.4 Proteomics methods

3.2.4.1 Glu-C-mediated PDEδ protein digestion

Deltacovalin-bound and unbound DMSO-treated protein PDEδ (4 µg/sample) were treated with guanidine hydrochloride (6.5 M) and boiled for 10 min at 95 °C for denaturation. Samples were reduced using 1 mM DTT, followed by a 30-min incubation at room temperature, and then alkylated using 5.5 mM CAA with a 20-min incubation at room temperature. Ammonium bicarbonate buffer was then added to reduce the guanidine hydrochloride concentration to less than 0.8 M. Subsequently, Glu-C (0.5 µg) was added, and the samples were incubated overnight

at ambient temperatures. The digestion was stopped using TFA (0.2 % v/v), and the samples were stage tipped. For this, the samples were immobilized on C18 material-containing stage tips, which were activated using methanol and washed before use. The samples were then rinsed using stage tip buffer A and then eluted through stage tip buffer B. Finally, samples were dried using SpeedVac centrifugation and then submitted to the in-house HRMS Team for analysis.

The sample was dissolved in 40 µL of 0.1 % TFA in water, sonicated at room temperature for 15 min, and centrifuged at 15,000 x g for 1 min. Next, 3 µL of sample was loaded onto a pre-column cartridge for desalting, incubated for 5 min, and eluted using 0.1 % TFA in water at a flow rate of 30 µL/min. Throughout the whole analysis, the sample was back-flushed from the pre-column to the nano-HPLC column. Elution was conducted using a two-buffer system: solvent A containing 0.1 % (v/v) FA in water and solvent B containing 0.1 % (v/v) FA in ACN. To achieve elution, a solvent gradient starting from 5 % solvent B and increasing to 30 % solvent B over 35 min with a flow rate of 300 nL/min, while keeping the column at 40 °C. The column of the nano HPLC was rinsed by raising the proportion of solvent B to 60 % over the course of 5 min, followed by a quick rapid increase to 95 % within 5 min. The column was then rinsed for another 5 min before being flushed back to the initial conditions and a 14-min equilibration step of the system. For the duration of the whole gradient, a TOP10 shot-gun proteomics method for the MS and MS/MS analysis was utilized. In the case of full MS scan experiments, a mass range of 300 to 1650 m/z was scanned employing a resolution of 70,000. MS/MS scans were performed at a resolution of 17,500 for the most intense ions with at least a doubly charged state. The evaluation of the data was carried out using MaxQuant.[141] The spectra were queried against the PDE6D sequence (Uniprot ID O43924) and a contamination database with a 1 % false discovery rate, utilizing a decoy database to analyze the false discovery rate. For database search, oxidation of methionine and N-terminal acetylation of proteins, carbamidomethylation of cysteines, and artificial modification of glutamic acids have been set as variable modifications. Cleavages by Glu-C were analyzed based on the enzyme that was used for digestion.

3.2.4.2 Phosphoproteome profiling

This experiment was performed together with Dr. Elena Rudashevskaya (MPI Dortmund, Waldmann lab) and the in-house HRMS team.

To investigate the impact of a compound on cellular signaling pathways on a global level, mass spectrometry-based phosphoproteomics was employed. PA-TU-8902 cells (8 x 10^6 cells/dish) were seeded in three 15 cm dishes and left to incubate in a humidified atmosphere at 37 °C and 5 % CO_2 overnight. Next, the medium was replaced, and the cells were treated with 5 µM

Deltacovalin or DMSO for 2 h at 37 °C and 5 % CO_2. After the treatment, cells were washed twice with PBS and once with TBS and then lysed using boiling phosphoproteomics lysis buffer (see 3.2.1.14), and the protein concentration was assessed using Pierce™ 660 nm Protein Assay. Prior to phosphopeptide enrichment, proteins were digested. For this purpose, the samples (1 mg) were diluted with water, and a bead slurry containing hydrophobic and hydrophilic Sera-Mag™ SpeedBead™ magnetic particles (1:1 ratio) was prepared. Next, the lysate samples and the bead slurry were mixed, and ACN (70 % v/v) was added to precipitate the protein onto the beads. The mixture was incubated for 10 minutes at room temperature, mixed, and then further incubated for an additional 10 minutes until the protein aggregation process was completed. The supernatant was then collected utilizing a magnetic rack. Afterwards, the beads were washed with ACN, followed by ethanol (70 % v/v), and then solvent residues were removed by drying the beads for 5 minutes at room temperature. Subsequently, phosphoproteomics digestion buffer containing a Trypsin/Lys-C mix was added, and the samples were digested overnight, shaking at 1000 rpm at 37 °C. The next day, the digestion reaction was stopped using TFA (10 % v/v), and the supernatant was collected in a fresh tube. One-fifth of the sample was desalted using stag tip purification and then analyzed for LC-MSMS-based proteome profiling. Briefly, the stage tips containing C18 material were activated using methanol, washed, and then the samples were immobilized. After rinsing the samples with stage tip buffer A, they were eluted using stage tip buffer B. Lastly, samples were dried through SpeedVac evaporation. The rest of the protein digest underwent phosphopeptide enrichment. To enrich the samples, magnetic TiO_2 particles (2 mg) were prepared by rinsing them once with ethanol and three times with phosphoproteomics loading buffer. After the protein digest was mixed with phosphoproteomics loading buffer in a 1:1 ratio, the mixture was centrifuged for 5 minutes at 10,000 x g and 4°C to remove the precipitate. The resulting supernatant was then combined with magnetic TiO_2 particles and allowed to incubate for 20 minutes at ambient temperature with continuous mixing. The particles were washed once with phosphoproteomics loading buffer and three times each with phosphoproteomics wash buffers 1 and 2. For the elution of enriched phosphopeptides, the phosphoproteomics elution buffer was added to the samples, followed by a 10-minute incubation at ambient temperature. This process was repeated three times in total. The supernatants were collected in a low-binding reaction tube containing TFA, resulting in a final concentration of 3 % (v/v) TFA. Finally, the phosphopeptides were desalted through stage tips containing two layers of SDB-RPS matrix material. The matrix was washed and equilibrated using ACN, phosphoproteomics stage tip buffers A and B. After loading the samples, the matrix was washed with phosphoproteomics stage tip buffer B twice and then eluted using phosphoproteomics stage tip buffer C. The eluted samples

were dried using the SpeedVac and then sent for phosphoproteome analysis along with the previously prepared proteome profiling samples. The in-house HRMS facility performed further sample processing for the HPLC-MS/MS-based analysis.

For this purpose, samples were thawed and dissolved in 20 µL of 0.1 % (v/v) TFA in water, followed by a 15-min sonication step at room temperature. Samples were centrifuged for 1 min at 15,000 x g, and for desalting, 6 µL of the respective sample was loaded onto a pre-column cartridge for 5 min and eluted using 1 % TFA (v/v) in water at a flow rate of 30 µL/min. Throughout the entire analysis, samples were back-flushed from the pre-column to the nano-HPLC column. Elution was conducted using a two-buffer system: solvent A containing 0.1 % (v/v) FA in water and solvent B containing 0.1 % (v/v) FA in ACN. To achieve elution, a solvent gradient starting from 5 % solvent B and increasing to 20 % solvent B over 110 min with a flow rate of 300 nL/min, while keeping the column at 40 °C. The column of the nano HPLC was rinsed by raising the proportion of solvent B to 32 % over the course of 20 min, followed by a quick rapid increase to 95 % within 1 min. The column was then rinsed for another 3.5 min before being flushed back to the initial conditions and a 9-min equilibration step of the system. For the duration of the whole gradient, a TOP10 shot-gun proteomics method for the MS and MS/MS analysis was utilized. In the case of full MS scan experiments, a mass range of 375 to 1500 m/z was scanned employing a resolution of 120,000. MS/MS scans were performed at a resolution of 30,000 for the most intense ions with at least a doubly charged state. ProteomeDiscover was utilized for data evaluation. The spectra were queried against the human taxonomy of Uniprot and a contamination database with a 1 % false discovery rate, utilizing a decoy database to analyze the false discovery rate. For database search, carbamidomethylation on cysteine residues has been designated as a static modification. Additionally, phosphorylations on serine, threonine, and tyrosine, as well as acetylation on N-termini, loss of methionine at N-termini, and oxidation of methionine have been set as variable modifications. Depending on the enzyme used for digestion, Trypsin-specific cleavages allowing up to 4 missed cleavages were included in the analysis. Next, a site probability threshold above 75 was employed for phosphosites, and data were normalized to the total peptide content. For statistical analysis, phosphopeptide abundance ratios of DMSO controls for EGF-stimulated and non-EGF-stimulated samples, as well as compound-treated non-EGF-stimulated samples to non-EGF-stimulated DMSO controls, were calculated in pairs and then logarithmically transformed (log2). Finally, T-tests were conducted, and a table including UniProt IDs, gene names, peptides, phosphorylated residues, log2 fold changes, and corresponding p-values was generated for KSEA analysis.

4. IDENTIFICATION OF SMALL-MOLECULE ENHANCERS OF NATURAL KILLER CELL TUMORICIDAL ACTIVITY

4.1 Results

4.1.1 Identification of small molecule enhancers of NK cell-mediated eradication of A549^{Green} cells

To identify small-molecule modulators that restore the effector function of suppressed natural killer cells, Dr. Elisabeth Hennes (Waldmann group) established a phenotypic co-culture assay that mimics the tumor microenvironment, known as the NK cell-mediated cancer cell cytolysis assay. The co-culture setup consists of the human lung cancer cell line A549 and human lymphocytes in the presence of the immune modulatory factors IL-15, TGFβ, and PGE_2 to create an artificial TME. Lymphocytes are preferred over NK cells due to the laborious process of purifying primary NK cells, which often yields a limited amount of material, thereby reducing screening throughput. Hence, primary lymphocytes sourced from peripheral blood mononuclear cells (PBMCs) obtained from healthy donors were employed, including NK cells, T cells, and B cells. B cells do not have any cytotoxic activity, and naïve cytotoxic T cells cannot mediate target cell killing without priming by antigen-presenting cells. Therefore, they cannot be activated by activating IL-15 only.[150,151] While IL-15 activates NK cells, TGFβ and PGE_2 suppress NK cell-mediated cytotoxicity. To enable automated discrimination between lymphocytes and A549 cells and to quantify cancer cell killing, A549 cells were stably transfected with eGFP-tagged histone 2Bj to allow detection of the resulting green nuclei of A549^{Green} cells. The A549^{Green} cell count was monitored using kinetic real-time live-cell image-based analysis for up to 144 h. *Part of the presented results were reported in Dr. Elisabeth Hennes's doctoral thesis.*

For the assay, A549^{Green} cells were co-cultured with lymphocytes and different combinations of immunomodulatory additives (see Figure 14A). In a co-culture of A549^{Green} and lymphocytes without any supplements (unstimulated condition), the cancer cells follow a normal growth pattern of lag, log, and stationary phase. However, upon addition of IL-15, cancer cell growth continues for about 24-48 h until primary NKs are activated, after which the A549^{Green} cell count stagnates and finally decreases. Addition of either PGE_2 or TGFβ to the IL-15-supplemented co-culture reduced NK cell-mediated cytolysis, leading to increased cancer cell growth. The combination of both inhibitory factors, i.e., PGE_2 or TGFβ, with activating IL-15, referred to as cytokine mix, led to a growth behavior resembling the unstimulated condition. To validate NK cell activity in an orthogonal setup, IFN-γ, and granzyme B (Gzm B) levels were explored as they are directly linked to NK cell effector function (Figure 14F). For IFN-γ level quantification, supernatants of the NK

cell-mediated cancer cell cytolysis assay were collected and subjected to an ELISA (Figure 14B). In the unstimulated condition, secreted IFN-γ was barely detectable, whereas the presence of IL-15 greatly increased the levels. Conversely, the introduction of both TGFβ and PGE_2 individually or in combination as cytokine mix decreased IFN-γ levels. A similar trend was also observed for the Gzm B levels (Figure 14C). The unstimulated lymphocytes displayed low granzyme B levels, and IL-15 addition led to a noticeable increase, which was reduced by the cytokine mix. To confirm that $A549^{Green}$ cytolysis is mediated by NK cells, the assay was also validated with purified NK cells (Figures 14D and 14E).

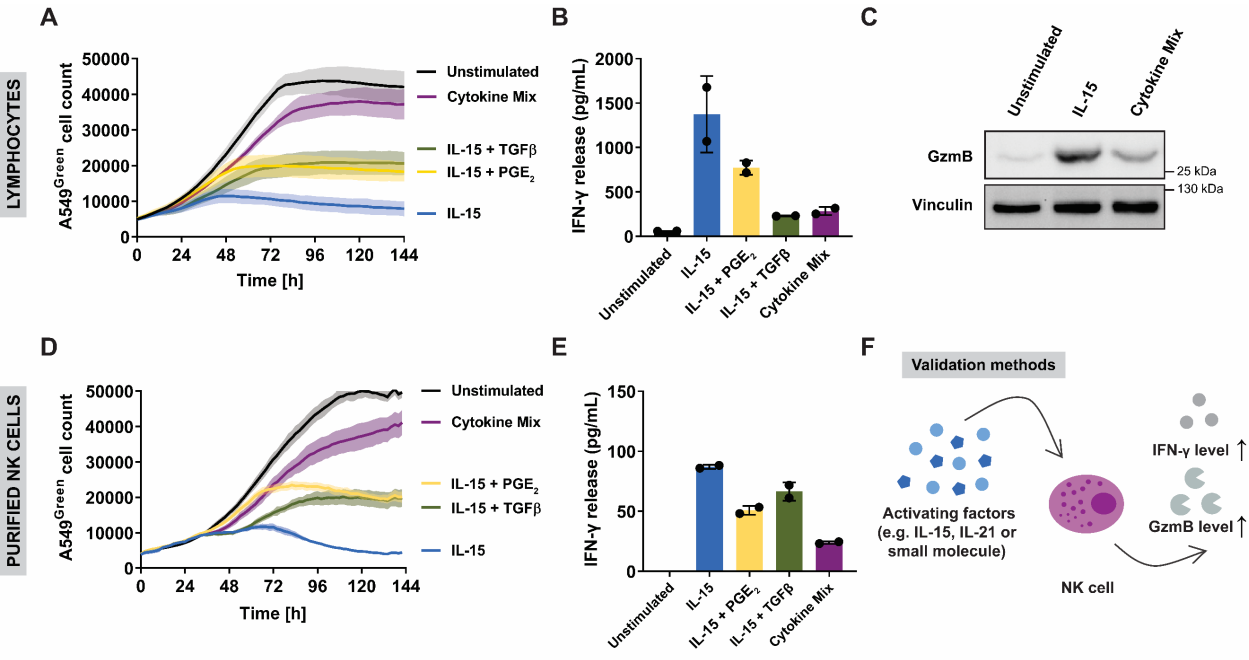

Figure 14: NK cell-mediated cancer cell cytolysis assay and validation workflow. A) NK cell-mediated cancer cell cytolysis assay using lymphocytes. $A549^{Green}$ was co-cultured with lymphocytes and treated with different factors, i.e., IL-15 (30 ng/mL), TGFβ (30 ng/mL), and PGE_2 (200 ng/mL), Cytokine mix: IL-15, TGFβ and PGE_2. The $A549^{Green}$ cell count was quantified *via* the H2BjeGFP fluorescence by means of live-cell imaging for 144 h. A representative graph is shown for n=3 (mean values ± SD, N=3 and E:T 60:1). B) Secreted IFN-γ levels by lymphocytes determined in supernatants of the NK cell mediated cancer cell cytolysis assay *via* ELISA. Cells were treated with varying combinations of the factors IL-15, TGFβ, and PGE_2. Representative graph of n=3 is shown (mean values ± SD, N=2). C) Granzyme B (GzmB) levels of lymphocytes. Cells were treated with IL-15 only or in combination with TGFβ and/or PGE_2 for 48 h prior to the quantification of protein levels *via* immunoblotting. Representative blot is shown (n=3). D) NK cell-mediated cancer cell cytolysis utilizing isolated NK cells. IL-15 (7.5 ng/mL), TGFβ (7.5 ng/mL), and PGE_2 (200 ng/mL). Representative graph is shown for n=3 (mean values ± SD, N=3 and E:T 10:1). Results by Dr. Elisabeth Hennes. E) IFN-γ secretion by NK cells stimulated with IL-15 or in combination with TGFβ and/or PGE_2 detected in supernatants of the NK cell-mediated cancer cell cytolysis assay. Representative graph is shown for n=3 (mean values ± SD, N=2). F) Validation methods for NK cell cytotoxic activity.

To identify bioactive small-molecule enhancers of NK cell-mediated cancer cell cytolysis, the assay was transferred to and miniaturized at the Compound Management and Screening Center (COMAS) in Dortmund (Figure 15). A library of 29,502 compounds, including unique in-house synthesized and commercial compounds, was utilized for the medium-throughput screening campaign. The co-culture assay was performed in 1536-well format at 11 µM for hit identification and 384-well format for EC_{50} value determination (Z'-value: 0.3-0.4). The cell count was determined after 144 h of incubation. The required effector-to-target (E:T) ratios of the selected donors were previously assessed to achieve meaningful signal-to-background (S/B: 2-14) ratios.

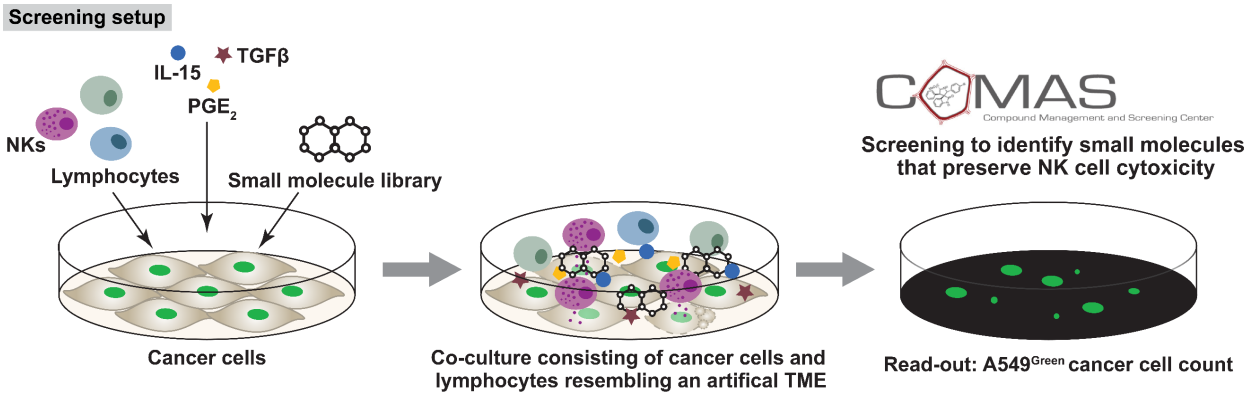

Figure 15: NK cell-mediated cancer cell cytolysis assay medium-throughput screening setup.

The screening campaign yielded several hit compounds that induce the desired phenotype, including inhibitors of bromodomain and extra-terminal domain (BET) proteins, glycogen synthase kinase 3β (GSK-3β), TGFβ type I receptor (TGFβR-1), and phosphatidylinositol 3-kinase (VPS34) (see Table 6). As the screening assay readout was $A549^{Green}$ cell count, it was crucial to investigate whether compounds decrease the cell count in the absence of lymphocytes to exclude false-positive hits. Therefore, the effect of compounds on $A549^{Green}$ cell viability was evaluated using Hoechst-33342 staining and the CTG™ assay. For hit compounds to be further investigated, the IC_{50} for impairment of $A549^{Green}$ viability and the EC_{50} value of the NK cell-mediated cancer cell cytolysis assay should differ at least fourfold. The hits that met the selection criteria underwent further investigation studies. Therefore, hit compounds were analyzed in detail to determine their influence on $A549^{Green}$ cell viability in a manual setup to establish suitable concentration ranges for subsequent experiments. For this purpose, $A549^{Green}$ cells were treated with serial dilutions of compounds, and kinetic real-time live cell image-based analysis was employed to monitor the cell count. Thereafter, hit molecules were validated in the NK cell-mediated cancer cell cytolysis assay using lymphocytes and/or purified NKs. Subsequently, orthogonal assays were employed to validate NK cell cytotoxic activity. Hence, the effect of the

hits on IFN-γ secretion and the level of granzyme B were explored as these are directly linked to NK cell effector function. GSK-3β inhibitors CHIR-99021 and BIO, VPS34 inhibitor SAR405, BRD2/3/4 PROTAC MZ-1, and TGFβ-R1 inhibitors RepSox, SB-525334, SB-505124, TP-008, GW788388, Galunisertib, and LY2109761 have met the selection criteria. Therefore, they were subjected to further validation experiments.

Table 6: List of relevant screening campaign hits alongside their reported targets. Automated cytolysis assay data are mean values ±S.D., n=3. CHIR-99021 and BIO were tested at 10 µM and 11 µM, respectively. The influence of hit compounds on cell viability was evaluated *via* the cell count using Hoechst-33342 staining* or CellTiterGlo™ (CTG)# assay. Data are mean values ±S.D., n=3. Compounds emphasized in gray were omitted from further analysis due to cytotoxic effects. *Data summarized in this table are COMAS screening results.*

Compound	Automated NK cell-mediated cell cytolysis assay EC_{50} [µM] or percentual activity [%]	$A549^{Green}$ viability IC_{50} *via* cell count* / CTG™, # [µM]	Mode of action
CHIR-99021	29 %	> 17*	GSK-3β inhibitors
BIO	35 %	n.d.	
SAR405	0.74 ± 0.30	13.17 ± 1.83#	VPS34 inhibitor
VPS34-IN1	0.72 ± 0.22	6.77 ± 0.18*	
PIK-III	1.30 ± 0.27	> 6*	
Compound 19 PIK-III analogue	1.60 ± 0.37	> 6*	
MZ-1	0.13 ± 0.04	1.33*	PROTAC of BRD4, BRD2 and BRD3
(+)-JQ1	0.14 ± 0.03	0.06*	BET bromodomain inhibitor
BAY-299	0.30 ± 0.02	1.47*	
OTX015	0.34 ± 0.08	0.45*	
Molibresib besylate	0.37 ± 0.13	0.17*	
I-BET151	1.30 ± 0.13	3.10*	
RepSox	0.18 ± 0.03	> 1.7*	TGFβ type I receptor inhibitors
SB-525334	0.33 ± 0.02	11.51 ± 2.16#	
SB-505124	0.47 ± 0.13	>6#	
TP-008	0.98 ± 0.24	>3#	
GW788388	1.19 ± 0.39	>30#	
Galunisertib	2.07 ± 0.46	> 17*	
LY-2109761	>3.4	> 6*	

4.1.2 GSK-3β inhibitors boost the cytotoxicity of NK cells.

The GSK-3β kinase is involved in various cellular processes, including proliferation, differentiation, and immune response.[152] GSK-3β serves as a negative regulator of various NK cell-activating signals, and its overexpression is associated with a decrease in NK cell cytotoxicity and impaired metabolism.[153] The medium-throughput screening has identified the small molecule-based GSK-3β inhibitors CHIR-99021 and BIO as hits, demonstrating cytolysis activity of 29 % at 10 µM and 35 % at 11 µM, respectively. These inhibitors were previously reported to enhance NK cell maturation, cytotoxic activity, and cytokine production.[154-156]

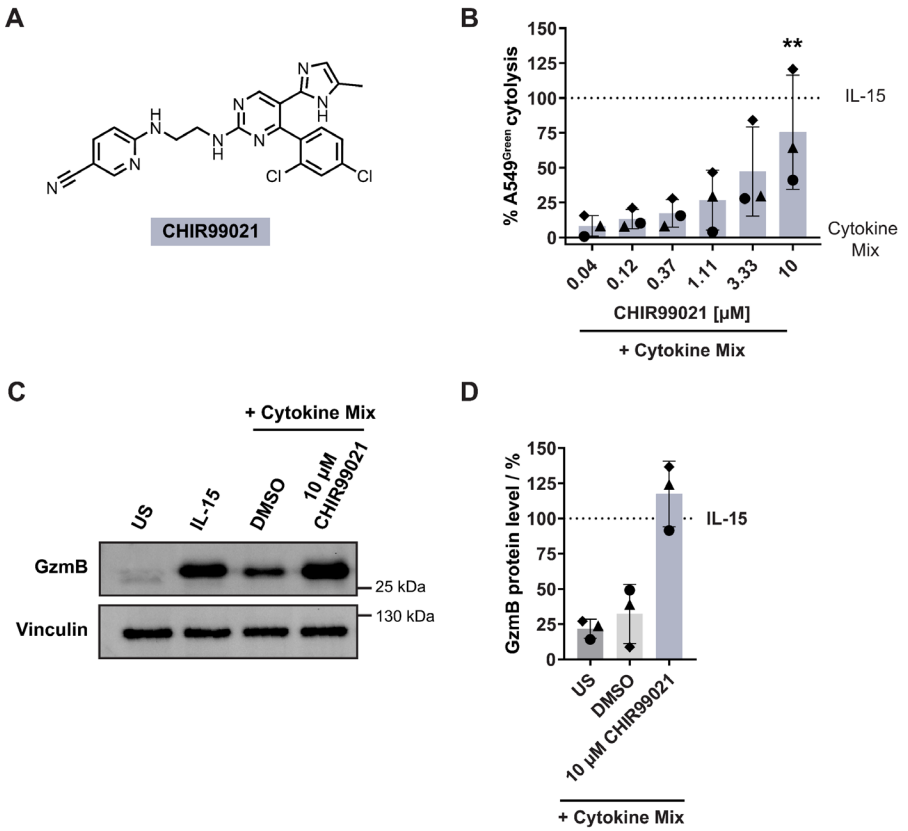

Figure 16: Influence of CHIR99021 on NK cell cytotoxicity. A) Chemical structure of CHIR99021. B) NK cell-mediated cancer cell cytolysis assay performed with lymphocytes treated with CHIR99021. The percentage of A549^{Green} was determined using the area under the curve (AUC), and the obtained data were normalized to the IL-15 condition as 100 % cytolysis and to the cytokine mix condition as 0 % cytolysis. Data are mean values ± SD (n=3, N=3), *, P < 0.05; **, P < 0.01; ***, P < 0.001; ****, P < 0.0001 (one-way ANOVA, comparison to cytokine mix condition)). C and D) CHIR99021 enhances granzyme B levels of lymphocytes after 48 h. C) Representative immunoblot of n=3. US: unstimulated condition. D) Quantified levels of granzyme B protein normalized to IL-15 treatment as 100 %. Mean values ± SD (n=3). Different symbols represent the activity of lymphocytes from individual donors.

In the NK cell-mediated cancer cell cytolysis assay, CHIR99021 was found to effectively increase NK cell tumoricidal activity in a concentration-dependent manner (see Figure 16B). A compound concentration of 10 µM significantly increased the A549^{Green} cytolysis rate by 75 %. To confirm

NK cell activity, granzyme B levels in lymphocytes were analyzed in the presence of the cytokine mix and CHIR99021 (see Figure 16C and D). Compared to lymphocytes treated with the cytokine mix lymphocytes, which exhibited 32 % granzyme B protein levels, the CHIR99021-treated cytokine mix condition resulted in 117 %, representing an increase of approximately 85 % in comparison to the IL-15 condition, which was set to 100 %. In addition, previous literature showed that in the presence of CHIR99021, NK cell-based IFN-γ production was elevated.[154]

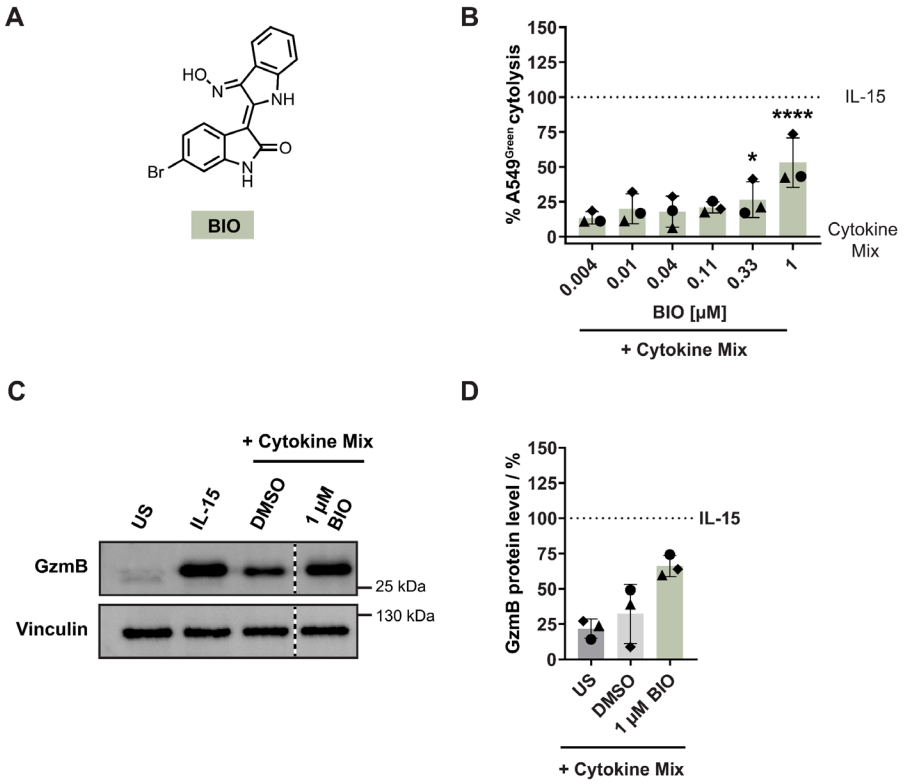

Figure 17: GSK3β inhibitor BIO enhances NK cell cytotoxicity. A) Chemical structure of 6-bromo-indirubin-3'-oxime (BIO). B) NK cell-mediated cancer cell cytolysis assay performed with lymphocytes treated with BIO (mean values ± SD, n=3, N=3). *, P < 0.05; **, P < 0.01; ***, P < 0.001; ****, P < 0.0001 (one-way ANOVA, comparison to cytokine mix-treated control)). C and D) BIO enhances GzmB protein levels of lymphocytes after 48 h. C) Representative immunoblot of n=3. D) Quantified levels of GzmB normalized to IL-15 treatment as 100%. Mean values ± SD (n=3).

The GSK-3β inhibitor BIO significantly elevated the A549^{Green} cytolysis rate by 53 % at 1 µM and 26 % at 0.33 µM when contrasted with the cytokine mix compared to 0% cytolysis under the cytokine mix condition, and 100% cytolysis under the activating IL-15 condition. (Figure 17B). In line with this, the levels of granzyme B protein increased by 34 % in the presence of BIO compared to the DMSO-cytokine mix control (Figure 17C and 17D).

Taken together, the identification of previously reported NK cell-activating GSK-3β inhibitors CHIR-99021 and BIO has underscored the potential of the NK cell-mediated cancer cell cytolysis assay in identifying small molecule enhancers of NK cell cytotoxic activity.

4.1.3 VPS34 inhibitor SAR405 enhances NK cell cytotoxicity

The VPS34 inhibitor SAR405 was identified as a third hit. VPS34 is crucial for autophagy initiation as well as progression, and its dysregulation is associated with many human diseases, including cancer.[157] In the medium-throughput screening, SAR405 greatly enhanced NK cell cytotoxicity with an EC_{50} of 0.74 µM. The influence of SAR405 on A549^{Green} viability was manually assessed (see Figure 18B) to determine concentration ranges for further validation experiments. Compared to the DMSO control, which was set to 100 %, 10 and 3.33 µM SAR405 reduced A549^{Green} viability to 66.3 and 80.2 %, respectively. Therefore, concentrations below 3.33 µM were used for subsequent experiments. In the NK cell-mediated cancer cell cytolysis assay, TGFβ is one of the utilized immunosuppressive cytokines. To explore the potential modulation of TGFβ signaling by SAR405, it was subjected to a TGFβ responsive Smad binding element (*SBE4*) dependent reporter gene assay (RGA) performed in HEK293T cells. The addition of SAR405 did not alter the reporter activity compared to the TGFβ-DMSO control (see Figure 18C).

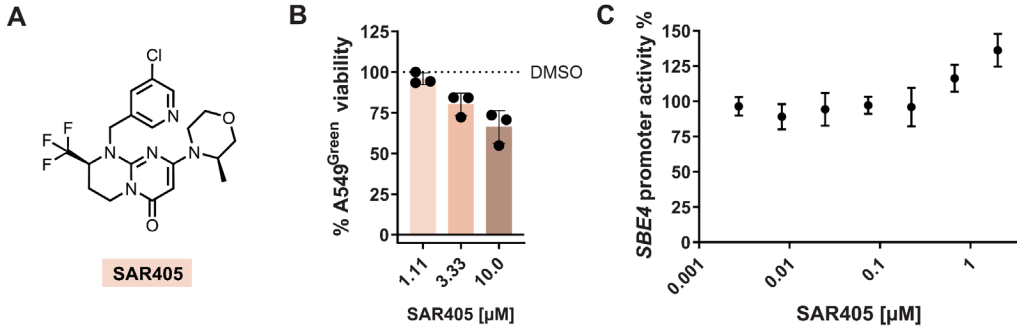

Figure 18: Influence of SAR405 on A549^{Green} viability and TGFβ pathway activity. A) Chemical structure of SAR405. B) Influence of SAR405 on A549^{Green} cell viability after 96 h. The viability was assessed by determining the AUC of the obtained cell count data and normalizing it to their corresponding DMSO control, which was set to 100 %. Data are mean values ± SD (n=3). C) Activity of SAR405 in the *SBE4*-dependent reporter gene assay (RGA). Transiently-transfected HEK293T cells express the firefly luciferase (Fluc) under the control of TGFβ-responsive Smad-binding element (SBE) and the *Renilla* luciferase (Rluc), which is constitutively expressed. HEK293T was treated with SAR405 and TGFβ for 24 h. Fluc signals were normalized to corresponding Rluc signals, and DMSO-TGFβ was set to 100 %. Data are representative of n=3 (mean values ± SD, N=3).

SAR405 underwent manual testing in the NK cytolysis assay using lymphocytes to confirm its enhancing activity on NK cell cytotoxicity (Figure 19A). Manual testing using the VPS34 inhibitor SAR405 confirmed the significantly increased NK cell-mediated A549^{Green} cytolysis in a concentration-dependent manner. The highest used concentration of SAR405, 2.5 µM, potentiated NK cell cytotoxicity in the presence of the cytokine mix to 91.3 %, and even lower concentrations of 1.25 and 0.63 µM were found to significantly enhance the cytolysis rate to 73.4 % and 50.4 %, respectively. The levels of IFN-γ secretion and Gzm B in lymphocytes were assessed in the presence of SAR405 to validate the obtained results, as they positively correlate

with NK cell effector function. The compound elevated IFN-γ as well as Gzm B protein (49.6 % at 2.5 µM) levels compared to the cells that were treated with the cytokine mix (Figure 19B and C). Next, the cytolysis assay was performed using purified NK cells to validate that the observed phenotype was a result of NK cell activity, as no link to NK cell tumoricidal activity is known for SAR405. Using purified NK cells, similar results were obtained, and the addition of SAR405 to the cytokine mix-treated co-culture significantly increased $A549^{Green}$ cytolysis at 1.25 and 2.5 µM (Figure 19D). Subsequent analysis of IFN-γ secretion levels showed dose-dependent upregulation by the VPS34 inhibitor (Figure 19E) and, thus, validated the cytotoxic activity of the NK cells. Additional VPS34 inhibitor hits, including VPS-IN1, PIK-III, and Compound 19 PIK-III analogue showed an inadequate window between $A549^{Green}$ viability IC_{50} and NK cell cytolysis assay EC_{50} and, therefore, were excluded from further characterization (Table 6).

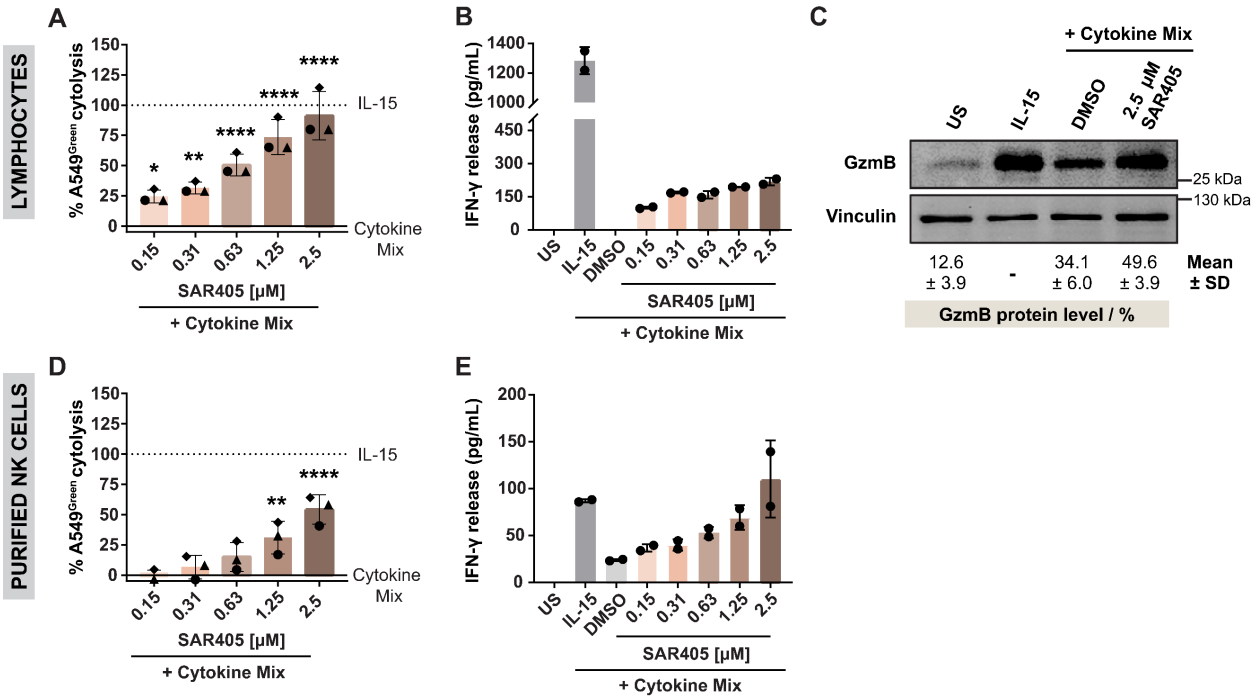

Figure 19: SAR405 elevates NK cell cytotoxicity. A and D) NK cell-mediated cancer cell cytolysis assay using lymphocytes (A) and purified NK cells (D) treated with a serial dilution of VPS34 inhibitor SAR405 (mean values ± SD, N=3, n=3). *, P < 0.05; **, P < 0.01; ***, P < 0.001; ****, P < 0.0001 (one-way ANOVA, comparison to cytolysis rate of cytokine mix-treated control)). B and E) Influence of SAR405 on IFN-γ levels secreted by lymphocytes (B) and purified NK cells (E). Data are representative of n=3 (mean values ± SD, N=2). C) Gzm B protein levels in lymphocytes after 48 h treatment with cytokine mix and SAR405 treatment. Immunoblot is representative of n=3. Quantified Gzm B levels were normalized to the levels of the reference protein vinculin and the IL-15 condition, which was set to 100 %. Data are mean values ± SD (n=3).

4.1.4 PROTAC MZ-1 enhances NK cell cytotoxicity

The screen identified the PROteolysis Targeting Chimera (PROTAC) MZ-1 as second hit compound with EC_{50} of 0.13 µM class for which no link to upregulated NK cell tumoricidal activity has been reported yet (Table 6). MZ-1 is a heterobifunctional compound consisting of the BRD2/3/4 ligand (+)-JQ-1 and the E3 ligase recognition moiety van Hippel-Lindau (VHL) ligand, connected by a polyethylene glycol (PEG) linker. It triggers intracellular degradation of bromodomain-containing proteins (BRD) 2, 3, and 4 *via* the proteasome.[158] The proteins BRD2, 3, and 4 play crucial roles in the regulation of transcriptional processes and are frequently dysregulated in cancer.[159] *Part of the experiments presented in this chapter were conducted together with Alisa Reich and were reported in her master's thesis.*

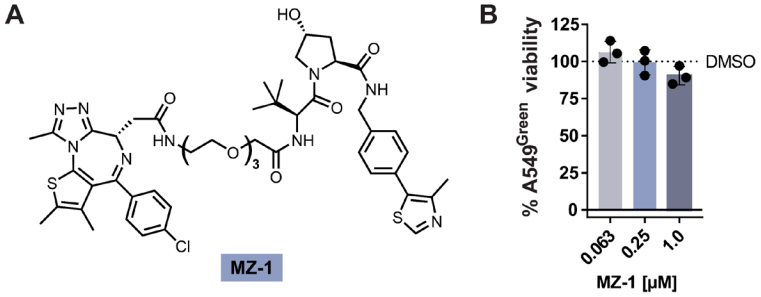

Figure 20: Influence of MZ-1 on A549^{Green} viability. A) Chemical structure of MZ-1. B) A549^{Green} viability upon treatment using varying MZ-1 concentrations after 96 h. The viability was assessed by determining the AUC of the obtained cell count data and normalizing it to their corresponding DMSO control, which was set to 100 %. Data are mean values ± SD (n=3). *Assay was performed by Alisa Reich*.

A concentration of 1 µM MZ-1 only slightly reduced A549^{Green} viability to 90.4 % compared to the DMSO control, whereas concentrations of 0.25 and 0.063 µM did not influence the viability of the lung cancer cell line (Figure 20A).

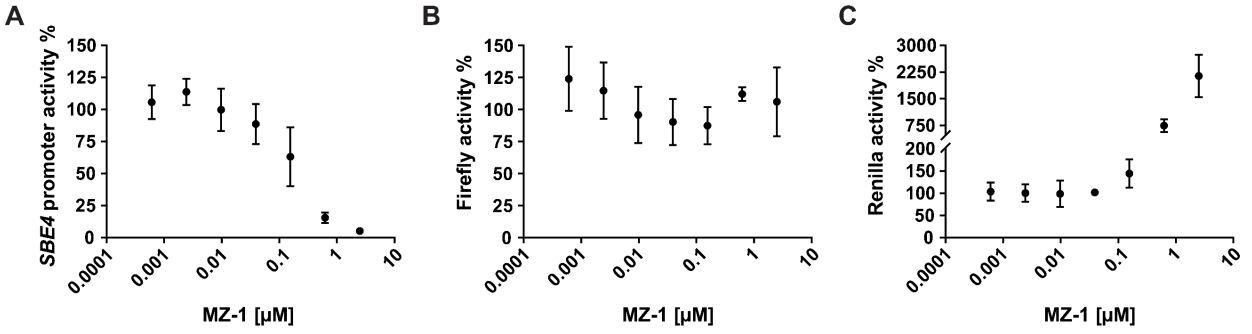

Figure 21: Influence of MZ-1 on TGFβ pathway activity. A) Activity of MZ-1 in the *SBE4*-dependent RGA in HEK293T treated with MZ-1 and TGFβ for 24 h. Fluc signals were normalized to the corresponding Rluc signals, and DMSO-TGFβ was set to 100 %. B and C) Influence of MZ-1 on Fluc (B) and Rluc (C) signals. Data are representative for n=3 (mean values ± SD, N=3). *Assay was performed by Alisa Reich*.

As no link of MZ-1 to NK cell tumoricidal activity is known, its influence on the TGFβ pathway activity was investigated by means of a *SBE4*-dependent RGA. The normalized data set indicated a decrease in *SBE4* promoter activity with increasing compound concentrations, suggesting that MZ-1 has inhibitory activity on TGFβ signaling (Figure 21A). Further analysis of the individual luciferase datasets (Figure 21B and C) revealed that MZ-1 modulated *Renilla* luciferase activity with a positive correlation to increasing compound concentrations, while no meaningful change in firefly luciferase activity was observed. In conclusion, MZ-1 did not substantially affect the firefly reporter signal. Further experiments are needed to confirm that the PROTAC does not modulate TGFβ pathway activity.

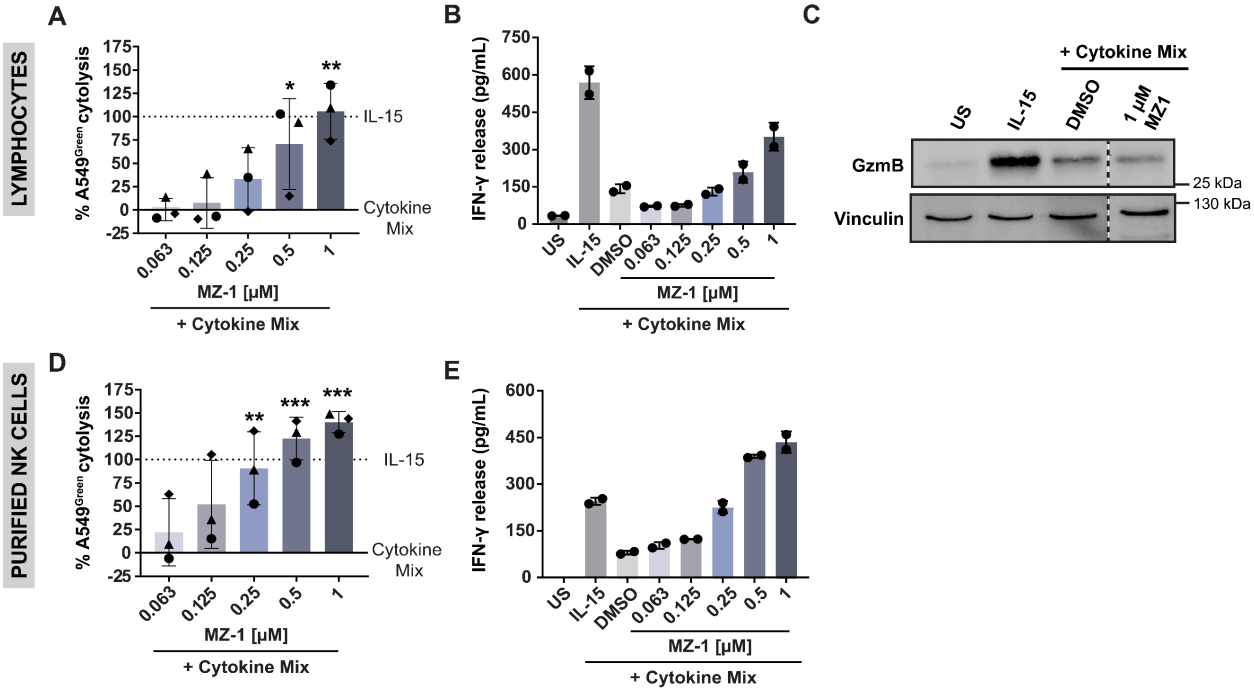

Figure 22: MZ-1 elevates NK cell tumoricidal activity. A and D) NK cell-mediated cancer cell cytolysis assay using lymphocytes (A) and purified NK cells (D) treated with a serial dilution of MZ-1 (mean values ± SD, N=3, n=3). *, P < 0.05; **, P < 0.01; ***, P < 0.001; ****, P < 0.0001 (one-way ANOVA, comparison to cytolysis rate of cytokine mix-treated control)). B and E) Influence of MZ-1 on IFN-γ levels secreted by lymphocytes (B) and purified NK cells (E). Data are representative of n=3 (mean values ± SD, N=2). C) Gzm B protein levels in lymphocytes after treatment with cytokine mix with or without MZ-1 for 48 h. Immunoblot is representative of n=3. Dashed lines show cropped images originating from the same immunoblot.

Subsequently, MZ-1 was subjected to NK-mediated cancer cytolysis, Gzm B, and IFN-γ secretion validation assays to confirm its impact on NK cell tumoricidal activity (Figure 22). In the lymphocyte setup (Figure 22A), cells treated with MZ-1-cytokine mix exhibited a significantly increased cytolysis rate at 0.5 and 1 µM compound concentrations. Analysis of the IFN-γ levels of the cytolysis assay supernatants validated these findings. In comparison to the DMSO control,

MZ-1 concentration-dependently increased IFN-γ secretion (Figure 22B). Next, the Gzm B levels of lymphocytes treated with MZ-1-cytokine mix were examined, revealing no meaningful change in protein levels (Figure 22C). MZ-1 significantly enhanced the tumoricidal activity of purified NK cells at 0.25, 0.5, and 1 µM in the presence of the cytokine mix exceeding the cytolysis rate of the IL-15-treated cells (Figure 22D). The increased secretion of IFN-γ in the presence of MZ-1 observed in the lymphocyte setup were also confirmed using purified NK cells (Figure 22E).

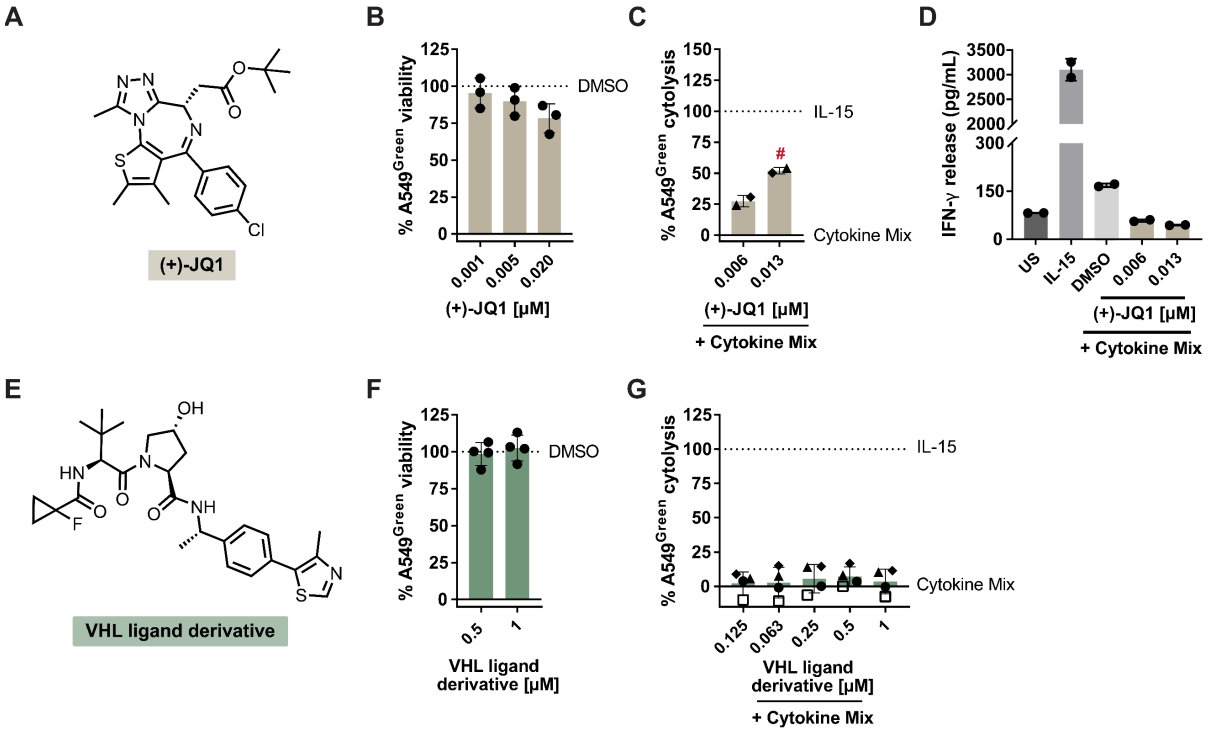

Figure 23: (+)-JQ1 and a VHL ligand derivative do not enhance NK cell cytotoxicity. A) (+)-JQ1 chemical structure. B) A549^{Green} viability upon (+)-JQ-1 treatment after 96 h. Data are mean values ± SD (n=3). C) Influence of (+)-JQ1 on NK cell cytotoxicity. NK cell-mediated cancer cell cytolysis assay utilizing lymphocytes. Data are mean values ± SD (n=2). # = reduced A549^{Green} cell viability through (+)-JQ1 treatment. D) Assessment of IFN-γ levels of A549^{Green}-lymphocyte cytolysis assay supernatants treated with (+)-JQ1. Data are mean values ± SD (n=2). *Results shown in B) – D) were obtained by Alisa Reich.* E) Chemical structure of the VHL ligand derivative. *The compound was kindly provided by Nikolas Klinke (Gersch lab, CGC Dortmund)*. F) A549^{Green} viability after 96 h treatment using VHL ligand derivative. G) NK cell-mediated cancer cell cytolysis assay using VHL ligand derivative-treated lymphocytes. F and G) Data are mean values ± SD (n=4).

Next, the individual counterparts of MZ-1,i.e., (+)-JQ1 and a VHL ligand derivative, were explored to investigate whether the NK cell activity-enhancing properties of the PROTAC can be attributed to them (Figure 23). While (+)-JQ1 was found to be a false positive hit in the medium-throughput screening, the counter viability screen revealed its high toxicity towards A549^{Green} cells (Table 6). For this reason, the influence of (+)-JQ1 on A549^{Green} viability was analyzed prior to conducting further experiments (Figure 23B). A concentration of 0.02 µM of (+)-JQ1 reduced A549^{Green}

viability to 78.3 %, while 0.005 µM only slightly decreased viability to 89.8 %. Following this, the influence of (+)-JQ1 on the NK cell cytolysis rate was assessed. The results demonstrated that concentrations of 0.013 and 0.006 µM of (+)-JQ1 did not enhance NK cell cytotoxicity (Figure 23C). This observation was further validated by the unaltered levels of IFN-γ secretion (Figure 23D). The VHL ligand derivative did not affect A549^{Green} viability or the NK cell cytolysis rate (Figure 23F and G). Hence, the activity of MZ-1 observed in the NK cell cytolysis assay cannot be attributed to (+)-JQ or the VHL ligand derivative. Additional bromodomain inhibitors tested in the COMAS screening, such as BAY-299 and OTX015, also showed an insufficient window between the NK cell cytolysis EC_{50} and the viability IC_{50} of A549^{Green} cells (Table 6).

4.1.5 TGFβR-1 inhibitors boost NK cell cytotoxicity

One more compound class that was identified by the COMAS medium-throughput screen are the TGFβR-1 inhibitors RepSox, SB-525334, SB505124, GW788388, galunisertib, and LY2109761 (Table 6).[160-165] The identification of these hits was not unanticipated, as TGFβ was employed as an immunosuppressive factor in the NK cell-mediated cancer cell cytolysis assay. The TGFβ signaling pathway plays a pivotal role in regulating various cellular processes, including apoptosis, differentiation, proliferation, and immune responses.[43] TGFβ is a highly potent immuno-suppressive factor that is produced by various cancer types and thereby promotes cancer immune evasion.[166] For side-to-side comparison of the activity of the TGFβR-1 inhibitor hits, they were subjected to the A549^{Green} viability assay and *SBE4*-dependent RGA. This was followed by evaluating their activity in the NK cell-mediated cancer cell cytolysis assay and validation of NK cell cytotoxicity through Gzm B and IFN-γ level assessment. *The results presented in this chapter were partially conducted in collaborative work with Alisa Reich and reported in her master's thesis. Results of SBE4-dependent RGAs and viability assays were obtained by her.*

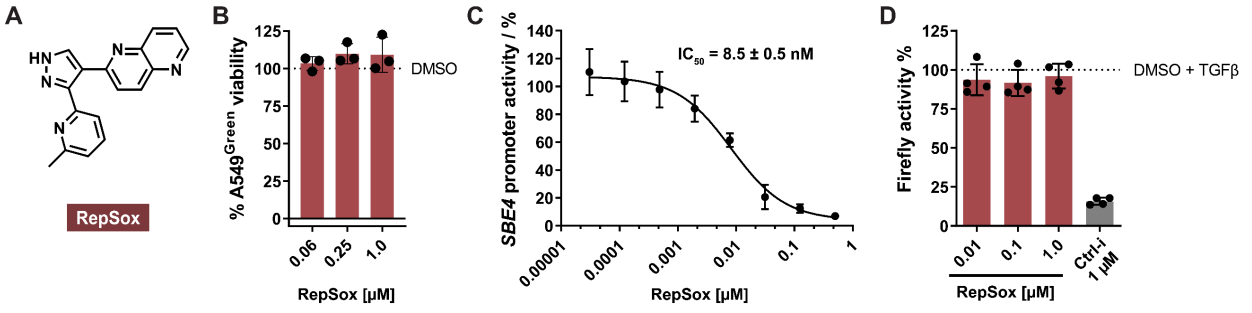

Figure 24: Effect of RepSox on A549^{Green} viability and TGFβ pathway activity. A) Chemical structure of RepSox. B) A549^{Green} viability upon RepSox treatment after 96 h. Data are mean values ± SD (n=3). C) Dose-response curve of RepSox obtained with the *SBE4*-dependent RGA. HEK293T cells were treated

with TGFβ and a serial dilution of RepSox for 24 h. Fluc signals were normalized to corresponding Rluc signals, and related to the DMSO-TGFβ condition, which was set to 100 %. Data are mean values ± SD (n=4). D) Direct influence of RepSox on firefly luciferase activity. Lysates from HEK293T expressing firefly luciferase induced by TGFβ were treated with varying Repsox concentrations or DMSO as a control for 1 h. Obtained data were normalized to DMSO-TGFβ which was designated as 100 %. Data are mean values ± SD (n=4).

RepSox was the most potent enhancer of NK cell cytotoxicity among the TGFβR-1 inhibitors identified in the screening, exhibiting an EC_{50} value of 0.18 µM (Table 6). Up to 1 µM RepSox did not influence the viability of $A549^{Green}$ cells (Figure 24B). The compound suppresses TGFβ signaling activity in the *SBE4*-dependent RGA, yielding an IC_{50} of 8.5 nM (Figure 24C). The possibility of compounds directly modulating the RGA readout was excluded through direct evaluation of firefly luciferase activity. RepSox did not influence the enzymatic activity of the firefly luciferase, while the control inhibitor (see 3.2.1.16) reduced the activity to 15.8 % (Figure 24D).

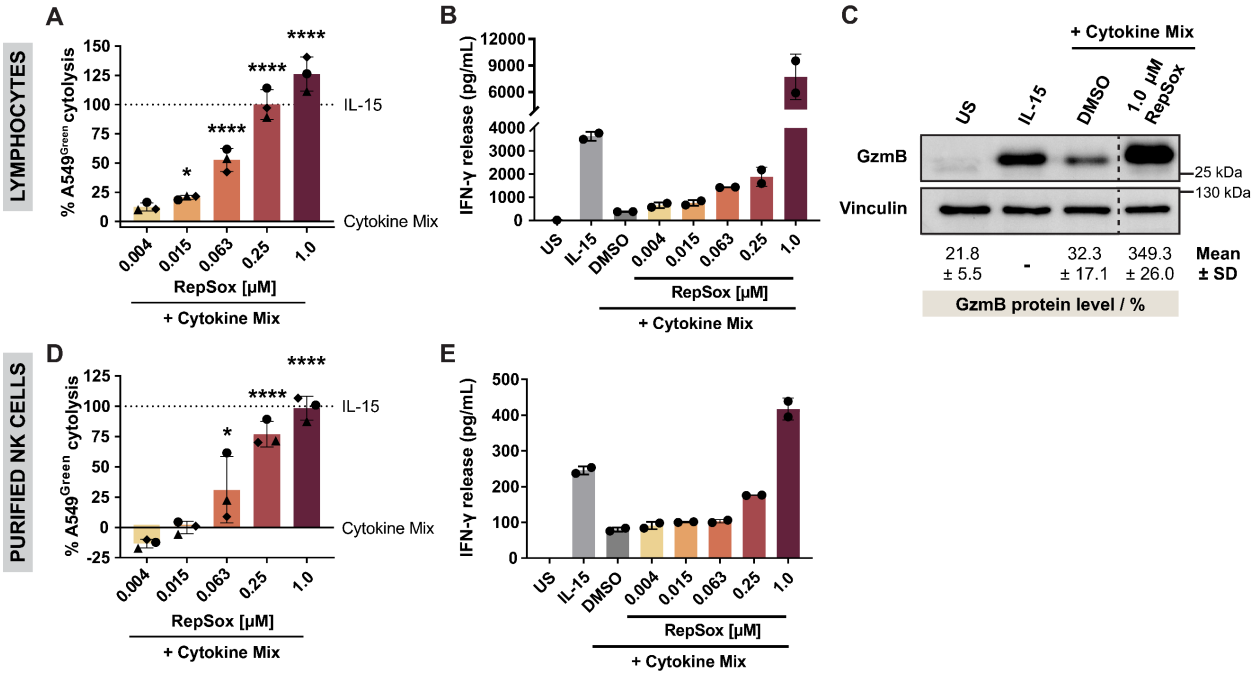

Figure 25: RepSox boosts NK cell cytotoxicity. A and D) NK cell-mediated cancer cell cytolysis assay using lymphocytes (A) and purified NK cells (D) treated with a serial dilution of RepSox. Data are mean values ± SD (n=3). *, P < 0.05; **, P < 0.01; ***, P < 0.001; ****, P < 0.0001 (one-way ANOVA, comparison to cytolysis rate of cytokine mix-treated control)). B and E) Effect of RepSox on IFN-γ levels secreted by lymphocytes (B) and purified NK cells (E). Data are representative for n=3 (mean values ± SD, N=2). C) Gzm B protein levels in lymphocytes after treatment with cytokine mix with or without RepSox for 48 h. Immunoblot is representative of n=3. Dashed lines show cropped images originating from the same immunoblot. Quantified Gzm B levels were normalized to reference protein vinculin and to the IL-15, which was set to 100 %. Data are mean values ± SD (n=3).

The RepSox-promoting effect on NK cell tumoricidal activity could be confirmed using the manual assay setup (Figure 25A). The compound significantly increased the A549^{Green} cytolysis rate, reaching the level of IL-15-treated lymphocytes at 0.25 µM, and surpassing IL-15 at 1 µM. The EC_{50} value based on this data was found to be 119.6 nM. In the following step, RepSox underwent testing for its influence on IFN-γ secretion and Gzm B levels and positively affected the levels for both proteins, surpassing the levels of IL-15 treated lymphocytes at 1 µM (Figure 25B and C). RepSox was found to greatly increase the levels of IFN-γ by up to 7-fold depending on the donor and Gzm B by 349.3 %. To confirm these findings, RepSox underwent testing using purified NK cells (Figure 25D and E). Indeed, RepSox significantly boosts A549^{Green} cytolysis of purified NK cells in a concentration-dependent manner (Figure 25D). The EC_{50} value corresponding to these data was 103.4 nM (Figure S1). The levels of IFN-γ secretion were elevated in the presence of RepSox in the cytokine mix treated cells. (Figure 25E).

Following RepSox, SB-525334 greatly enhanced NK cell cytotoxicity, displaying an EC_{50} measured at 0.33 µM in the screening (Table 6). SB-525334 reduced A549^{Green} viability to 69.8 % at 5.0 µM, whereas lower concentrations did not alter the viability (Figure 26B). The compound dose-dependently inhibited TGFβ pathway signaling activity, with an IC_{50} of 31.4 nM (Figure 26C). Compared to the positive control, SB-525334 did not affect the enzymatic activity of the firefly luciferase (Figure 26D).

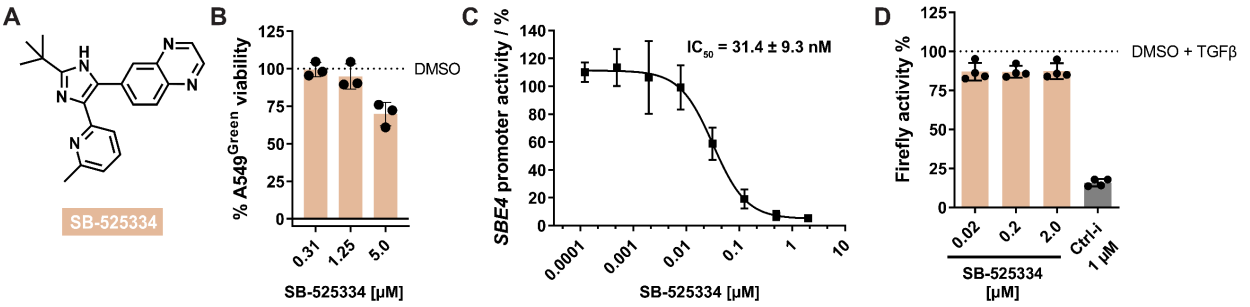

Figure 26: Effect of SB-525334 on A549^{Green} viability and TGFβ pathway activity. A) SB-525334 chemical structure B) Influence of SB-525334 on A549^{Green} viability after 96 h treatment. Data are mean values ± SD (n=3). C) Dose-response analysis conducted with the *SBE4*-dependent RGA using HEK293T cells treated with TGFβ and a serial dilution of SB-525334 or DMSO for 24 h. Fluc signals were normalized to corresponding Rluc signals, and DMSO-TGFβ was set to 100 %. Data are mean values ± SD (n=4). D) Impact of SB-525334 on the enzymatic activity of firefly luciferase. Firefly luciferase-containing HEK293T lysates were treated with SB-525334 or DMSO for 1 h prior to determining the luciferase activity. Data were normalized to DMSO-TGFβ, which was designated as 100 %. Data are mean values ± SD (n=4).

SB-525334's potentiating effect on NK cell-mediated cancer cell cytolysis was confirmed through the NK cell-mediated cancer cell cytolysis assay (Figure 27A). Concentrations ranging from 0.07 to 2.0 µM significantly enhanced A549^{Green} cytolysis. IFN-γ levels positively correlated with the SB-525334 concentrations in lymphocytes (Figure 27B). In comparison to the IL-15 control, which was designated as 100 %, the Gzm B levels of SB-525334-treated lymphocytes were 83.8 %, whereas the Gzm B levels of the inhibitory cytokine mix were 31.6 % (Figure 27C).

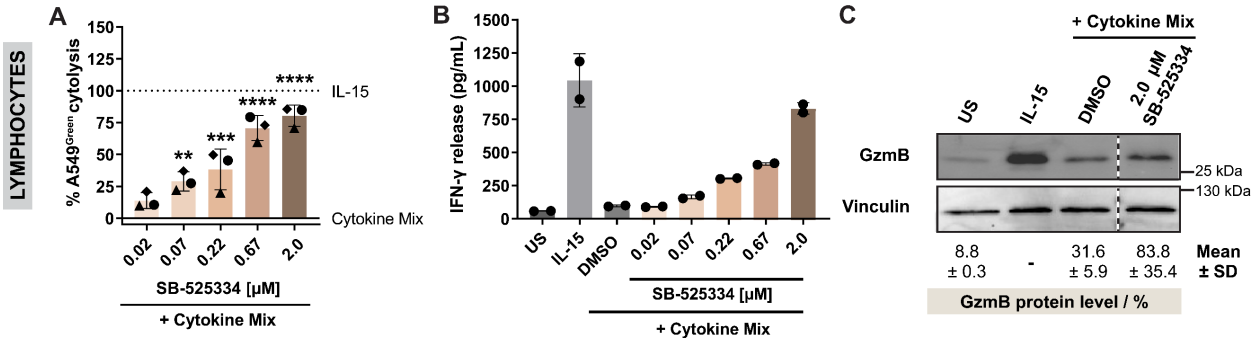

Figure 27: SB-525334 has a potentiating effect on NK cell cytotoxicity. A) NK cell-mediated cancer cell cytolysis assay using lymphocytes treated with SB-525334. Data are mean values ± SD (n=3). *, P < 0.05; **, P < 0.01; ***, P < 0.001; ****, P < 0.0001 (one-way ANOVA, comparison to cytolysis rate of cytokine mix-treated control)). B) Influence of SB-525334 on IFN-γ levels secreted by lymphocytes. Data are representative of n=3 (mean values ± SD, N=2). C) Gzm B protein levels in lymphocytes after treatment with cytokine mix with or without RepSox for 48 h. Immunoblot is representative of n=3, except for the US condition, which is representative of n=2. Dashed lines show cropped images originating from the same immunoblot. Quantified Gzm B levels were normalized to reference protein vinculin, and IL-15 treatment was set to 100 %. Data are mean values ± SD (n=3).

The TGFβR-1 inhibitor, which ranked third in terms of NK cell cytotoxicity-promoting activity, was SB-505124, with an EC_{50} of 0.47 µM (Table 6). SB-505124 caused a viability reduction of 72.3 % in A549^{Green} cells at 4.0 µM, but this effect was not observed at lower concentrations (Figure 28B). In the *SBE4*-dependent RGA, the compound exhibited an IC_{50} of 57.2 nM, while the compound did not affect the enzymatic activity of firefly luciferase (Figure 28C and D).

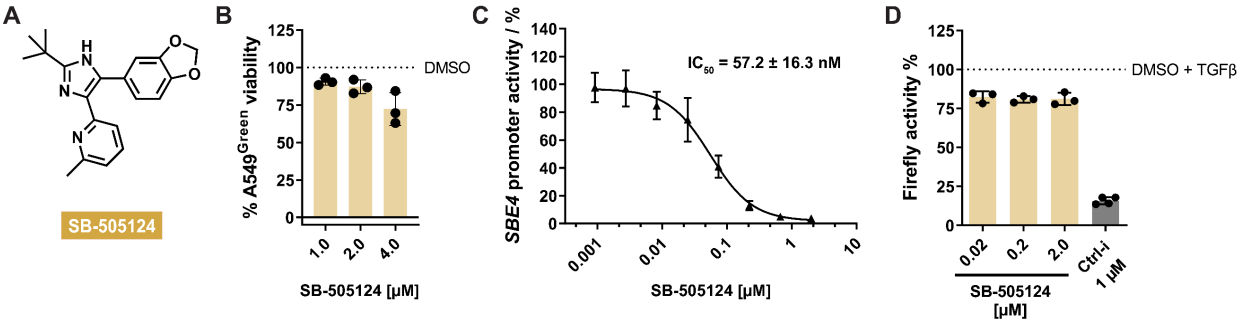

Figure 28: Influence of SB-505124 on A549^{Green} viability and TGFβ pathway activity. A) Chemical structure of SB-505124. B) Viability of A549^{Green} cells treated with SB-505124 after 96 h. Data are mean values ± SD (n=3). C) Activity of SB-505124 in the *SBE4*-dependent RGA using HEK293T cells after 24 h. Fluc signals were normalized to corresponding Rluc signals, and DMSO-TGFβ (set to 100 %). Data are mean values ± SD (n=3). D) Enzymatic activity of firefly luciferase in HEK293T lysate treated with SB-505124 or DMSO for 1 h. Data were normalized to DMSO-TGFβ (set to 100 %). Data are mean values ± SD (n=3).

Assessment of the impact of SB-505124 on NK cell-mediated cancer cell cytolysis showed a significant increase in the cytolysis rate at compound concentrations of 1.0 and 2.0 µM using lymphocytes. (Figure 29A). The IFN-γ secretion levels were elevated in presence of SB-505334, validating the cytotoxic activity of NK cells (Figure 29B). Additionally, Gzm B levels increased to 74.3 % in lymphocytes treated with SB-505124 (Figure 29C).

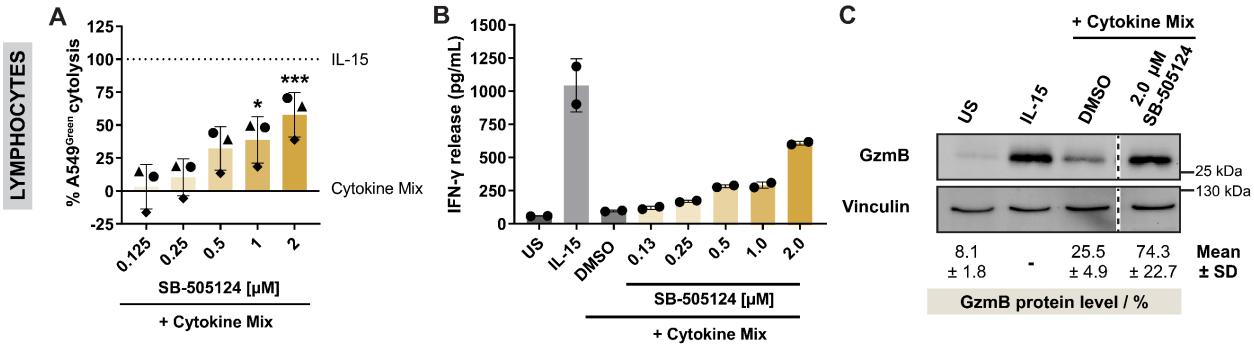

Figure 29: SB-505124 promotes NK cell cytotoxicity. A) Activity of SB-505124-treated lymphocytes in the NK cell-mediated cancer cell cytolysis assay. Data are mean values ± SD (n=3). *, P < 0.05; **, P < 0.01; ***, P < 0.001; ****, P < 0.0001 (one-way ANOVA, comparison to cytolysis rate of cytokine mix-treated control)). B) IFN-γ levels of SB-505124-treated lymphocytes. Data are representative of n=3 (mean values ± SD, N=2). C) Evaluation of Gzm B protein levels of SB-505124-treated lymphocytes after 48 h. Immunoblot is representative of n=3, except for the US condition, which is representative of n=2. Dashed lines show cropped images originating from the same immunoblot. Quantified Gzm B levels were adjusted to vinculin as a reference and then related to the IL-15 condition, designated as 100 %. Data are mean values ± SD (n=3).

Next in line was the TGFβR-1 inhibitor GW788388, with its EC_{50} of 1.19 µM in the automated NK cell cytolysis assay (Table 6). Evaluation of the influence of GW788388 on A549^{Green} viability demonstrated that compound concentrations ranging from 1.25 to 20.0 µM had no effect on the viability (Figure 30B). Subjecting GW788388 to the *SBE4*-dependent RGA resulted in an IC_{50} of 77.5 nM (Figure 30C). The activity of firefly luciferase did not change when exposed to varying concentrations of GW788388 (Figure 30D).

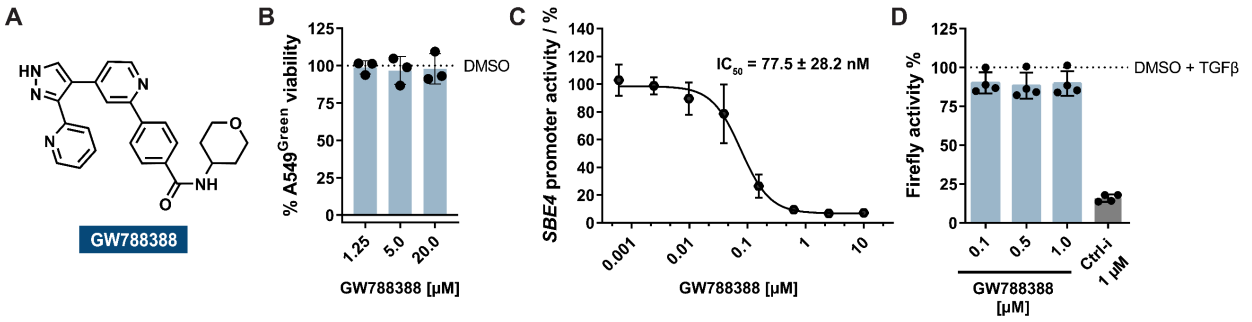

Figure 30: Influence of GW788388 on A549^{Green} viability and TGFβ pathway activity. A) Chemical structure of GW788388. B) A549^{Green} viability in presence of GW788388 after 96 h. Data are mean values ± SD (n=3). C) *SBE4* promoter activity in GW788388-treated HEK293T cells after 24 h. Fluc signals were normalized to corresponding Rluc signals, and DMSO-TGFβ (set to 100 %). Data are mean values ± SD (n=3). D) Enzymatic activity of firefly luciferase in HEK293T lysate treated with GW788388 or DMSO for 1 h. Data were normalized to DMSO-TGFβ (set to 100 %). Data are mean values ± SD (n=4).

Although there was a positive correlation between GW788388 concentrations and IFN-γ secretion level, no concentration-dependent activity was observed in the NK cell-mediated cancer cell cytolysis assay (Figure 31A and B). Only 6.67 µM of GW788388 significantly increased the cytolytic activity of NK cells. Furthermore, Gzm B levels were elevated to 71.8 % in presence of GW788388-treated lymphocytes (Figure 31C).

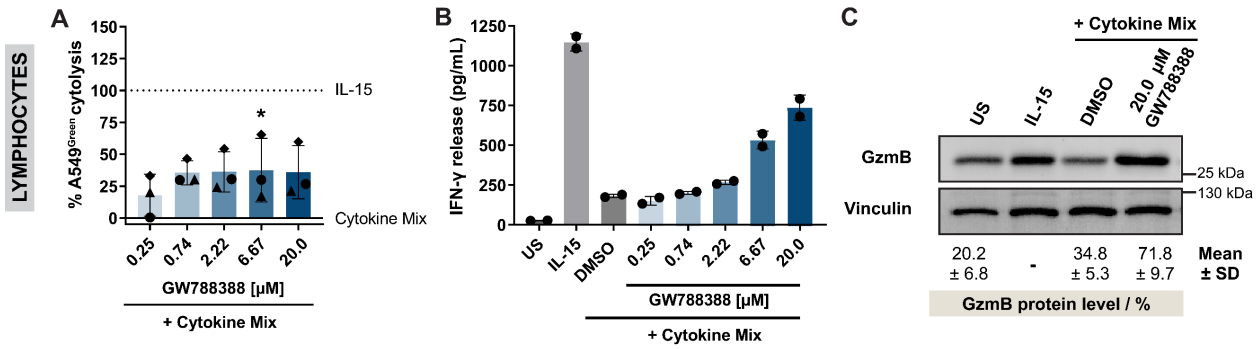

Figure 31: GW788388 enhances NK cell cytotoxicity. A) Effect of GW788388 treatment on lymphocytes in the NK cell-mediated cancer cell cytolysis assay. Data are mean values ± SD (n=3). *, P < 0.05; **, P < 0.01; ***, P < 0.001; ****, P < 0.0001 (one-way ANOVA, comparison to cytolysis rate of cytokine mix-treated control)). B) IFN-γ levels of GW788388-treated lymphocytes. Data are representative of n=3 (mean

values ± SD, N=2). C) Influence of GW788388-treatment on Gzm B protein levels of lymphocytes after 48 h. Immunoblot is representative of n=3. Quantified Gzm B levels were adjusted to vinculin as a reference and then related to the IL-15 condition, set to 100 %. Data are mean values ± SD (n=3).

Galunisertib exhibited moderate NK cell cytotoxicity-promoting activity, as indicated by its EC_{50} of 2.07 µM (Table 6). In the tested range of 1.25 to 20.0 µM galunisertib did not affect the viability of $A549^{Green}$ cells (Figure 32B). The activity of the *SBE4* promoter was suppressed in a concentration-dependent manner, leading to an IC_{50} of 114.0 nM, while Fluc activity remained unaltered (Figure 32C and D).

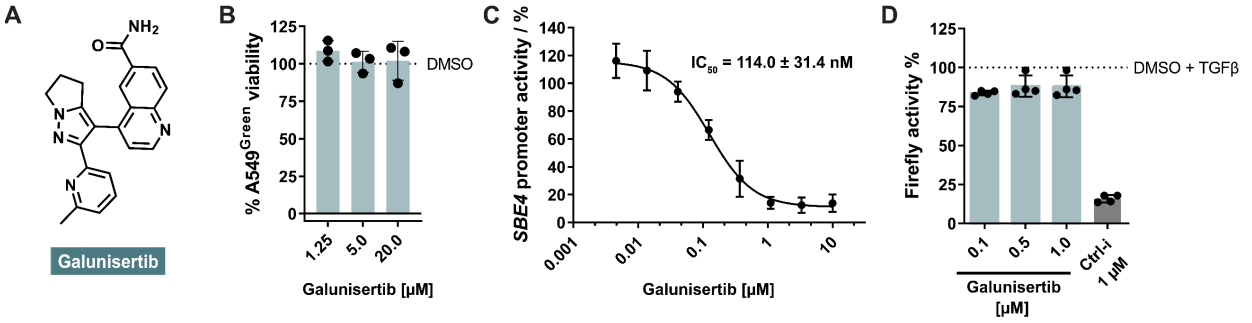

Figure 32: Influence of galunisertib on $A549^{Green}$ viability and TGFβ pathway activity. A) Chemical structure of galunisertib. B) Viability of galunisertib-treated $A549^{Green}$ cells after 96 h. Data are mean values ± SD (n=3). C) Effect of galunisertib in the *SBE4*-dependent RGA using HEK293T cells after 24 h. Fluc signals were normalized to corresponding Rluc signals, and DMSO-TGFβ (set to 100 %). Data are mean values ± SD (n=4). D) Firefly luciferase activity in HEK293T lysate in presence of galunisertib or DMSO for 1 h. Data were normalized to DMSO-TGFβ (set to 100 %). Data are mean values ± SD (n=4).

The presence of galunisertib in the NK cell cytolysis assay resulted in a significant increase in A54 9^{Green} cytolysis at 6.67 and 20 µM, and the same trend was also observed for IFN-γ secretion levels (Figure 33A and B). The apoptosis-inducing protein Gzm B levels were also upregulated to 82.9 % in lymphocytes exposed to 10 µM galunisertib in comparison to IL-15 treatment, which corresponded to 100 % Gzm B protein levels (Figure 33C).

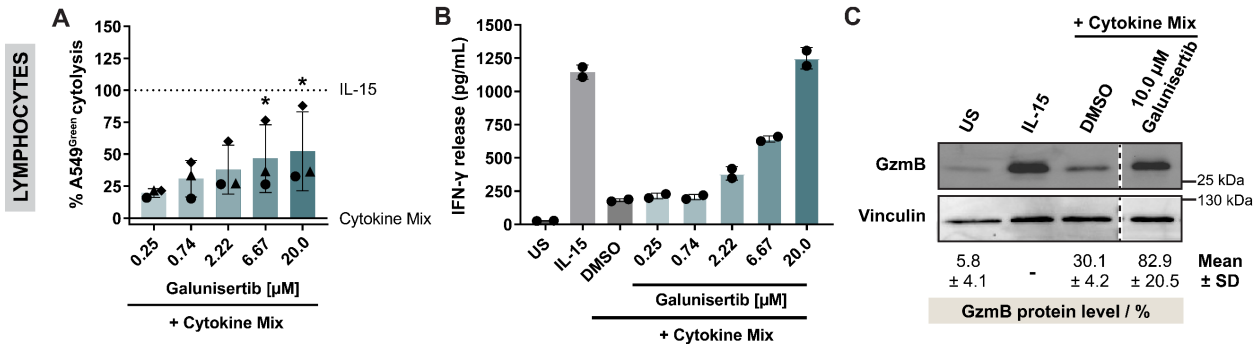

Figure 33: Galunisertib promotes NK cell cytotoxicity. A) NK cell-mediated cancer cell cytolysis assay using galunisertib-treated lymphocytes. Data are mean values ± SD (n=3). *, P < 0.05; **, P < 0.01; ***, P

< 0.001; ****, P < 0.0001 (one-way ANOVA, comparison to cytolysis rate of cytokine mix-treated control)). B) Effect of galunisertib on IFN-γ levels secreted by lymphocytes. Data are representative of n=3 (mean values ± SD, N=2). C) Gzm B protein levels in lymphocytes after treatment with cytokine mix with DMSO or galunisertib for 48 h. Immunoblot is representative of n=3. Dashed lines show cropped images originating from the same immunoblot. Quantified Gzm B levels were normalized to reference protein vinculin, and IL-15 condition, which was set to 100 %. Data are mean values ± SD (n=3).

Finally, LY2109761 showed the lowest activity in promoting NK cell cytolysis among the tested TGFβR-1 inhibitors, with an EC_{50} > 3.4 µM (Table 6). Investigations of the effect of LY2109761 on A549^{Green} viability showed that concentrations ranging from 4.0 to 10.0 µM had no impact on the viability (Figure 34A). Subjecting LY2109761 to the *SBE4*-dependent RGA resulted in an IC_{50} of 861.0 nM, whereas the activity of firefly luciferase remained unchanged when exposed to varying concentrations of LY2109761 (Figure 34C and D).

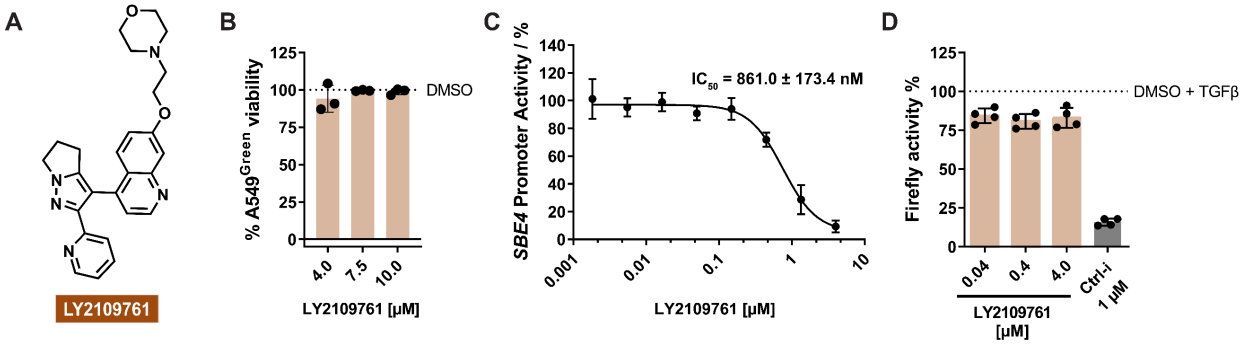

Figure 34: Effect of LY2109761 on A549^{Green} viability and TGFβ pathway activity. A) Chemical structure of LY2109761. B) Influence of LY2109761 on A549^{Green} viability after 96 h treatment. Data are mean values ± SD (n=3). C) Dose-response analysis conducted using the *SBE4*-dependent RGA using HEK293T cells treated with TGFβ and a serial dilution of LY2109761 or DMSO for 24 h. Fluc signals were normalized to corresponding Rluc signals, and DMSO-TGFβ was set to 100 %. Data are mean values ± SD (n=4). D) Impact of LY2109761 on the enzymatic activity of the firefly luciferase. Firefly luciferase-containing HEK293T lysates were treated with LY2109761 or DMSO for 1 h. Data were normalized to DMSO-TGFβ, which was designated as 100 %. Data are mean values ± SD (n=4).

Assessment of the impact of LY2109761 on NK cell-mediated cancer cell cytolysis showed a significant increase in the cytolysis rate at 10.0 µM utilizing lymphocytes. (Figure 35A). The IFN-γ secretion levels were moderately elevated in the lymphocyte-A549^{Green} co-culture treated with LY2109761, validating the cytotoxic activity of NK cells (Figure 35B). Moreover, Gzm B levels were elevated to 101.2 % in LY2109761-treated lymphocytes (Figure 35C).

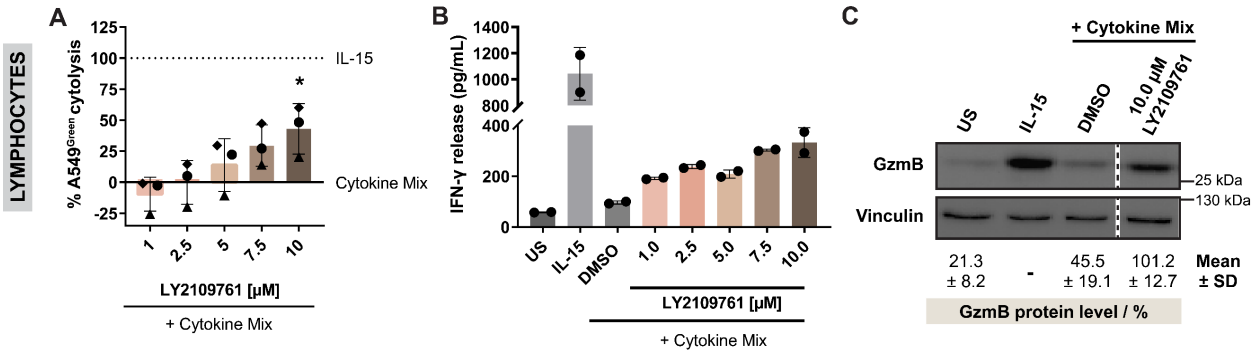

Figure 35: LY2109761 boosts NK cell cytotoxicity. A) NK cell-mediated cancer cell cytolysis assay using lymphocytes treated with LY2109761. Data are mean values ± SD (n=3). *, P < 0.05; **, P < 0.01; ***, P < 0.001; ****, P < 0.0001 (one-way ANOVA, comparison to cytolysis rate of cytokine mix-treated control)). B) Impact of LY2109761 on IFN-γ levels secreted by lymphocytes. Data are representative of n=3 (mean values ± SD, N=2). C) Gzm B protein levels in lymphocytes after treatment with LY2109761 or DMSO alongside the cytokine mix 48 h. Immunoblot is representative of n=3. Dashed lines show cropped images originating from the same immunoblot. Quantified levels of the apoptosis-inducing protein Gzm B. Data were normalized to reference protein vinculin, and the IL-15 condition, which was set to 100 %. Data are mean values ± SD (n=3).

In summary, there was a positive correlation between the TGFβ pathway inhibitory efficacy and the NK cell cytotoxicity enhancing activity for the tested TGFβR-1 inhibitors obtained from the screening. Out of the six TGFβ-R1 inhibitors, RepSox showed the strongest potency in suppressing TGFβ signaling, with an IC_{50} of 8.5 nM as assessed with the *SBE4*-dependent RGA. Correspondingly, RepSox was the most effective in potentiating the NK cell tumoricidal activity with an EC_{50} value of 180 nM. GW788388 exhibited a moderate IC_{50} of 114 nM for the reduction of SBE4 reporter expression. In accordance with these results, the NK cytotoxicity in the presence of GW788388 showed an EC_{50} of 1.19 µM. LY2109761 was the weakest inhibitor of TGFβ signaling, displaying an IC_{50} value of 861 nM. Supporting these results are supported by the consistently lower cytotoxic activity of NK cells upon LY2109761 treatment with an EC_{50} greater than 3.4 µM. This trend could be supported by the $A549^{Green}$ cytolysis rate values obtained from manual investigations.

4.1.6 RepSox as powerful promoter of NK cell cytotoxicity

4.1.6.1 Identification of secondary targets of RepSox

I. Comparison of NK cell tumoricidal enhancing activity of RepSox and TP-008

RepSox emerged as the most potent hit among the identified TGFβR-1 inhibitors, and the results of the performed follow-up experiments confirmed its notable NK cell cytotoxicity potentiating influence (Figure 25). The compound completely abolished the immunosuppressive effects of TGFβ and PGE_2 in the cytolysis assay. Using the lymphocyte setup, RepSox enhanced NK cell-mediated cancer cell lysis to an extent, surpassing the positive IL-15 by 1.2-fold. Consistent with these findings are the increase in IFN-γ secretion and Gzm B levels upon treatment with RepSox, exceeding the IL-15 control by 7- and 3.5-fold, respectively. Treatment of purified NK cells with RepSox and the cytokine mix increased their tumoricidal activity to the level of IL-15, and the secretion of IFN-γ was 1.9-fold higher compared to IL-15. Furthermore, other investigated TGFβR-1 inhibitors did not exhibit this potency, indicating the possible presence of a second target modulated by RepSox that could further enhance its NK cell cytotoxicity.

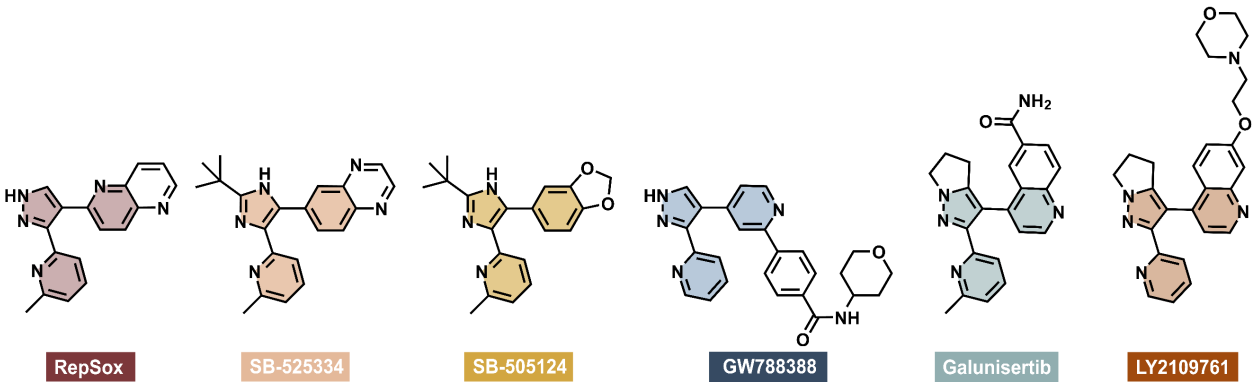

Figure 36: Comparison of the chemical structures of investigated TGFβ-R1 inhibitors.

The selected TGFβR-1 inhibitors have similar scaffolds (Figure 36). All contain specific tri-heterocyclic core with either a pyridyl-pyrazole (RepSox, GW788388, galunisertib, and LY2109761) or pyridyl-imidazole entity (SB-525334 and SB-505124). Compounds with this chemotype share several off-targets, including misshapen like kinase 1 (MINK1), mitogen-activated protein kinase 14 (p38α), receptor-interacting serine/threonine-protein kinase 2 (RIPK2), as well as vascular endothelial growth factor receptors (VEGFR).[167-170] For this reason, the effect of TP-008, a highly selective inhibitor of TGFβR-1 and Activin-like kinase 4 (ALK4) with a different chemotype, on the tumoricidal activity of NK cells was analyzed.[171] A KINOMEscan conducted by Hanke *et al*. assessed the activity of TP-008 at 1 µM towards 469 kinases and found

no further targets.[172] *Results presented for TP-008 in this subchapter were performed by Sandra Koska and were reported in her master's thesis.*

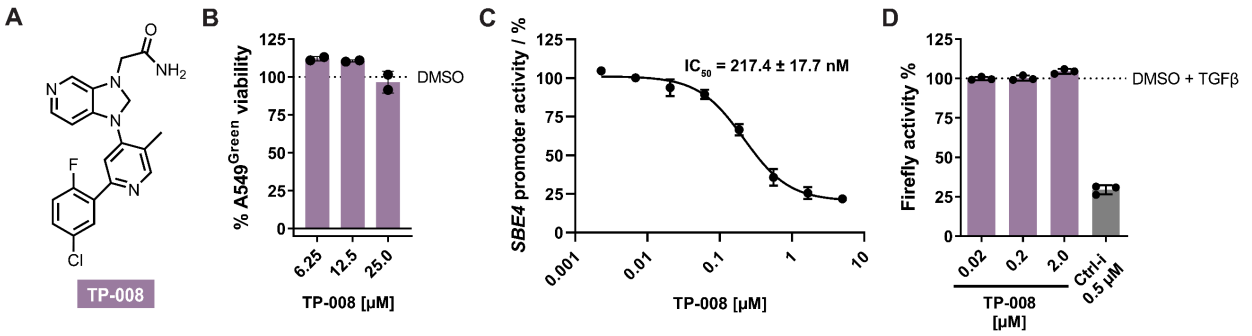

Figure 37: Influence of TP-008 on A549^{Green} viability and TGFβ pathway activity. A) Chemical structure of TP-008. B) A549^{Green} viability in presence of TP-008 after 96 h. Data are mean values ± SD (n=2). C) *SBE4* promoter activity in TP-008-treated HEK293T cells after 24 h. Fluc signals were normalized to corresponding Rluc signals, and DMSO-TGFβ (set to 100 %). Data are mean values ± SD (n=3). D) Firefly luciferase activity in HEK293T lysate treated with DMSO or TP-008 for 1 h. Data were normalized to the DMSO-TGFβ condition (set to 100 %). Data are mean values ± SD (n=3).

The highly selective TGFβR-1 inhibitor, TP-008, was also a screening hit with an EC_{50} value of 0.98 µM (Table 6). TP-008 was subjected to the A549$_{Green}$ viability, *SBE4*-dependent RGA, and firefly luciferase assay to enable side-to-side comparison with the other TGFβR-1 inhibitors. A concentration range of 6.25 to 25.0 µM TP-008 did not alter A549^{Green} viability (Figure 37B). The inhibitor suppressed *SBE4* reporter expression in a dose-dependent fashion, yielding an IC_{50} of 217.4 nM, while the firefly luciferase activity was not influenced by the compound (Figure 37C and D).

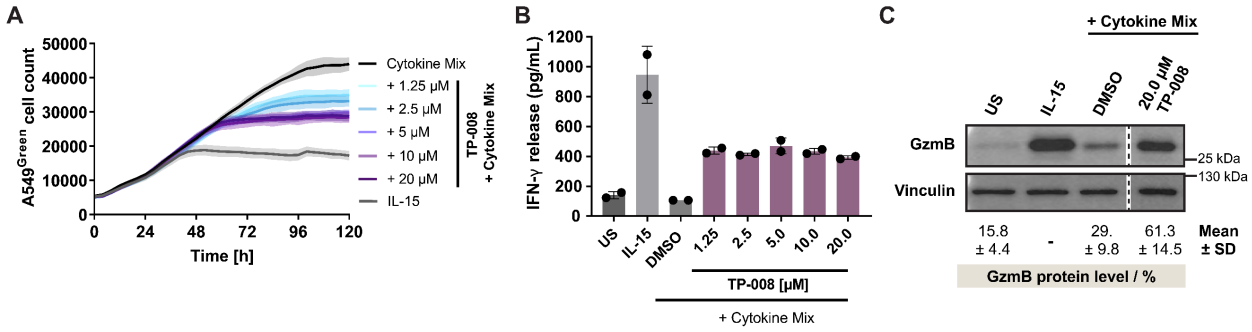

Figure 38: TP-008 promotes cytotoxicity of NK cells. A) NK cell-mediated cancer cell cytolysis assay using TP-008-treated lymphocytes. Data are representative of n=3 (mean values ± SD N=3). B) Effect of TP-008 on IFN-γ levels secreted by lymphocytes. Data are representative of n=3 (mean values ± SD, N=2). C) Gzm B protein levels in lymphocytes after treatment with cytokine mix with TP-008 or DMSO as control for 48 h. Immunoblot is representative of n=3. Quantified Gzm B levels were normalized to reference protein vinculin, and the IL-15 condition, which was set to 100 %. Data are mean values ± SD (n=3).

Moreover, TP-008 moderately elevated the tumoricidal activity of NK cells, even at the highest concentration of 20 µM (Figure 38A). These findings imply that the compound may only counteract the inhibitory effect of TGFβ signaling. Aligned with this data were the slightly elevated IFN-γ secretion levels upon TP-008 treatment, which did not show any correlation with increasing compound concentrations (Figure 38B). Furthermore, the compound also increased Gzm B protein levels in lymphocytes to 61.3 % (Figure 38C).

Next, the effects of RepSox and TP-008 on the individual immunosuppressive factors were investigated in lymphocytes (Figure 39). Compared to the IL-15-TGFβ control, RepSox recovered the $A549^{Green}$ cytolysis rate by 123.6 % (Figure 39A). Furthermore, RepSox was capable of reversing the suppressive effect of PGE_2, resulting in a 70.3 % increase in $A549^{Green}$ cell destruction. Hence, RepSox counteracted the effects of both inhibitory factors. This observation was confirmed through the addition of RepSox to the cytokine mix control, which resulted in a cytolysis rate increase of 115.6 %. TP-008 also abolished the suppressive influence of TGFβ, which resulted in a cytolysis rate increase of 55.9 % (Figure 39B). However, compared to the IL-15-PGE_2 control, the addition of TP-008 did not alter the $A549^{Green}$ cytolysis. Supplementation of the cytokine mix with TP-008 increased $A549^{Green}$ cell eradication by 49.6 %, which further supported that TP-008 solely antagonizes TGFβ signaling.

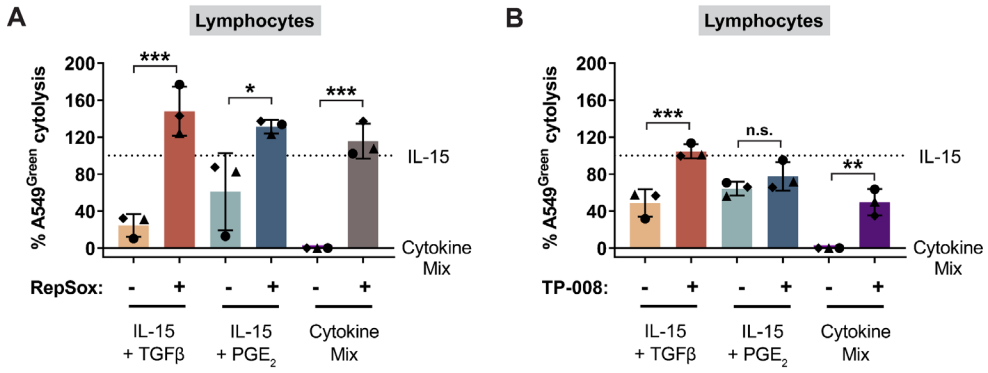

Figure 39: Comparison of the NK cell cytotoxicity in presence of TP-008 or RepSox. NK cell cytotoxicity under the influence of inhibitory factors TGFβ and PGE_2 combined with 1 µM RepSox (A) or 20 µM TP-008 (B) was analyzed using lymphocytes. DMSO was used as a control. Data are mean values ± SD (n=3); P < 0.05; **, P < 0.01; ***, P < 0.001; ****, P < 0.0001, n.s.: not significant (two-way ANOVA).

RepSox's ability to antagonize both immunosuppressive factors was also validated using purified NK cells (Figure 40). Again, RepSox neutralized the effects of TGFβ and PGE_2, resulting in a 100.1 % and 55.9 % increase in cytolysis, respectively, compared to the corresponding DMSO control. The addition of RepSox to the cytokine mix completely abrogated its suppressive effect.

These results strengthen that RepSox may have a second target, apart from TGFβR-1, contributing to increased NK cell cytotoxicity.

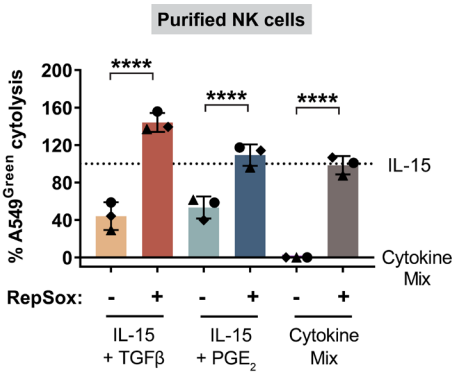

Figure 40: RepSox counteracts the inhibitory effect of TGFβ and PGE_2. Treatment of purified NK cells with 1 µM RepSox or DMSO to assess its effect on NK cell cytotoxicity under the influence of inhibitory factors TGFβ and PGE_2. Data are mean values ± SD (n=3); P < 0.05; **, P < 0.01; ***, P < 0.001; ****, P < 0.0001, n.s.: not significant (two-way ANOVA).

II. RepSox off-target kinases as potential secondary on-target for NK cytotoxicity

RepSox and other structurally related TGFβR-1 inhibitors have various common off-target kinases. A comprehensive analysis of these off-target kinases revealed two kinase family members linked to modulating NK cell activity: VEGFR and MINK1.[169]. VEGFRs are receptor tyrosine kinases that play a significant role in angiogenesis, and deregulated angiogenesis is a crucial process for tumor progression and metastasis.[173] A study by Lee *et al.* showed that VEGFR-3 protein levels are significantly increased in acute myeloid leukemia (AML) patients and that its expression levels display an inverse correlation with NK cell cytotoxicity.[174] Additionally, the authors demonstrated that VEGFR-3 inhibition recovers the tumoricidal activity and IFN-γ secretion levels of NK cells. Therefore, the activity of the triple VEGFR-1/2/3 inhibitor (*in vitro* IC_{50}: 34, 21 and 13 nM, respectively), nintedanib, was investigated for NK cell-mediated cancer cell cytolysis, both individually and in combination with the specific TGFβR-1 inhibitor TP-008.[175] The aim of investigating the TP-008-nintedanib combination was to determine if it could mimic the activity of RepSox. *Results presented in this subchapter were performed by Sandra Koska and were reported in her master's thesis.*

First, nintedanib was subjected to the A549^{Green} viability assay, and the A549^{Green} growth behavior paralleled the DMSO control (Figure 41B). Next, nintedanib's impact on NK cell tumoricidal activity was assessed (Figure 41C). The compound did not enhance NK cell cytotoxicity, and the combination with TP-008 did not profoundly change the cytolysis rate compared to the TP-008-only control. Furthermore, an influence of nintendanib on IFN-γ secretion was ruled out (Figure 41D).

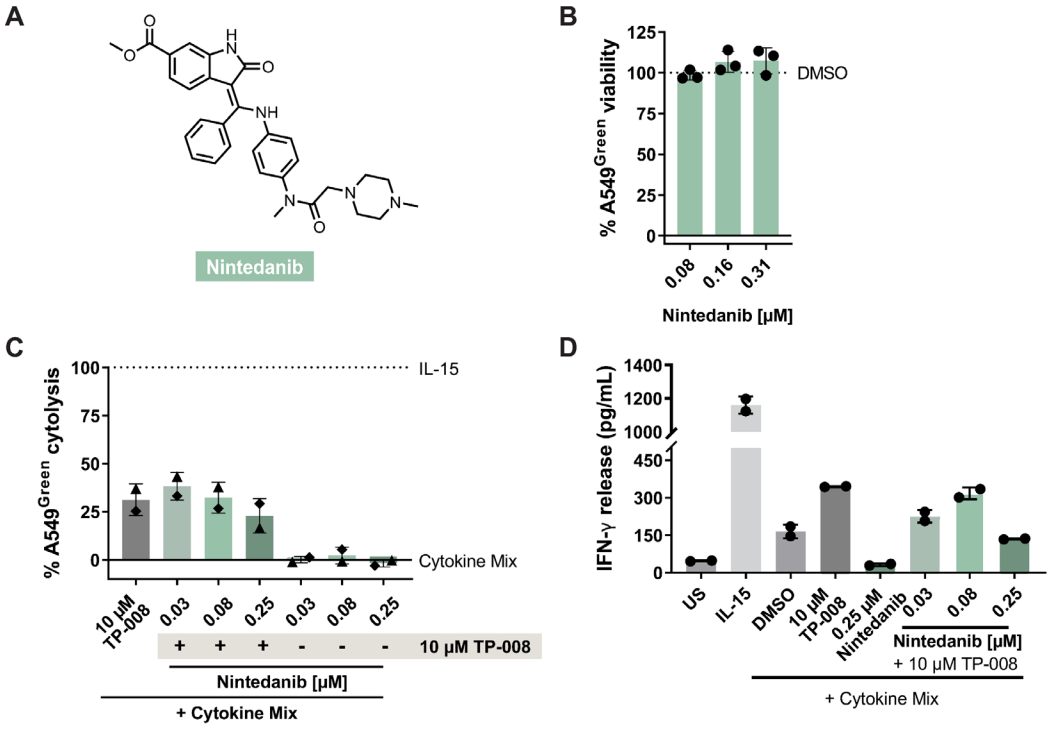

Figure 41: Nintedanib does not enhance NK cell cytotoxicity. A) Chemical structure of nintedanib. B) A549^{Green} viability in presence of nintedanib after 96 h. Data are mean values ± SD (n=3). C) NK cell-mediated cancer cell cytolysis assay utilizing lymphocytes treated with nintedanib and TP-008 individually or combined. The percentage of A549^{Green} was determined using the AUC) and the obtained data were normalized to the IL-15 condition as 100 % cytolysis and to the cytokine mix condition as 0 % cytolysis. Data are representative of n=2 (mean values ± SD N=3). D) Effect of nintedanib on IFN-γ levels secreted by lymphocytes. Data are representative of n=3 (mean values ± SD, N=2).

The serine-threonine kinase MINK1 has multiple cell regulatory functions, including growth, division, and differentiation.[176] Previous literature demonstrated that MINK1 directly affects the activation of SMAD2.[176] The existing link between MINK1 and TGFβ signaling served as basis for investigation of its relevance for NK cell cytolytic activity. For this purpose, the MINK1 inhibitor DMX-5804 (*in vitro* IC_{50}: 6.6 nM) was utilized (Figure 42).[177] After assessment of suitable concentration ranges of DMX-5804 *via* the A549^{Green} viability assay, the effect of the inhibitor on NK cell cytotoxicity was investigated. No meaningful enhancement of NK cell cytotoxicity or

IFN-γ secretion levels were observed at the tested concentrations of DMX-5804 (Figure 42C and D).

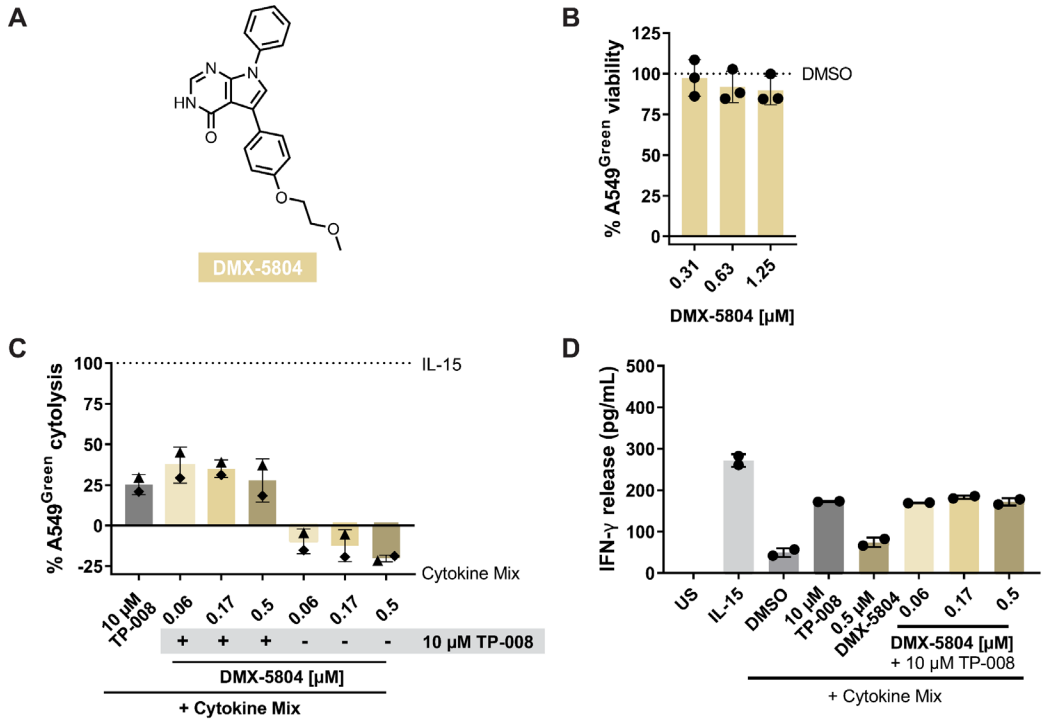

Figure 42: DMX-5804 does not enhance NK cell cytotoxicity. A) Chemical structure of DMX-5804. B) A549^{Green} viability in presence of DMX-5804 after 96 h. Data are mean values ± SD (n=3). A) NK cell-mediated cancer cell cytolysis assay utilizing lymphocytes treated with DMX-5804 and TP-008 individually or combined. The percentage of A549^{Green} was determined using the AUC) and the obtained data were normalized to the IL-15 condition as 100 % cytolysis and to the cytokine mix condition as 0 % cytolysis. Data are representative of n=2 (mean values ± SD, N=3). B) Effect of DMX-5804 on IFN-γ levels secreted by lymphocytes. Data are representative of n=3 (mean values ± SD, N=2).

III. Characterization of RepSox as a Notch signaling modulator

According to the findings of Zhang *et al.*, RepSox promotes Notch signaling and upregulated Notch1 and Notch intracellular domain (NICD) protein levels in human pluripotent stem cells.[178] There are four isoforms of the Notch receptor (Notch 1-4) in humans, but only Notch 1 and 2 are expressed in NK cells.[179] In NK cells, Notch signaling is essential for their functional maturation, and active Notch signaling strongly correlates with NK tumoricidal activity as well as IFN-γ secretion.[179-181] Hence, the relevance of Notch signaling for NK cell tumoricidal activity was investigated in the NK cell-mediated cancer cell cytolysis assay. For this purpose, the two Notch pathway inhibitors were used, DAPT, a γ-secretase inhibitor, and Inhibitor of mastermind recruitment (IMR-1), an inhibitor of Notch transcription activation complex (Figure 43).[182,183] *Part of the results presented in this chapter were partly conducted with Sandra Koska and reported in her master's thesis.*

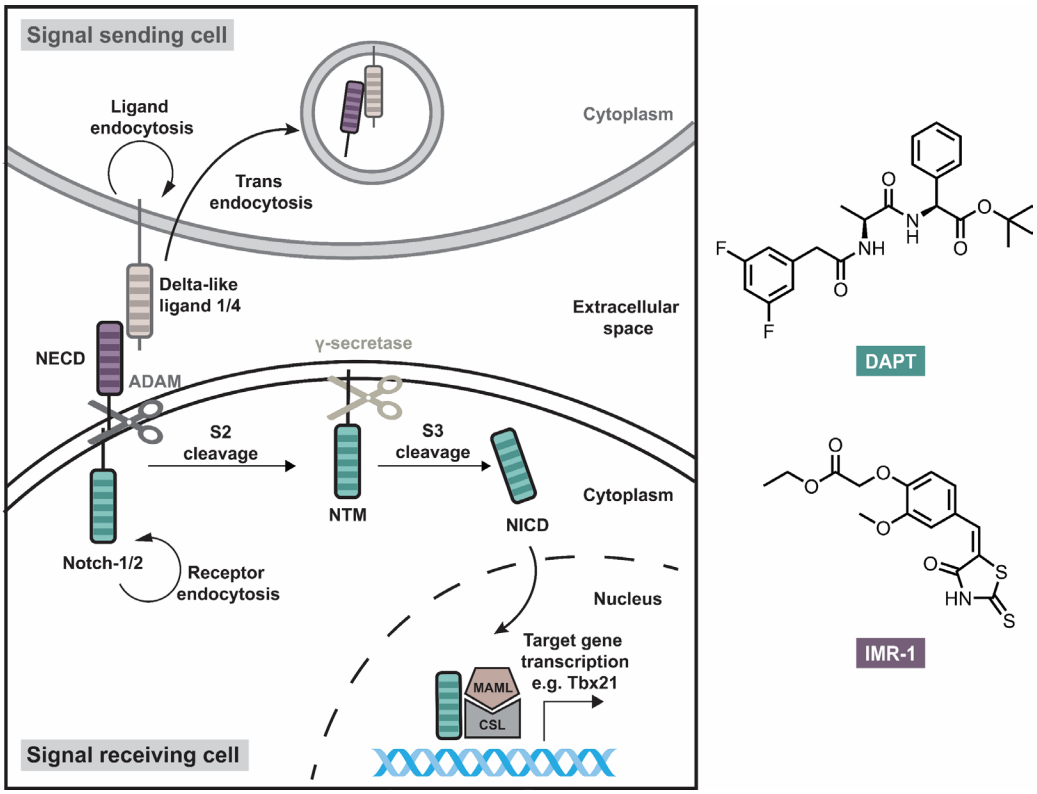

Figure 43: Schematic representation of the Notch signaling pathway. Notch ligand (e.g., Delta-like ligand 1 or 4) binding to its transmembrane receptor Notch 1/-2 triggers a biphasic cleavage process. The initial proteolytic S2 cleavage step is mediated by ADAM metalloproteases prompting the formation of the Notch transmembrane domain (NTM). This is followed by the S3 cleavage directed by γ-secretase, resulting in the release of Notch intracellular domain (NICD). This is followed by a NICD translocation to the nucleus and complex formation with CSL (CBF1, Suppressor of Hairless, Lag-1) transcription factor. The assembled complex then recruits co-activators, including Mastermind-like (MAML), to promote target gene expression. Figure is based on Nickoloff *et al.*[184]

RepSox was tested in conjunction with Notch signaling inhibitors IMR-1 and DAPT (Figure 44). While the addition of 20 µM IMR-1 to RepSox significantly reduced A549^{Green} cytolysis compared to the RepSox-only control, cancer cytolysis remained unaffected by individual treatment with the Notch inhibitor (Figure 44A). The IFN-γ secretion levels were also decreased in a concentration-responsive pattern in the RepSox-IMR-1-treated condition, while IMR-1 alone had no influence (Figure 44B). Moreover, the inhibitory influence of IMR-1 on NK cell effector function was confirmed through Gzm B protein assessment, which displayed decreased protein content for the RepSox-IMR-1-treated condition (Figure 44C). Gzm B protein levels under the influence of IMR-1 only remained unchanged. A comparable trend was observed for treatments using a RepSox-DAPT combination. The addition of DAPT to RepSox significantly weakened the cytolysis rate (Figure 44D), as validated by the reduced IFN-γ and Gzm B levels (Figure 44E and F). Furthermore, DAPT alone did not alter NK cell effector functions.

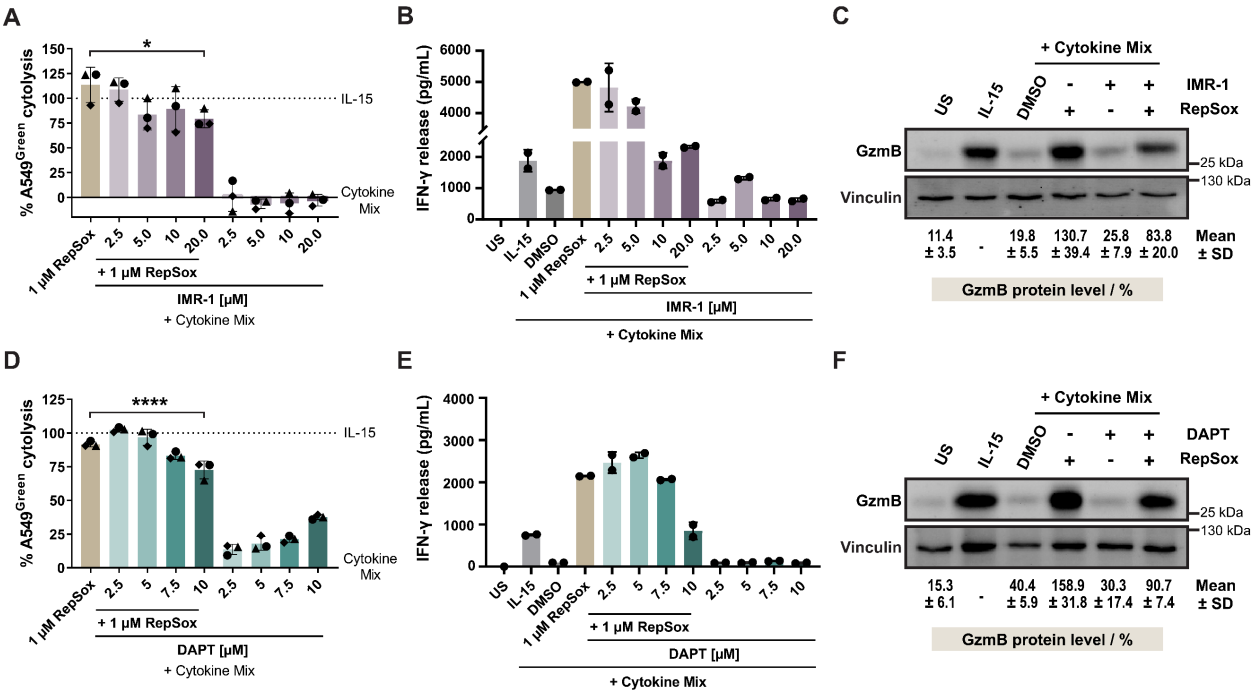

Figure 44: Notch signaling inhibition attenuates NK cell cytotoxicity. A) NK cell-mediated cancer cell cytolysis assay utilizing RepSox and IMR-1, either individually or combined using lymphocytes. Data are representative of n=3 (mean values ± SD, N=3). *, P < 0.05; **, P < 0.01; ***, P < 0.001; ****, P < 0.0001 (one-way ANOVA). B) Effect of IMR-1 on IFN-γ levels secreted by lymphocytes. Data are representative of n=3 (mean values ± SD, N=2). C) Gzm B protein levels in lymphocytes after treatment with cytokine mix and differing combinations of 1 µM RepSox, 20 µM IMR-1, or DMSO as a control for 48 h. Immunoblot is representative of n=4. Quantified Gzm B levels were normalized to reference protein vinculin, and the IL-15 condition, which was set to 100 %. Data are mean values ± SD (n=4). D) Influence of DAPT on NK cell-mediated cancer cell cytolysis. A co-culture of lymphocytes and A549^{Green} cells were treated with varying combinations of RepSox and DAPT in presence of the cytokine mix. Data are representative of n=3 (mean values ± SD). E) Effect of IMR-1 on IFN-γ levels secreted by lymphocytes. Data are mean values ± SD (n=3, N=2). F) Gzm B protein levels in lymphocytes after treatment with cytokine mix and

differing combinations of 1 µM RepSox, 10 µM DAPT, or DMSO as control for 48 h. Immunoblot is representative of n=3. Data are mean values ± SD (n=3, IL-15 condition = 100 %).

Subsequently, the Notch signaling activity of lymphocytes in response to RepSox treatment was explored (Figure 45). In this regard, the protein abundance of the NTM and NICD was examined. RepSox did not alter NTM or NICD quantity of the unstimulated or IL-15-condition (Figure 45A). In contrast to the cytokine mix, which reduced NICD protein abundance, RepSox boosted its levels in presence of the cytokine mix. NTM levels remained unchanged for the cytokine mix-treated conditions. To evaluate whether NICD upregulation is associated with RepSox-mediated inhibition of TGFβ signaling, the effect of TP-008 was examined (Figure 45B). TP-008 did not upregulate NICD levels of the unstimulated, IL-15-treated and cytokine mix conditions. In conclusion, RepSox solely counteracts the suppressive effect of the cytokine mix on NICD protein levels as no additional increase in NICD levels was seen when IL-15 was added. Given that this effect was not observed for TP-008, it further strengthens the existence of a second relevant target for NK cell effector function.

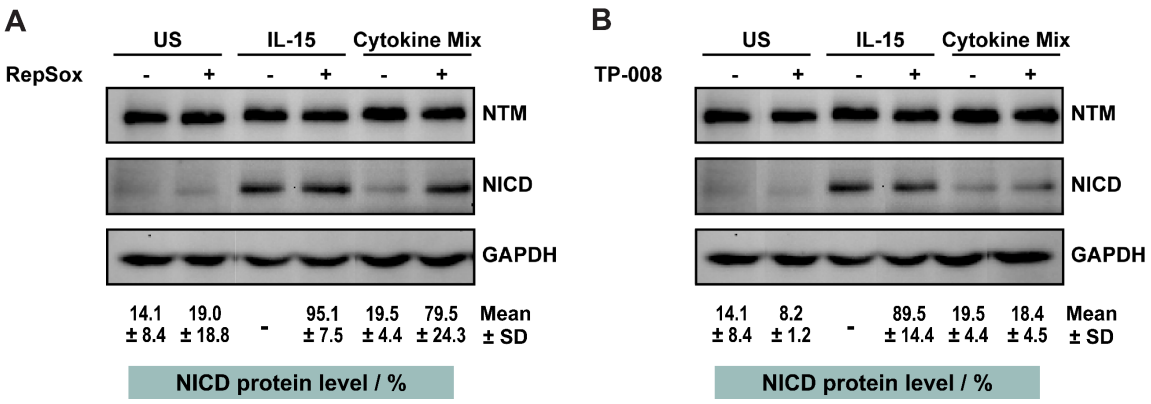

Figure 45: RepSox restores NICD protein levels. Effect of RepSox (A) and TP-008 (B) on Notch signaling activity evaluated through analysis of NICD and NTM protein levels. Lymphocytes were treated with 1 µM RepSox, 10 µM TP-008, or DMSO for 48 h. Immunoblot is representative of n=3 for RepSox and n=2 for TP-008. Quantified NICD levels were normalized to reference protein glyceraldehyde-3-phosphate dehydrogenase (GAPDH), and the IL-15 condition was set to 100 %. Data are mean values ± SD (n=3 for RepSox, n=2 for TP-008). *Immunoblots were performed by Sandra Koska*.

IV. Identification of RepSox as a modulator of the PGE_2/EP2/4 signaling axis

RepSox has been recognized as a potent inhibitor of TGFβ signaling. However, the results of this thesis have established its ability to antagonize the immunosuppressive effects of both TGFβ and PGE_2. Immunosuppressive PGE_2 modulates the cytotoxicity of NK cells *via* prostaglandin EP2 and EP4, which results in enhanced adenylate cyclase activity.[49] This, in turn, leads to the upregulation of intracellular cAMP levels as well as NK cell inhibitory receptors (e.g., NKG2A) and simultaneously to the downregulation of NK cell-activating receptors, including NKG2D, NKp30, NKp44, NKp46, and CD16, as well as effector molecules like IFN-γ, granzymes, and perforin.[42,47,50] The impact of RepSox on the PGE_2/EP2/4 signaling axis has not been studied yet. Therefore, the role of RepSox in this cancer-relevant pathway was investigated. *Part of the results presented in this subchapter were obtained in collaboration with Dr. Astrid Kahnt (Goethe University Frankfurt).*

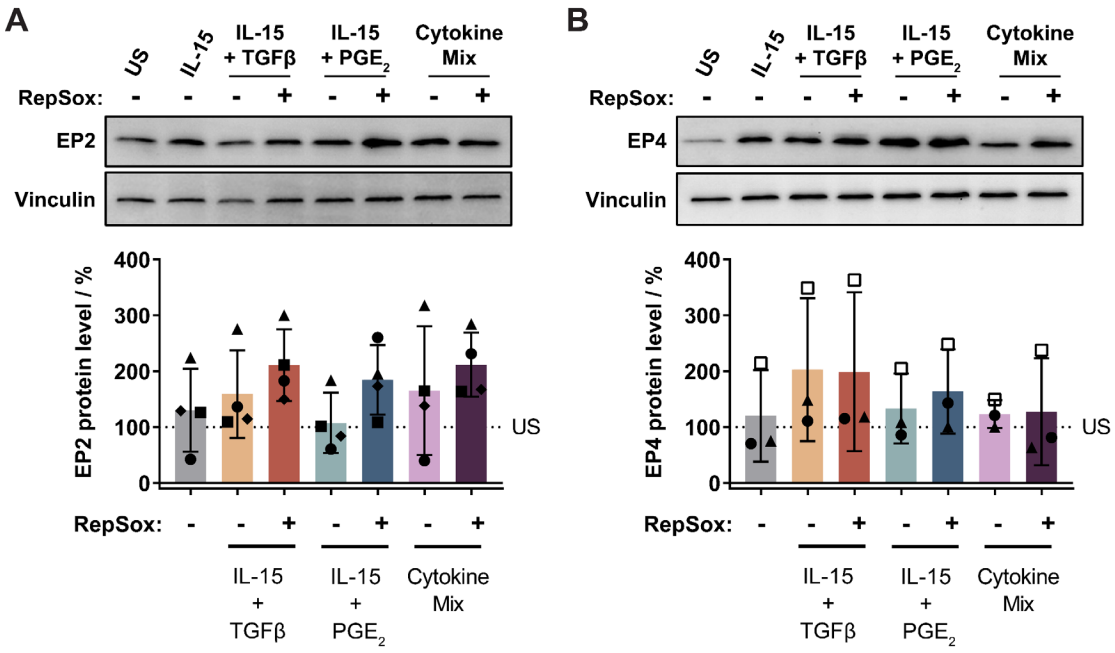

Figure 46: RepSox does not affect EP2/4 protein abundance. Impact of RepSox on EP2 (A) and EP4 (B) protein levels. Lymphocytes were treated with 1 µM RepSox or DMSO for 48 h. Immunoblots are representative of n=4 for EP2 and n=3 for EP4. Quantified EP2/4 protein levels were normalized to the reference protein vinculin, and the US condition, which was set to 100 %. Data are mean values ± SD (n=4 for EP2, n=3 for EP4).

The initial step entailed exploring the role of RepSox on EP2/4 levels (Figure 46). The compound was combined with the individual inhibitory factors TGFβ and PGE_2 or the cytokine mix. No meaningful alterations in the protein content of EP2 (Figure 46A) or EP4 (Figure 46B) could be observed under the influence of RepSox.

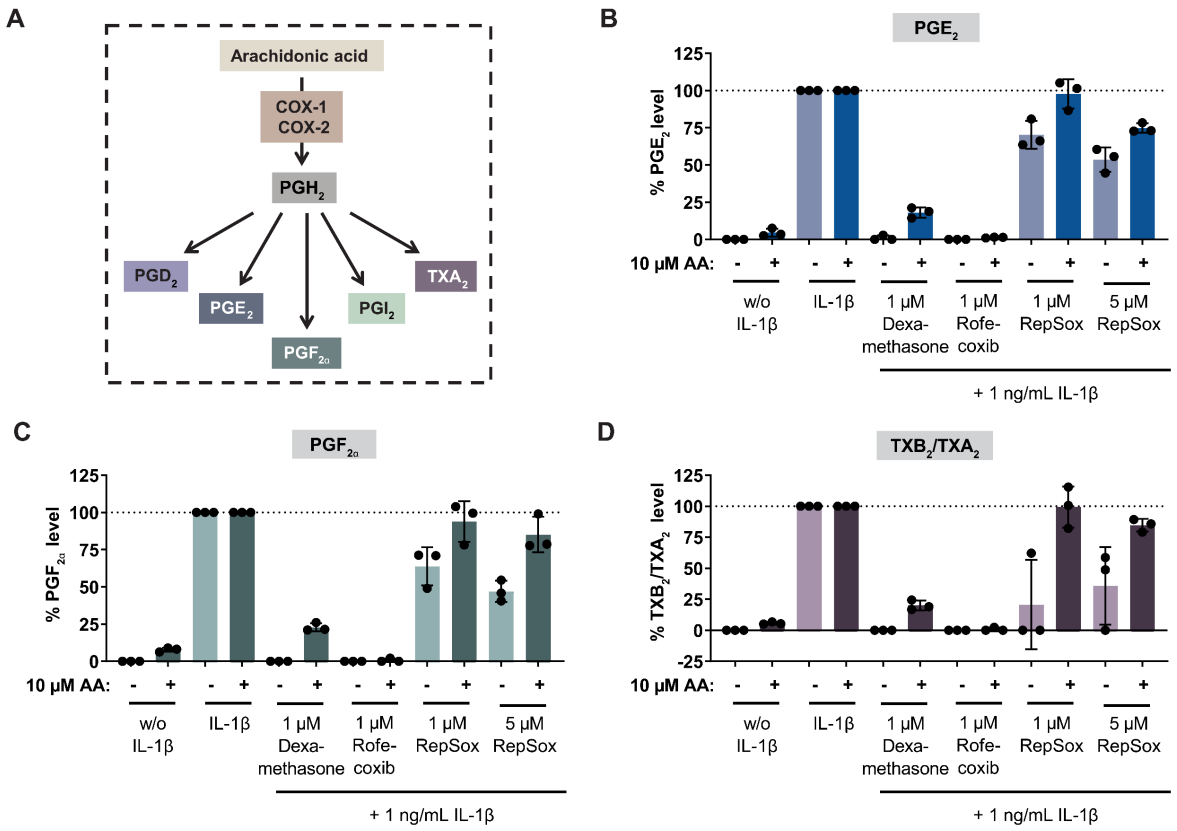

Figure 47: RepSox modulates cellular prostanoid and thromboxane levels. A) Cyclooxygenases COX-1 and -2 process arachidonic acid (AA) into PGH_2, which is subsequently metabolized to PGD_2, PGE_2, $PGF_{2\alpha}$, PGI_2, and TXA_2 through numerous downstream synthases.[185] B-D) Evaluation of the impact of RepSox on prostanoid and thromboxane generation in A549 cells. Data in the presence or absence of AA were normalized to their corresponding IL-1β control, which was set to 100 % (mean ± SD, n=3). Dexamethasone and Rofecoxib were used as controls. While Dexamethasone suppresses IL-1β-stimulated COX-2 expression, Rofecoxib selectively inhibits COX-2 in a reversible manner. *Assay was performed by Dr. Astrid Kahnt.*

This was followed by an assessment of RepSox's influence on prostanoid and thromboxane production in A549 cells, which are directly linked to COX-1/-2 activity. COX-1 and -2 promote tumorigenesis through an increase of immunosuppressive PGE_2 levels, thereby reducing the tumoricidal activity of NK cells.[49,186] Both cyclooxygenases are involved in the biosynthesis of prostaglandins (PG) and thromboxanes (TB) derived from the metabolization of arachidonic acid (AA) (Figure 47A). COX-1 is constitutively expressed, whereas COX-2 expression was stimulated utilizing the cytokine IL-1β. Accordingly, levels of PGE_2, $PGF_{2\alpha}$, and TXA_2/TXB_2 were elevated in A549 cells (Figure 47B-D). PGD_2 and PGI_2 were not inducible in A549 cells. The glucocorticoid Dexamethasone and the COX-2 inhibitor Rofecoxib were used as controls. Dexamethasone suppresses COX-2 expression in IL-1β-stimulated cells and phospholipase A2 (PLA2) protein synthesis. Inhibition of PLA2 levels decreases the release of AA from membrane

phospholipids, which simultaneously affects prostaglandin and thromboxane levels.[187-189] This is in line with the obtained results, which demonstrate that PGE_2, $PGF_{2\alpha}$, and TXA_2/TXB_2 levels were reduced in the presence of Dexamethasone (Figure 47B-D), whereas AA was able to moderately restore the levels. The reversible COX-2-specific inhibitor Rofexocib abolished the formation of prostaglandins PGE_2, $PGF_{2\alpha}$, and thromboxane TXA_2/TXB_2 regardless of AA presence (Figure 47B-D).[190] Following treatment with RepSox, PGE_2 levels were reduced to 70.2 % at 1 µM and 53.6 % at 5 µM (Figure 47B). $PGF_{2\alpha}$ levels were notably decreased in the presence of RepSox, reaching 63.8 % at 1 µM and 40.0 % at 5 µM compound concentration (Figure 47C). Additionally, a pronounced decrease of $PGF_{2\alpha}$ to 20.7 % and 35.8 % was observed for 1 and 5 µM RepSox treatment, respectively (Figure 47D). The content of PGE_2, $PGF_{2\alpha}$ as well as TXB_2/TXA_2 were recovered by the introduction of AA. These findings suggest that RepSox might directly modulate the activity of COX-1/-2 in a reversible manner and acts downstream of AA release.

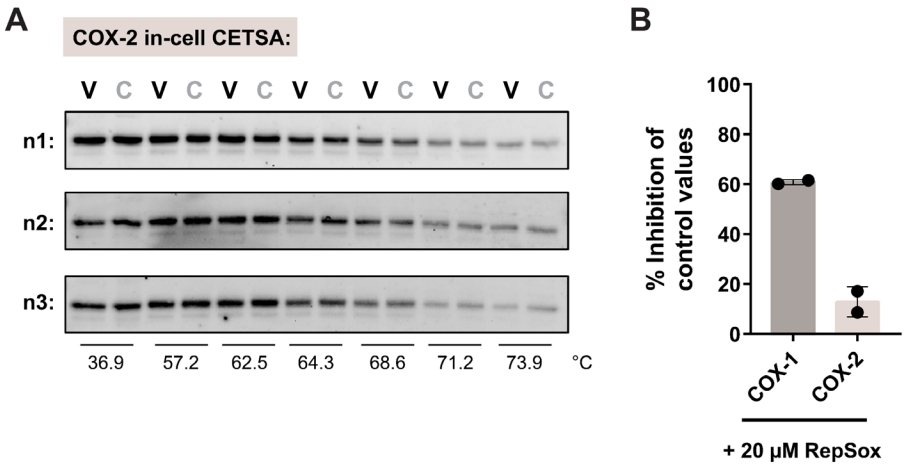

Figure 48: RepSox downregulates COX-1 activity. A) COX-2 cellular thermal shift assay (CETSA) in BxPC-3 cells. Cells were treated with 50 µM RepSox (C) or DMSO (V) for 15 min. C: compound and V: vehicle. Immunoblots of three biological replicates are shown (n=3). B) Influence of RepSox on the *in vitro* COX-1 and COX-2 activity. Human COX-1 and -2 proteins were combined with AA (3 and 1.2 µM, respectively), 25 µM of 10-acetyl-3,7-dihydroxyphenoxazine (ADHP), and 20 µM RepSox and enzymatic activity was assessed through fluorimetric detection (mean ± SD, N=2). *Assay was performed by Eurofins Discovery.*

Therefore, target engagement studies were carried out using a cellular thermal shift assay (CETSA) in BxPC-3 cells.[191,192] These cells exhibited sufficient COX-2 expression levels without needing activation by stimulating factors. For this purpose, cells were treated with RepSox or DMSO for 15 min, followed by performance of the thermal shift assay. Next, COX-2 presence in the soluble protein fraction was evaluated by means of immunoblotting. DMSO and RepSox samples treated with the same temperature were loaded side-by-side to facilitate melting response comparison. RepSox treatment did not change the thermal stability of COX-2

(Figure 48A). However, CETSA is limited to protein melting temperature alterations, which may not always be affected by ligand binding. Consequently, the influence of RepSox on purified human COX-1 and COX-2 was explored by means of a biochemical assay. The activity of the cyclooxygenases was assessed by measuring the conversion of AA to prostaglandins. The formed products react with ADHP, leading to a colorimetric change as they oxidize to resorufin *via* horseradish peroxidase (HRP).[193] This color change is directly proportional to COX-1 and COX-2 activity. RepSox was able to suppress COX-1, reaching 61 % inhibition at 20 µM, while COX-2 activity demonstrated a minor reduction of 13 % (Figure 48B). In summary, RepSox most likely reduced prostaglandin and thromboxane levels in A549 cells by inhibiting COX-1 activity.

4.1.6.2 In-depth analysis of the influence of RepSox on NK cell functions

The NK cell function is strictly regulated through an equilibrium of activating and inhibitory signals through several receptors expressed on their surface.[194] In order to examine the mechanism of through which RepSox restored NK cell function in the presence of immunosuppressive factors PGE_2 and TGFβ within the TME-mimicking co-culture assay, a comprehensive study of NK cell surface receptors using flow cytometric analysis with two distinct antibody panels. These panels cover different surface receptors attributed to various NK cell functions. *Results presented in this chapter were obtained in collaboration with Jens Niemann (Watz lab, IfADo, Dortmund).*

In the first panel, the NK cell immunophenotype resulting from RepSox treatment was analyzed for a total of 19 functional markers associated with NK cell activation, adhesion, characterization, cytotoxicity, and inhibition (Figure 49A). To map the obtained data of the individual conditions in a lower-dimensional space, they underwent t-distributed stochastic neighbor embedding (t-SNE) (Figure 49B). The ungated condition represented the entire dataset. Unstimulated NK cells displayed a considerably distinct immunophenotype, compared to the IL-15-treated population. Furthermore, no meaningful change in NK cell distribution was observed by the addition of RepSox to IL-15. Conversely, the phenotype under the influence of the cytokine mix closely matched the unstimulated state. The introduction of RepSox to the cytokine mix changed the NK cell distribution in a manner equivalent to the activating IL-15 condition.

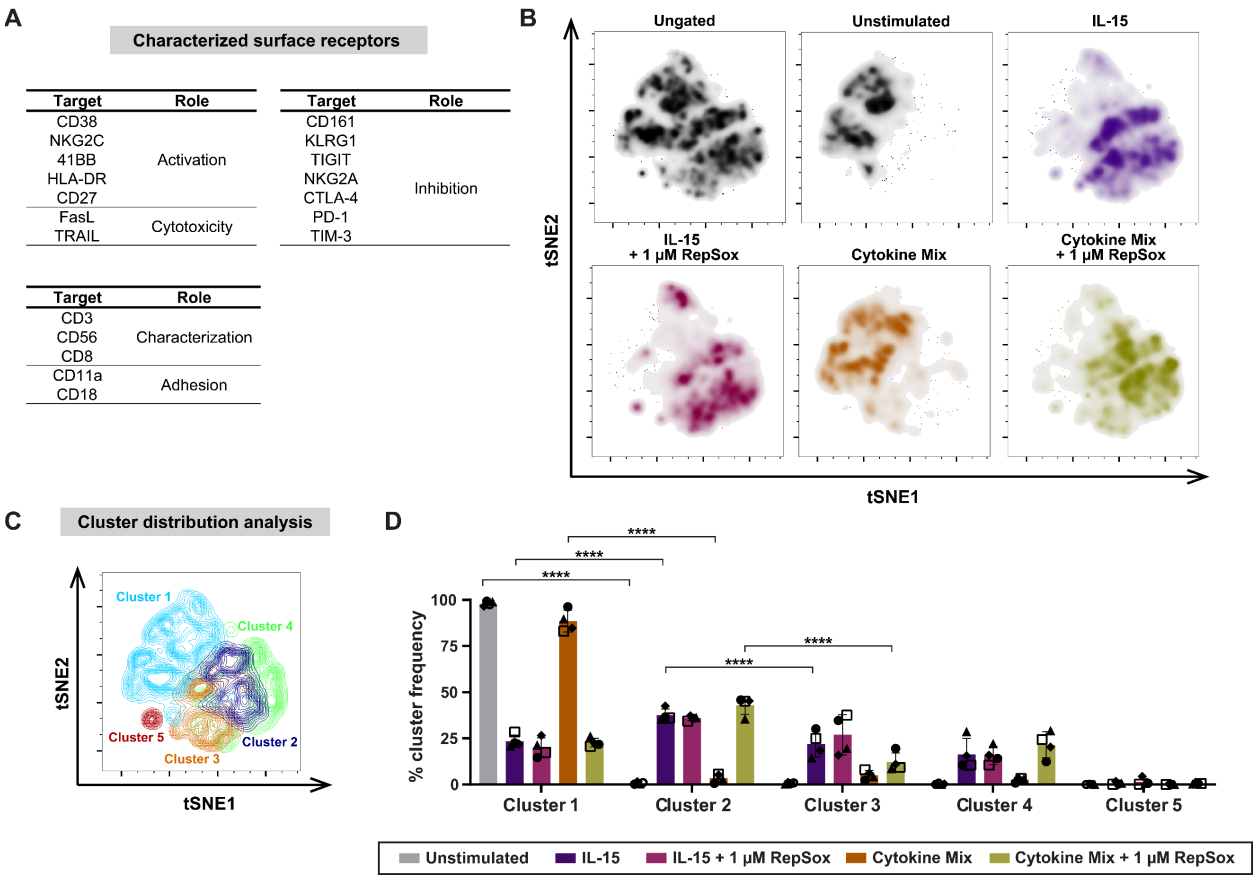

Figure 49: Impact of RepSox treatment on NK cell functions. A set of 19 NK cell surface proteins attributed to their activation, adhesion, cytotoxicity, identity, and inhibition were explored. Lymphocytes were treated with RepSox in combination with IL-15 or the cytokine mix for 48 h. Next, NK cell surface receptors were stained and samples were analyzed by means of flow cytometry. Subsequent to gating on live, single NK cells ($CD3^-$ and $CD56^+$), the functional markers across the entire population were explored. Data are mean values of four biological replicates (n=4). A) Overview of investigated NK cell surface markers. B) Obtained data underwent dimensionality reduction *via* t-distributed stochastic neighbor embedding (t-SNE). C) Cluster distribution analysis of NK cells based on their surface receptor expression pattern. Cluster frequency for the used conditions is displayed in D). The profiles were obtained utilizing the FlowJo™ plugin PhenoGraph algorithm.

Evaluation of the expression profile of the complete array of analyzed surface antigens across the used conditions resulted in a total of five clusters (Figure 49C and D). NK cells within cluster 1 exhibited an inactive or suppressed immunophenotype, with cluster frequencies of 98.1 % of the unstimulated and 88.5 % of the cytokine mix condition (Figure 49D). NK cells with an active immunophenotype were distributed across clusters 2 to 5. The addition of IL-15, regardless of RepSox treatment, attenuated cluster 1 frequency, while an increase in clusters 2-5 could be observed. The immunosuppressive factors within the cytokine mix diminished the activating effect of IL-15. This was reversed through RepSox addition. Cytokine mix-RepSox treated cells can be found across clusters 2-4, strengthening its association with an active NK cell

immunophenotype. The results of the cluster frequency analysis align with the phenotypic analysis (Figure 49B).

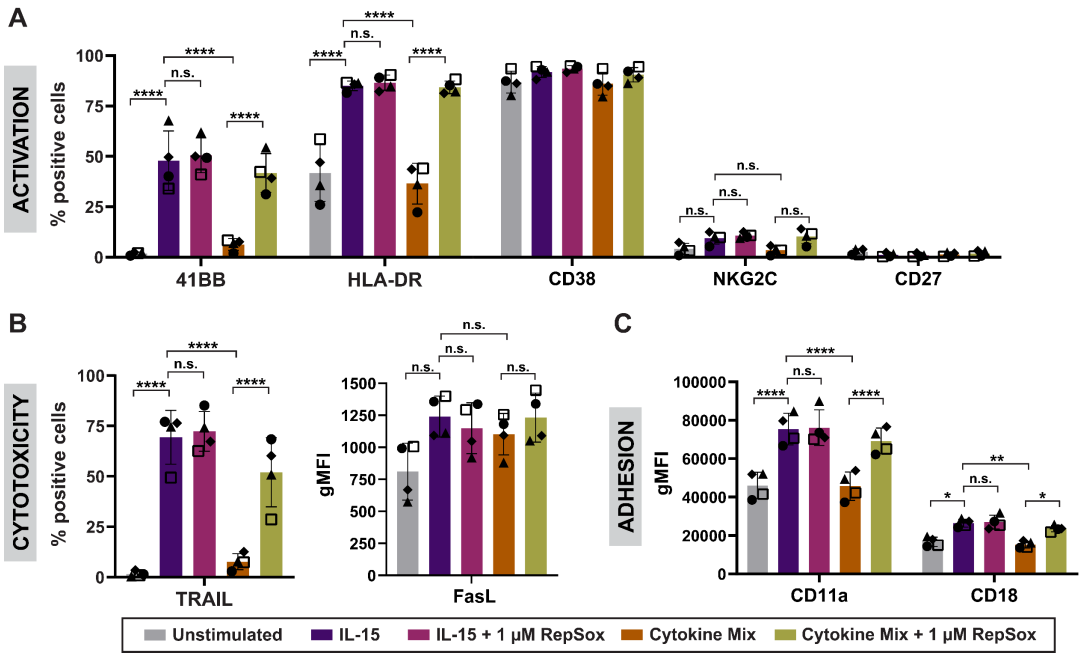

Figure 50: RepSox affects surface receptor levels essential for NK cell activity. Quantified protein levels of NK cell functional markers pivotal for their activation (A), cytotoxicity (B), and adhesion (C). Data are mean values ± S.D (n=4); P < 0.05; **, P < 0.01; ***, P < 0.001; ****, P < 0.0001, n.s.: not significant (two-way ANOVA).

Subsequently, the influence of the utilized conditions on the individual NK cell surface receptors was analyzed (Figures 50 and 51). The receptors 41BB, HLA-DR, CD38, NKG2C, and CD27 have a crucial role in NK cell activation (Figure 50A).[195-198] However, only 41BB and HLA-DR levels were significantly altered in this setup. For both proteins, levels were low in the unstimulated condition, while IL-15 upregulated 41BB and HLA-DR levels. RepSox addition to IL-15 did not affect 41BB and HLA-DR abundance. The cytokine mix, however, reduced their expression to a level comparable to the unstimulated state, and RepSox addition restored the protein levels. Moreover, TRAIL and FasL levels, both involved in NK cell cytotoxicity, were examined.[199,200] However, only TRAIL displayed significant changes in protein levels (Figure 50B). In the unstimulated condition, TRAIL-positive cells were not observed. The introduction of IL-15 led to an upregulation, while the activating effect was antagonized by the cytokine mix. RepSox restored the levels of TRAIL in the presence of the cytokine mix. Furthermore, we investigated CD11a and CD18, which are essential receptors for NK cell adhesion that enable the interaction with target and immune cells.[201] For the adhesion-relevant receptors, a similar trend could be identified (Figure 50C).

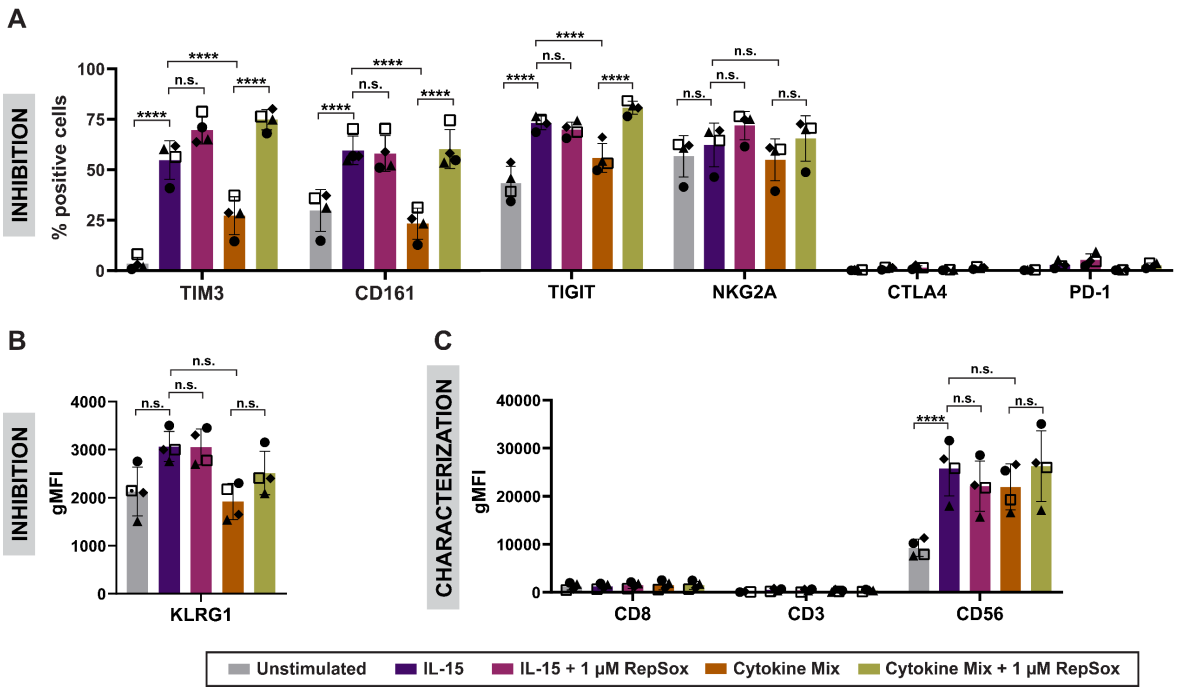

Figure 51: RepSox influences surface receptor levels essential for NK cell inhibition. Quantified protein levels of NK cell-inhibitory markers (A), cytotoxicity (B), and adhesion (C). Data are mean values ± S.D (n=4); P < 0.05; **, P < 0.01; ***, P < 0.001; ****, P < 0.0001, n.s.: not significant (two-way ANOVA).

Finally, a set of NK inhibitory receptors was investigated, namely TIM3, CD161, TIGIT, NKG2A, CTLA4, PD-1, and KLRG1.[202-204] The activating conditions (i.e., IL-15, IL-15-RepSox, and cytokine mix-RepSox) upregulated TIM3, CD161, and TIGIT levels, while the unstimulated or inhibitory conditions (i.e., US and cytokine mix) attenuated protein levels (Figure 51A and B).

The second antibody panel focused on NK cell-activating receptors, involving analysis of surface receptors NKp30, NKp44, NKp46, 2B4, CD16, DNAM-1, and NKG2D.[205,206] The acquired data were presented in tSNE plots for all tested conditions (Figure 52B). The immunophenotype of the NK cell-suppressing conditions (i.e., US, and the cytokine mix) exhibited a considerable alignment. Moreover, the NK cell distributions of the NK cell-activating treatments (i.e., IL-15, IL-15-RepSox, and cytokine RepSox) showed a strong resemblance.

A

Characterized surface receptors

Target	Role
NKp30 NKp44 NKp46 2B4 CD16 DNAM-1 NKG2D	Activation

Target	Role
CD3 CD56	Characterization

B

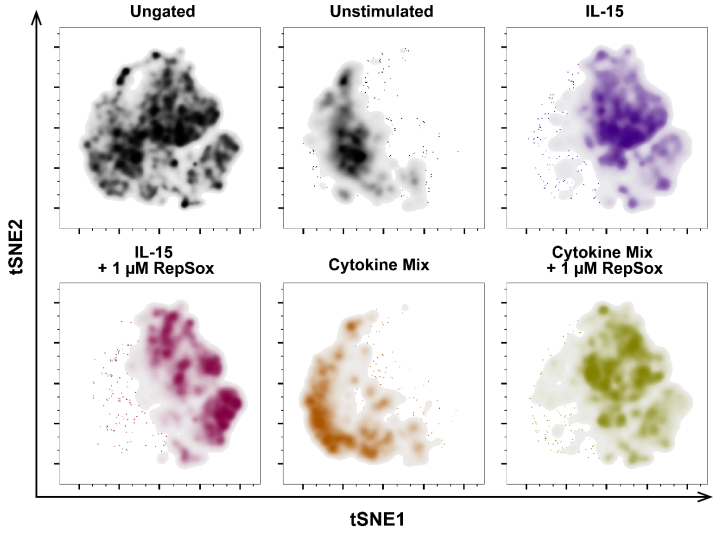

Figure 52: Impact of RepSox treatment on NK cell activation. Lymphocytes underwent RepSox-treatment in combination with IL-15 or the cytokine mix for 48 h. Surface receptors were detected *via* flow cytometric analysis. After gating on live, single NK cells ($CD3^-$ and $CD56^+$), NK cell activation markers across the entire population were investigated. Data are mean values of four biological replicates (n=4). A) List of analyzed NK cell surface markers. B) Obtained data underwent dimensionality reduction *via* t-SNE.

The investigation of NKp30, NKG2D, and DNAM-1 revealed that the protein levels were influenced in the same manner as observed for the other receptors, while NKp46 protein levels were inversely correlated (Figure 53).

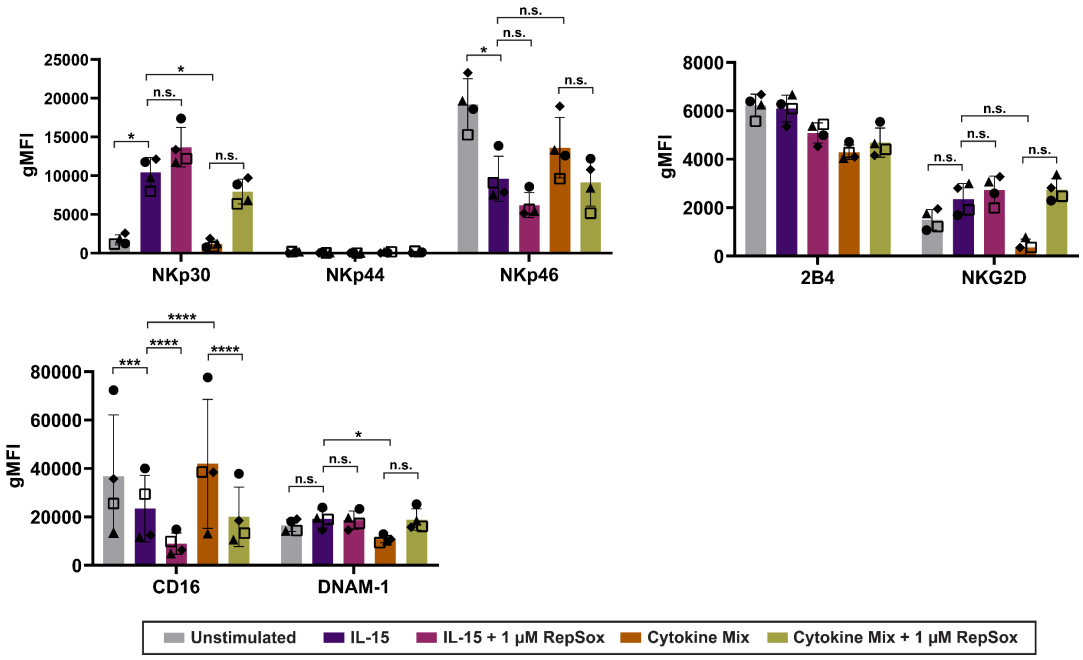

Figure 53: Effect of RepSox on NK surface receptor levels crucial for activation. Quantified protein levels of NK cell-activating surface receptors. Data are mean values ± S.D (n=4); P < 0.05; **, P < 0.01; ***, P < 0.001; ****, P < 0.0001, n.s.: not significant (two-way ANOVA).

Taken together, the RepSox affected many NK cell surface receptors crucial for their activation, adhesion, and cytotoxicity in the presence of the cytokine mix in both panels. However, the immunophenotype of RepSox-treated cells resembled the IL-15 condition, indicating that the TGFβR-1 inhibitors solely antagonized the suppressive effects of PGE_2 and TGFβ and did not influence NK cell activity individually. This observation was strengthened by the IL-15-RepSox condition, which did not show an additional effect in comparison to the IL-15-only condition. Additionally, RepSox also upregulated NK cell inhibitory receptors under the influence of the cytokine mix, which is important, as NK cell function is regulated by a balance of activating and inhibitory receptors. The concurrent increase of NK cell inhibitory receptors plays a critical role in preventing abnormal regulation of NK cell activity.

4.2 Discussion

4.2.1 Identification of small molecule enhancers of NK cell-mediated eradication of A549^{Green} cells

NK cells play a pivotal role in the body's defense against cancer development.[207] They are responsible for identifying and eradicating cancer cells through immunosurveillance[17,208]. However, the selective pressure driven by the immune system-mediated elimination of cancer cells by the immune system creates a favorable environment for the survival of cancerous cells that can evade immunosurveillance and aid the formation of the TME.[17] The TME harbors various immunosuppressive factors, including kynurenine, IL-10, TGFβ, and PGE_2, which are secreted by cancer cells and the cancer-supportive tissue, resulting in the inhibition of NK cell effector function.[42,207]

Several points support the utilization of NK cells for immunotherapies. A key reason is that NK cell therapies do not call for individual customization due to the remote likelihood of graft-versus-host disease (GVHD).[209] This facilitates the generation of an "off-the-shelf" product, resulting in reduced time and costs for the manufacturing process.[209] NK cell-based immunotherapies have shown promising results in treating hematopoietic malignancies; however, using them to target solid tumors has displayed insufficient therapeutic efficiency.[27,209] A major obstacle is the immunosuppressive nature of the TME that compromises NK cell response, ultimately resulting in an exhausted phenotype.[27,60,210] Therefore, the Waldmann group developed a phenotypic co-culture assay that mimics the inhibitory nature of the TME to identify small-molecule modulators that prevent NK cell exhaustion. The assay involves the NK cell susceptible lung adenocarcinoma cell line A549, lymphocytes, and immunomodulating factors IL-15, TGFβ, and PGE_2 to create an artificial TME.[211] While IL-15 activates NK cell effector function, TGFβ and PGE_2 abrogate its effect and reduce NK cell-mediated cytotoxicity.[44,212] In order to distinguish between cancer cells and lymphocytes, A549 cells were stably transfected with an eGFP-tagged histone H2B type 1-J construct, resulting in the generation of A549^{Green} cells. This enabled the quantification of NK cell-mediated A549^{Green} cytolysis in an automated setup and was, therefore, amenable for medium-throughput use.

Among the 29,502 compounds subjected to the medium-throughput screening, several compounds were validated for their ability to restore NK cell cytotoxicity through diverse mechanisms. Despite the successful identification of novel small molecule enhancers of NK cytotoxicity, a couple of challenges for the NK cell-mediated cancer cell cytolysis assay were recognized. In the course of the hit validation process, a false-positive hit that abrogated the eGFP

fluorescence in A549^{Green} cells was identified. Therefore, this compound did not affect viability and was not eliminated during the extensive counterscreens. Also, several inhibitors of TGFβR-1 were identified, however, PGE_2 antagonists were not found among the hits. This might be related to the requirement of dual blockade of EP2 and EP4 receptors on NK cells to counteract the suppressive effect of PGE_2 and activate their effector function.[213]

In total, 11 hit compounds were validated, and apart from the literature-reported TGFβR-1 and GSK-3β inhibitors known for enhancing NK cell cytotoxicity, a VPS34 and BRD2/3/4 PROTAC were identified, previously unassociated with NK cell cytotoxicity.

4.2.2 GSK-3β inhibitors boost the cytotoxicity of NK cells.

Two GSK3β inhibitors, namely CHIR99021 and BIO, were identified in the medium-throughput screening. CHIR99021 and BIO increased the A549^{Green} cytolysis rate under the influence of the inhibitory cytokine mix by 75 % and 53 %, respectively. The presence of both compounds elevated Gzm B protein levels, validating the cytotoxic activity of NK cells. GSK3β is a negative regulator for NK cell activating signals, and its overexpression is linked to defective metabolism and NK cell cytolytic activity abrogation.[153,214] Moreover, GSK3β inhibition has been shown to enhance NK cell maturation, cytokine production, and cytotoxicity.[154,155] In conclusion, the identification of previously reported GSK3β inhibitors in the screening assay serves as strong validation for the potential of the NK cell-mediated cancer cell cytolysis assay in identifying small molecule-enhancers of NK cell cytotoxicity.

4.2.3 VPS34 inhibitor SAR405 enhances NK cell cytotoxicity

The screening for NK cell-mediated cancer cell-cytolysis identified the VPS34 inhibitor SAR405 as a hit compound, which had not yet been reported to affect NK cell cytolytic activity. In the cytolysis assay using lymphocytes, the increase in NK cell tumoricidal activity, mediated by SAR405, was positively correlated with the compound concentration. The highest concentration significantly elevated A549^{Green} cytolysis, reaching 91.3 % cytolysis at 2.5 µM. Furthermore, the VPS34 inhibitor elevated lymphocyte IFN-γ and Gzm B protein levels. The cytotoxicity-enhancing effect and upregulation of IFN-γ secretion in presence of SAR405 were also validated using purified NK cells. Additionally, SAR405 did not inhibit TGFβ pathway signaling, as the *SBE4* promoter activity remained unchanged. There is currently no link in the literature supporting a connection between VPS34 inhibition and elevated NK cell cytotoxicity. The activity of the VPS34

kinase is crucial for initiating and progressing autophagy.[215] The immunosuppressive factor PGE_2 boosts intracellular cAMP levels, which, in turn, modulate autophagic flux.[216,217] Autophagy-induction facilitates the degradation of Gzm B, consequently reducing NK cell tumoricidal activity.[218] Therefore, suppressing autophagy through inhibition of lipid kinase VPS34 using SAR405 may restore Gzm B levels in NK cells, leading to an upregulation of NK cell cytolytic activity.

Immune checkpoint inhibitors (ICIs), including FDA-approved PD-1/PD-L1 targeting, pembrolizumab, or nivolumab, have significantly improved patient survival rates against certain malignancies (e.g., advanced melanomas or kidney cancer), revolutionizing cancer treatments.[51-53] However, immunotherapies based on ICIs demonstrate greater efficacy in the treatment of "hot" tumors (i.e., pro-inflammatory signature and highly infiltrated infiltration) but do not confer a benefit in the treatment of "cold" tumors (i.e., low inflammation and infiltration).[219,220] A study conducted by Noman *et al*. explored the effect of VPS34 inhibitors, including SAR405, on the TME. VPS34 inhibition potentiated the efficacy of ICIs by transitioning cold" tumors to "hot" ones by reprogramming the TME and immune cell landscape.[221] The findings underscore the relevance of pharmacological inhibition of VPS34 for cancer immunotherapies.

4.2.4 PROTAC MZ-1 enhances NK cell cytotoxicity

The BRD2/3/4 MZ-1 was an additional hit that was not previously linked to augmented NK cell cytolysis efficiency. MZ-1 boosted NK cell cytotoxic response in the lymphocyte co-culture to the aligned with the IL-15 control at 1 µM, which was confirmed by the enhanced IFN-γ secretion levels in presence of the PROTAC. However, the levels of the apoptosis-inducing protein GzmB did not change regardless of MZ-1 treatment. Furthermore, the impact of MZ-1 on NK cell cytotoxicity was corroborated using purified NK cells. The increased cytolytic activity, as well as the IFN-γ of purified NK cells, reached the level of the IL-15 control. Moreover, MZ-1 was subjected to the *SBE4*-dependent RGA. While the activity of Renilla was found to be positively correlated with increasing concentrations of MZ-1, it did not inhibit *SBE4* promoter activity and, thus, TGFβ pathway signaling.

Furthermore, it was ruled out that the NK cell effector function promoting the activity of MZ-1 can be attributed to (+)-JQ1 or the VHL ligand derivative. Chen *et al*. have demonstrated that distinct cellular responses emerged when BRD4 was inhibited by small molecules, depleted using RNA interference, or degraded using PROTACs.[222] The inhibition of BRD4 was cytostatic, whereas

PROTAC-induced degradation was cytotoxic. The authors uncovered that the degradation via PROTACs results in the formation of neo-tetrapeptides that are capable of deactivating Inhibitors of Apoptosis (IAP) proteins, consequently leading to elevated caspase activation and triggering apoptosis-driven cell death. Active IAP signaling confers protection to target cells from NK cell tumoricidal activity, in turn, opposing IAP signaling using MZ-1 may increase $A549^{Green}$ susceptibility towards NK cell-driven cytotoxicity.[222,223] Other BET inhibitors (BETi) investigated in the screening, including BAY-299 and OTX015, displayed an insufficient window between the NK cell cytolysis EC_{50} and the viability IC_{50} of $A549^{Green}$ cells, and were therefore excluded from further analysis.

The anti-cancer effects of BET inhibition have been well-established in previous studies.[224,225] In addition to that, BETis, including (+)-JQ1 and I-BET151, modulate NK cell effector function by increasing the expression of MICA on cancer cells.[226] A recent study by Reggiani *et al*. found that BRD2/3/4 inhibitors (+)-JQ1 and OTX015 enhance NK cell tumoricidal activity through downregulation of NK inhibitory receptors (e.g., LAG3 and TIGIT) and immune checkpoints (PD-1/PD-L1 and CTLA4).[227] They showed that BRD4 controls the expression of SMAD3 in NK cells, which is pivotal for TGFβ signaling-mediated immune cell suppression.[227,228] Furthermore, the authors demonstrated that abrogation of SMAD3/BRD4 activity promotes NK cell effector functions, which may be an attractive strategy for reinvigorating NK cell-mediated cancer cell cytolysis within the TME.

4.2.5 TGFβR-1 inhibitors boost NK cell cytotoxicity

The TGF-β signaling pathway is essential for regulating a wide range of cellular processes, including differentiation, proliferation, apoptosis, and immune responses. Dysregulation of this pathway has been observed in several types of cancer and has a potent immunosuppressive on cytotoxic T cells and NK cells, and thereby evokes cancer immune evasion.[43,44,229] Several TGFβR-1 inhibitors were identified for their NK cell cytotoxicity-promoting activity through the screen, and a set of compounds: RepSox, SB-525334, SB-505124, GW788388, galunisertib, and LY2109761 were assayed across various automated and manual assays, the acquired data were concisely summarized (Figure 54).

A

Compound	NK cell cytolysis screening assay EC_{50} [µM]	*SBE4*-dependent reporter gene assay IC_{50} [nM]
RepSox	0.18 ± 0.03	8.5 ± 0.5
SB-525334	0.33 ± 0.02	31.4 ± 9.3
SB-505124	0.47 ± 0.13	57.2 ± 16.3
GW788388	1.19 ± 0.39	77.5 ± 28.1
Galunisertib	2.07 ± 0.46	114.0 ± 31.4
LY2109761	>3.4	861.0 ± 173.4

B

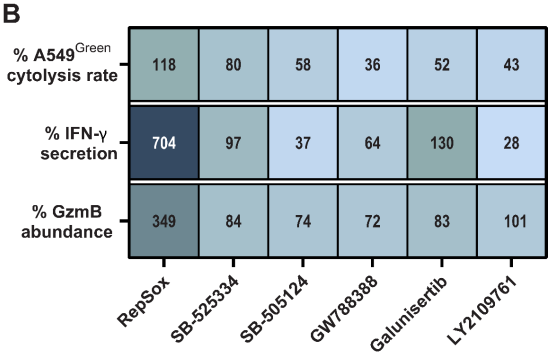

Figure 54: Comprehensive overview of the effectiveness of TGFβR-1 inhibitors in enhancing NK cell cytotoxicity. A) Comparison of the cytolytic activity of TGFβR-1 inhibitors in the automated NK cell-mediated cytolysis screening assay and the suppressive activity in the *SBE4*-dependent reporter gene assay. B) Heatmap representation of the potency of TGFβR-1 inhibitors in the NK cell-mediated cytolysis assay and their influence on IFN-γ secretion and GzmB protein levels.

Indeed, there is a proportional relationship between the potency of inhibiting the TGFβ signaling activity and enhancing NK cell cytotoxic activity for the hit compounds (Figure 54A). RepSox was the most potent modulator of NK cell tumoricidal activity, followed by SB-525334, SB-505124, GW788388, galunisertib, and LY2109761. Subsequently, data from the manual NK cell-mediated cancer cell cytolysis and the Gzm B protein and IFN-γ secretion level validation assays were compared (Figure 54B). The $A549^{Green}$ cytolysis rate parallels the trend of the screening assay. While there were weak correlations between Gzm B abundance and NK cell-mediated cancer cell cytolysis, no evident trend for IFN-γ secretion was observed.

Interestingly, previous literature has reported the potency of SB-525334 in counteracting the resistance mediated by fatty acid synthase to NK cell tumoricidal activity in cisplatin-resistant lung cancer cells through modulation of PD-L1 abundance.[230] Furthermore, galunisertib enhanced the effectiveness of NK cell-mediated neuroblastoma elimination when used in combination with the ADCC-inducing antibody dinutuximab.[231] Generally, TGFβ inhibition has been a promising approach to overcoming immunosuppression of NK cells.[232-234]

In summary, RepSox distinguished itself from the other identified TGFβR-1 hits for its augmenting influence on NK cell tumoricidal activity and surpassed the level of IL-15 in lymphocytes, displaying an $A549^{Green}$ cytolysis rate of 118 %, IFN-γ secretion, and Gzm B amount increase of 704 % and 349 %, respectively.

4.2.6 RepSox as powerful promoter of NK cell cytotoxicity

RepSox has a substantial potency in activating NK cell cytotoxicity, a thorough investigation into the compound's mechanism of action was performed to identify its mechanism of action. All of the investigated TGFβR-1 inhibitors have a common chemotype and share several off-targets, including MINK1, p38α, RIPK2, and VEGFR.[167-170] Therefore, the highly selective TGFβR-1 inhibitor TP-008 was evaluated in NK cell-mediated cancer cell cytolysis and the IFN-γ secretion and Gzm B validation assays. TP-008 only partially restored NK cell cytotoxicity, displaying an $A549^{Green}$ cytolysis rate of 36 % at 20 µM, implying that it exclusively inhibited TGFβ signaling. Following this, the effects of RepSox and TP-008 on the individual immunosuppressive factors, i.e. TGFβ and PGE_2, were compared in lymphocytes. RepSox significantly diminished the effect of both inhibitory factors, whereas TP-008 only antagonized the effect of TGFβ, which is in line with its activity in the cytolysis assay. A notable observation was that the IL-15-TGFβ condition treated with TP-008 showed an $A549^{Green}$ cytolysis rate restoration of 100 %. While the addition of RepSox to the same condition resulted in an elevation of 148 % in the $A549^{Green}$ cytolysis rate in lymphocytes and 144 % in purified NKs. The pronounced impact of RepSox on the cancer cytolysis rate in presence of TGFβ, along with its antagonizing effect on PGE_2, indicated the possible existence of a second molecular target that enhances RepSox potency on NK cell cytolytic activity. Interestingly, previous research evaluating the biological activity of TGFβR-1 inhibitors continually indicated that RepSox activity can not be exclusively attributed to TGFβR-1 inhibition.[178,235,236]

Based on previously published literature and the findings of this thesis, different signaling pathways linked to NK cell cytotoxicity were explored as potential second molecular targets that, alongside TGFβR-1 inhibition, potentiated RepSox influence on NK cell cytotoxicity.

I. RepSox off-target kinases as potential secondary on-target for NK cytotoxicity

The two kinase family members, VEGFR and MINK1, were identified by previous studies as potential off-targets of RepSox. Both kinases have an established link to NK cell cytotoxicity.[174,176] Therefore, the triple VEGFR-1/2/3 inhibitor, nintedanib, and MINK 1 inhibitor DMX-5804 were combined with TP-008 to assess whether RepSox's potential to enhance NK cell cytotoxicity can be replicated. For inhibition of both targets, no meaningful increase in NK cell cytotoxicity or IFN-γ secretion was observed compared to the TP-008 control. These observations may be due to the fact that the study demonstrating VEGFR-3 inhibition recovered NK cell tumoricidal activity was performed using mouse-derived NK cells.[174] MINK1 modulates the activation of SMAD2.[176]

The MINK1 inhibitor, DMX-5804, may be inactive because TP-008 itself is a nanomolar TGFβ signaling inhibitor that suppresses SMAD cascade activation.

II. Characterization of RepSox as a Notch signaling modulator

A study by Zhang *et al*. showed that RepSox upregulated Notch signaling and elevated Notch1 and NICD protein levels.[178] Additionally, previous studies have highlighted the importance of Noch signaling for proper NK function, and NK cells of cancer patients often have defective Notch signaling.[179-181,237]

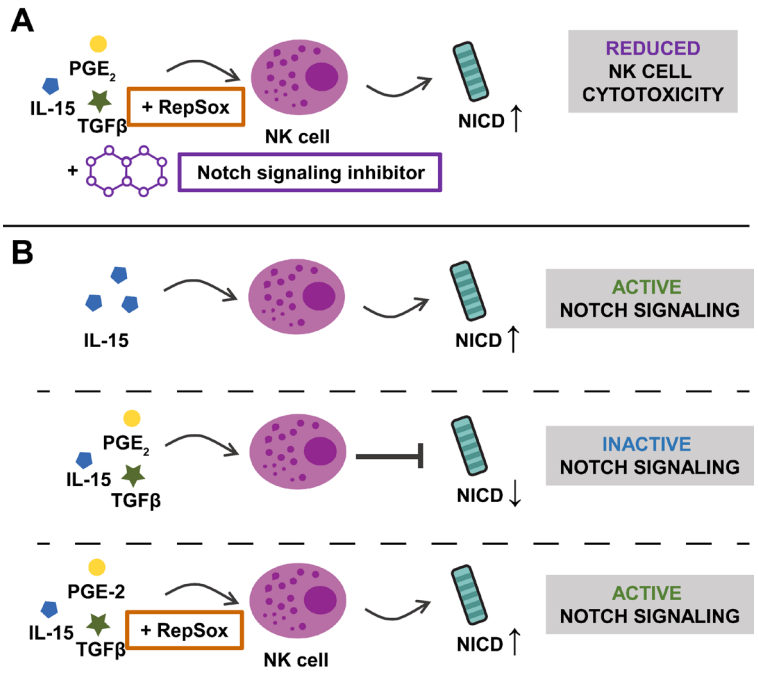

Figure 55: Schematic summary of RepSox impact on Notch signaling. A) Investigation of the effect of Notch signaling inhibitors on NK cell cytotoxicity under the influence of RepSox and the cytokine mix (=IL-15, TGFβ, and PGE_2). B) Influence of NK cell-mediated cancer cell conditions IL-15, cytokine mix, and RepSox on Notch signaling. *Figure is based on the results obtained in this thesis.*

Therefore, the influence of Notch signaling modulation was explored in the NK cell-mediated cancer cell cytolysis assay. For this purpose, RepSox was tested in combination with Notch signaling inhibitors IMR-1 and DAPT (Figure 55A). RepSox-IMR-1 co-treatments in presence of the cytokine mix displayed a significant reduction of the $A549^{Green}$ cytolysis rate. Aligned with these observations are the reduced Gzm B and IFN-γ secretion levels. A substantial reduction of NK cell cytotoxicity is also observed for RepSox-DAPT co-treatments, exhibiting a similar trend for the protein abundance of Gzm B and IFN-γ secretion. Taken together, these results established that Notch signaling is relevant for NK cell cytotoxicity in the cytolysis assay setup.

Subsequently, the influence of RepSox on Notch signaling was investigated *via* analysis of NTM and NICD protein abundance (Figure 55B). IL-15 upregulated the NICD content, however, the introduction of RepSox to IL-15 did not change NICD levels. The presence of the cytokine mix led to the downregulation of NICD protein levels, while the RepSox-cytokine condition recovered the abundance. To investigate whether the restored NICD level depended on TGFβ signaling, TP-008 was investigated. The specific TGFβR-1 inhibitor did not influence NICD levels. Furthermore, the NTM levels were not altered in any of the tested conditions. Overall, these results demonstrate that RepSox did not modulate Notch signaling but antagonized the effect of the cytokine mix. As the NICD restoration was not observed for TP-008 treatment, the idea of a second relevant target for RepSox was further supported.

III. Identification of RepSox as a modulator of the PGE_2/EP2/4 signaling axis

Given that RepSox was able to counteract not only the immunosuppressive effect of TGFβ, but also that of PGE_2, its influence on the PGE_2/EP2/4 signaling axis was studied. The immunosuppressive lipid molecule PGE_2 can be generated from COX-1 and COX-2-derived precursors.[45,238] PGE_2 can bind to G protein-coupled receptors EP2 and EP4 on NK cells, stimulating adenylate cyclase activity that, in turn, downregulates NK cell activating receptors and thus impair NK cell function.[45,47]

First, the impact of RepSox on EP2 and EP4 protein levels was investigated. However, no significant changes in EP2/4 levels were observed following RepSox treatment. Subsequently, the influence of the compound on cellular prostanoid and thromboxane levels in A549 cells was explored. A549 cells generated PGE_2, $PGF_{2\alpha}$, and TXA_2/TXB_2, whereas PGD_2 and PGI_2 were not inducible. Previous studies have thoroughly examined the suppressive role of PGE_2 on NK cell function. In contrast, the effect of $PGF_{2\alpha}$ and TXA_2/TXB_2 on NK cells remains unclear. However, existing literature suggests that both TXA_2/TXB_2 and $PGF_{2\alpha}$ promote tumor progression.[239] Treatment with 1 µM of RepSox reduced PGE_2, PGF2α, and TXA2/TXB2 levels to 70.2 %, 20.7 %, and 63.8 %, respectively. A higher concentration of 5 µM resulted in a 53.6 % reduction in PGE_2, a 40.0 % reduction in $PGF_{2\alpha}$, and a 35.8 % decrease in the level of TXA_2/TXB_2. Additionally, the introduction of AA recovered the levels of the analyzed prostaglandins and thromboxane. Collectively, these results indicate that RepSox may directly modulate COX-1/-2 in a reversible manner. Accordingly, RepSox activity on both cyclooxygenases was tested. An in-cell CETSA in BxPC-3 cells using 50 µM RepSox showed no shift in the melting temperature of COX-2. Therefore, a biochemical assay on RepSox was conducted to explore its impact on COX-1/2 activity. RepSox effectively inhibits COX-1 activity, with an inhibition of 61% at 20 µM. A

study by N. Kundu *et al*. indicated that suppressing COX-1/-2 leads to decreased MHC I expression in tumor cells, enhancing susceptibility to NK cell cytotoxicity.[240] Hence, the potency of RepSox may be associated with its ability to antagonize MHC I-mediated NK cell suppression and simultaneous inhibition of TGFβ signaling.

4.2.6.3 In-depth analysis of RepSox-mediated NK cell functions

Unlike cytotoxic T cells, natural killer (NK) cells can eliminate their target cells without prior sensitization. Nonetheless, the activation of NK cells is tightly regulated by a balance between activating and inhibitory receptors expressed on their surface.[241,242] To understand the mechanism of RepSox-mediated NK cell activation on a molecular level, the protein levels of various NK cell receptors attributed to their activation, adhesion, characterization, cytotoxicity, and inhibition were analyzed using two panels. The first panel focused on all NK cell functions, whereas the second panel was exclusively focused on NK cell activating receptors. For both panels, the immunophenotype of the activating conditions, i.e., IL-15, IL-15, and RepSox, as well as cytokine mix and RepSox, exhibited a considerable resemblance. Additionally, the immunophenotype of the NK cell inhibitory conditions US and cytokine mix also showed strong alignments. These findings parallel the cytotoxic activity of the NK cells that was observed in the NK cell-mediated cancer cell cytolysis assay. Furthermore, a cluster distribution analysis revealed that the inactive or suppressed immunophenotype NK cells were mainly in one cluster, whereas the active immunophenotype NK cells were distributed across the remaining clusters. Next, the protein levels of the individual surface receptors were analyzed. The introduction of IL-15 increased the levels of activating and cytotoxicity receptors such as 41BB, HLA-DR, NKp30, NKG2D, TRAIL, and FasL compared to the US condition. On the other hand, the addition of the cytokine mix reduced these receptors, which is in agreement with previous studies showing that the inhibitory factors can TGFβ and PGE_2 can reduce HLA-DR, TRAIL, NKG2D, and NKp30.[42,49,243-245] Moreover, the RepSox treatment restored the levels of surface receptors for activation and cytotoxicity to the levels observed with IL-15 treatment. Notably, an inverse trend was observed for CD16 protein levels. IL-15 significantly downregulated CD16, and the introduction of RepSox further decreased its levels. However, the cytokine mix restored CD16 levels to the level of the US condition, and the addition of RepSox reduced the levels of the surface receptor. The activating surface receptor CD16 is crucial for antibody-dependent cell-mediated cytotoxicity (ADCC) and according to literature reports, activated NK cells attenuate CD16 through the metalloprotease ADAM17.[246,247] The receptors CD11a and CD18 are crucial for NK cell

adhesion, facilitating interaction with target and immune cells.[201] For both adhesion molecules, upregulation was observed under activating conditions, while downregulation occurred under inactive and suppressive conditions. These findings are in agreement with the role of adhesion molecules, enabling them to interact with target cells, which is especially pivotal in an active state. The inhibitory receptors TIM3, CD161, and TIGIT showed a comparable trend in protein levels under the same conditions. As NK cell function is regulated by a balance of activating and inhibitory receptors, the simultaneous upregulation of NK cell inhibitory receptors may be crucial to avoid aberrant regulation of NK cell activity. The introduction of RepSox to IL-15 did not contribute further to the content of NK cell surface receptors. Therefore, the RepSox effect can be reduced to its TGFβ and PGE_2 signaling modulation.

4.3 Conclusion and future perspectives

A bottleneck in NK cell-based immunotherapies is the maintenance of the viability and cytotoxicity of NKs upon reaching the TME. Therefore, the discovery of small-molecule enhancers of NK cell tumoricidal activity is in high demand. The Waldmann group successfully developed a novel TME-mimicking phenotypic co-culture assay monitoring NK cell activity in a time-resolved manner. A direct co-culture was utilized without separate incubations of the cellular components or additives. Assay miniaturization facilitated the performance of a medium-throughput screening to identify novel small molecules enhancing NK cell performance. Several hit compounds, including GSK-3β, TGFβR-1, and unannotated compounds VPS34 for NK cell cytotoxicity and BRD2/3/4 PROTAC were identified through this screening.

Among the hit compounds, the activity of TGFβR-1 inhibitor RepSox was particularly noteworthy. Not only did the compound relieve the effect of TGFβ, but also PGE_2. Based on literature research, the RepSox potential molecular target was investigated. Finally, its ability to relieve the effect of both inhibitory factors was attributed to the simultaneous inhibition of COX-1. RepSox's dual on-target activities highlight the benefits of polypharmacology, which challenges the one-drug-on-target paradigm. In contrast to RepSox, the specific TGFβR-1 inhibitor, TP-008, only partially restored NK cell activity.

In summary, the NK cell-mediated cancer cell cytolysis assay represents an innovative strategy for the discovery of small molecules that elevate NK cell cytotoxicity in the presence of immune-suppressive factors present in the TME. This approach may contribute to the elucidation of the inhibitory networks inherent within the TME and concurrently offers the potential to discover new targets that are relevant for NK cell-based immunotherapies that improve their activation, tumoricidal activity, and persistence at the tumor site.

5. TARGETING PDEδ USING THE COVALENT DELTASONAMIDE DERIVATIVE DELTACOVALIN

5.1 Results

5.1.1 Target engagement study of the Deltacovalin-PDEδ interaction

The Waldmann group has successfully developed multiple generations of PDEδ inhibitors that directly bind to the prenyl-binding pocket, thereby impeding its interaction with KRas.[102-104] The first two generations, Deltarasin and Deltazinone, exhibited low nanomolar binding activity to PDEδ *in vitro*. However, micromolar concentrations were required to enhance the growth of KRas-dependent cell lines. This gap between the *in vitro* and *in cellulo* activity is likely attributed to the rapid release of inhibitors from the prenyl-binding pocket of PDEδ, a process facilitated by Arl2/3 proteins. Therefore, a generation PDEδ inhibitors were designed, the Deltasonamides. Despite its picomolar affinity and formation of up to seven hydrogen bonds with PDEδ, the release of Deltasonamide 1 from the prenyl-binding pocket *via* Arl2/3 poses a great challenge. To avoid the Arl2/3-mediated release of PDEδ inhibitors, a covalent inhibitor named Deltacovalin based on the Deltasonamide 1 structure was designed and optimized by Dr. Pablo Martin-Gago (Waldmann lab) (Figure 56).

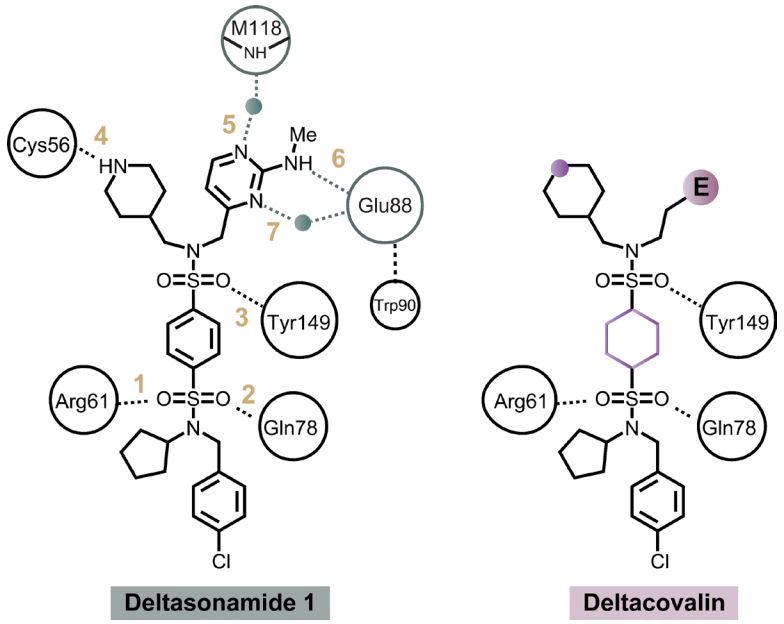

Figure 56: Covalent PDEδ inhibitor Deltacovalin is derived from Deltasonamide 1. Deltasonamide 1-PDEδ interactions are stabilized by seven hydrogen bonds with Cys56, Arg61, Gln78, Glu88, Met118, and Tyr149. The structure of covalent PDEδi Deltacovalin is based on Deltasonamide 1. E: electrophilic group.

Previous results by Dr. Pablo Martin-Gago detecting compound stability *via* LC-MS showed that Deltacovalin is more than 99 % stable for 24 h in HEPES buffer at 37 °C. Furthermore, the covalent complex formation of the inhibitor was confirmed using a MALDI-based tethering assay, demonstrating that 6 % of PDEδ was in complex with Deltacovalin after 2 h, 20 % after 6 h, and 90 % after 20 h.

First indications for the covalent bond of Deltacovalin to PDEδ were obtained using a mass spectrometry-based orthogonal setup (Figure 57). For this, PDEδ was incubated with Deltacovalin or DMSO for 48 h, followed by denaturation, reduction, alkylation, and digestion using GluC. Analysis of the resulting peptides via LC-MS/MS revealed that the digested PDEδ peptide responsible for the covalent bond was modified, as evidenced by the reduced levels of unmodified peptide under Deltacovalin treatment compared to DMSO. At the same time, there was an increase in modified peptide, confirming covalent bond formation of Deltacovalin to PDEδ.

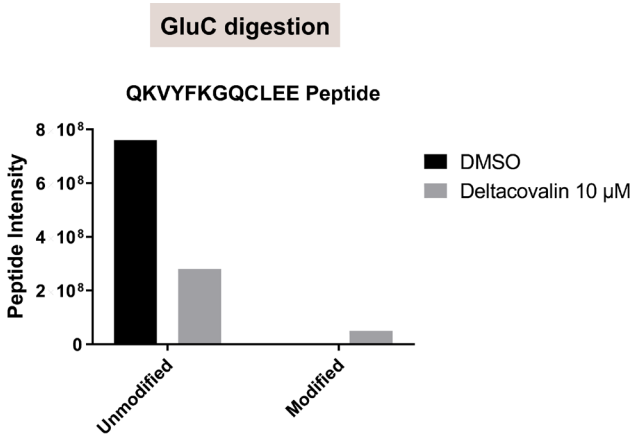

Figure 57: Deltacovalin covalently binds to PDEδ. Purified PDEδ was incubated with 10 µM Deltacovalin or DMSO for 48 h, prior to digestion using GluC and analysis of the resulting peptides. Representative for n=1.

A co-crystal structure of the PDEδ-Deltacovalin complex was solved in collaboration with Dr. Raphael Gasper (head of the in-house crystallography and biophysics facility), validating the covalent bond formation between PDEδ and the covalent inhibitor (Figure 58). The co-crystal structure revealed that Deltacovalin binds in the prenyl-binding pocket of PDEδ through hydrogen bonds with Cys56, Arg61, Gln78, Gln116, Met118, and Tyr149.

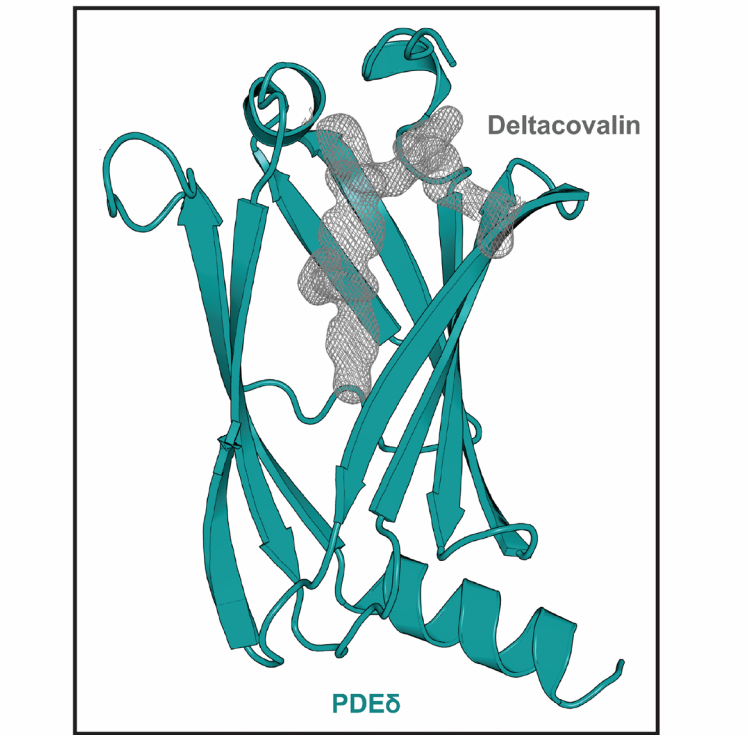

Figure 58: Co-crystal structure of Deltacovalin bound to human PDEδ. Deltacovalin binds to PDEδ's prenyl-binding pocket, and its interaction with the protein is stabilized *via* hydrogen bonds with Cys56, Arg61, Gln78, Gln116, Met118, and Tyr149. The electron density (2Fo-Fc) of Deltacovalin and PDEδ's covalently modified amino acid residue is countered in grey at 1.0 σ.

A fluorescence polarization assay was performed to investigate the potential displacement of Deltacovalin from the binding pocket of PDEδ by Arl2 (Figure 59). For this, PDEδ protein was combined with compound and a fluorescein-labeled atorvastatin probe that binds to PDEδ in the presence or absence of Arl2·GppNHp.

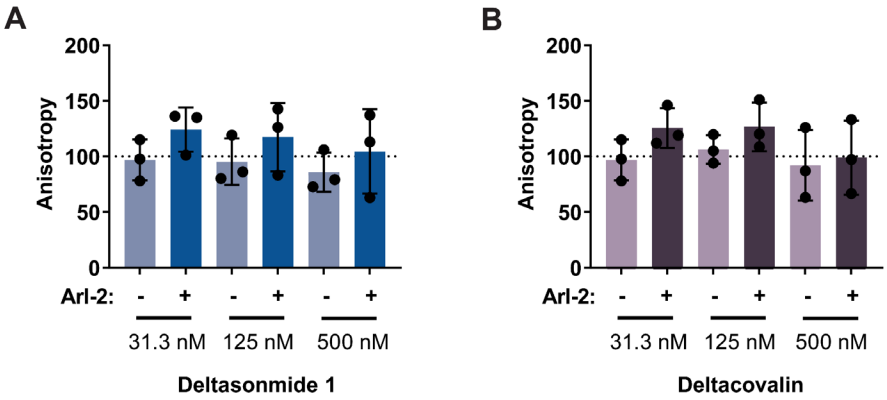

Figure 59: Analysis of Arl2-mediated release of PDEδ inhibitors. Arl2 mediated ligand release was assessed utilizing a fluorescence polarization (FP) assay. PDEδ was incubated with a fluorescein-labeled atorvastatin probe and compound in presence or absence of Arl2·GppNHp. Data are mean values ± SD (n=3). *Results by Dr. Ruirui Zhang*.

The introduction of Arl2·GppNHp to the samples containing the non-covalent control Deltasonamide 1 increased anisotropy at all investigated concentrations, indicating the Arl2-mediated release of the compound from the PDEδ binding pocket (Figure 59A). This trend was also observed for 31.3 and 125 nM Deltacovalin, whereas the anisotropy at 500 nM remained unchanged, indicating that this concentration was sufficient to bypass Arl2-mediated compound release (Figure 59B).

To analyze the impact of Deltacovalin on the thermal stability of human PDEδ and to confirm its engagement with PDEδ in a cellular context, in-cell and lysate-based CETSA were performed (Figure 59). The compound and heat-treatment steps for in-cell CETSA were performed within intact Jurkat cells, while these steps were performed in cell lysates for lysate-based CETSAs. The addition of 10 µM Deltacovalin to intact cells resulted in a profound increase in the mean melting temperature of 16.6 °C (Figure 59A). A substantial shift of the mean melting temperature of 6.5 °C of the PDEδ protein was also observed in the lysate-based CETSA using Deltacovalin-treated Jurkat cell lysates (Figure 59B).

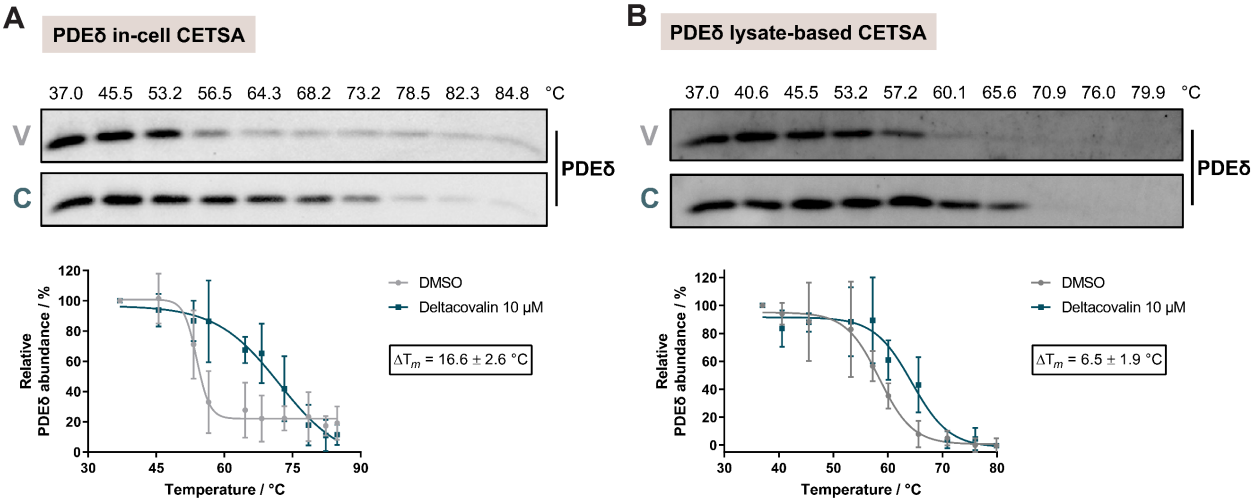

Figure 59: Deltacovalin increases the melting temperature of PDEδ. A) PDEδ In-cell CETSA. Jurkat cells were treated with 10 µM Deltacovalin (C) or DMSO (V) for 2 h. Subsequently, a thermal shift assay was performed, cells were lysed, and the soluble fraction was analyzed by means of immunoblotting using a PDEδ antibody (mean ± SD, n=3). B) Lysate-based CETSA for PDEδ. Jurkat cell lysate was treated with 10 µM Deltacovalin (C) or DMSO (V) for 10 min at room temperature before performing a thermal shift assay. The soluble protein fraction was analyzed *via* immunoblotting using a PDEδ antibody (mean ± SD, n=3).

5.1.2 Cell growth inhibition of Deltacovalin-mediated PDEδ inhibition

5.1.2.1 Mammalian cell lines

To explore the growth inhibitory potential of Deltacovalin, various cell lines with different KRas dependencies and mutational statuses were selected based on previous research.[248-253] The dependency on KRas is determined empirically, with different cell lines showing varying degrees of dependence on KRas activity for their growth as indicated by viability experiments following KRas depletion *via* knockdown.[248-253] The cell line selection focused on pancreatic ductal adenocarcinoma (PDAC), colorectal adenocarcinoma (CRC), and lung adenocarcinoma (LAC) due to the high prevalence of KRas mutations. Specifically, KRas is mutated in 86 % of PDAC, 41 % of CRC, and 32 % of LAC.[78] The selected panel of KRas dependent and independent cell lines are summarized in Table 7.

Table 7: List of investigated cell lines and their reported KRas dependencies. PDAC: pancreatic ductal adenocarcinoma, CRC: colorectal adenocarcinoma, and LAC: lung adenocarcinoma. $BRAF^{V600E}$ mutations are oncogenic and downstream of the Ras-ERK signaling cascade.

Cell line	Mutational status	# of mutant alleles	KRas dependency[248-253]	Tissue
PA-TU-8902	G12V	1	Dependent	PDAC
MIAPaCa-2	G12C	2	Dependent	
PANC-1	G12D	1	Independent	
BxPC-3	wt	-	wt / Independent	
SW480	G12V	2	Dependent	CRC
HCT116	G13D	1	Independent	
LS-174T	G12D	1	Independent	
HT-29	wt	-	wt / BRAF V600E	
NCI-H358	G12C	1	Dependent	LAC
NCI-H441	G12V	1	Dependent	
SK-LU-1	G12D	1	Independent	
A549	G12S	2	Independent	

Initially, the covalent inhibitor Deltacovalin underwent kinetic real-time live-cell imaging-based analysis to evaluate its impact on the growth of PDAC cell lines using KRas-dependent PA-TU-8902 cells (harboring G12V mutation in KRas) and KRas-independent BxPC-3 cells (with wt KRas). The non-covalent PDEδ inhibitor Deltasonamide 1, which is also the parental compound of Deltacovalin, was included as a control.

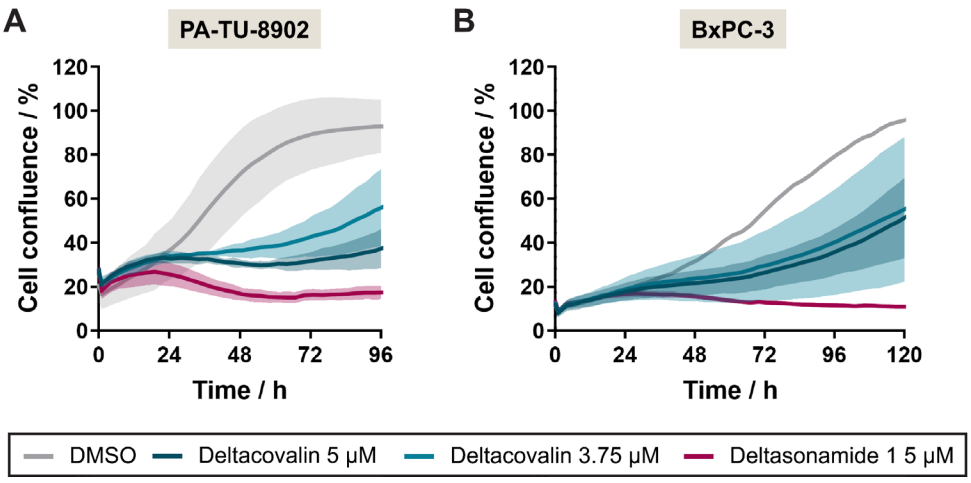

Figure 60: Covalent PDEδ inhibitor Deltacovalin influences PDAC cell line growth. PA-TU-8902 (A) and BxP-3 cells (B) were treated with Deltacoavalin (3.75 µM and 5 µM) and Deltasonamide 1 (5 µM). The cell growth was then monitored using kinetic real-time live-cell imaging-based analysis. Data are representative for n=3 (mean values ± S.D (N=3). *Results by Dr. Elena Reckzeh*.

Continuous treatment of PDAC PA-TU-8902 cells using 5 µM or 3.75 µM Deltacovalin resulted in suppression of cell growth, whereas 5 µM Deltasonamide reduced cell confluence (Figure 60A). The cell growth of BxPC-3 under the influence of 3.75 µM and 5 µM Deltacovalin 1 initially stagnated for up to 48 to 72 h and then continued to grow, whereas the addition of 5 µM Deltasonamide 1 reduced cell confluence (Figure 60B).

The PDEδ inhibitors behave similarly in both cell lines, and no benefit of covalent inhibition could be observed. Moreover, previous results indicated that compound concentrations above 5 µM showed toxic effects on both cell lines. Therefore, wash-out experiments were conducted to minimize off-target effects on cell growth by using short compound treatment times followed by a compound wash-out. This also allowed to to obtain initial insights into whether Deltacovalin's interaction with PDEδ is covalent and/or irreversible *in cellulo* and to evaluate the duration of the inhibition. For this, the PDAC cells were exposed to the PDEδ inhibitors for 4, 5, and 6 h.

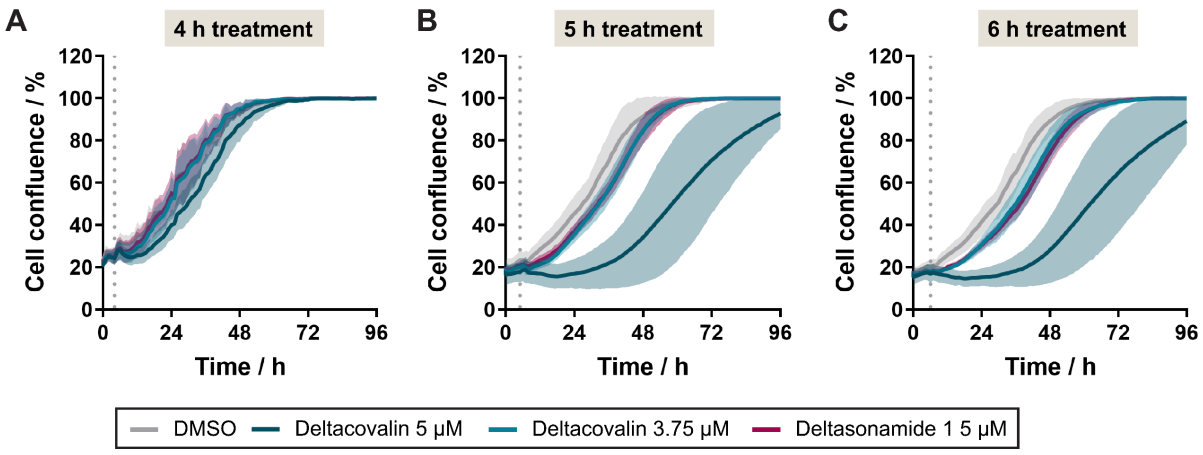

Figure 61: Covalent PDEδ inhibitor Deltacovalin influences PA-TU-8902 cell growth. KRas-dependent PA-TU-8902 cells were treated with Deltacoavalin (3.75 µM and 5 µM) and Deltasonamide 1 (5 µM) and the PDEδ inhibitors washed out after 4 h, 5 h, and 6 h. The cell growth was then monitored for a total of 96 h using kinetic real-time live-cell imaging-based analysis. Wash-out is indicated *via* a dotted line in graphs (⋯). Data are mean values ± S.D (n=3)

A washout performed after 4 h showed no significant impact on PA-TU-8902 confluency (Figure 61A). However, treatment with 5 µM Deltacovalin for 5 or 6 h led to a substantial shift in the growth curve, delaying the attainment of 100 % confluence (Figure 61B and C). The lower concentration of 3.75 µM did not influence the confluence of the cells. Moreover, this effect was not observed for 5 µM Deltasonamide, indicating that Deltacovalin binds covalently to PDEδ in cells after 5 h of treatment.

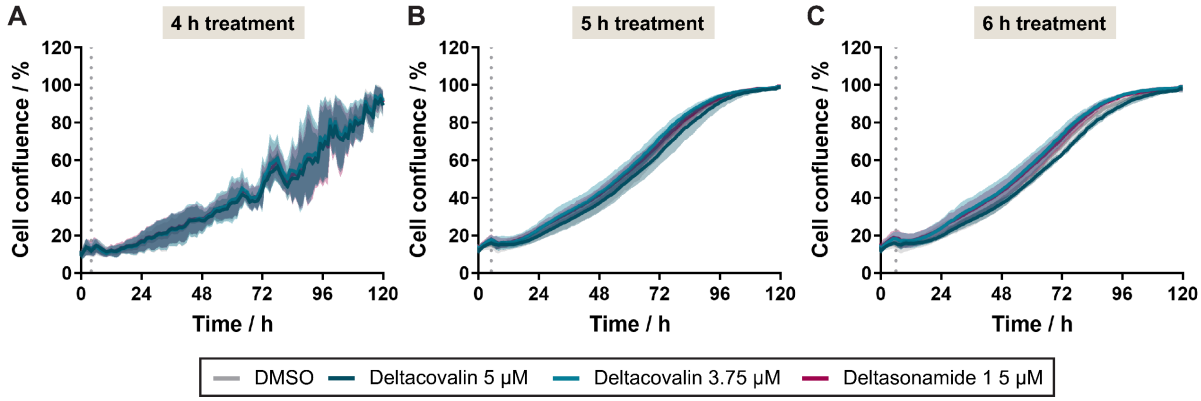

Figure 62: PDEδ inhibitor Deltacovalin does not impact BxPC-3 cell growth. KRas-independent BxPC-3 cells were treated with Deltacoavalin (3.75 µM and 5 µM) and Deltasonamide 1 (5 µM) prior to performance of a wash-out after 4 h (A), 5 h (B), and 6 h (C). Wash-out is indicated *via* a dotted line in graphs (⋯). BxPC-3 cell growth was monitored for a total of 120 h using kinetic real-time live-cell imaging-based analysis. Data are mean values ± S.D (n=3).

Next, the impact of Deltacovalin on the KRas-independent PDAC cell line BxPC-3 (harboring wt KRas) was assessed (Figure 62). The wash-out after 4, 5, and 6 h demonstrated that neither Deltacovalin nor non-covalent inhibitor Deltasonamide 1 influenced the growth of BxPC-3 (Figure 62A-C). The cell confluence of the compound-treated conditions paralleled the DMSO control.

In summary, continuous treatment experiments showed that the covalent inhibitor affected both cell lines similarly. However, the KRas-dependent cell line PA-TU-8902 showed sensitivity to 5 µM Deltacovalin after treatment for 5 h followed by a wash-out, whereas no effect was observed on the KRas-independent cell line BxPC-3. The wash-out experiment also indicated that covalent PDEδ inhibition was effective in PA-TU-8902 cells compared to non-covalent Deltasonamide 1, suggesting it might not be affected by Arl2/3-mediated release in *cellulo*. Based on the results of the wash-out experiments, a sequential treatment experiment was optimized to investigate the effect of Deltacovalin on cell growth without interference from off-target effects. For this purpose, various cell lines with different KRas mutational statuses and dependencies were investigated. During the sequential treatments, cells were treated with Deltacovalin or non-covalent Deltasonamide 1 for 5 h, followed by a wash-out, i.e., a ‘‘compound holiday,’’ and repeated compound treatment-wash-out cycles.

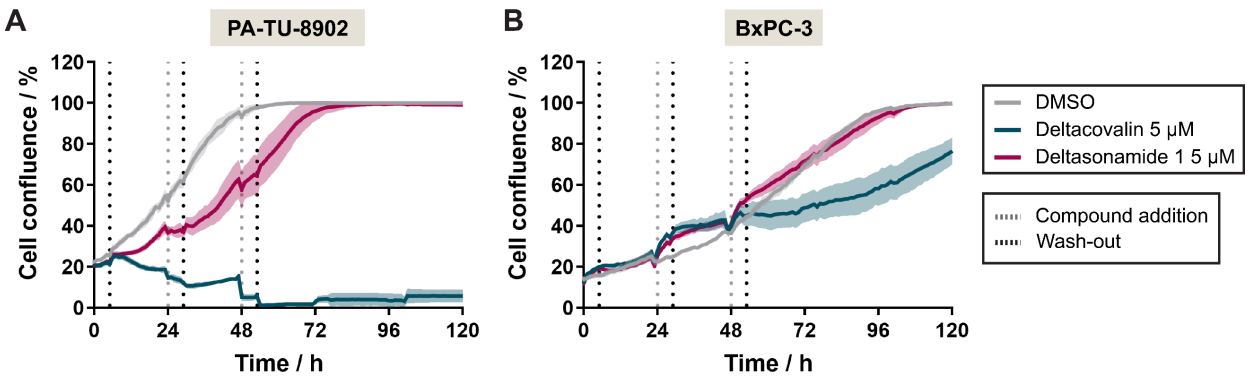

Figure 63: Sequential treatment of PDAC cells using Deltacovalin. PA-TU-8902 (A) and BxPC-3 (B) were treated for 5 h with 5 µM of the covalent PDEδ inhibitor Deltacovalin or the non-covalent control Deltasonamide 1, followed by a wash-out, and a retreatment every 24 h for a total of three treatments. The cell confluence was monitored for a total of 120 h using kinetic real-time live-cell imaging. Data are mean values ± S.D (n=3).

In a sequential treatment experiment, PA-TU-8902 and BxPC-3 cells underwent treatment with either 5 µM Deltacovalin or Deltasonamide for 5 h, followed by a wash-out. This treatment was repeated every 24 h for a total of three rounds of treatment (Figure 63). PA-TU-8902 cells exhibited growth reduction with every administered Deltacovalin treatment, while the third treatment completely eradicated the remaining cells (Figure 63A). Deltasonamide 1 also

demonstrated a minor impact on cell growth following each treatment. However, in presence of the non-covalent inhibitor Deltasonamide PA-TU-8902 cells reached full confluence over the monitored incubation time. The first two treatments of 5 µM Deltacovalin did not affect the BxPC-3 cell confluence, whereas the third treatment showed subtle alteration of the cell growth (Figure 63B). The introduction of Deltasonamide 1 did change the growth behavior.

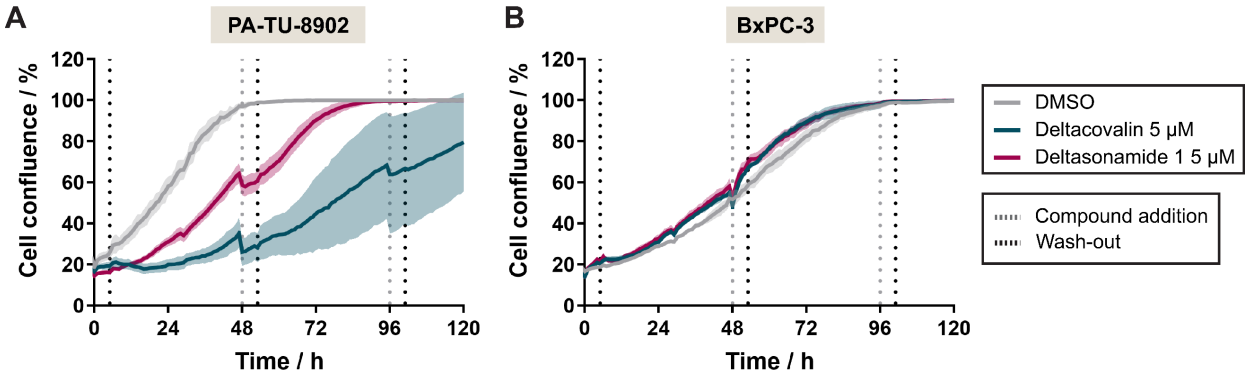

Figure 64: Sequential treatment of PA-TU-8902 and BxPC-3 cells with Deltacovalin. PA-TU-8902 (A) and BxPC-3 (B) were treated for 5 h with 5 µM of the covalent PDEδ inhibitor Deltacocalin or the non-covalent control Deltasonamide 1, followed by a wash-out, and a retreatment every 48 h for a total of three treatments. The cell confluence was monitored for a total of 120 h using kinetic real-time live-cell imaging-based analysis. Data are mean values ± S.D (n=3).

Since Deltacovalin affects the growth of KRas-independent BxPC-3 cells, the duration of compound-free intervals was extended to 48 h instead of previously used 24 h (Figure 64). However, the cell confluence of BxPC-3 remained unaltered in the presence of the PDEδ inhibitors (Figure 64B). The growth of PA-TU-8902 cells was merely reduced and not abrogated through sequential compound treatments (Figure 64A). While the first Deltacovalin treatment suppressed cell growth, the following treatment only marginally affected the cell growth compared to Deltasonamide. The non-covalent control, Deltasonamide 1, also reduced the cell confluence in the course of these treatment intervals, but less effective in comparison to Deltacovalin. Therefore, the treatments were further optimized to identify a treatment scheme that abrogated the growth of KRas-dependent PA-TU-8902, without affecting the growth of KRas-independent BxPC-3 cells.

Next, the compound treatment duration was reduced to 4 h, and the cells were treated four times. For this purpose, the cells underwent two 4 h treatment cycles, separated by a 24-h compound-free interval, and after a 48-h treatment pause, cells underwent two more compound treatment cycles (Figure 65). Sequential treatment with 5 µM Deltacovalin of PA-TU-8902 using the adjusted setup initially showed a suppressive effect on the cell confluence for 72 h (Figure 65A). After the

third and fourth treatments, the cells continued growing. Throughout the treatment intervals with Deltacovalin or Deltasonamide 1, the growth of BxPC-3 cells remained unchanged compared to the DMSO control (Figure 65B).

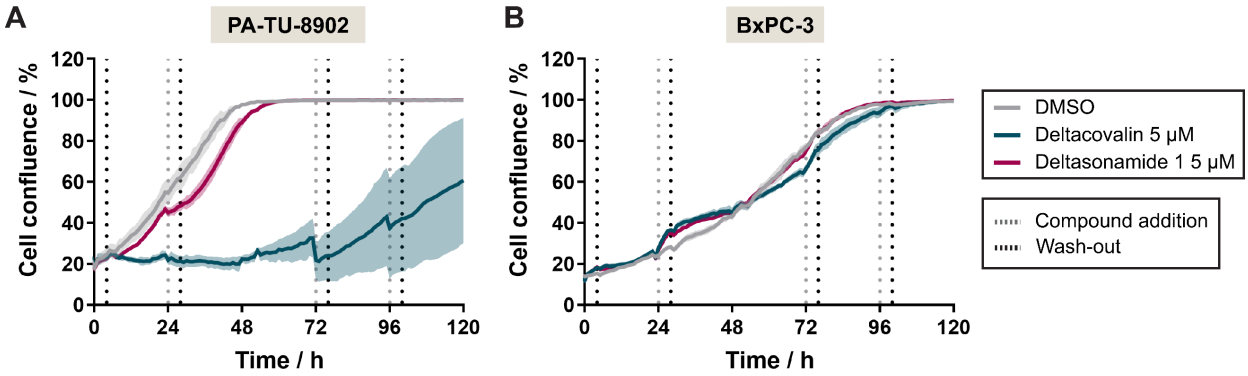

Figure 65: Sequential treatment PA-TU-8902 and BxPC-3 utilizing Deltacovalin. PA-TU-8902 (A) and BxPC-3 (B) were treated with 5 µM of the covalent PDEδ inhibitor Deltacocalin or the non-covalent control Deltasonamide 1 for 4 h. This was followed by a wash-out, a retreatment after 24 h, and a 48-h break before two additional treatments with a 24-h break in between treatments. The cell confluence was monitored for a total of 120 h using kinetic real-time live-cell imaging-based analysis. Data are mean values ± S.D (n=3).

Finally, the intervals of the sequential treatment were adapted to four 4 h treatments separated by 24 h compound-free breaks in between. Using this optimized experimental setup, the impact of Deltacovalin on 12 cell lines derived from various tissues, namely PDAC, CRC, and LAC, was investigated. The selected cell lines exhibited different KRas mutations and dependencies, enabling an in-depth analysis of Deltacovalin's effect.

Under the influence of 5 µM Deltacovalin, PA-TU-8902 cells showed a progressive cell growth reduction following each treatment (Figure 66A). Additionally, 3.75 µM of the covalent compound greatly shifted the growth curve compared to the corresponding DMSO control. Deltasonamide 1 also delayed PA-TU-8902 cell growth throughout the treatment duration. Furthermore, there was no evident influence of the PDEδ inhibitors on the cell confluence of KRas-independent BxPC-3 cells (Figure 66B). The treatment of KRas-dependent MIAPaCa-2 cells (KRas G12C) using Deltacovalin or Deltasonamide 1 showed a similar trend to that of the PA-TU-8902 cells under all conditions (Figure 66C). PANC-1 cells (KRas G12D) are independent of KRas, and the addition of PDEδ inhibitors did not change their growth (Figure 66D). In conclusion, the influence of Deltacovalin treatment on cell growth of the tested PDAC cell lines paralleled their KRas dependency status.

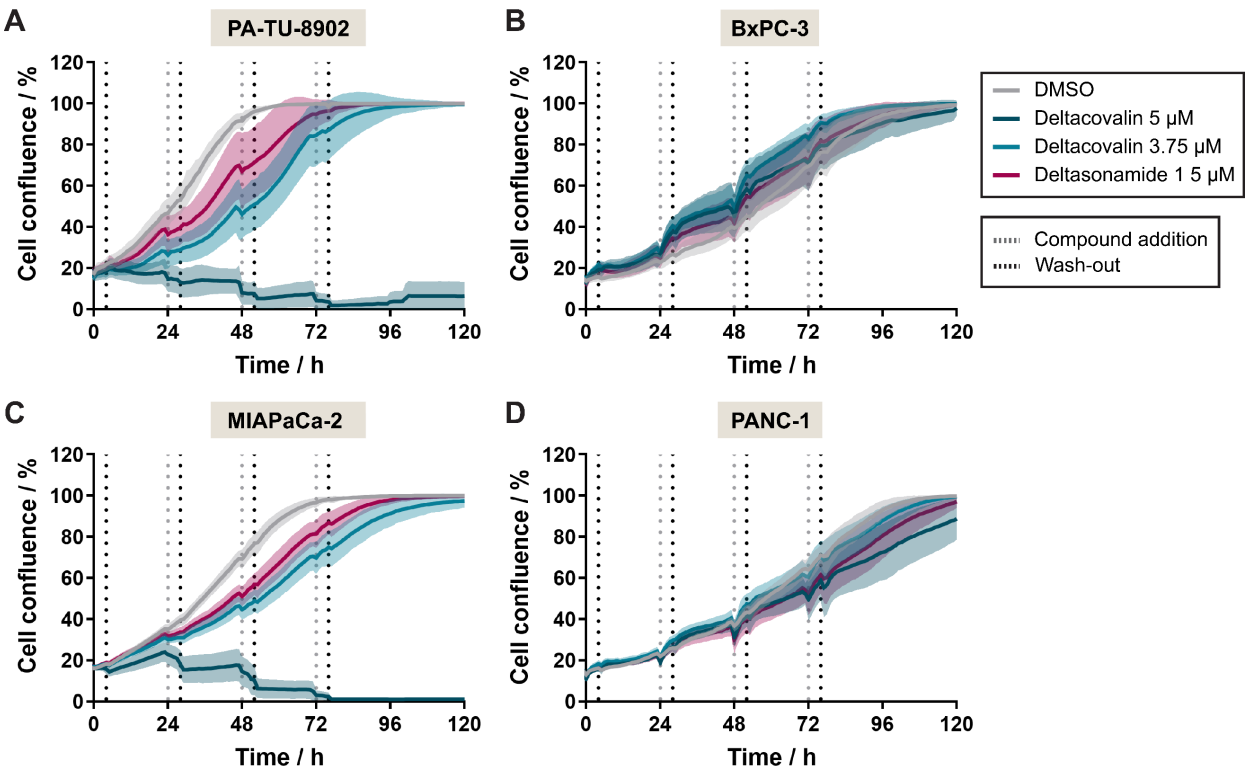

Figure 66: Sequential treatment of PDAC cell lines with Deltacovalin. PA-TU-8902 (A), BxPC-3 (B), MIAPaCa-2 (C), and PANC-1 (D) were treated for 4 h using 5 µM Deltacovalin or Deltasonamide 1, followed by a wash-out, and a retreatment every 24 h for a total of four treatments. The cell confluence was monitored for a total of 120 h using kinetic real-time live-cell imaging-based analysis. Data are mean values ± S.D (n=3).

Next, a set of CRC cell lines bearing different KRas mutations and dependencies was assayed (Table 7). The growth of KRas-dependent SW480 cells (KRas G12V) was greatly affected by PDEδ inhibition (Figure 67A). The introduction of 5 µM Deltacovalin had the most pronounced impact on reducing cell growth, followed by 3.75 µM Deltacovalin and then 5 µM Deltadonamide 1. Next, the influence of Deltacovalin on the KRas-independent cell line HCT116 (KRas G13D) was assessed. While 5 µM Deltacovalin fully suppressed the cell growth over the course of the treatment, resulting in the cell death of all HCT116 cells (Figure 67B). Additionally, 3.75 µM Deltacovalin and 5 µM Deltasonamide shifted the cell growth. Furthermore, the PDEδ inhibitors did not affect the cell confluence of the KRas-independent cell line LS-174T (KRas G12D) (Figure 67C). While the cell confluence of HT-29 cells bearing wt KRas was inhibited under the influence of 5 µM Deltacovalin, the remaining conditions paralleled the growth of the DMSO control (Figure 67D).

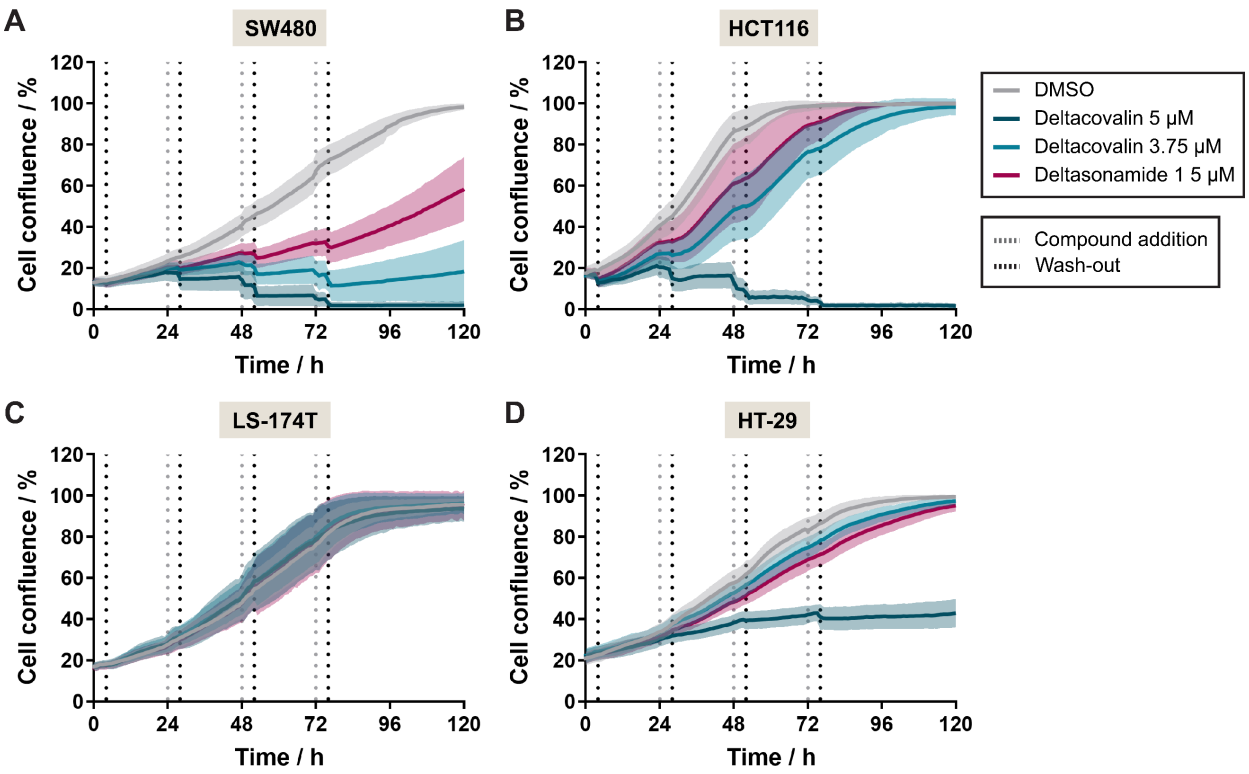

Figure 67: Sequential treatment of CRC cell lines with Deltacovalin. SW480 (A), HCT116 (B), LS-174T (C), and PANC-1 (D) were treated for 4 h using 5 µM Deltacovalin or Deltasonamide 1, followed by a wash-out, and a retreatment every 24 h for a total of four treatments. The cell confluence was monitored for a total of 120 h using kinetic real-time live-cell imaging-based analysis. Data are mean values ± S.D (n=3).

The third set of investigated cell lines involved lung adenocarcinoma cell lines (Table 7). The first tested cell line, NCI-H358 (KRas G12C), was KRas dependent and was moderately sensitive towards treatment with 5 µM Deltacovalin (Figure 68A). The lower concentration of 3.75 µM as well as 5 µM Deltasonamide slightly shifted the respective growth curves. Following this, the impact of the inhibitors on KRas-dependent NCI-H441 (KRas G12V) cells was explored, which exhibited no influence on cell growth (Figure 68B). SK-LU-1 cells (KRas G12D) are KRas independent. However, 5 µM Deltacovalin substantially decreased their growth (Figure 68C). A549 cells (KRas G12S) are KRas-independent, which was consistent with their unaffected cell growth under the influence of the tested compounds (Figure 68D).

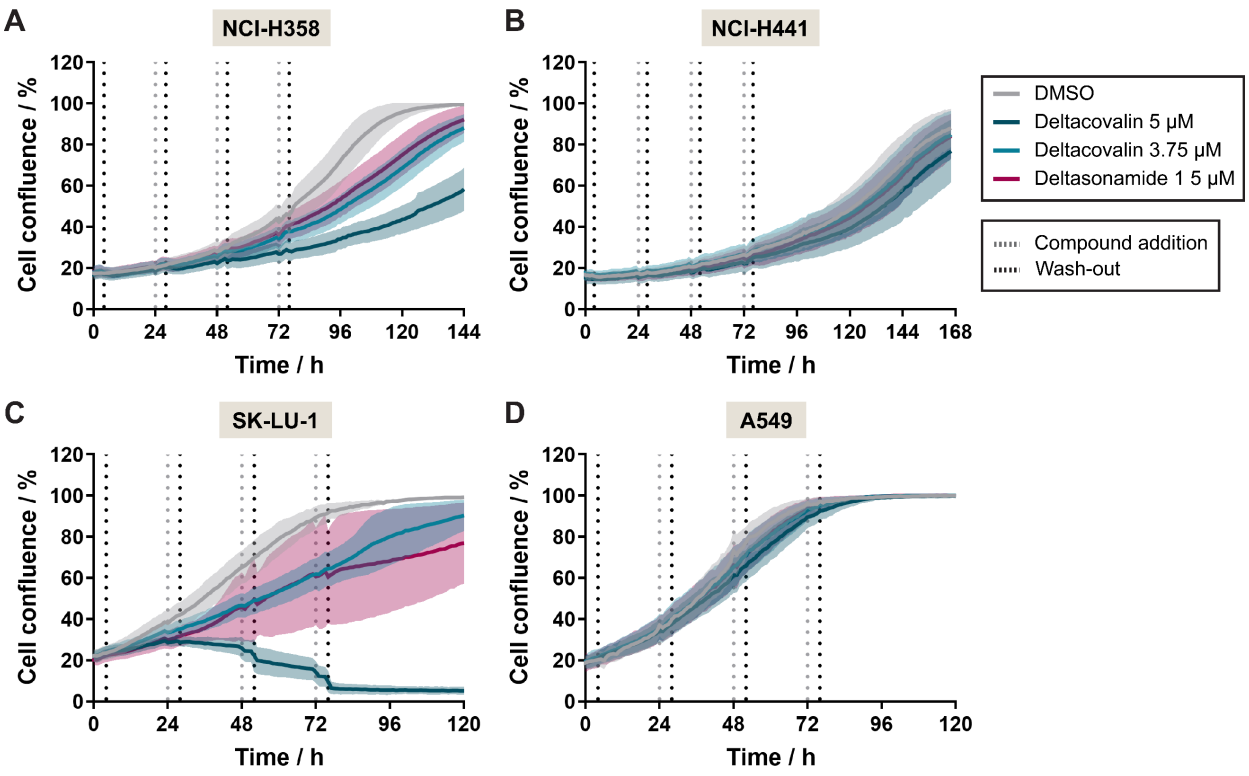

Figure 68: Sequential treatment of CRC cell lines with Deltacovalin. NCI-H358 (A), NCI-H441 (B), SK-LU-1 (C), and A549 (D) were treated for 4 h with 5 µM Deltacovalin or Deltasonamide 1, followed by a wash-out, and a retreatment every 24 h for a total of four treatments. The cell confluence was monitored for a total of 120 h using kinetic real-time live-cell imaging-based analysis. Data are mean values ± S.D (n=3).

Taken together, the KRas dependency status is mostly in agreement with the effect on cell growth upon Deltacovalin-mediated PDEδ inhibition. A clear growth reduction trend was observed in PDAC, while the investigated CRC and LAC cell lines only partially grew according to their designated KRas dependency status under the influence of PDEδ inhibition.

5.1.3 Efficacy of Deltacovalin-mediated PDEδ inhibition in KRas-driven murine model

Prior to the performance of *in vivo* studies, the validation of the efficacy in murine cell lines was crucial before progressing to more complex mouse models harboring a $KRas^{G12D}$ mutation and an inducible TP53 deletion.[144] Hence, initial investigations were conducted to explore the impact of Deltacovalin on the cell growth of murine cell lines through single and sequential treatment experiments (see 5.1.3.1). Next, pharmacokinetics (PK) and pharmacodynamics (PD) studies were conducted to determine the ADME (A: adsorption, D: distribution, M: metabolism, and E: excretion) parameters for Deltacovalin to establish a suitable dosing regimen for mouse studies (see 5.1.3.2).

5.1.3.1 Sequential treatment of murine cell lines

Deltacovalin was tested on different human cell lines with various KRas mutations and dependencies. Following this, its impact on three murine KRas-driven lung adenocarcinoma cell lines, namely KP1035, KPACK135-1, and KPACK135-10, was studied. These cell lines carried a KRas G12D mutation and were TP53 deficient, as these two mutations frequently co-cluster in lung adenocarcinomas.[254] The cell lines were generated and provided by the research group of Prof. Dr. Reinhardt (University Hospital Essen).[139]

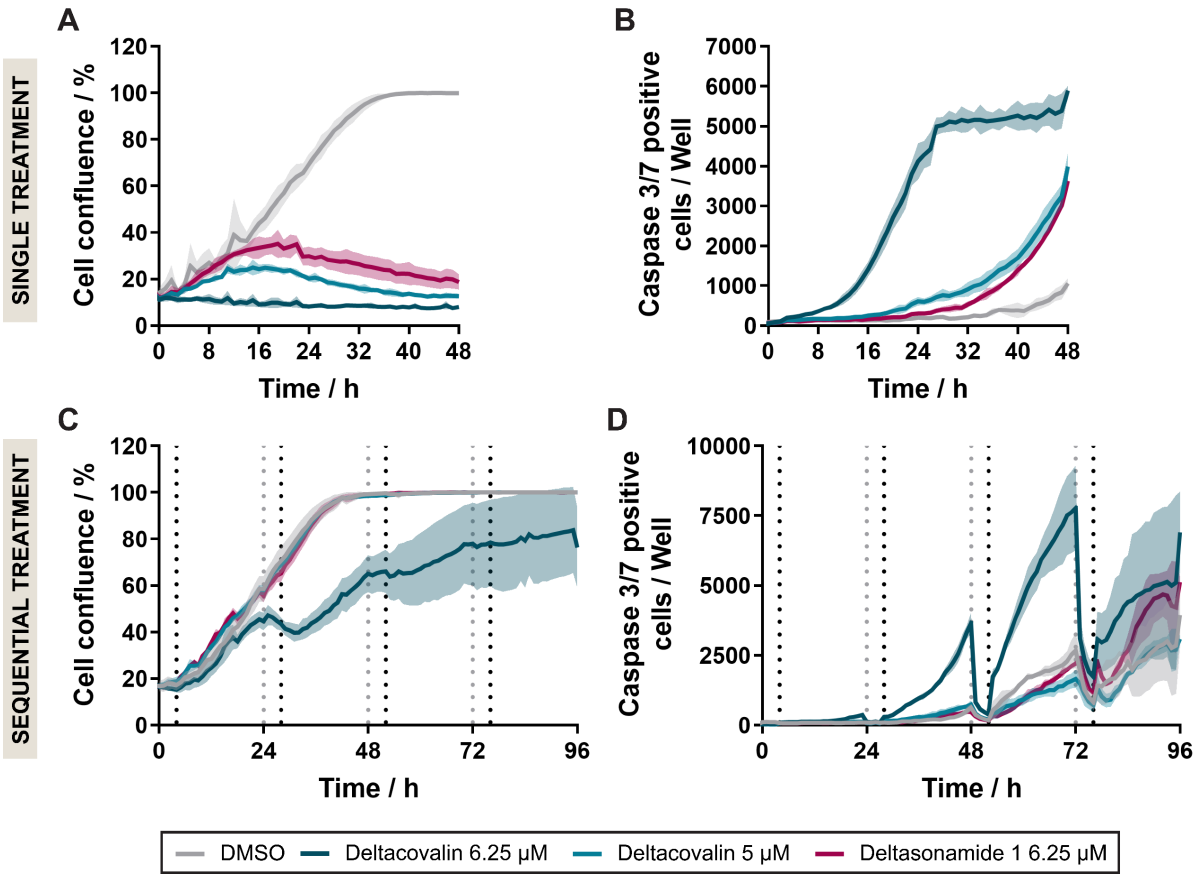

Figure 69: Effect of Deltacovalin on murine KP1035 cells growth. KP1035 cells were treated with Deltacovalin, Deltasonamide, or DMSO as a control in the presence of a caspase 3/7 reagent. KP1035 cell growth (A) and caspase 3/7 activity (B) were monitored for 48 h by means of kinetic real-time live-cell imaging. Data are representative of n=3 (mean ± S.D, N=3). C and D) KP1035 cells were treated for 4 h with Deltacovalin, Deltasonamide, or DMSO, followed by a wash-out and the addition of the caspase 3/7 reagent. Retreatments were performed every 24 h for a total of four treatments. The cell confluence was monitored, and caspase 3/7 activity were monitored for a total of 96 h using kinetic real-time live-cell imaging. Data are representative of n=3 (mean ± S.D, N=3). Wash-outs (⋯) and treatments (⋯) are indicated *via* dotted lines in graphs.

In the initial murine cell line, KP1035, both PDEδ inhibitors demonstrated an inhibitory effect on cell growth while simultaneously elevating caspase 3/7 activity and, thus, apoptosis (Figure 69A and B). A concentration of 6.25 µM Deltacovalin was the most effective, followed by 5 µM

Deltacovalin and 6.25 µM of the non-covalent control, Deltasonamide 1. Next, Deltacovalin was subjected to sequential treatment of murine KP1035. The covalent inhibitor only moderately affected the cell growth of KP1035 cells, whereas 5 µM Deltacovalin and 6.25 µM Deltasonamide had no effect (Figure 69C). Simultaneous with the reduction of cell growth, an elevation of caspase 3/7 activity was observed for 6.25 µM Deltacovalin (Figure 69 D).

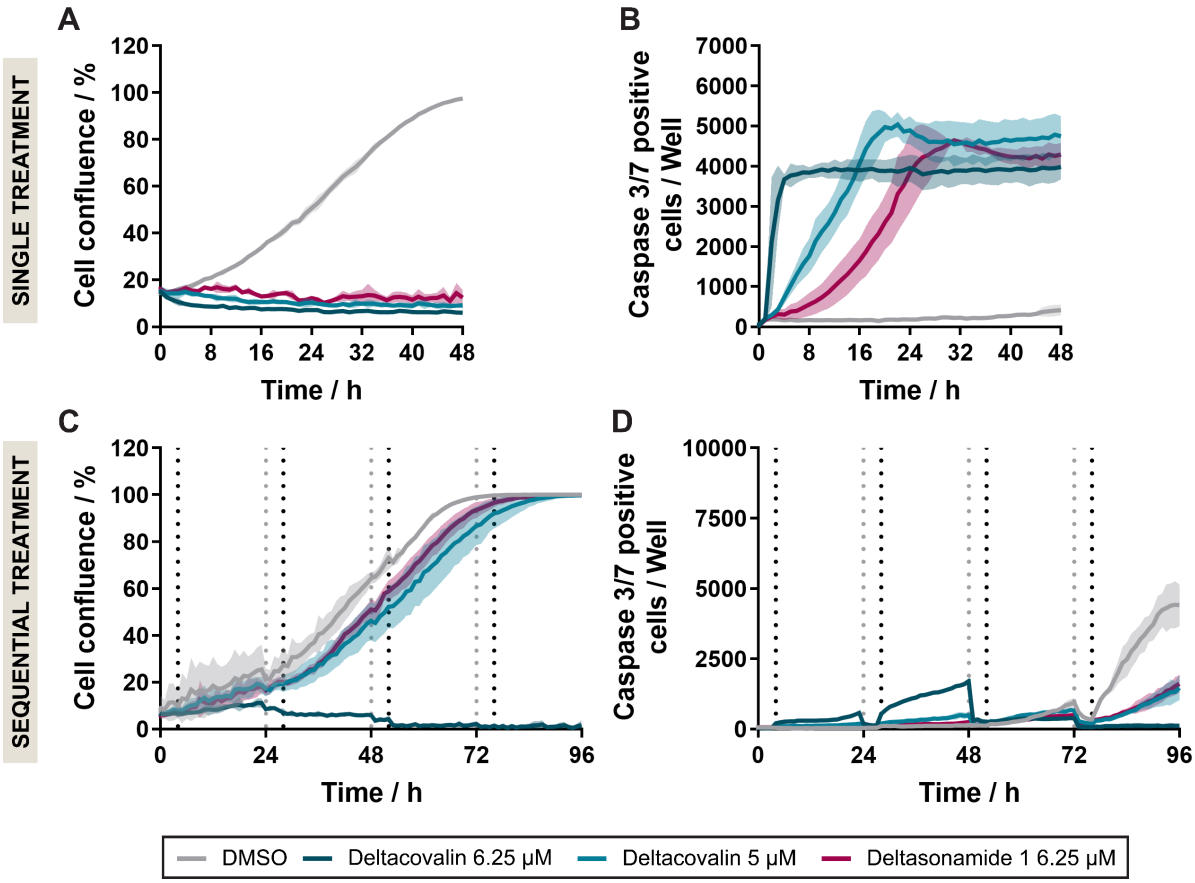

Figure 70: Impact of Deltacovalin on murine KPACK135-1 growth. KPACK-135-1 cells were treated with Deltacovalin, Deltasonamide, or DMSO as a control in the presence of a caspase 3/7 reagent. KPACK-135-1 growth (A) and caspase 3/7 activity (B) were monitored for 48 h by means of kinetic real-time live-cell imaging-based analysis. Data are representative of n=3 (mean ± S.D, N=3). C and D) KPACK-135-1 cells were treated for 4 h with Deltacovalin, Deltasonamide, or DMSO, followed by a wash-out and the addition of the caspase 3/7 reagent. Retreatments were performed every 24 h for a total of four treatments. The cell confluence and caspase 3/7 activity were monitored for a total of 96 h using kinetic real-time live-cell imaging. Data are representative of n=3 (mean ± S.D, N=3).

Similarly, the effectiveness of a single Deltacovalin treatment on the second murine cell line, KPACK135-1, was evaluated. Deltacovalin and Deltasonamide 1 inhibited the growth of KPACK135-1 cells while also upregulating caspase 3/7 activity (Figure 70A and B). For this cell line, caspase 3/7 was most efficiently elevated by 6.25 µM of Deltacovalin, while 5 µM was less efficient, and treatment with 6.25 µM Deltasonamide 1 was the least efficient in comparison. In

the sequential treatment experiment, 6.25 µM Deltacovalin completely inhibited cell growth, while 5 µM and 6.25 µM Deltasonamide did not affect the growth behavior (Figure 70C). The caspase 3/7 activity increased between the 24 h and 48 h time interval, which is in line with the decrease of the cell confluence in the same time frame (Figure 70C and D). Interestingly, the analysis of KPACK135-10 cells exhibited cell growth pattern in both single and sequential treatment experiments comparable to KPACK135-1 cells (Figure 71).

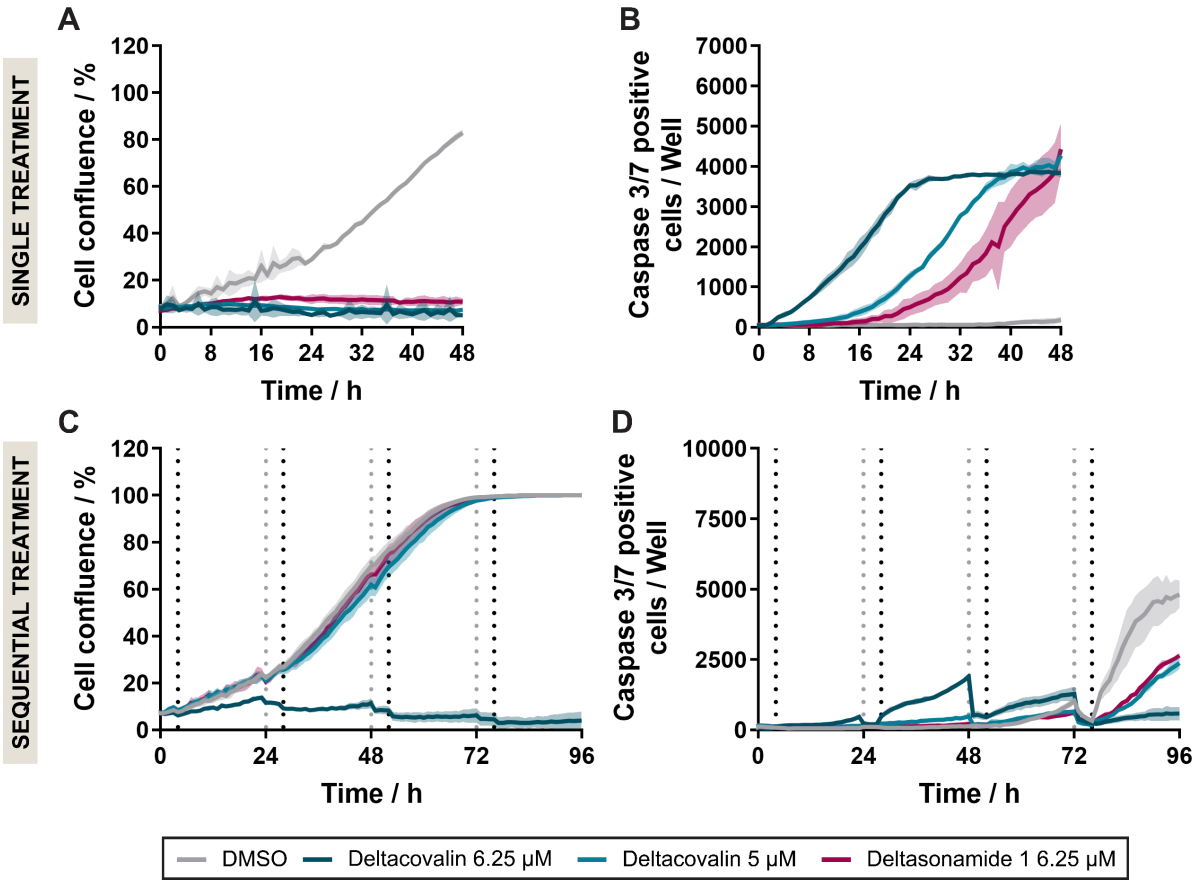

Figure 71: Influence of Deltacovalin on murine KPACK135-10 cells. KPACK-135-10 cells were treated with Deltacovalin, Deltasonamide, or DMSO as a control in the presence of a caspase 3/7 reagent. KPACK-135-10 cell growth (A) and caspase 3/7 activity (B) were monitored for 48 h by means of kinetic real-time live-cell imaging-based analysis. Data are representative of n=3 (mean ± S.D, N=3). C and D) KPACK-135-10 cells were treated for 4 h with Deltacovalin, Deltasonamide, or DMSO, followed by a wash-out and the addition of the caspase 3/7 reagent. Retreatments were performed every 24 h for a total of four treatments. The cell confluence and caspase 3/7 activity were monitored for a total of 96 h using kinetic real-time live-cell imaging-based analysis. Data are representative of n=3 (mean ± S.D, N=3).

5.1.3.2 In vivo efficacy of Deltacovalin-mediated PDEδ inhibition

Before conducting *in vivo* experiments in mice, PK/PD studies were conducted by Pharmacelsus at the request of Dr. Anke Unger from the Lead Discovery Center (LDC) in Dortmund. This was crucial for understanding the half-life and bioavailability of Deltacovalin and adjusting its dosage regimen without the risk of toxicity, which could raise safety concerns. Additionally, the aqueous solubility of Deltacovalin was determined by LDC. Therefore, the kinetic solubility of 500 µM Deltacovalin in HEPES buffer at pH 7.4 was compared to a 50% (v/v) ACN buffer, and the covalent inhibitor Deltacovalin was soluble up to a concentration of 320.9 µM.

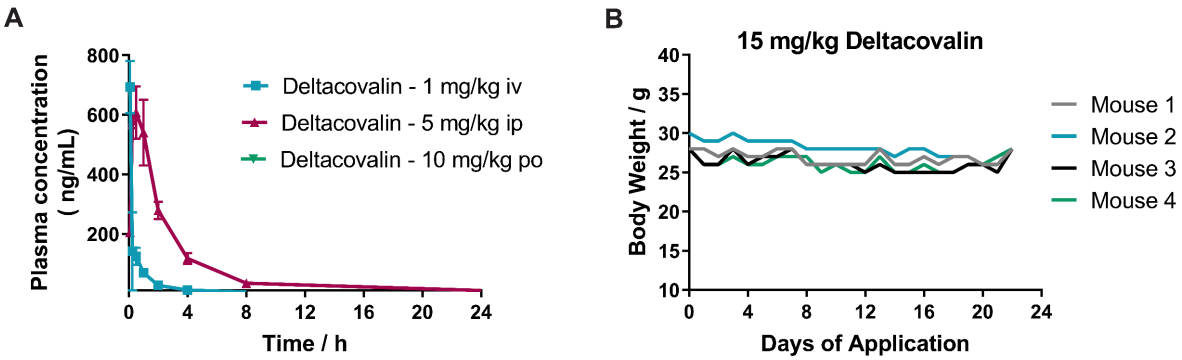

C

PK parameter	1 mg/kg Cpd	5 mg/kg Cpd	10 mg/kg Cpd	15 mg/kg Cpd
Dose route	IV	IP	PO	IP
Vehicle	20 % (v/v) DMSO and 80 % (v/v) PEG400	5 % (v/v) DMSO, 30 % (v/v) HP-β-CD, 0.5 % (v/v) HPMC in water		
C_{max} (ng/mL)	-	608	4	2402.0
t_{max} (h)	-	0.5	1.0	0.5
$t_{1/2}z$ (h)	7.3	6.0	12.5	5.7
Vz/f (L/kg)	-	21.1	7674.0	16.2
CL/f (L/(h*kg))	-	2.5	474.2	1.9
F (%)	-	114	0.7	-

Figure 72: Summary of mouse PK studies using Deltacovalin. A) Determination of optimal dose route of Deltacovalin for mouse *in vivo* studies-. Intravenous administrations (IV) were performed using 20 % (v/v) DMSO and 80 % (v/v) PEG400 as a vehicle, whereas 5 % (v/v) DMSO, 30 % (v/v) 2-hydroxypropyl-beta-cyclodextrin (HP-β-CD), and 0.5 % (v/v) hydroxypropylmethylcellulose (HPMC) in water was used for intraperitoneal (IP) and oral administrations (PO). B) Impact of a 22-day long daily 15 mg/kg Deltacovalin treatment on mice using ip application monitored *via* body weight tracking. C) Summarized PK parameters for Deltacovalin treatment using differing dosage routes and concentrations. Cpd: compound, C_{max}: maximal cpd concentration found in plasma, t_{max}: time to reach maximum cpd concentration, $t_{1/2}$: cpd half-life, V/f: volume of distribution, CL/f: total body clearance, and F: bioavailability. *PK studies were performed by Pharmacelsus.*

Initial testing of the intravenous (IV), intraperitoneal (IP), and oral administration (PO) methods revealed that Deltaocvalin has poor oral availability. The most effective method of administration was IP (Figure 72A and C). Administration of 5 mg/kg of Deltacovalin via the IP route resulted in

the highest compound concentration in the plasma after 30 min. This was also displayed in the high distribution volume of 21.1 L/kg and a high bioavailability of 114 %. The covalent inhibitor has a half-life of 6 h, and its clearance, determined by the blood flow through the liver, falls within the medium range according to Pharmacelsus' criteria (<10 % low, 10-75 % medium, >75 % high). The untreated mouse blood flow through the liver is 5.4 L/(h*kg), and it decreased to 2.5 L/(h*kg) in the presence of Deltacovalin, resulting in a clearance of 46 %. Moreover, according to the LDC selection criteria, the clearance value should be less than 2.5 L/(h*kg), which is true for Deltacovalin. A daily Deltacovalin treatment using a dose of 15 mg/kg for 22 day did not affect mouse survival, as reflected by the unchanged body weight as well as beneficial PK parameter values for the compound (Figure 72B and C). Mice displayed normal behavior, and no clinical signs were observable after dosing. Furthermore, PK parameter data for 15 mg/kg IP Deltacovalin application was comparable to the lower concentration of 5 mg/kg (Figure 72C). However, administration of higher concentrations of 20 or 50 mg/kg were poorly tolerated by the mice, and consequently, treatments using these concentrations were not continued.

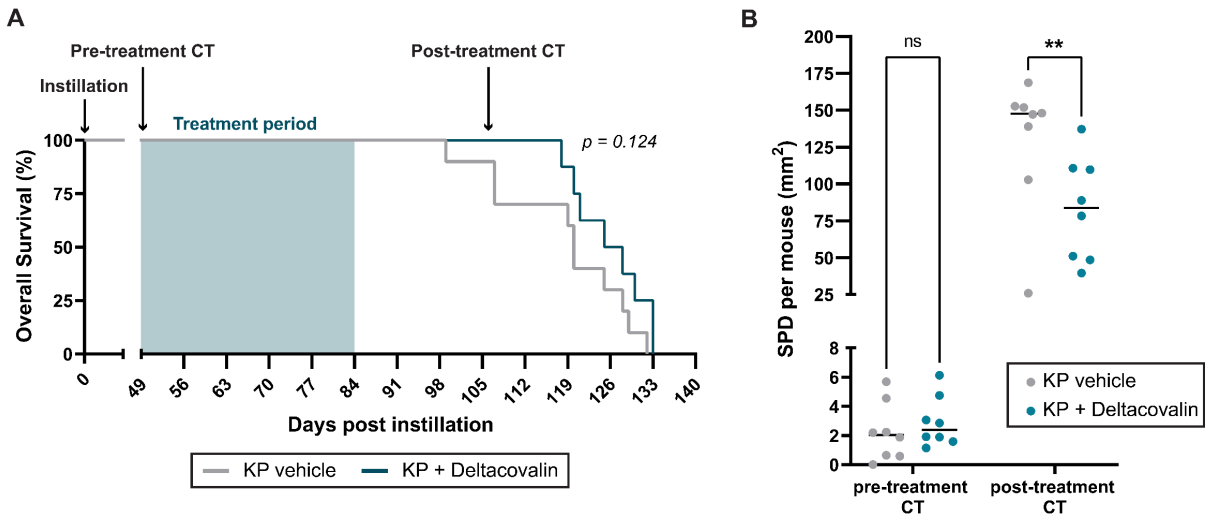

Figure 73: *In vivo* efficacy of Deltacovalin in mice. A) Overall survival of the KP mice in presence of Deltacovalin. Following the instillation of $KRas^{G12D}$ and $TP^{-/-}$ tumors in mice for seven weeks, mice were treated daily with 15 mg/kg Deltacovalin for 21 days. Subsequently, the survival of the individual mice was consistently monitored (n=10 for KP vehicle, n=8 for KP + Deltacovalin). Comparison of the survival of the individual groups was performed using the log-rank (Mantel-Cox) test. B) Comparison of the tumor size pre- and post-treatment in presence of Deltacovalin. The tumor size was determined by calculating the sum of the product of the diameters (SPD), obtained through the length and width of all lung tumors in the individual mice (n=8); P < 0.05; **, P < 0.01; ***, P < 0.001; ****, P < 0.0001, n.s.: not significant (two-way ANOVA). *In vivo studies were performed by Maxim Hützen (Jachimowicz lab, MPI for Biology of Ageing).*

The *in vivo* efficacy of Deltacovalin was studied using the KP mouse model, which carries $KRas^{G12D}$ and $TP53^{fl/fl}$ tumors. The KP mouse model holds significant relevance due to the frequent co-clustering of these two mutations in lung cancer patients. In a cohort of 146 patients, 25 % displayed both mutations, leading to a simultaneous decrease in overall survival.[139] The deletion of TP53 in $KRas^{G12D}$ mutant lung tumors in mice was initiated by administering an Adeno-Cre virus. Tumor development took approximately seven weeks and was checked through a pre-treatment computed tomography (CT) scan. Subsequently, a 21-day regimen of daily 15 mg/kg Deltacovalin treatment was administered, with consistent monitoring of the mice. A post-treatment CT scan was performed after 15 weeks. After 99 days, a noticeable increase in overall survival was observed with Deltacovalin treatment compared to the vehicle control (Figure 73A). However, this shift is not significant. Moreover, the tumor volume before and after treatment was analyzed. Treatment with a daily dose of 15 mg/kg Deltacovalin resulted in a significant decrease in tumor size (Figure 73B).

In summary, Deltacovalin impacted the cell growth of KRas-driven murine KP cell lines and extended the survival of an incurable KP mouse line.

5.1.4 Influence of Deltacovalin on the phosphoproteome

To elucidate the impact of Deltacovalin on the protein phosphorylation state and the signaling pathways *in cellulo*, phosphoproteome profiling was conducted. For this purpose, PA-TU-8902 cells were treated with 5 µM Deltacovalin or DMSO for 2 h, followed by cell lysis. Subsequently, an on-bead digestion was performed, and phosphopeptides enrichment was performed using magnetic TiO_2 particles prior to HPLC-MS/MS-based analysis. Data analysis was conducted using the Kinase-Substrate Enrichment Analysis (KSEA) tool .[255-257] This tool calculates a kinase z-score based on the overall phosphorylation status of its target substrates while disregarding sites on the kinase itself. The KSEA tool relies on experimentally identified or annotated phosphosites from PhosphoSitePlus.[258] In order to improve coverage, the NetworKIN prediction tool was implemented into the analysis.[259] The prediction tool assigns each phosphorylation site to one or more kinase families. It uses a probabilistic network analysis between substrate and kinase, e.g., based on physical protein interaction, using the STRING database.[260] The resulting list of Kinase z-scored data was then further subjected to Reactome-based pathway analysis (Figure 74).[261]

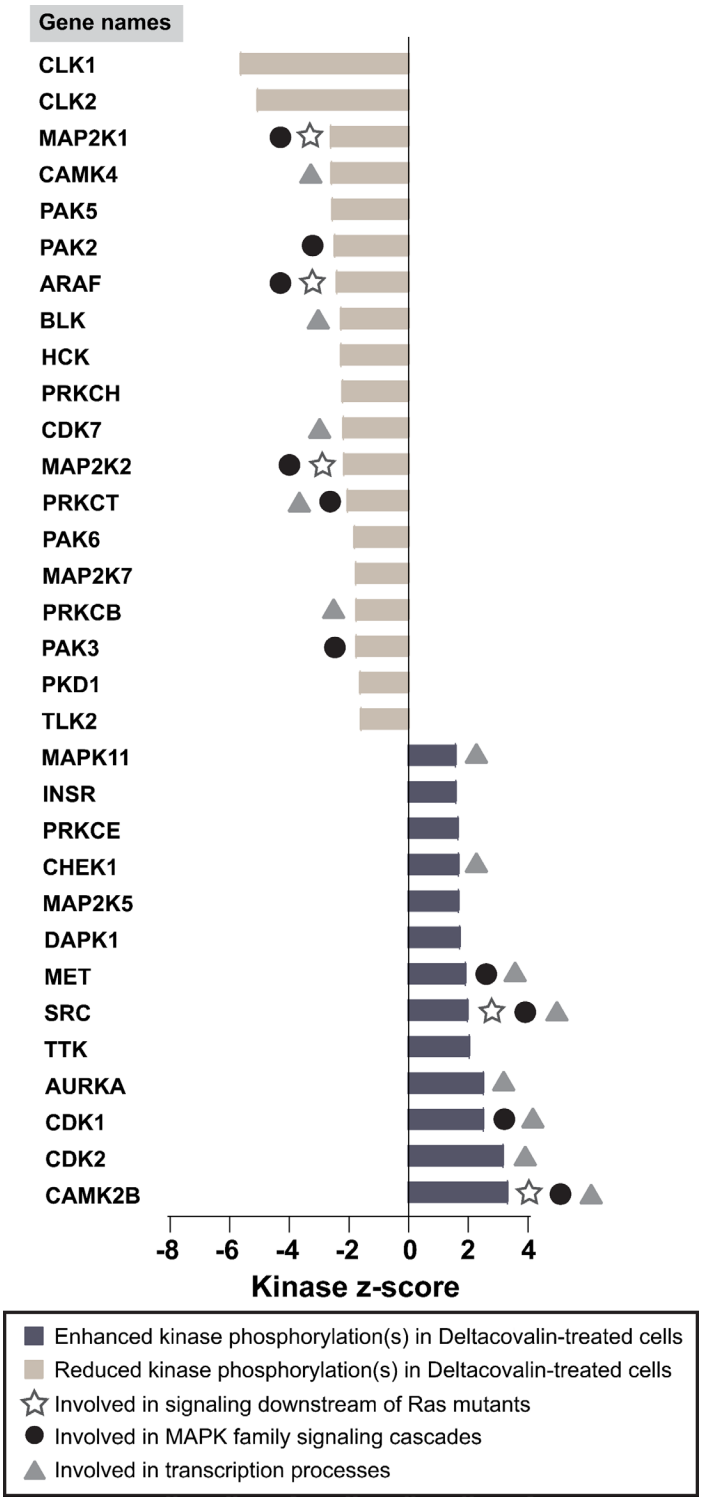

Figure 74: Influence of Deltacovalin on the phosphoproteome. PA-TU-8902 cells were treated with 5 µM Deltacovalin or DMSO for 2 h prior to analysis of the phosphoproteome. Data represents three biological replicates (n=3). Data analysis was conducted using the KSEA, NetworKIN, and Reactome tools. The following analysis parameters were employed for the KSEA analysis: $p < 0.05$, kinase substrate cutoff < 5. Only KSEA tool hits with kinase z-score >1.7 and < -1.7 were displayed.

Based on this analysis, Deltacovalin affected the phosphorylation of various proteins downstream of Ras mutant signaling. It increased the phosphorylation of Calcium/calmodulin-dependent protein kinase type II subunit beta (CAMK2B) and Proto-oncogene tyrosine-protein kinase Src (Src) (Figure 74). At the same time, it decreased the phosphorylation of Dual specificity mitogen-activated protein kinase kinase 2 (MEK2), Serine/threonine-protein kinase A-Raf (A-RAF), and Dual specificity mitogen-activated protein kinase kinase 1 (MEK1). Furthermore, the phosphorylation of various proteins associated with the MAPK signaling cascade was upregulated, including CAMK2B, Cyclin-dependent kinase 1 (CDK1), Src, Hepatocyte growth factor receptor (MET). Simultaneously, a reduction in phosphorylation was observed for proteins relevant to the MAPK signaling cascade, including Serine/threonine-protein kinase PAK 3 (PAK 3), Protein kinase C eta (PKC-η), MEK2, A-RAF, PAK 2, and MEK. In the presence of Deltacovalin, phosphorylations of proteins involved in transcription processes were found to be modulated. An increase in phosphorylation was observed for CAMK2B, CDK1, CDK2, Src, MET, Serine/threonine-protein kinase Chk1 (Chk1), and mitogen-activated protein kinase 11 (MAPK11), as well as Aurora Kinase A. Conversely, a decrease in phosphorylation was observed for calmodulin-dependent protein kinase IV (CaMK4), B-lymphoid tyrosine kinase (Blk), Cyclin-dependent kinase 7 (CDK7), and protein kinase C beta type (PRKCB). Furthermore, Cd2-like kinases (CLKs) 1 and 2 displayed reduced kinase phosphorylations, which are essential for splicing processes.[262]

The data obtained by the KSEA-based analysis were also subjected to ShinyGO gene-set enrichment tool (Figure S3).[263] The KEGG pathway diagram indicated that components pivotal for KRas signaling were enriched, including Raf, ERK, Src, CAMK, and PKC, confirming the obtained analysis results in Figure 70.[264-267] Taken together, the impact of Deltacovalin on downstream signaling of Ras mutants and MAPK family cascades aligns with its mode of action, which involves the displacement of KRas from the plasma membrane through PDEδ inhibition.

5.1.4 Investigation of Deltacovalin's influence on lysosomotropism and phospholipidosis

The chemical structure of Deltacovalin is derived from Deltasonamide. Previous literature has indicated that this compound is lysosomotropic.[268] Lysosomotropic compounds are generally hydrophobic and contain basic structural entities (e.g., amines), enabling them to penetrate and sequester in lysosomes.[269] The accumulation of compounds in the lysosomes is enabled through protonation, resulting in increased lysosomal pH and disrupting lysosomal functions.[270] Therefore, Deltacovalin's potential to accumulate in lysosomes was evaluated as well (Figure 75). Intact U-

2OS cells were incubated with the PDEδ inhibitors Deltasonamide 1 and Deltacovalin before introducing the lysosomotropic fluorescent dye LysoTracker™ Red DND-99. The lysosomotropic drug chloroquine was included as a control.[269]

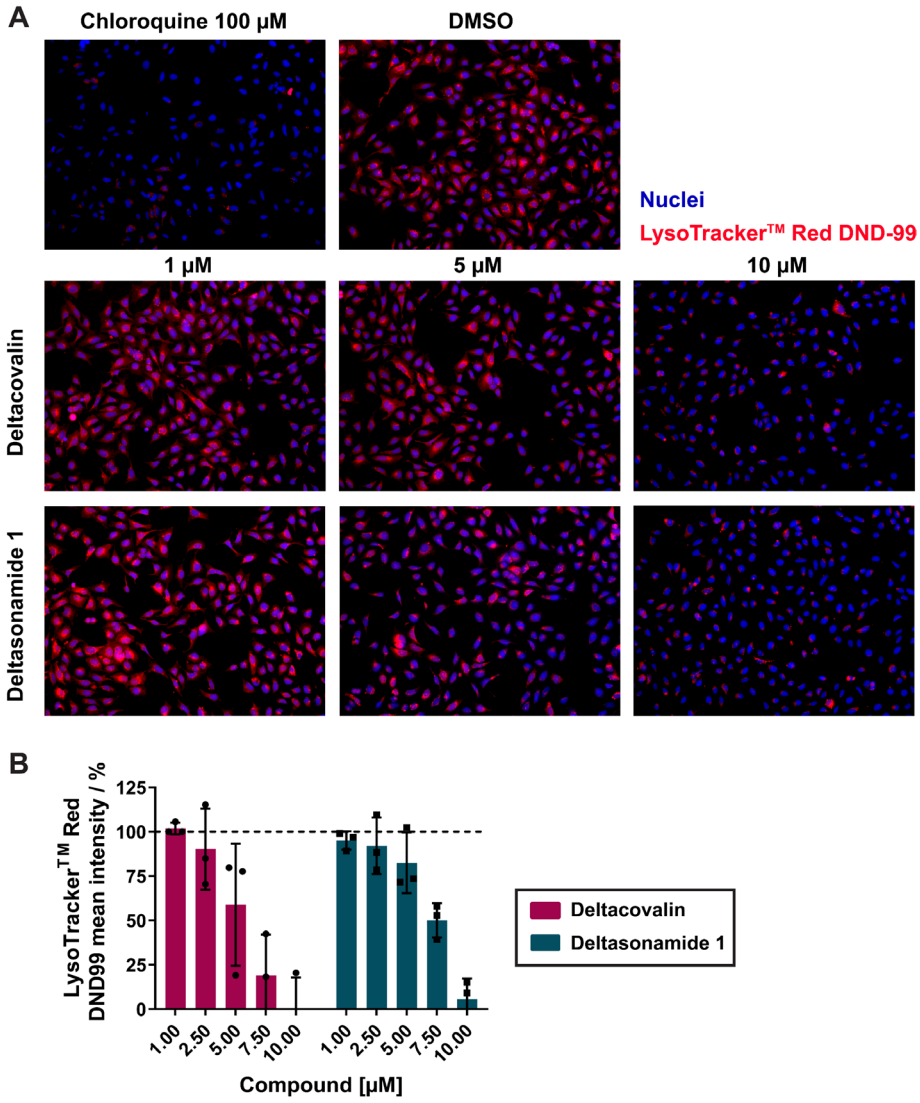

Figure 75: Deltacovalin sequesters in lysosomes. U-2OS cells were treated with Deltacovalin, Deltaosnamide, or DMSO for 1 h. This was followed by fixation and staining using Hoechst-33342 and LysoTracker™ Red DND-99. A) Representative images for n=3, magnification 10X. B). The quantitative data was normalized with the DMSO control set as 100% and chloroquine control as 0%. Data are mean values ± SD (n=3).

Compared to the DMSO control, Deltacovalin decreased the fluorescence intensity of the LysoTracker™ Red DND-99 dye in a concentration-dependent manner (Figure 75A). A concentration of 10 µM Deltacovalin abrogated the fluorescence of the lysosomotropic fluorophore to a similar extent as observed for chloroquine. 5 µM of the covalent inhibitor reduced the LysoTracker™ Red DND-99 intensity by 41.2 %, and 1 µM did not exhibit lysosomotropic

effects (Figure 75B). This was in line with the lysosomotropic activity of Deltasonamide 1 (Figure 75A and B).

An increased pH value caused by the accumulation of compounds in the lysosomes is associated with the excessive accumulation of phospholipids in cells, a process known as phospholipidosis.[271] Since the PDEδ inhibitors Deltacovalin and Deltasonamide 1 both exhibit lysosomotropic effects, they were subjected to the HCS LipidTox™ Red reagent-based phospholipidosis assay. For this purpose, U-2OS cells were incubated with Deltasonamide 1, Deltacovalin, and phospholipidosis dye HCS LipidTox™ Red for 48 h. Sertraline was used as a positive control.[272] Notably, elevated phospholipid content was detected in the presence of 1.25 and 2.5 µM Deltacovalin or Deltasonamide (Figure 76).

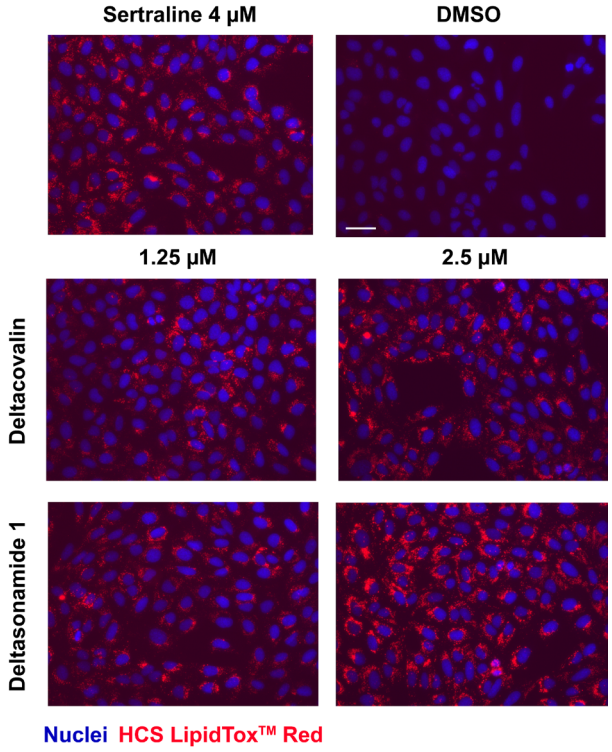

Figure 76: Deltacovalin causes phospholipidosis. U-2OS cells were treated with Deltacovalin, Deltasonamide or DMSO as well as HCS LipidTox™ Red reagent for 48 h prior to nuclei staining using Hoechst-33342. Representative images for n=3, magnification 20X. *Assay was performed by. Dr. Belén Lucas.*

In summary, both PDEδ inhibitors, Deltacovalin, and Deltasonamide 1 accumulated in the lysosomes and increased the cellular phospholipid concentration. This commonality can be attributed to the structural similarity of the covalent inhibitor to the Deltasonamide 1 scaffold, which both are basic and lipophilic.

5.2 Discussion

5.2.1 *In cellulo* and *in vivo* characterization of Deltacovalin-mediated PDEδ inhibition

Successful targeting of KRas has been a great challenge for many years. The clinical success of covalent inhibitors (e.g., BTK inhibitor ibrutinib) has underscored the great potential of covalent targeting of proteins.[273] This ultimately led to the development of the first KRasG12C targeting inhibitors, sotorasib (LUMAKRAS®) and adagrasib (KRAZATI®), which were FDA-approved for the second line of treatment of non-small cell lunger cancer (NSCLC) in 2021 and 2022, respectively.[95,97,98] Patients receiving KRas G12C-specific treatment developed resistance through secondary mutations or mutations in HRas and NRas, compensating for KRas inhibition.[99] An alternative approach to abrogate the aberrant activity of oncogenic KRas involves displacing it from its plasma membrane localization, which is pivotal for proper signal transmission. The Waldmann group has developed several generations of PDEδ inhibitors that interact with the prenyl-binding pocket of the protein, thereby blocking KRas-PDEδ interaction. However, the rapid Arl2/3-mediated release of PDEδ inhibitors reduces their ability to impede KRas signaling. Hence, a new series of covalent PDEδ inhibitors based on Deltasonamide 1 as were designed to bypass Arl2/3-mediated compound release. Deltasonamide 1 was selected as a starting point due to its strong binding to PDEδ in the picomolar range, enabled through seven hydrogen bonds, resulting in the reduction of Arl2-mediated release. The most promising covalent inhibitor, Deltacovalin, was further characterized in this thesis. Initially, a co-crystal structure confirmed the covalent engagement of Deltacovalin to PDEδ. Target engagement of Deltacovalin was confirmed in intact cells and cell lysates. Furthermore, Arl2-mediated release of Deltacovalin was not observed at the highest compound concentration, as compared to Deltasonamide 1. However, even though Deltacovalin has a nanomolar affinity for PDEδ, a concentration of 500 nM of the compound was required to prevent Arl2-mediated release. There are two potential contributing factors for this observation: 1) The incubation was conducted at room temperature, which may have decelerated covalent bond formation of Deltacovalin, and 2) the simultaneous introduction of PDEδ, Deltacovalin, and Arl2, which may have led to the stabilization of the PDEδ ‘‘off-conformation’’ and thus, interference with Deltacovalin binding.

PDEδ inhibitors Deltasonamide 1 and Deltacovalin exhibited similar behavior in KRas dependent and independent cell lines, and therefore, no benefit of the covalent inhibition was observed. Moreover, previous investigations revealed that higher concentrations of the inhibitors resulted in cytotoxic effects on the cells. For this reason, a wash-out experiment was performed to study the impact of covalent PDEδ inhibition without possible off-target effects. Deltacovalin was assayed

using the KRas-dependent PDAC cells PA-TU-8902 and KRas independent BxPC-3 cells. Compound treatment times exceeding 5 hours substantially delayed cell growth of KRas-dependent PA-TU-8902 cells under the influence of Deltacovalin compared to the non-covalent control. Additionally, BxPC cell growth remained unaltered. These results gave the first indications for a covalent mechanism of action of Deltacovalin in PA-TU-8902. Furthermore, they also suggested that Deltacovalin may reduce the growth of KRas-dependent cell lines, while KRas-independent cell lines remained unaffected. This was followed by optimizing a sequential treatment assay setup to identify a treatment regime that allowed investigation of the impact of Deltacovalin on cell lines with different KRas mutational statuses and dependencies in the absence of possible off-target toxicity. For this experiment, cells were treated with compound for a short period, followed by a wash-out, i.e., a "compound holiday," and then a repetition of the compound treatment and wash-out cycles.

The initially attempted three consecutive 5 h compound treatments with 24 h treatment-free intervals not only impacted the growth of the PA-TU-8902 cell line, but also affected the growth of the KRas-independent BxPC-3 cells. As a result, the treatment-free intervals were extended to 48 h. Although the extended intervals did not alter the growth of the BxPC-3 cells, they were not sufficient to decrease the growth of the KRas-dependent cell line. To address this, two 4 h treatments with a 24 h compound break in between followed by a 48 h break, and two additional 4 h treatments were implemented. Again, the BxPC-3 cell growth followed a pattern similar to the DMSO control, while the growth of PA-TU-8902 was only partially reduced. The 48 h compound breaks may be insufficient due to the turnover of PDEδ proteins. The halftime for PDEδ degradation is around 40 h in HeLa cells, whereas synthesis exhibits an halftime of 113 h.[274,275]

For the final sequential treatment setup, four consecutive 4 h treatments with 24 h treatment-free intervals were used for exploring Deltacovalins influence in 12 PDAC, CRC, and LAC cell lines with different KRas dependencies and mutational statuses (Figure 77). Investigated PDAC cell lines included PA-TU-8902, MIAPaCa-2, PANC-1, and BxPC-3. Both KRas-dependent cell lines PA-TU-8902 and MIAPaCa-2 were sensitive toward Deltacovalin treatment. PANC-1 and BxPC-3 exhibited no sensitivity under the influence of the covalent inhibitor. The CRC cells SW480 were KRas-dependent and showed profound sensitivity upon addition of PDEδ inhibitors . HCT116 cells were categorized as KRas-independent by Singh *et al*.[248] However, their cell growth was diminished in the presence of the covalent inhibitor. Moreover, the CRC cells were on the border to be categorized as a dependent cell line, and a study performed by Janes *et al*. showed that HCT116 are sensitive towards treatment using KRas inhibitors.[252]

LS-174T cell growth was not influenced by the introduction of the Deltacovalin, which is in agreement with its KRas independent status. The cell growth of oncogenic BRAF^{V600E} mutation carrying HT-cells was moderately affected.[276]

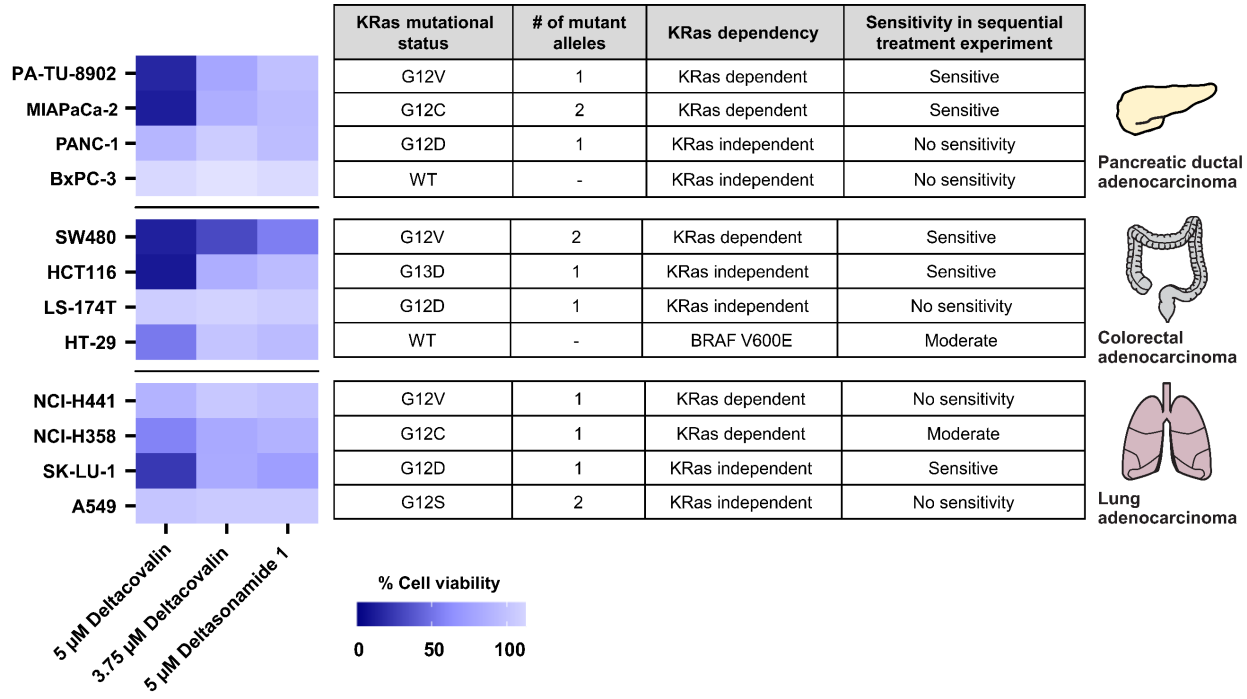

KRas mutational status	# of mutant alleles	KRas dependency	Sensitivity in sequential treatment experiment
G12V	1	KRas dependent	Sensitive
G12C	2	KRas dependent	Sensitive
G12D	1	KRas independent	No sensitivity
WT	-	KRas independent	No sensitivity
G12V	2	KRas dependent	Sensitive
G13D	1	KRas independent	Sensitive
G12D	1	KRas independent	No sensitivity
WT	-	BRAF V600E	Moderate
G12V	1	KRas dependent	No sensitivity
G12C	1	KRas dependent	Moderate
G12D	1	KRas independent	Sensitive
G12S	2	KRas independent	No sensitivity

Figure 77: Overview of the sequential treatment results of PDAC, CRC, and LAC cell lines. The cell viability was determined using the AUC, which corresponds to the sensitivity of the cell line to PDEδ inhibitor treatment. A smaller AUC indicated a higher sensitivity of the cell line towards compound treatment and, thus, a lower cell viability. BRAF^{V600E} mutations are oncogenic and downstream of the Ras-ERK signaling cascade.

Finally, lung cancer cell lines NCI-H441 and NCI-H358 are both KRAS-dependent. However, their cell growth either remained unaltered in the presence of Deltacovalin or was only moderately reduced.

Table 8: Comparison of Ras isoform abundance in selected cell lines. Data obtained from Hood *et al.*[277]

Cell line	KRas4A	KRas4B	HRas	NRas
MIAPaCa-2	4.0 %	51.9 %	13.6 %	33.9 %
HCT116	10.9 %	48.7 %	21.4 %	33.4 %
HT-29	8.7 %	39.5 %	19.2 %	32.6 %
NCI-H358	9.5 %	68.1 %	4.6 %	19.8 %
NCI-H441	16.1 %	66.7 %	5.3 %	17.9 %

One possible explanation for this observation could be the varying abundance of Ras isoforms in cells. Of the two KRas splice variants, KRas4A and KRasB, PDEδ can only translocate KRas4b from the plasma membrane.[277,278] Hood *et al*. investigated mutated Ras isoform patterns of various cancer cell lines.[277] Based on the data obtained from the study, the levels of the individual Ras isoforms in MIAPaCa-2, HCT116, HT-29, NCI-H358 and NCI-H441 cells were compared in Table 8. KRas4A and HRas have the lowest abundance across all compared cell lines. In comparison to the other cell lines, the LAC cell lines NCI-H358 and NCI-H441 exhibit lower levels of HRas and NRas, whereas KRas4B abundance is increased. Moreover, KRas4A levels are higher in the Deltacovalin resistant cell lines NCI-H441. Another contributing factor could be the imbalanced expression ratios of wildtype and mutant KRas observed for both cell lines, which approximately corresponds to 1:1 for NCI-H441 cells.[277] SK-LU-1 were categorized as KRas independent, and during the course of the sequential treatments, the presence of Deltacovalin decreased their cell growth. Finally, KRas-independent A549 cells were evaluated and displayed no sensitivity towards PDEδ inhibition. In conclusion, the KRas dependency status mostly parallels sensitivity towards Deltacovalin-mediated PDEδ inhibition, with the exception of the investigated lung cancer cell lines.

The murine cell lines KP1035, KPACK135-1, and KPACK135-10 harbor a KRas G12D mutation and a TP53 deletion, as these mutations often co-occur in lung adenocarcinomas. As the doubling time of the murine cell line was approximately 12-13 h, increased compound concentrations (i.e. 6.25 instead of 5 µM) were required for the sequential treatment experiments: For all three cell lines, 6.25 µM and 5 µM of Deltacovalin and 6.25 µM Deltasonamide 1 completely attenuated their growth during single treatments. The effect of the compounds was also accompanied by an elevation of caspase 3/7 activity, indicating upregulation of apoptosis in the murine cells. However, apoptosis activation in KP1035 was more delayed, which aligns with the results obtained for the sequential treatment. Deltacovalin solely delayed the cell growth of KP1035, and Deltasonamide 1 did not affect their growth. The other two cell lines, KPACK135-1 and KPACK135-10, displayed sensitivity towards the presence of Deltacovalin. The efficacy of Deltacovalin in the KRas mutated murine cell lines opened up the opportunity to explore the potency of the covalent PDEδ in mouse models. Hence, PK/PD studies were conducted, revealing that despite the high *in vitro* compound solubility, the oral availability of Deltacovalin was poor and that the IP administration method is most effective for compound treatment *in vivo*. Deltacovalin displayed suitable bioavailability, compound distribution, and clearance in non-tumor-bearing mice. A treatment regimen of 15 mg/kg Deltacovalin daily for 21 days was found suitable for *in vivo* studies in mice. The *in vivo* efficacy was studied in a KP mouse line carrying the KRas G12D

mutation and an inducible TP53 deletion, similar to the tested KP cell lines. Deltacovalin extended the overall survival of the KP mouse line and significantly reduced the tumor volume. To date, the KP mouse model remains incurable. However, previous studies have shown that cisplatin treatments can extend survival in mice similar to Deltacovalin treatments, without completely eliminating tumors.[139] Interestingly, checkpoint inhibitors targeting PD-1 are ineffective in the KP mouse model.[279]

5.2.2 Influence of Deltacovalin on the phosphoproteome

The impact of Deltacovalin on the cellular phosphorylation state revealed that various proteins involved in signaling downstream of Ras, the MAPK family signaling cascades as well as transcription processes were influenced by the presence of the covalent PDEδ inhibitor Deltacovalin. A list of selected modulated proteins alongside their role within KRas signaling is summarized in Table 9.

Table 9: List of selected KRas signaling-relevant proteins with changed phosphorylation levels following treatment Deltacovalin-treatment. PM: plasma membrane.

Gene name	Protein name	Role within KRas signaling
ARAF	A-RAF	Regulation of tumor growth[264]
MAP2K1	MEK1	Essential for oncogenic signal transduction within the KRas/B-RAF pathway[280]
MAP2K2	MEK2	
PKC	PKC	PKC-mediated phosphorylation of S181 within the polybasic region of KRas enhances its translocation from the PM to intracellular membranes[267]
SRC	Src	Oncogenic KRas upregulates Src protein levels, which is required to promote metastasis and drug resistance[265]

The kinases MEK1 and MEK2 are both crucial for the oncogenic signal transduction of KRas, whereas A-RAF regulates tumor growth. In cells treated with Deltacovalin, a reduction in kinase phosphorylations for MEK1, MEK2, and A-RAF was observed, aligning with the PDEδ-mediated disruption of KRas signaling by the covalent inhibitor. This trend could also be observed for the PKC kinase. Interestingly, the PKC is involved in the regulation of KRas localization. Furthermore, oncogenic KRas increases the levels of the Src protein, which are necessary for enhancing metastasis and drug resistance. The presence of Deltacovalin enhanced the phosphorylation of the Src kinase.

The presence of Deltacovalin modulated the phosphorylation of various proteins involved in transcription processes, as well as CLK1 and 2, which are crucial for splicing processes. This could be explained by the oncogenic activity of KRas, which increases various transcription factors and deregulates the cellular transcriptome.[281]

Taken together, these results provide additional validation of the impact of Deltacovalin on inhibiting KRas signaling activity.

5.2.3 Investigation of Deltacovalin's influence on lysosomotropism and phospholipidosis

Earlier studies demonstrated that Deltasonamide 1, which is the parental compound of Deltacovalin, is lysosomotropic.[268] Deltacovalin accumulates in the lysosomes, a property shared with Deltasonamide 1. A great challenge for PDEδ inhibitorss was the noticeable difference observed between the picomolar *in vitro* and micromolar *in cellulo* potency. Moreover, the real-time kinetic imaging experiments demonstrated that while 5 µM of Deltacovalin effectively eradicated cancer cells, 3.75 µM only resulted in minor to negligible effects. Previous studies have shown that the concentration of chloroquine accumulated in the lysosomes can reach up to 20 mM.[282] The accumulation of Deltacovalin in the lysosomes may result in an imbalance of molecules available in the cytosol for PDEδ inhibition. This assumption is strengthened by the observation that the dose-response analysis of Deltazinone, a non-lysosomotropic substance, exhibited a concentration-dependent effect on cell viability.

To this day, the physiological consequence of lysosomotropism is not fully comprehended. Conversely, cancer cells exhibit increased lysosomal function, which is essential for maintaining their elevated metabolism and proliferation. The PI3K-AKT inhibitor AZD5363 suppressed autophagy without the induction of apoptosis, but in combination with the lysosomotropic compound chloroquine, a significant reduction of tumor volume was enabled.[269] This provides an opportunity for therapeutic interventions targeting lysosomal membrane permeabilization, which can result in cell death.[269] Compounds with lysosomotropic properties can compromise the function of lysosomal enzymes, leading to the formation of multilamellar bodies that trigger phospholipid buildup, a phenomenon known as phospholipidosis.[271] Both PDEδ inhibitors increased phospholipid levels after 48 h of treatment.

5.3 Conclusion and future perspectives

Although Deltasonamide is a picomolar PDEδ inhibitor forming up to seven hydrogen bonds, the compound was still susceptible to Arl2/3-mediated displacement. The Waldmann group developed a new type of covalent PDEδ inhibitor to resist displacement by Arl2/3. Deltacovalin, the most promising covalent inhibitor, demonstrated significant benefits in treating the KRas-dependent cell line PA-TU-8902 while showing no impact on the growth of KRas-independent BxPC-3 cells. The response of cell growth of human and murine cell lines to Deltacovalin treatment mostly aligned with the KRas dependency status of the respective cell lines. Deltacovalin treatment significantly reduced tumor volume of a KRas-driven KP mouse line. Additionally, various proteins relevant to KRas signaling were modulated by Deltacovalin treatment. It was found that Deltacovalin and Deltasonamide 1 are lysosomotropic and result in the induction of phospholipidosis. However, the selectivity of Deltacovalin *in cellulo* is yet to be determined.

Taken together, Deltacovalin has proven to be a potent, covalent inhibitor of KRas signaling, offering an alternative strategy impeding this oncogenic signaling pathway.

6. REFERENCES

1 Upadhyay, A. Cancer: An unknown territory; rethinking before going ahead. *Genes & diseases* **8**, 655-661, doi:10.1016/j.gendis.2020.09.002 (2021).

2 Quail, D. F. & Joyce, J. A. Microenvironmental regulation of tumor progression and metastasis. *Nature Medicine* **19**, 1423-1437, doi:10.1038/nm.3394 (2013).

3 Sung, H. *et al.* Global Cancer Statistics 2020: GLOBOCAN Estimates of Incidence and Mortality Worldwide for 36 Cancers in 185 Countries. *CA: A Cancer Journal for Clinicians* **71**, 209-249, doi:https://doi.org/10.3322/caac.21660 (2021).

4 Jassim, A., Rahrmann, E. P., Simons, B. D. & Gilbertson, R. J. Cancers make their own luck: theories of cancer origins. *Nature Reviews Cancer* **23**, 710-724, doi:10.1038/s41568-023-00602-5 (2023).

5 Ujvari, B. *et al.* Genetic diversity, inbreeding and cancer. *Proceedings of the Royal Society B: Biological Sciences* **285**, 20172589, doi:doi:10.1098/rspb.2017.2589 (2018).

6 Hanahan, D. & Weinberg, Robert A. Hallmarks of Cancer: The Next Generation. *Cell* **144**, 646-674, doi:10.1016/j.cell.2011.02.013 (2011).

7 Hanahan, D. Hallmarks of Cancer: New Dimensions. *Cancer Discovery* **12**, 31-46, doi:10.1158/2159-8290.Cd-21-1059 (2022).

8 Menon, S., Shin, S. & Dy, G. Advances in Cancer Immunotherapy in Solid Tumors. *Cancers* **8**, 106 (2016).

9 Desai, R., Coxon, A. T. & Dunn, G. P. Therapeutic applications of the cancer immunoediting hypothesis. *Seminars in Cancer Biology* **78**, 63-77, doi:https://doi.org/10.1016/j.semcancer.2021.03.002 (2022).

10 Dunn, G. P., Old, L. J. & Schreiber, R. D. The immunobiology of cancer immunosurveillance and immunoediting. *Immunity* **21**, 137-148 (2004).

11 Burnet, F. M. Immunological aspects of malignant disease. *Lancet (London, England)* **1**, 1171-1174, doi:10.1016/s0140-6736(67)92837-1 (1967).

12 Thomas, L. On immunosurveillance in human cancer. *The Yale journal of biology and medicine* **55**, 329-333 (1982).

13 van der Burg, S. H., Arens, R., Ossendorp, F., van Hall, T. & Melief, C. J. M. Vaccines for established cancer: overcoming the challenges posed by immune evasion. *Nature Reviews Cancer* **16**, 219-233, doi:10.1038/nrc.2016.16 (2016).

14 Mittal, D., Gubin, M. M., Schreiber, R. D. & Smyth, M. J. New insights into cancer immunoediting and its three component phases--elimination, equilibrium and escape. *Current opinion in immunology* **27**, 16-25, doi:10.1016/j.coi.2014.01.004 (2014).

15 Sato, T. *et al.* Interleukin 10 in the tumor microenvironment: a target for anticancer immunotherapy. *Immunologic research* **51**, 170-182, doi:10.1007/s12026-011-8262-6 (2011).

16 Yan, J., Smyth, M. J. & Teng, M. W. L. Interleukin (IL)-12 and IL-23 and Their Conflicting Roles in Cancer. *Cold Spring Harbor perspectives in biology* **10**, doi:10.1101/cshperspect.a028530 (2018).

17 Schreiber, R. D., Old, L. J. & Smyth, M. J. Cancer Immunoediting: Integrating Immunity's Roles in Cancer Suppression and Promotion. *Science* **331**, 1565-1570, doi:doi:10.1126/science.1203486 (2011).

18 Lasek, W. Cancer immunoediting hypothesis: history, clinical implications and controversies. *Central European Journal of Immunology* **47**, 168-174, doi:10.5114/ceji.2022.117376 (2022).

19 Esfahani, K. *et al.* A review of cancer immunotherapy: from the past, to the present, to the future. *Current oncology (Toronto, Ont.)* **27**, S87-s97, doi:10.3747/co.27.5223 (2020).

20 Anderson, N. M. & Simon, M. C. The tumor microenvironment. *Current biology : CB* **30**, R921-r925, doi:10.1016/j.cub.2020.06.081 (2020).

REFERENCES

21 Tiwari, A., Trivedi, R. & Lin, S.-Y. Tumor microenvironment: barrier or opportunity towards effective cancer therapy. *Journal of Biomedical Science* **29**, 83, doi:10.1186/s12929-022-00866-3 (2022).

22 Jin, M.-Z. & Jin, W.-L. The updated landscape of tumor microenvironment and drug repurposing. *Signal Transduction and Targeted Therapy* **5**, 166, doi:10.1038/s41392-020-00280-x (2020).

23 de Visser, K. E. & Joyce, J. A. The evolving tumor microenvironment: From cancer initiation to metastatic outgrowth. *Cancer Cell* **41**, 374-403, doi:https://doi.org/10.1016/j.ccell.2023.02.016 (2023).

24 Herberman, R. B., Nunn, M. E. & Lavrin, D. H. Natural cytotoxic reactivity of mouse lymphoid cells against syngeneic acid allogeneic tumors. I. Distribution of reactivity and specificity. *International journal of cancer* **16**, 216-229, doi:10.1002/ijc.2910160204 (1975).

25 Kiessling, R., Klein, E. & Wigzell, H. "Natural" killer cells in the mouse. I. Cytotoxic cells with specificity for mouse Moloney leukemia cells. Specificity and distribution according to genotype. *European journal of immunology* **5**, 112-117, doi:10.1002/eji.1830050208 (1975).

26 Abel, A. M., Yang, C., Thakar, M. S. & Malarkannan, S. Natural Killer Cells: Development, Maturation, and Clinical Utilization. *Frontiers in Immunology* **9**, doi:10.3389/fimmu.2018.01869 (2018).

27 Mace, E. M. Human natural killer cells: Form, function, and development. *Journal of Allergy and Clinical Immunology* **151**, 371-385, doi:10.1016/j.jaci.2022.09.022 (2023).

28 Waldhauer, I. & Steinle, A. NK cells and cancer immunosurveillance. *Oncogene* **27**, 5932-5943, doi:10.1038/onc.2008.267 (2008).

29 Nowbakht, P. *et al.* Ligands for natural killer cell–activating receptors are expressed upon the maturation of normal myelomonocytic cells but at low levels in acute myeloid leukemias. *Blood* **105**, 3615-3622, doi:10.1182/blood-2004-07-2585 (2005).

30 Prager, I. & Watzl, C. Mechanisms of natural killer cell-mediated cellular cytotoxicity. *Journal of Leukocyte Biology* **105**, 1319-1329, doi:https://doi.org/10.1002/JLB.MR0718-269R (2019).

31 Davis, D. M. *et al.* The human natural killer cell immune synapse. *Proceedings of the National Academy of Sciences of the United States of America* **96**, 15062-15067, doi:10.1073/pnas.96.26.15062 (1999).

32 Watzl, C. in *Advances in Immunology* Vol. 124 (ed Frederick W. Alt) 137-170 (Academic Press, 2014).

33 Prager, I. *et al.* NK cells switch from granzyme B to death receptor–mediated cytotoxicity during serial killing. *Journal of Experimental Medicine* **216**, 2113-2127, doi:10.1084/jem.20181454 (2019).

34 Chowdhury, D. & Lieberman, J. Death by a Thousand Cuts: Granzyme Pathways of Programmed Cell Death. *Annual Review of Immunology* **26**, 389-420, doi:https://doi.org/10.1146/annurev.immunol.26.021607.090404 (2005).

35 Janiszewski, T. *et al.* Noninvasive optical detection of granzyme B from natural killer cells with enzyme-activated fluorogenic probes. *Journal of Biological Chemistry* **295**, 9567-9582, doi:https://doi.org/10.1074/jbc.RA120.013204 (2020).

36 Ben-Shmuel, A., Sabag, B., Biber, G. & Barda-Saad, M. The Role of the Cytoskeleton in Regulating the Natural Killer Cell Immune Response in Health and Disease: From Signaling Dynamics to Function. *Frontiers in Cell and Developmental Biology* **9**, doi:10.3389/fcell.2021.609532 (2021).

37 Konjević, G. M., Vuletić, A. M., Mirjačić Martinović, K. M., Larsen, A. K. & Jurišić, V. B. The role of cytokines in the regulation of NK cells in the tumor environment. *Cytokine* **117**, 30-40, doi:https://doi.org/10.1016/j.cyto.2019.02.001 (2019).

REFERENCES

38 Ferrari de Andrade, L. *et al.* Inhibition of MICA and MICB Shedding Elicits NK-Cell-Mediated Immunity against Tumors Resistant to Cytotoxic T Cells. *Cancer immunology research* **8**, 769-780, doi:10.1158/2326-6066.Cir-19-0483 (2020).

39 Xing, S. & Ferrari de Andrade, L. NKG2D and MICA/B shedding: a 'tag game' between NK cells and malignant cells. *Clinical & Translational Immunology* **9**, e1230, doi:https://doi.org/10.1002/cti2.1230 (2020).

40 Ran, G. h. *et al.* Natural killer cell homing and trafficking in tissues and tumors: from biology to application. *Signal Transduction and Targeted Therapy* **7**, 205, doi:10.1038/s41392-022-01058-z (2022).

41 Terrén, I., Orrantia, A., Vitallé, J., Zenarruzabeitia, O. & Borrego, F. NK Cell Metabolism and Tumor Microenvironment. *Frontiers in Immunology* **10**, doi:10.3389/fimmu.2019.02278 (2019).

42 Domagala, J. *et al.* The Tumor Microenvironment-A Metabolic Obstacle to NK Cells' Activity. *Cancers (Basel)* **12**, doi:10.3390/cancers12123542 (2020).

43 Zhang, M. *et al.* TGF-β Signaling and Resistance to Cancer Therapy. *Frontiers in Cell and Developmental Biology* **9**, doi:10.3389/fcell.2021.786728 (2021).

44 Viel, S., Besson, L., Marotel, M., Walzer, T. & Marçais, A. Regulation of mTOR, Metabolic Fitness, and Effector Functions by Cytokines in Natural Killer Cells. *Cancers* **9**, 132 (2017).

45 Patterson, C., Hazime, K. S., Zelenay, S. & Davis, D. M. Prostaglandin E_2 impacts multiple stages of the natural killer cell antitumor immune response. *European journal of immunology* **54**, 2350635, doi:https://doi.org/10.1002/eji.202350635 (2024).

46 Wang, D. & DuBois, R. N. Eicosanoids and cancer. *Nature Reviews Cancer* **10**, 181-193, doi:10.1038/nrc2809 (2010).

47 Dean, P. T. & Hooks, S. B. Pleiotropic effects of the COX-2/PGE2 axis in the glioblastoma tumor microenvironment. *Frontiers in Oncology* **12**, doi:10.3389/fonc.2022.1116014 (2023).

48 Yang, J. *et al.* Inhibition of PI3K-AKT Signaling Blocks PGE2-Induced COX-2 Expression in Lung Adenocarcinoma. *OncoTargets and Therapy* **13**, 8197-8208, doi:10.2147/OTT.S263977 (2020).

49 Park, A. *et al.* Prostaglandin E2 Secreted by Thyroid Cancer Cells Contributes to Immune Escape Through the Suppression of Natural Killer (NK) Cell Cytotoxicity and NK Cell Differentiation. *Frontiers in Immunology* **9**, doi:10.3389/fimmu.2018.01859 (2018).

50 Harizi, H. Reciprocal crosstalk between dendritic cells and natural killer cells under the effects of PGE2 in immunity and immunopathology. *Cellular & Molecular Immunology* **10**, 213-221, doi:10.1038/cmi.2013.1 (2013).

51 Drake, C. G., Lipson, E. J. & Brahmer, J. R. Breathing new life into immunotherapy: review of melanoma, lung and kidney cancer. *Nature Reviews Clinical Oncology* **11**, 24-37, doi:10.1038/nrclinonc.2013.208 (2014).

52 Buchbinder, E. I. & Desai, A. CTLA-4 and PD-1 Pathways: Similarities, Differences, and Implications of Their Inhibition. *American journal of clinical oncology* **39**, 98-106, doi:10.1097/coc.0000000000000239 (2016).

53 Sharma, P. & Allison, J. P. The future of immune checkpoint therapy. *Science* **348**, 56-61, doi:10.1126/science.aaa8172 (2015).

54 Huang, P. W. & Chang, J. W. Immune checkpoint inhibitors win the 2018 Nobel Prize. *Biomedical journal* **42**, 299-306, doi:10.1016/j.bj.2019.09.002 (2019).

55 Mitra, A. *et al.* From bench to bedside: the history and progress of CAR T cell therapy. *Frontiers in Immunology* **14**, doi:10.3389/fimmu.2023.1188049 (2023).

56 Peterson, C., Denlinger, N. & Yang, Y. Recent Advances and Challenges in Cancer Immunotherapy. *Cancers (Basel)* **14**, doi:10.3390/cancers14163972 (2022).

57 Shin, M. H. *et al.* NK Cell-Based Immunotherapies in Cancer. *Immune network* **20**, e14, doi:10.4110/in.2020.20.e14 (2020).

REFERENCES

58 Page, A., Chuvin, N., Valladeau-Guilemond, J. & Depil, S. Development of NK cell-based cancer immunotherapies through receptor engineering. *Cellular & Molecular Immunology* **21**, 315-331, doi:10.1038/s41423-024-01145-x (2024).

59 Dahlberg, C. I. M., Sarhan, D., Chrobok, M., Duru, A. D. & Alici, E. Natural Killer Cell-Based Therapies Targeting Cancer: Possible Strategies to Gain and Sustain Anti-Tumor Activity. *Frontiers in Immunology* **6**, doi:10.3389/fimmu.2015.00605 (2015).

60 Maskalenko, N. A., Zhigarev, D. & Campbell, K. S. Harnessing natural killer cells for cancer immunotherapy: dispatching the first responders. *Nature Reviews Drug Discovery* **21**, 559-577, doi:10.1038/s41573-022-00413-7 (2022).

61 Offringa, R., Kötzner, L., Huck, B. & Urbahns, K. The expanding role for small molecules in immuno-oncology. *Nature Reviews Drug Discovery* **21**, 821-840, doi:10.1038/s41573-022-00538-9 (2022).

62 van der Zanden, S. Y., Luimstra, J. J., Neefjes, J., Borst, J. & Ovaa, H. Opportunities for Small Molecules in Cancer Immunotherapy. *Trends in Immunology* **41**, 493-511, doi:https://doi.org/10.1016/j.it.2020.04.004 (2020).

63 Yu, Y. The Function of NK Cells in Tumor Metastasis and NK Cell-Based Immunotherapy. *Cancers* **15**, 2323 (2023).

64 Lian, G., Mak, T. S.-K., Yu, X. & Lan, H.-Y. Challenges and Recent Advances in NK Cell-Targeted Immunotherapies in Solid Tumors. *International Journal of Molecular Sciences* **23**, 164 (2022).

65 Wang, F. *et al.* Small-molecule agents for cancer immunotherapy. *Acta Pharmaceutica Sinica B* **14**, 905-952, doi:https://doi.org/10.1016/j.apsb.2023.12.010 (2024).

66 Kirsten, W. H. & Mayer, L. A. Morphologic responses to a murine erythroblastosis virus. *Journal of the National Cancer Institute* **39**, 311-335 (1967).

67 Harvey, J. J. AN UNIDENTIFIED VIRUS WHICH CAUSES THE RAPID PRODUCTION OF TUMOURS IN MICE. *Nature* **204**, 1104-1105, doi:10.1038/2041104b0 (1964).

68 Shimizu, K. *et al.* Three human transforming genes are related to the viral ras oncogenes. *Proceedings of the National Academy of Sciences of the United States of America* **80**, 2112-2116, doi:10.1073/pnas.80.8.2112 (1983).

69 Hall, A., Marshall, C. J., Spurr, N. K. & Weiss, R. A. Identification of transforming gene in two human sarcoma cell lines as a new member of the ras gene family located on chromosome 1. *Nature* **303**, 396-400, doi:10.1038/303396a0 (1983).

70 Goitre, L., Trapani, E., Trabalzini, L. & Retta, S. F. in *Ras Signaling: Methods and Protocols* (eds Lorenza Trabalzini & Saverio Francesco Retta) 1-18 (Humana Press, 2014).

71 Vetter, I. R. & Wittinghofer, A. The guanine nucleotide-binding switch in three dimensions. *Science* **294**, 1299-1304, doi:10.1126/science.1062023 (2001).

72 Hancock, J. F., Magee, A. I., Childs, J. E. & Marshall, C. J. All ras proteins are polyisoprenylated but only some are palmitoylated. *Cell* **57**, 1167-1177, doi:10.1016/0092-8674(89)90054-8 (1989).

73 Hancock, J. F., Paterson, H. & Marshall, C. J. A polybasic domain or palmitoylation is required in addition to the CAAX motif to localize p21ras to the plasma membrane. *Cell* **63**, 133-139, doi:10.1016/0092-8674(90)90294-o (1990).

74 Wu, X. *et al.* Small molecular inhibitors for KRAS-mutant cancers. *Frontiers in Immunology* **14**, doi:10.3389/fimmu.2023.1223433 (2023).

75 Huang, L., Guo, Z., Wang, F. & Fu, L. KRAS mutation: from undruggable to druggable in cancer. *Signal Transduction and Targeted Therapy* **6**, 386, doi:10.1038/s41392-021-00780-4 (2021).

76 Cox, A. D., Fesik, S. W., Kimmelman, A. C., Luo, J. & Der, C. J. Drugging the undruggable RAS: Mission Possible? *Nature Reviews Drug Discovery* **13**, 828-851, doi:10.1038/nrd4389 (2014).

REFERENCES

77 Buscail, L., Bournet, B. & Cordelier, P. Role of oncogenic KRAS in the diagnosis, prognosis and treatment of pancreatic cancer. *Nature reviews. Gastroenterology & hepatology* **17**, 153-168, doi:10.1038/s41575-019-0245-4 (2020).

78 Moore, A. R., Rosenberg, S. C., McCormick, F. & Malek, S. RAS-targeted therapies: is the undruggable drugged? *Nature Reviews Drug Discovery* **19**, 533-552, doi:10.1038/s41573-020-0068-6 (2020).

79 Schmick, M. *et al.* KRas Localizes to the Plasma Membrane by Spatial Cycles of Solubilization, Trapping and Vesicular Transport. *Cell* **157**, 459-471, doi:https://doi.org/10.1016/j.cell.2014.02.051 (2014).

80 Schmick, M., Kraemer, A. & Bastiaens, P. I. H. Ras moves to stay in place. *Trends in Cell Biology* **25**, 190-197, doi:https://doi.org/10.1016/j.tcb.2015.02.004 (2015).

81 Florio, S. K., Prusti, R. K. & Beavo, J. A. Solubilization of Membrane-bound Rod Phosphodiesterase by the Rod Phosphodiesterase Recombinant δ Subunit*. *Journal of Biological Chemistry* **271**, 24036-24047, doi:https://doi.org/10.1074/jbc.271.39.24036 (1996).

82 Zhang, H. *et al.* Photoreceptor cGMP Phosphodiesterase δ Subunit (PDEδ) Functions as a Prenyl-binding Protein*. *Journal of Biological Chemistry* **279**, 407-413, doi:https://doi.org/10.1074/jbc.M306559200 (2004).

83 Zhang, H. *et al.* in *Methods in Enzymology* Vol. 403 42-56 (Academic Press, 2005).

84 Zhang, H., Constantine, R., Frederick, J. M. & Baehr, W. The prenyl-binding protein PrBP/δ: A chaperone participating in intracellular trafficking. *Vision Research* **75**, 19-25, doi:https://doi.org/10.1016/j.visres.2012.08.013 (2012).

85 Ismail, S. A. *et al.* Arl2-GTP and Arl3-GTP regulate a GDI-like transport system for farnesylated cargo. *Nature Chemical Biology* **7**, 942-949, doi:10.1038/nchembio.686 (2011).

86 Hanzal-Bayer, M., Linari, M. & Wittinghofer, A. Properties of the Interaction of Arf-like Protein 2 with PDEδ. *Journal of Molecular Biology* **350**, 1074-1082, doi:https://doi.org/10.1016/j.jmb.2005.05.036 (2005).

87 Cox, A. D., Fesik, S. W., Kimmelman, A. C., Luo, J. & Der, C. J. Drugging the undruggable RAS: Mission possible? *Nature reviews. Drug discovery* **13**, 828-851, doi:10.1038/nrd4389 (2014).

88 Punekar, S. R., Velcheti, V., Neel, B. G. & Wong, K.-K. The current state of the art and future trends in RAS-targeted cancer therapies. *Nature Reviews Clinical Oncology* **19**, 637-655, doi:10.1038/s41571-022-00671-9 (2022).

89 Dias Carvalho, P. *et al.* KRAS Oncogenic Signaling Extends beyond Cancer Cells to Orchestrate the Microenvironment. *Cancer research* **78**, 7-14, doi:10.1158/0008-5472.Can-17-2084 (2018).

90 Lesina, M. *et al.* Stat3/Socs3 Activation by IL-6 Transsignaling Promotes Progression of Pancreatic Intraepithelial Neoplasia and Development of Pancreatic Cancer. *Cancer Cell* **19**, 456-469, doi:https://doi.org/10.1016/j.ccr.2011.03.009 (2011).

91 Sunaga, N. *et al.* Oncogenic KRAS-induced interleukin-8 overexpression promotes cell growth and migration and contributes to aggressive phenotypes of non-small cell lung cancer. *International journal of cancer* **130**, 1733-1744, doi:https://doi.org/10.1002/ijc.26164 (2012).

92 Ling, J. *et al.* KrasG12D-Induced IKK2/β/NF-κB Activation by IL-1α and p62 Feedforward Loops Is Required for Development of Pancreatic Ductal Adenocarcinoma. *Cancer Cell* **21**, 105-120, doi:https://doi.org/10.1016/j.ccr.2011.12.006 (2012).

93 Molina-Arcas, M. & Downward, J. Exploiting the therapeutic implications of KRAS inhibition on tumor immunity. *Cancer Cell* **42**, 338-357, doi:https://doi.org/10.1016/j.ccell.2024.02.012 (2024).

REFERENCES

94 Ostrem, J. M., Peters, U., Sos, M. L., Wells, J. A. & Shokat, K. M. K-Ras(G12C) inhibitors allosterically control GTP affinity and effector interactions. *Nature* **503**, 548-551, doi:10.1038/nature12796 (2013).

95 Research CfDEa. FDA grants accelerated approval to sotorasib for KRAS G12C mutated NLCSC. U.S. Food and Drug Administration; 2021. (Accessed 4th of April 2024). <https://www.fda.gov/drugs/resources-information-approved-drugs/fda-grants-accelerated-approval-sotorasib-kras-g12c-mutated-nsclc>.

96 Lanman, B. A. *et al.* Discovery of a Covalent Inhibitor of KRAS(G12C) (AMG 510) for the Treatment of Solid Tumors. *Journal of medicinal chemistry* **63**, 52-65, doi:10.1021/acs.jmedchem.9b01180 (2020).

97 Fell, J. B. *et al.* Identification of the Clinical Development Candidate MRTX849, a Covalent KRAS(G12C) Inhibitor for the Treatment of Cancer. *Journal of medicinal chemistry* **63**, 6679-6693, doi:10.1021/acs.jmedchem.9b02052 (2020).

98 Research CfDEa. FDA grants accelerated approval to adagrasib for KRAS G12C-mutated NSCLC. U.S. Food and Drug Administration; 2022. (4th of April 2024). <https://www.fda.gov/drugs/resources-information-approved-drugs/fda-grants-accelerated-approval-adagrasib-kras-g12c-mutated-nsclc>.

99 Batrash, F., Kutmah, M. & Zhang, J. The current landscape of using direct inhibitors to target KRASG12C-mutated NSCLC. *Experimental Hematology & Oncology* **12**, 93, doi:10.1186/s40164-023-00453-8 (2023).

100 Kim, D. *et al.* Pan-KRAS inhibitor disables oncogenic signalling and tumour growth. *Nature* **619**, 160-166, doi:10.1038/s41586-023-06123-3 (2023).

101 Haidar, M. & Jacquemin, P. Past and Future Strategies to Inhibit Membrane Localization of the KRAS Oncogene. *Int J Mol Sci* **22**, doi:10.3390/ijms222413193 (2021).

102 Zimmermann, G. *et al.* Small molecule inhibition of the KRAS–PDEδ interaction impairs oncogenic KRAS signalling. *Nature* **497**, 638-642, doi:10.1038/nature12205 (2013).

103 Papke, B. *et al.* Identification of pyrazolopyridazinones as PDEδ inhibitors. *Nature Communications* **7**, 11360, doi:10.1038/ncomms11360 (2016).

104 Martín-Gago, P. *et al.* A PDE6δ-KRas Inhibitor Chemotype with up to Seven H-Bonds and Picomolar Affinity that Prevents Efficient Inhibitor Release by Arl2. *Angewandte Chemie International Edition* **56**, 2423-2428, doi:https://doi.org/10.1002/anie.201610957 (2017).

105 Martín-Gago, P. *et al.* Covalent Protein Labeling at Glutamic Acids. *Cell Chemical Biology* **24**, 589-597.e585, doi:https://doi.org/10.1016/j.chembiol.2017.03.015 (2017).

106 Voices of chemical biology. *Nat Chem Biol* **11**, 378-379, doi:10.1038/nchembio.1820 (2015).

107 Makurvet, F. D. Biologics vs. small molecules: Drug costs and patient access. *Medicine in Drug Discovery* **9**, 100075, doi:https://doi.org/10.1016/j.medidd.2020.100075 (2021).

108 Beck, H., Härter, M., Haß, B., Schmeck, C. & Baerfacker, L. Small molecules and their impact in drug discovery: A perspective on the occasion of the 125th anniversary of the Bayer Chemical Research Laboratory. *Drug Discovery Today* **27**, 1560-1574, doi:https://doi.org/10.1016/j.drudis.2022.02.015 (2022).

109 Cesa, L. C., Mapp, A. K. & Gestwicki, J. E. Direct and Propagated Effects of Small Molecules on Protein–Protein Interaction Networks. *Frontiers in Bioengineering and Biotechnology* **3**, doi:10.3389/fbioe.2015.00119 (2015).

110 Che, Y., Gilbert, A. M., Shanmugasundaram, V. & Noe, M. C. Inducing protein-protein interactions with molecular glues. *Bioorganic & Medicinal Chemistry Letters* **28**, 2585-2592, doi:https://doi.org/10.1016/j.bmcl.2018.04.046 (2018).

111 Mayor-Ruiz, C. *et al.* Plasticity of the Cullin-RING Ligase Repertoire Shapes Sensitivity to Ligand-Induced Protein Degradation. *Molecular Cell* **75**, 849-858.e848, doi:https://doi.org/10.1016/j.molcel.2019.07.013 (2019).

REFERENCES

112 Sakamoto, K. M. *et al.* Protacs: Chimeric molecules that target proteins to the Skp1–Cullin–F box complex for ubiquitination and degradation. *Proceedings of the National Academy of Sciences* **98**, 8554-8559, doi:doi:10.1073/pnas.141230798 (2001).

113 Dias, D. A., Urban, S. & Roessner, U. A historical overview of natural products in drug discovery. *Metabolites* **2**, 303-336, doi:10.3390/metabo2020303 (2012).

114 Laraia, L. & Waldmann, H. Natural product inspired compound collections: evolutionary principle, chemical synthesis, phenotypic screening, and target identification. *Drug Discovery Today: Technologies* **23**, 75-82, doi:https://doi.org/10.1016/j.ddtec.2017.03.003 (2017).

115 Dobson, C. M. Chemical space and biology. *Nature* **432**, 824-828, doi:10.1038/nature03192 (2004).

116 Wetzel, S., Bon, R. S., Kumar, K. & Waldmann, H. Biology-oriented synthesis. *Angewandte Chemie (International ed. in English)* **50**, 10800-10826, doi:10.1002/anie.201007004 (2011).

117 van Hattum, H. & Waldmann, H. Biology-Oriented Synthesis: Harnessing the Power of Evolution. *Journal of the American Chemical Society* **136**, 11853-11859, doi:10.1021/ja505861d (2014).

118 Cremosnik, G. S., Liu, J. & Waldmann, H. Guided by evolution: from biology oriented synthesis to pseudo natural products. *Natural Product Reports* **37**, 1497-1510, doi:10.1039/D0NP00015A (2020).

119 Over, B. *et al.* Natural-product-derived fragments for fragment-based ligand discovery. *Nature Chemistry* **5**, 21-28, doi:10.1038/nchem.1506 (2013).

120 Karageorgis, G., Foley, D. J., Laraia, L., Brakmann, S. & Waldmann, H. Pseudo Natural Products-Chemical Evolution of Natural Product Structure. *Angewandte Chemie (International ed. in English)* **60**, 15705-15723, doi:10.1002/anie.202016575 (2021).

121 Davies, C. *et al.* Identification of a Novel Pseudo-Natural Product Type IV IDO1 Inhibitor Chemotype. *Angewandte Chemie International Edition* **61**, e202209374, doi:https://doi.org/10.1002/anie.202209374 (2022).

122 Schenone, M., Dančík, V., Wagner, B. K. & Clemons, P. A. Target identification and mechanism of action in chemical biology and drug discovery. *Nature Chemical Biology* **9**, 232-240, doi:10.1038/nchembio.1199 (2013).

123 Johnson, S. A. & Hunter, T. Kinomics: methods for deciphering the kinome. *Nature Methods* **2**, 17-25, doi:10.1038/nmeth731 (2005).

124 O' Connor, C. J., Laraia, L. & Spring, D. R. Chemical genetics. *Chemical Society Reviews* **40**, 4332-4345, doi:10.1039/C1CS15053G (2011).

125 Croston, G. E. The utility of target-based discovery. *Expert Opinion on Drug Discovery* **12**, 427-429, doi:10.1080/17460441.2017.1308351 (2017).

126 Eggert, U. S. The why and how of phenotypic small-molecule screens. *Nature Chemical Biology* **9**, 206-209, doi:10.1038/nchembio.1206 (2013).

127 Paananen, J. & Fortino, V. An omics perspective on drug target discovery platforms. *Briefings in bioinformatics* **21**, 1937-1953, doi:10.1093/bib/bbz122 (2020).

128 Tabana, Y., Babu, D., Fahlman, R., Siraki, A. G. & Barakat, K. Target identification of small molecules: an overview of the current applications in drug discovery. *BMC Biotechnology* **23**, 44, doi:10.1186/s12896-023-00815-4 (2023).

129 Sauer, P. & Bantscheff, M. Thermal Proteome Profiling for Drug Target Identification and Probing of Protein States. *Methods in molecular biology (Clifton, N.J.)* **2718**, 73-98, doi:10.1007/978-1-0716-3457-8_5 (2023).

130 Fang, H. *et al.* Recent advances in activity-based probes (ABPs) and affinity-based probes (AfBPs) for profiling of enzymes. *Chemical science* **12**, 8288-8310, doi:10.1039/d1sc01359a (2021).

REFERENCES

131 Li, G. *et al.* Currently Available Strategies for Target Identification of Bioactive Natural Products. *Frontiers in Chemistry* **9**, doi:10.3389/fchem.2021.761609 (2021).

132 Cravatt, B. F., Wright, A. T. & Kozarich, J. W. Activity-Based Protein Profiling: From Enzyme Chemistry to Proteomic Chemistry. *Annual Review of Biochemistry* **77**, 383-414, doi:https://doi.org/10.1146/annurev.biochem.75.101304.124125 (2008).

133 Meissner, F., Geddes-McAlister, J., Mann, M. & Bantscheff, M. The emerging role of mass spectrometry-based proteomics in drug discovery. *Nature Reviews Drug Discovery* **21**, 637-654, doi:10.1038/s41573-022-00409-3 (2022).

134 Savitski, M. M. *et al.* Tracking cancer drugs in living cells by thermal profiling of the proteome. *Science* **346**, 1255784, doi:10.1126/science.1255784 (2014).

135 Mader, M. M. *et al.* Which Small Molecule? Selecting Chemical Probes for Use in Cancer Research and Target Validation. *Cancer Discovery* **13**, 2150-2165, doi:10.1158/2159-8290.Cd-23-0536 (2023).

136 Titov, D. V. & Liu, J. O. Identification and validation of protein targets of bioactive small molecules. *Bioorganic & Medicinal Chemistry* **20**, 1902-1909, doi:https://doi.org/10.1016/j.bmc.2011.11.070 (2012).

137 Wyatt, P. G., Gilbert, I. H., Read, K. D. & Fairlamb, A. H. Target validation: linking target and chemical properties to desired product profile. *Current topics in medicinal chemistry* **11**, 1275-1283, doi:10.2174/156802611795429185 (2011).

138 Cromm, P. M. & Crews, C. M. Targeted Protein Degradation: from Chemical Biology to Drug Discovery. *Cell Chemical Biology* **24**, 1181-1190, doi:https://doi.org/10.1016/j.chembiol.2017.05.024 (2017).

139 Schmitt, A. *et al.* ATM Deficiency Is Associated with Sensitivity to PARP1- and ATR Inhibitors in Lung Adenocarcinoma. *Cancer research* **77**, 3040-3056, doi:10.1158/0008-5472.Can-16-3398 (2017).

140 Zawel, L. *et al.* Human Smad3 and Smad4 are sequence-specific transcription activators. *Mol Cell* **1**, 611-617, doi:10.1016/s1097-2765(00)80061-1 (1998).

141 Cox, J. & Mann, M. MaxQuant enables high peptide identification rates, individualized p.p.b.-range mass accuracies and proteome-wide protein quantification. *Nature Biotechnology* **26**, 1367-1372, doi:10.1038/nbt.1511 (2008).

142 Lundgren, S. Focusing on Relevance: CETSA-Guided Medicinal Chemistry and Lead Generation. *ACS Medicinal Chemistry Letters* **10**, 690-693, doi:10.1021/acsmedchemlett.9b00112 (2019).

143 Carpenter, A. E. *et al.* CellProfiler: image analysis software for identifying and quantifying cell phenotypes. *Genome Biology* **7**, R100, doi:10.1186/gb-2006-7-10-r100 (2006).

144 DuPage, M., Dooley, A. L. & Jacks, T. Conditional mouse lung cancer models using adenoviral or lentiviral delivery of Cre recombinase. *Nat Protoc* **4**, 1064-1072, doi:10.1038/nprot.2009.95 (2009).

145 Kabsch, W. XDS. *Acta crystallographica. Section D, Biological crystallography* **66**, 125-132, doi:10.1107/s0907444909047337 (2010).

146 McCoy, A. J. *et al.* Phaser crystallographic software. *Journal of applied crystallography* **40**, 658-674, doi:10.1107/s0021889807021206 (2007).

147 Liebschner, D. *et al.* Macromolecular structure determination using X-rays, neutrons and electrons: recent developments in Phenix. *Acta crystallographica. Section D, Structural biology* **75**, 861-877, doi:10.1107/s2059798319011471 (2019).

148 Afonine, P. V. *et al.* Towards automated crystallographic structure refinement with phenix.refine. *Acta crystallographica. Section D, Biological crystallography* **68**, 352-367, doi:10.1107/s0907444912001308 (2012).

149 Emsley, P., Lohkamp, B., Scott, W. G. & Cowtan, K. Features and development of Coot. *Acta crystallographica. Section D, Biological crystallography* **66**, 486-501, doi:10.1107/s0907444910007493 (2010).

REFERENCES

150 Frauwirth, K. A. & Thompson, C. B. Activation and inhibition of lymphocytes by costimulation. *The Journal of clinical investigation* **109**, 295-299, doi:10.1172/jci14941 (2002).

151 LeBien, T. W. & Tedder, T. F. B lymphocytes: how they develop and function. *Blood* **112**, 1570-1580, doi:10.1182/blood-2008-02-078071 (2008).

152 Kwon, H.-J. *et al.* NK cell function triggered by multiple activating receptors is negatively regulated by glycogen synthase kinase-3β. *Cellular Signalling* **27**, 1731-1741, doi:https://doi.org/10.1016/j.cellsig.2015.05.012 (2015).

153 Pereira, M. S. F. *et al.* Deletion of Glycogen Synthase Kinase 3 Beta Reprograms NK Cell Metabolism. *Cancers (Basel)* **15**, doi:10.3390/cancers15030705 (2023).

154 Cichocki, F. *et al.* GSK3 Inhibition Drives Maturation of NK Cells and Enhances Their Antitumor Activity. *Cancer research* **77**, 5664-5675, doi:10.1158/0008-5472.Can-17-0799 (2017).

155 Fionda, C. *et al.* Inhibition of glycogen synthase kinase-3 increases NKG2D ligand MICA expression and sensitivity to NK cell-mediated cytotoxicity in multiple myeloma cells: role of STAT3. *Journal of immunology (Baltimore, Md. : 1950)* **190**, 6662-6672, doi:10.4049/jimmunol.1201426 (2013).

156 Augello, G. *et al.* The Role of GSK-3 in Cancer Immunotherapy: GSK-3 Inhibitors as a New Frontier in Cancer Treatment. *Cells* **9**, doi:10.3390/cells9061427 (2020).

157 Liu, Y., Yang, Q., Chen, S., Li, Z. & Fu, L. Targeting VPS34 in autophagy: An update on pharmacological small-molecule compounds. *European Journal of Medicinal Chemistry* **256**, 115467, doi:https://doi.org/10.1016/j.ejmech.2023.115467 (2023).

158 Zengerle, M., Chan, K. H. & Ciulli, A. Selective Small Molecule Induced Degradation of the BET Bromodomain Protein BRD4. *ACS chemical biology* **10**, 1770-1777, doi:10.1021/acschembio.5b00216 (2015).

159 Wang, Z.-Q. *et al.* Bromodomain and extraterminal (BET) proteins: biological functions, diseases, and targeted therapy. *Signal Transduction and Targeted Therapy* **8**, 420, doi:10.1038/s41392-023-01647-6 (2023).

160 Gellibert, F. *et al.* Identification of 1,5-Naphthyridine Derivatives as a Novel Series of Potent and Selective TGF-β Type I Receptor Inhibitors. *Journal of medicinal chemistry* **47**, 4494-4506, doi:10.1021/jm0400247 (2004).

161 Grygielko, E. T. *et al.* Inhibition of gene markers of fibrosis with a novel inhibitor of transforming growth factor-beta type I receptor kinase in puromycin-induced nephritis. *The Journal of pharmacology and experimental therapeutics* **313**, 943-951, doi:10.1124/jpet.104.082099 (2005).

162 DaCosta Byfield, S., Major, C., Laping, N. J. & Roberts, A. B. SB-505124 Is a Selective Inhibitor of Transforming Growth Factor-β Type I Receptors ALK4, ALK5, and ALK7. *Molecular Pharmacology* **65**, 744-752, doi:10.1124/mol.65.3.744 (2004).

163 Gellibert, F. *et al.* Discovery of 4-{4-[3-(pyridin-2-yl)-1H-pyrazol-4-yl]pyridin-2-yl}-N-(tetrahydro-2H- pyran-4-yl)benzamide (GW788388): a potent, selective, and orally active transforming growth factor-beta type I receptor inhibitor. *Journal of medicinal chemistry* **49**, 2210-2221, doi:10.1021/jm0509905 (2006).

164 Yingling, J. M. *et al.* Preclinical assessment of galunisertib (LY2157299 monohydrate), a first-in-class transforming growth factor-β receptor type I inhibitor. *Oncotarget* **9**, 6659-6677, doi:10.18632/oncotarget.23795 (2018).

165 Li, H. Y. *et al.* Optimization of a dihydropyrrolopyrazole series of transforming growth factor-beta type I receptor kinase domain inhibitors: discovery of an orally bioavailable transforming growth factor-beta receptor type I inhibitor as antitumor agent. *Journal of medicinal chemistry* **51**, 2302-2306, doi:10.1021/jm701199p (2008).

REFERENCES

166 Li, M. O., Wan, Y. Y., Sanjabi, S., Robertson, A. K. & Flavell, R. A. Transforming growth factor-beta regulation of immune responses. *Annu Rev Immunol* **24**, 99-146, doi:10.1146/annurev.immunol.24.021605.090737 (2006).

167 Elkins, J. M. *et al.* Comprehensive characterization of the Published Kinase Inhibitor Set. *Nature Biotechnology* **34**, 95-103, doi:10.1038/nbt.3374 (2016).

168 Lotz-Jenne, C. *et al.* A high-content EMT screen identifies multiple receptor tyrosine kinase inhibitors with activity on TGFβ receptor. *Oncotarget* **7** (2016).

169 Vogt, J., Traynor, R. & Sapkota, G. P. The specificities of small molecule inhibitors of the TGFß and BMP pathways. *Cellular Signalling* **23**, 1831-1842, doi:https://doi.org/10.1016/j.cellsig.2011.06.019 (2011).

170 Inman, G. J. *et al.* SB-431542 Is a Potent and Specific Inhibitor of Transforming Growth Factor-β Superfamily Type I Activin Receptor-Like Kinase (ALK) Receptors ALK4, ALK5, and ALK7. *Molecular Pharmacology* **62**, 65-74, doi:10.1124/mol.62.1.65 (2002).

171 Wang, H. *et al.* Design, synthesis and optimization of novel Alk5 (activin-like kinase 5) inhibitors. *Bioorg Med Chem Lett* **26**, 4334-4339, doi:10.1016/j.bmcl.2016.07.030 (2016).

172 Hanke, T. *et al.* A Highly Selective Chemical Probe for Activin Receptor-like Kinases ALK4 and ALK5. *ACS chemical biology* **15**, 862-870, doi:10.1021/acschembio.0c00076 (2020).

173 Liu, Y. *et al.* Recent progress on vascular endothelial growth factor receptor inhibitors with dual targeting capabilities for tumor therapy. *Journal of Hematology & Oncology* **15**, 89, doi:10.1186/s13045-022-01310-7 (2022).

174 Lee, J. Y., Park, S., Min, W.-S. & Kim, H.-J. Restoration of natural killer cell cytotoxicity by VEGFR-3 inhibition in myelogenous leukemia. *Cancer Letters* **354**, 281-289, doi:https://doi.org/10.1016/j.canlet.2014.08.027 (2014).

175 Roth, G. J. *et al.* Nintedanib: From Discovery to the Clinic. *Journal of medicinal chemistry* **58**, 1053-1063, doi:10.1021/jm501562a (2015).

176 Yu, D. *et al.* Dual roles of misshapen/NIK-related kinase (MINK1) in osteoarthritis subtypes through the activation of TGFβ signaling. *Osteoarthritis and Cartilage* **28**, 112-121, doi:https://doi.org/10.1016/j.joca.2019.09.009 (2020).

177 Fiedler, L. R. *et al.* MAP4K4 Inhibition Promotes Survival of Human Stem Cell-Derived Cardiomyocytes and Reduces Infarct Size In Vivo. *Cell Stem Cell* **24**, 579-591.e512, doi:https://doi.org/10.1016/j.stem.2019.01.013 (2019).

178 Zhang, J. *et al.* A Human Pluripotent Stem Cell-Based Screen for Smooth Muscle Cell Differentiation and Maturation Identifies Inhibitors of Intimal Hyperplasia. *Stem cell reports* **12**, 1269-1281, doi:10.1016/j.stemcr.2019.04.013 (2019).

179 Manaster, I. *et al.* Notch activation enhances IFNγ secretion by human peripheral blood and decidual NK cells. *Journal of Reproductive Immunology* **84**, 1-7, doi:https://doi.org/10.1016/j.jri.2009.10.009 (2010).

180 Felices, M. *et al.* Notch signaling at later stages of NK cell development enhances KIR expression and functional maturation. *Journal of immunology (Baltimore, Md. : 1950)* **193**, 3344-3354, doi:10.4049/jimmunol.1400534 (2014).

181 Perchet, T. *et al.* The Notch Signaling Pathway Is Balancing Type 1 Innate Lymphoid Cell Immune Functions. *Frontiers in Immunology* **9**, doi:10.3389/fimmu.2018.01252 (2018).

182 Dovey, H. F. *et al.* Functional gamma-secretase inhibitors reduce beta-amyloid peptide levels in brain. *Journal of Neurochemistry* **76**, 173-181, doi:https://doi.org/10.1046/j.1471-4159.2001.00012.x (2001).

183 Astudillo, L. *et al.* The Small Molecule IMR-1 Inhibits the Notch Transcriptional Activation Complex to Suppress Tumorigenesis. *Cancer research* **76**, 3593-3603, doi:10.1158/0008-5472.Can-16-0061 (2016).

184 Nickoloff, B. J., Osborne, B. A. & Miele, L. Notch signaling as a therapeutic target in cancer: a new approach to the development of cell fate modifying agents. *Oncogene* **22**, 6598-6608, doi:10.1038/sj.onc.1206758 (2003).

REFERENCES

185 Nørregaard, R., Kwon, T.-H. & Frøkiær, J. Physiology and pathophysiology of cyclooxygenase-2 and prostaglandin E2 in the kidney. *Kidney Research and Clinical Practice* **34**, 194-200, doi:https://doi.org/10.1016/j.krcp.2015.10.004 (2015).

186 Pannunzio, A. & Coluccia, M. Cyclooxygenase-1 (COX-1) and COX-1 Inhibitors in Cancer: A Review of Oncology and Medicinal Chemistry Literature. *Pharmaceuticals (Basel, Switzerland)* **11**, doi:10.3390/ph11040101 (2018).

187 Jun, S. S., Chen, Z., Pace, M. C. & Shaul, P. W. Glucocorticoids Downregulate Cyclooxygenase-1 Gene Expression and Prostacyclin Synthesis in Fetal Pulmonary Artery Endothelium. *Circulation Research* **84**, 193-200, doi:doi:10.1161/01.RES.84.2.193 (1999).

188 Sampey, A. V., Hutchinson, P. & Morand, E. F. Annexin I and dexamethasone effects on phospholipase and cyclooxygenase activity in human synoviocytes. *Mediators of inflammation* **9**, 125-132, doi:10.1080/09629350020018357 (2000).

189 Newton, R., Seybold, J., Kuitert, L. M., Bergmann, M. & Barnes, P. J. Repression of cyclooxygenase-2 and prostaglandin E2 release by dexamethasone occurs by transcriptional and post-transcriptional mechanisms involving loss of polyadenylated mRNA. *The Journal of biological chemistry* **273**, 32312-32321, doi:10.1074/jbc.273.48.32312 (1998).

190 Mengle-Gaw, L. J. & Schwartz, B. D. Cyclooxygenase-2 inhibitors: promise or peril? *Mediators of inflammation* **11**, 864195, doi:10.1080/09629350290000041 (2002).

191 Reckzeh, E. S., Brockmeyer, A., Metz, M., Waldmann, H. & Janning, P. Target Engagement of Small Molecules: Thermal Profiling Approaches on Different Levels. *Methods in molecular biology (Clifton, N.J.)* **1888**, 73-98, doi:10.1007/978-1-4939-8891-4_4 (2019).

192 Martinez Molina, D. *et al.* Monitoring drug target engagement in cells and tissues using the cellular thermal shift assay. *Science* **341**, 84-87, doi:10.1126/science.1233606 (2013).

193 Zhou, Z. *et al.* Developing a fluorescence substrate for HRP-based diagnostic assays with superiorities over the commercial ADHP. *Chinese Chemical Letters* **35**, 108970, doi:https://doi.org/10.1016/j.cclet.2023.108970 (2024).

194 Quatrini, L. *et al.* Human NK cells, their receptors and function. *European journal of immunology* **51**, 1566-1579, doi:10.1002/eji.202049028 (2021).

195 Navabi, S., Doroudchi, M., Tashnizi, A. H. & Habibagahi, M. Natural Killer Cell Functional Activity After 4-1BB Costimulation. *Inflammation* **38**, 1181-1190, doi:10.1007/s10753-014-0082-0 (2015).

196 Erokhina, S. A. *et al.* HLA-DR(+) NK cells are mostly characterized by less mature phenotype and high functional activity. *Immunology and cell biology* **96**, 212-228, doi:10.1111/imcb.1032 (2018).

197 Sconocchia, G. *et al.* CD38 Triggers Cytotoxic Responses in Activated Human Natural Killer Cells. *Blood* **94**, 3864-3871, doi:https://doi.org/10.1182/blood.V94.11.3864 (1999).

198 Hayakawa, Y. & Smyth, M. J. CD27 Dissects Mature NK Cells into Two Subsets with Distinct Responsiveness and Migratory Capacity1. *The Journal of Immunology* **176**, 1517-1524, doi:10.4049/jimmunol.176.3.1517 (2006).

199 Cardoso Alves, L. *et al.* Non-apoptotic TRAIL function modulates NK cell activity during viral infection. *EMBO reports* **21**, e48789, doi:https://doi.org/10.15252/embr.201948789 (2020).

200 Zamai, L. *et al.* Natural killer (NK) cell-mediated cytotoxicity: differential use of TRAIL and Fas ligand by immature and mature primary human NK cells. *The Journal of experimental medicine* **188**, 2375-2380, doi:10.1084/jem.188.12.2375 (1998).

201 Helander, T. S. & Timonen, T. in *Specificity, Function, and Development of NK Cells: NK Cells: The Effector Arm of Innate Immunity* (eds Klas Kärre & Marco Colonna) 89-99 (Springer Berlin Heidelberg, 1998).

REFERENCES

202 Sivori, S. *et al.* Inhibitory Receptors and Checkpoints in Human NK Cells, Implications for the Immunotherapy of Cancer. *Frontiers in Immunology* **11**, doi:10.3389/fimmu.2020.02156 (2020).

203 Kurioka, A. *et al.* CD161 Defines a Functionally Distinct Subset of Pro-Inflammatory Natural Killer Cells. *Frontiers in Immunology* **9**, doi:10.3389/fimmu.2018.00486 (2018).

204 Khan, M., Arooj, S. & Wang, H. NK Cell-Based Immune Checkpoint Inhibition. *Frontiers in Immunology* **11**, doi:10.3389/fimmu.2020.00167 (2020).

205 Mandal, A. & Viswanathan, C. Natural killer cells: In health and disease. *Hematology/Oncology and Stem Cell Therapy* **8**, 47-55, doi:https://doi.org/10.1016/j.hemonc.2014.11.006 (2015).

206 Cifaldi, L. *et al.* DNAM-1 Activating Receptor and Its Ligands: How Do Viruses Affect the NK Cell-Mediated Immune Surveillance during the Various Phases of Infection? *Int J Mol Sci* **20**, doi:10.3390/ijms20153715 (2019).

207 Russick, J., Torset, C., Hemery, E. & Cremer, I. NK cells in the tumor microenvironment: Prognostic and theranostic impact. Recent advances and trends. *Seminars in Immunology* **48**, 101407, doi:https://doi.org/10.1016/j.smim.2020.101407 (2020).

208 Mittal, D., Gubin, M. M., Schreiber, R. D. & Smyth, M. J. New insights into cancer immunoediting and its three component phases—elimination, equilibrium and escape. *Current opinion in immunology* **27**, 16-25, doi:https://doi.org/10.1016/j.coi.2014.01.004 (2014).

209 Zhang, C., Hu, Y. & Shi, C. Targeting Natural Killer Cells for Tumor Immunotherapy. *Frontiers in Immunology* **11**, doi:10.3389/fimmu.2020.00060 (2020).

210 Fang, F., Xiao, W. & Tian, Z. Challenges of NK cell-based immunotherapy in the new era. *Frontiers of Medicine* **12**, 440-450, doi:10.1007/s11684-018-0653-9 (2018).

211 Mou, X. *et al.* The Regulatory Effect of UL-16 Binding Protein-3 Expression on the Cytotoxicity of NK Cells in Cancer Patients. *Scientific Reports* **4**, 6138, doi:10.1038/srep06138 (2014).

212 Holt, D., Ma, X., Kundu, N. & Fulton, A. Prostaglandin E(2) (PGE (2)) suppresses natural killer cell function primarily through the PGE(2) receptor EP4. *Cancer immunology, immunotherapy : CII* **60**, 1577-1586, doi:10.1007/s00262-011-1064-9 (2011).

213 Francica, B. J. *et al.* Dual Blockade of EP2 and EP4 Signaling is Required for Optimal Immune Activation and Antitumor Activity Against Prostaglandin-Expressing Tumors. *Cancer Research Communications* **3**, 1486-1500, doi:10.1158/2767-9764.Crc-23-0249 (2023).

214 Liang, J., Yu, M., Li, Y., Zhao, L. & Wei, Q. Glycogen synthase kinase-3: A potential immunotherapeutic target in tumor microenvironment. *Biomedicine & Pharmacotherapy* **173**, 116377, doi:https://doi.org/10.1016/j.biopha.2024.116377 (2024).

215 Robke, L. *et al.* Phenotypic Identification of a Novel Autophagy Inhibitor Chemotype Targeting Lipid Kinase VPS34. *Angewandte Chemie International Edition* **56**, 8153-8157, doi:https://doi.org/10.1002/anie.201703738 (2017).

216 Grisan, F. *et al.* PKA compartmentalization links cAMP signaling and autophagy. *Cell Death & Differentiation* **28**, 2436-2449, doi:10.1038/s41418-021-00761-8 (2021).

217 Wauson, E. M., Dbouk, H. A., Ghosh, A. B. & Cobb, M. H. G protein-coupled receptors and the regulation of autophagy. *Trends in endocrinology and metabolism: TEM* **25**, 274-282, doi:10.1016/j.tem.2014.03.006 (2014).

218 Yao, C. *et al.* Rocaglamide enhances NK cell-mediated killing of non-small cell lung cancer cells by inhibiting autophagy. *Autophagy* **14**, 1831-1844, doi:10.1080/15548627.2018.1489946 (2018).

219 Wang, L. *et al.* Hot and cold tumors: Immunological features and the therapeutic strategies. *MedComm* **4**, e343, doi:10.1002/mco2.343 (2023).

REFERENCES

220 Galon, J. & Bruni, D. Approaches to treat immune hot, altered and cold tumours with combination immunotherapies. *Nature Reviews Drug Discovery* **18**, 197-218, doi:10.1038/s41573-018-0007-y (2019).

221 Noman, M. Z. *et al.* Inhibition of Vps34 reprograms cold into hot inflamed tumors and improves anti–PD-1/PD-L1 immunotherapy. *Science Advances* **6**, eaax7881, doi:doi:10.1126/sciadv.aax7881 (2020).

222 Chen, S.-H. *et al.* Constitutive protein degradation induces acute cell death via proteolysis products. *bioRxiv*, 2023.2002.2006.527237, doi:10.1101/2023.02.06.527237 (2023).

223 Dougan, M. *et al.* IAP inhibitors enhance co-stimulation to promote tumor immunity. *The Journal of experimental medicine* **207**, 2195-2206, doi:10.1084/jem.20101123 (2010).

224 Lai, J., Liu, Z., Zhao, Y., Ma, C. & Huang, H. Anticancer Effects of I-BET151, an Inhibitor of Bromodomain and Extra-Terminal Domain Proteins. *Front Oncol* **11**, 716830, doi:10.3389/fonc.2021.716830 (2021).

225 Shorstova, T., Foulkes, W. D. & Witcher, M. Achieving clinical success with BET inhibitors as anti-cancer agents. *British Journal of Cancer* **124**, 1478-1490, doi:10.1038/s41416-021-01321-0 (2021).

226 Abruzzese, M. P. *et al.* Inhibition of bromodomain and extra-terminal (BET) proteins increases NKG2D ligand MICA expression and sensitivity to NK cell-mediated cytotoxicity in multiple myeloma cells: role of cMYC-IRF4-miR-125b interplay. *Journal of Hematology & Oncology* **9**, 134, doi:10.1186/s13045-016-0362-2 (2016).

227 Reggiani, F. *et al.* BET inhibitors drive Natural Killer activation in non-small cell lung cancer via BRD4 and SMAD3. *Nature Communications* **15**, 2567, doi:10.1038/s41467-024-46778-8 (2024).

228 Millet, C. & Zhang, Y. E. Roles of Smad3 in TGF-beta signaling during carcinogenesis. *Critical reviews in eukaryotic gene expression* **17**, 281-293, doi:10.1615/critreveukargeneexpr.v17.i4.30 (2007).

229 Chen, B., Mu, C., Zhang, Z., He, X. & Liu, X. The Love-Hate Relationship Between TGF-β Signaling and the Immune System During Development and Tumorigenesis. *Front Immunol* **13**, 891268, doi:10.3389/fimmu.2022.891268 (2022).

230 Fionda, C. *et al.* Hitting More Birds with a Stone: Impact of TGF-β on ILC Activity in Cancer. *Journal of Clinical Medicine* **9**, 143 (2020).

231 Tran, H. C. *et al.* TGFβR1 Blockade with Galunisertib (LY2157299) Enhances Anti-Neuroblastoma Activity of the Anti-GD2 Antibody Dinutuximab (ch14.18) with Natural Killer Cells. *Clinical Cancer Research* **23**, 804-813, doi:10.1158/1078-0432.Ccr-16-1743 (2017).

232 Shaim, H. *et al.* Targeting the αv integrin/TGF-β axis improves natural killer cell function against glioblastoma stem cells. *The Journal of clinical investigation* **131**, doi:10.1172/JCI142116 (2021).

233 Kment, J. *et al.* Blockade of TGF-β and PD-L1 by bintrafusp alfa promotes survival in preclinical ovarian cancer models by promoting T effector and NK cell responses. *British Journal of Cancer* **130**, 2003-2015, doi:10.1038/s41416-024-02677-9 (2024).

234 Piccinelli, S., Romee, R. & Shapiro, R. M. The natural killer cell immunotherapy platform: An overview of the landscape of clinical trials in liquid and solid tumors. *Seminars in Hematology* **60**, 42-51, doi:https://doi.org/10.1053/j.seminhematol.2023.02.002 (2023).

235 Lietuvninkas, L., Baccouche, B. & Kazlauskas, A. The Multi-Kinase Inhibitor RepSox Enforces Barrier Function in the Face of Both VEGF and Cytokines. *Biomedicines* **11**, doi:10.3390/biomedicines11092431 (2023).

236 Roudnicky, F. *et al.* Inducers of the endothelial cell barrier identified through chemogenomic screening in genome-edited hPSC-endothelial cells. *Proceedings of the National Academy of Sciences* **117**, 19854-19865, doi:doi:10.1073/pnas.1911532117 (2020).

REFERENCES

237 Zakiryanova, G. K. *et al.* Notch signaling defects in NK cells in patients with cancer. *Cancer immunology, immunotherapy : CII* **70**, 981-988, doi:10.1007/s00262-020-02763-w (2021).

238 Gilman, K. E. & Limesand, K. H. The complex role of prostaglandin E(2)-EP receptor signaling in wound healing. *American journal of physiology. Regulatory, integrative and comparative physiology* **320**, R287-r296, doi:10.1152/ajpregu.00185.2020 (2021).

239 Wang, Q., Morris, R. J., Bode, A. M. & Zhang, T. Prostaglandin Pathways: Opportunities for Cancer Prevention and Therapy. *Cancer research* **82**, 949-965, doi:10.1158/0008-5472.Can-21-2297 (2022).

240 Kundu, N., Walser, T. C., Ma, X. & Fulton, A. M. Cyclooxygenase inhibitors modulate NK activities that control metastatic disease. *Cancer immunology, immunotherapy : CII* **54**, 981-987, doi:10.1007/s00262-005-0669-2 (2005).

241 Watzl, C. & Long, E. O. Signal Transduction During Activation and Inhibition of Natural Killer Cells. *Current Protocols in Immunology* **90**, 11.19B.11-11.19B.17, doi:https://doi.org/10.1002/0471142735.im1109bs90 (2010).

242 Pinheiro, P. F., Justino, G. C. & Marques, M. M. NKp30 - A prospective target for new cancer immunotherapy strategies. *British Journal of Pharmacology* **177**, 4563-4580, doi:https://doi.org/10.1111/bph.15222 (2020).

243 Mao, Y. *et al.* Inhibition of Tumor-Derived Prostaglandin-E2 Blocks the Induction of Myeloid-Derived Suppressor Cells and Recovers Natural Killer Cell Activity. *Clinical Cancer Research* **20**, 4096-4106, doi:10.1158/1078-0432.Ccr-14-0635 (2014).

244 Reimold, A. M., Kara, C. J., Rooney, J. W. & Glimcher, L. H. Transforming growth factor beta 1 repression of the HLA-DR alpha gene is mediated by conserved proximal promoter elements. *The Journal of Immunology* **151**, 4173-4182, doi:10.4049/jimmunol.151.8.4173 (1993).

245 Foltz, J. A., Moseman, J. E., Thakkar, A., Chakravarti, N. & Lee, D. A. TGFβ Imprinting During Activation Promotes Natural Killer Cell Cytokine Hypersecretion. *Cancers (Basel)* **10**, doi:10.3390/cancers10110423 (2018).

246 Ramírez-Labrada, A. *et al.* All About (NK Cell-Mediated) Death in Two Acts and an Unexpected Encore: Initiation, Execution and Activation of Adaptive Immunity. *Front Immunol* **13**, 896228, doi:10.3389/fimmu.2022.896228 (2022).

247 Romee, R. *et al.* NK cell CD16 surface expression and function is regulated by a disintegrin and metalloprotease-17 (ADAM17). *Blood* **121**, 3599-3608, doi:10.1182/blood-2012-04-425397 (2013).

248 Singh, A. *et al.* A Gene Expression Signature Associated with “K-Ras Addiction” Reveals Regulators of EMT and Tumor Cell Survival. *Cancer Cell* **15**, 489-500, doi:https://doi.org/10.1016/j.ccr.2009.03.022 (2009).

249 Singh, A. *et al.* TAK1 Inhibition Promotes Apoptosis in KRAS-Dependent Colon Cancers. *Cell* **148**, 639-650, doi:https://doi.org/10.1016/j.cell.2011.12.033 (2012).

250 Babij, C. *et al.* STK33 Kinase Activity Is Nonessential in KRAS-Dependent Cancer Cells. *Cancer research* **71**, 5818-5826, doi:10.1158/0008-5472.Can-11-0778 (2011).

251 Collisson, E. A. *et al.* Subtypes of pancreatic ductal adenocarcinoma and their differing responses to therapy. *Nature Medicine* **17**, 500-503, doi:10.1038/nm.2344 (2011).

252 Janes, M. R. *et al.* Targeting KRAS Mutant Cancers with a Covalent G12C-Specific Inhibitor. *Cell* **172**, 578-589.e517, doi:10.1016/j.cell.2018.01.006 (2018).

253 Tan, L., Cho, K. J., Neupane, P., Capon, R. J. & Hancock, J. F. An oxanthroquinone derivative that disrupts RAS plasma membrane localization inhibits cancer cell growth. *The Journal of biological chemistry* **293**, 13696-13706, doi:10.1074/jbc.RA118.003907 (2018).

254 Dietlein, F. *et al.* A Synergistic Interaction between Chk1- and MK2 Inhibitors in KRAS-Mutant Cancer. *Cell* **162**, 146-159, doi:https://doi.org/10.1016/j.cell.2015.05.053 (2015).

REFERENCES

255 Casado, P. *et al.* Kinase-Substrate Enrichment Analysis Provides Insights into the Heterogeneity of Signaling Pathway Activation in Leukemia Cells. *Science Signaling* **6**, rs6-rs6, doi:doi:10.1126/scisignal.2003573 (2013).

256 Hornbeck, P. V. *et al.* PhosphoSitePlus, 2014: mutations, PTMs and recalibrations. *Nucleic Acids Research* **43**, D512-D520, doi:10.1093/nar/gku1267 (2014).

257 Horn, H. *et al.* KinomeXplorer: an integrated platform for kinome biology studies. *Nature Methods* **11**, 603-604, doi:10.1038/nmeth.2968 (2014).

258 Hornbeck, P. V. *et al.* PhosphoSitePlus, 2014: mutations, PTMs and recalibrations. *Nucleic Acids Res* **43**, D512-520, doi:10.1093/nar/gku1267 (2015).

259 Linding, R. *et al.* Systematic discovery of in vivo phosphorylation networks. *Cell* **129**, 1415-1426, doi:10.1016/j.cell.2007.05.052 (2007).

260 Szklarczyk, D. *et al.* The STRING database in 2023: protein-protein association networks and functional enrichment analyses for any sequenced genome of interest. *Nucleic Acids Res* **51**, D638-d646, doi:10.1093/nar/gkac1000 (2023).

261 Griss, J. *et al.* ReactomeGSA - Efficient Multi-Omics Comparative Pathway Analysis. *Molecular & cellular proteomics : MCP* **19**, 2115-2125, doi:10.1074/mcp.TIR120.002155 (2020).

262 Song, M. *et al.* Cdc2-like kinases: structure, biological function, and therapeutic targets for diseases. *Signal Transduct Target Ther* **8**, 148, doi:10.1038/s41392-023-01409-4 (2023).

263 Ge, S. X., Jung, D. & Yao, R. ShinyGO: a graphical gene-set enrichment tool for animals and plants. *Bioinformatics* **36**, 2628-2629, doi:10.1093/bioinformatics/btz931 (2019).

264 Venkatanarayan, A. *et al.* CRAF dimerization with ARAF regulates KRAS-driven tumor growth. *Cell reports* **38**, 110351, doi:10.1016/j.celrep.2022.110351 (2022).

265 Poh, A. R. & Ernst, M. Functional roles of SRC signaling in pancreatic cancer: Recent insights provide novel therapeutic opportunities. *Oncogene* **42**, 1786-1801, doi:10.1038/s41388-023-02701-x (2023).

266 Nussinov, R. *et al.* Calmodulin and PI3K Signaling in KRAS Cancers. *Trends in cancer* **3**, 214-224, doi:10.1016/j.trecan.2017.01.007 (2017).

267 Bivona, T. G. *et al.* PKC regulates a farnesyl-electrostatic switch on K-Ras that promotes its association with Bcl-XL on mitochondria and induces apoptosis. *Mol Cell* **21**, 481-493, doi:10.1016/j.molcel.2006.01.012 (2006).

268 Schneidewind, T. *et al.* Combined morphological and proteome profiling reveals target-independent impairment of cholesterol homeostasis. *Cell Chemical Biology* **28**, 1780-1794.e1785, doi:https://doi.org/10.1016/j.chembiol.2021.06.003 (2021).

269 Korolenko, T. A., Johnston, T. P. & Vetvicka, V. Lysosomotropic Features and Autophagy Modulators among Medical Drugs: Evaluation of Their Role in Pathologies. *Molecules (Basel, Switzerland)* **25**, doi:10.3390/molecules25215052 (2020).

270 Seo, I. *et al.* Identification of lysosomotropic compounds based on the distribution and size of lysosomes. *Biochemical and Biophysical Research Communications* **450**, 189-194, doi:https://doi.org/10.1016/j.bbrc.2014.05.091 (2014).

271 Breiden, B. & Sandhoff, K. Emerging mechanisms of drug-induced phospholipidosis. *Biological chemistry* **401**, 31-46, doi:10.1515/hsz-2019-0270 (2019).

272 Shahane, S. A. *et al.* Detection of Phospholipidosis Induction: A Cell-Based Assay in High-Throughput and High-Content Format. *SLAS Discovery* **19**, 66-76, doi:https://doi.org/10.1177/1087057113502851 (2014).

273 Boike, L., Henning, N. J. & Nomura, D. K. Advances in covalent drug discovery. *Nature Reviews Drug Discovery* **21**, 881-898, doi:10.1038/s41573-022-00542-z (2022).

274 Zecha, J. *et al.* Peptide Level Turnover Measurements Enable the Study of Proteoform Dynamics. *Molecular & cellular proteomics : MCP* **17**, 974-992, doi:10.1074/mcp.RA118.000583 (2018).

275 ProteomicsDB database: retinal rod rhodopsin-sensitive cGMP 3',5'-cyclic phosphodiesterase subunit delta turnover.

276 Di Nicolantonio, F. *et al.* Wild-type BRAF is required for response to panitumumab or cetuximab in metastatic colorectal cancer. *Journal of clinical oncology : official journal of the American Society of Clinical Oncology* **26**, 5705-5712, doi:10.1200/jco.2008.18.0786 (2008).

277 Hood, F. E., Sahraoui, Y. M., Jenkins, R. E. & Prior, I. A. Ras protein abundance correlates with Ras isoform mutation patterns in cancer. *Oncogene* **42**, 1224-1232, doi:10.1038/s41388-023-02638-1 (2023).

278 Nuevo-Tapioles, C. & Philips, M. R. The role of KRAS splice variants in cancer biology. *Front Cell Dev Biol* **10**, 1033348, doi:10.3389/fcell.2022.1033348 (2022).

279 Borchmann, S. *et al.* Tripartite antigen-agnostic combination immunotherapy cures established poorly immunogenic tumors. *Journal for ImmunoTherapy of Cancer* **10**, e004781, doi:10.1136/jitc-2022-004781 (2022).

280 Cagnol, S. & Rivard, N. Oncogenic KRAS and BRAF activation of the MEK/ERK signaling pathway promotes expression of dual-specificity phosphatase 4 (DUSP4/MKP2) resulting in nuclear ERK1/2 inhibition. *Oncogene* **32**, 564-576, doi:10.1038/onc.2012.88 (2013).

281 Stelniec-Klotz, I. *et al.* Reverse engineering a hierarchical regulatory network downstream of oncogenic KRAS. *Molecular Systems Biology* **8**, 601, doi:https://doi.org/10.1038/msb.2012.32 (2012).

282 De Duve, C. *et al.* Lysosomotropic agents. *Biochemical Pharmacology* **23**, 2495-2531, doi:https://doi.org/10.1016/0006-2952(74)90174-9 (1974).

7. ABBREVIATIONS

Abbreviation	Definition
$A549^{Green}$	A549 cells expressing Histone H2B1J-eGFP
AA	Arachidonic Acid
ABPP	Activity-based proteome profiling
ADHP	10-acetyl-3,7-dihydroxyphenoxazine
AF	Alexa Fluorophor®
ALK4	Activin-like kinase 4
AKT	Protein kinase B
APC	Allophycocyanin
APS	Ammonium persulfate
A-RAF	Serine/threonine-protein kinase A-Raf
Arl2/3	ADP-ribosylation factor-like protein 2 and 3
ATCC	American Type Culture Collection
AUC	Area under curve
BIOS	Biology-oriented synthesis
BRD	Bromodomain-containing protein
BSA	Bovine serum albumin
BV	Brilliant Violet™
BUV	Brilliant Ultra Violet™
CAR	Chimeric antigen receptor
CDK	Cyclin-dependenkt kinase
CETSA	Cellular thermal shift assay
CLS	Cell Lines Service
COMAS	Compound Management and Screening Center
COX	Cyclooxygenase

ABBREVIATIONS

Abbreviation	Definition
CSL	CBF1, Suppressor of Hairless, Lag-1
DMEM	Dulbecco's Modified Eagle Medium
DMSO	Dimethyl sulfoxide
DNAM-1	DNAX accessory molecule-1
DRK	Deutsches Rotes Kreuz
DSMZ	Deutsche Sammlung von Mikroorganismen und Zellkulturen
EC_{50}	Half-maximal effective concentration
EGF	Epidermal growth factor
ELISA	Enzyme-linked immunosorbent assay
EP2/4	Prostaglandin E2 receptor 2/4
ERK	Extracellular signal-regulated kinase
E:T	Effector to target ratio
EtOH	Ethanol
FACS	Fluorescence-activated cell sorting
FBS	Fetal bovine serum
FDA	US Food and Drug Administration
FITC	Fluorescein-5-isothiocyanate
Fluc	Firefly luciferase
FTase	Farnesyltransferase
g	Gravity
G418	Geneticin
GAP	GTPase-activating protein
GAPDH	Glyceraldehyde 3-phosphate dehydrogenase
GDP	Guanosine diphosphate
GEF	Guanine nucleotide exchange factor

ABBREVIATIONS

Abbreviation	Definition
GFP	Green fluorescent protein
GGTase	Geranylgeranyltransferase
GSK3β	Glycogen synthase kinase 3β
GTP	Guanosine triphosphate
GVHD	Graft-versus-host disease
GzmB	Granzyme B
h	Hours
H2B	Histone 2B type j
HTS	High-throughput screen
HRP	Horseradish peroxidase
IC_{50}	Half-maximal inhibitory concentration
IDO1	Indolamine-2,3-dioxygenase 1
IFN	Interferon
IL	Interleukin
IMIDs	Immunomodulatory drugs
KRas	Kirsten rat sarcoma virus oncogene homolog
LB	Lysogeny broth
MEK	Mitogen-activated protein kinase kinase
MeOH	Methanol
MHC-I	Major histocompatibility complex I
MICA/B	MHC class I chain-related protein A/B
MINK1	Misshapen like kinase 1
mTOR	Mammalian target of rapamycin
NEAA	Non-essential amino acids
NICD	Notch intracellular domain

ABBREVIATIONS

Abbreviation	Definition
NK cell	Natural killer cell
NKG2D	Natural killer group 2-member D
NKp	Natural killer protein
nm	Nanometer
NP-40	Nonidet P-40
NTM	Notch transmembrane domain
p38α	Mitogen-activated protein kinase 14
PAGE	Polyacrylamide gel electrophoresis
PBMC	Peripheral blood mononuclear cell
PBS	Phosphate-buffered saline
PDEδ	Retinal rod rhodopsin-sensitive cGMP 3',5'-cyclic phospho-diesterase subunit delta
PE	Phycoerythrin
PerCP	Peridinin-Chlorophyll-Protein
PGE	Prostaglandin
PI3K	Phosphoinositide 3-kinase
PROTAC	Proteolysis targeting chimera
PTM	Posttranslational modification
PVDF	Polyvinylidene difluoride
RAF	Rapidly growing fibrosarcoma
Ras	Rat sarcoma
RGA	Reporter gene assay
RIPA	Radioimmunoprecipitation assay
RIPK2	Receptor-interacting serine/threonine-protein kinase 2
Rluc	Renilla luciferase
RTK	Receptor tyrosine kinase

Abbreviation	Definition
SBE4	Smad-binding element 4
SD	Standard deviation
SDS	Sodium dodecyl sulfate
TBS	Tris-buffered saline
TEAB	Triethylammonium carbonate
TEMED	Tetramethylethylendiamin
TFA	Trifluoric acid
TGFβ	Transforming growth factor β
TLR	Toll-like receptor
TPP	Thermal proteome profiling
Treg	Regulatory T cells
TRIS	Tris(hydroxymethyl)aminomethane
tSNE	t-distributed stochastic neighbor embedding
ULBP	UL16 binding protein
VEGF	Vascular endothelial growth factor
VEGFR	Vascular endothelial growth factor receptors
VHL	Von Hipple Lindau
VPS34	Phosphatidylinositol 3-kinase
wt	Wildtype

8. APPENDIX

8.1 Vector maps

I. pRL-TK-Rluc vector map

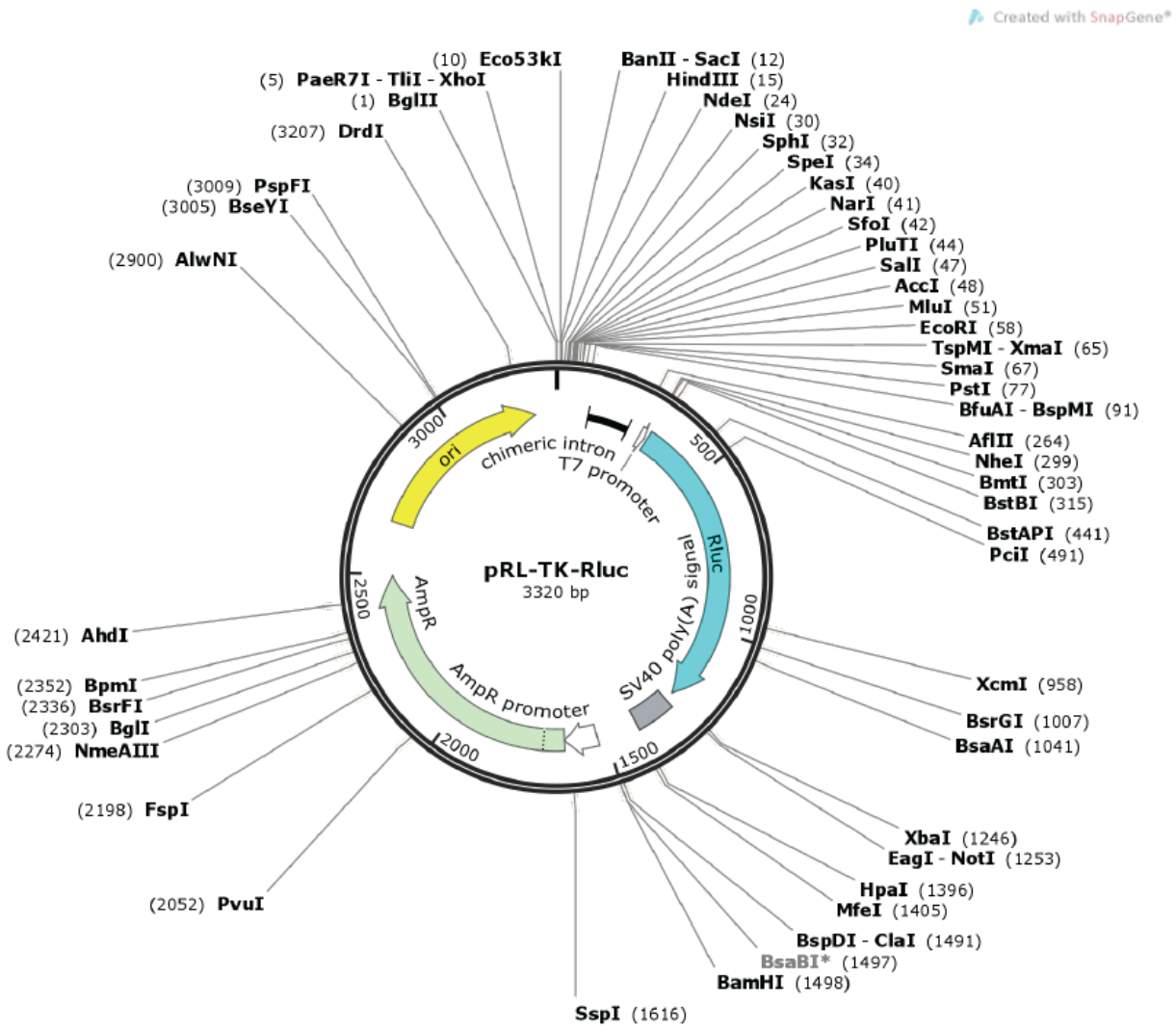

II. pBV-SBE4-Luc vector map

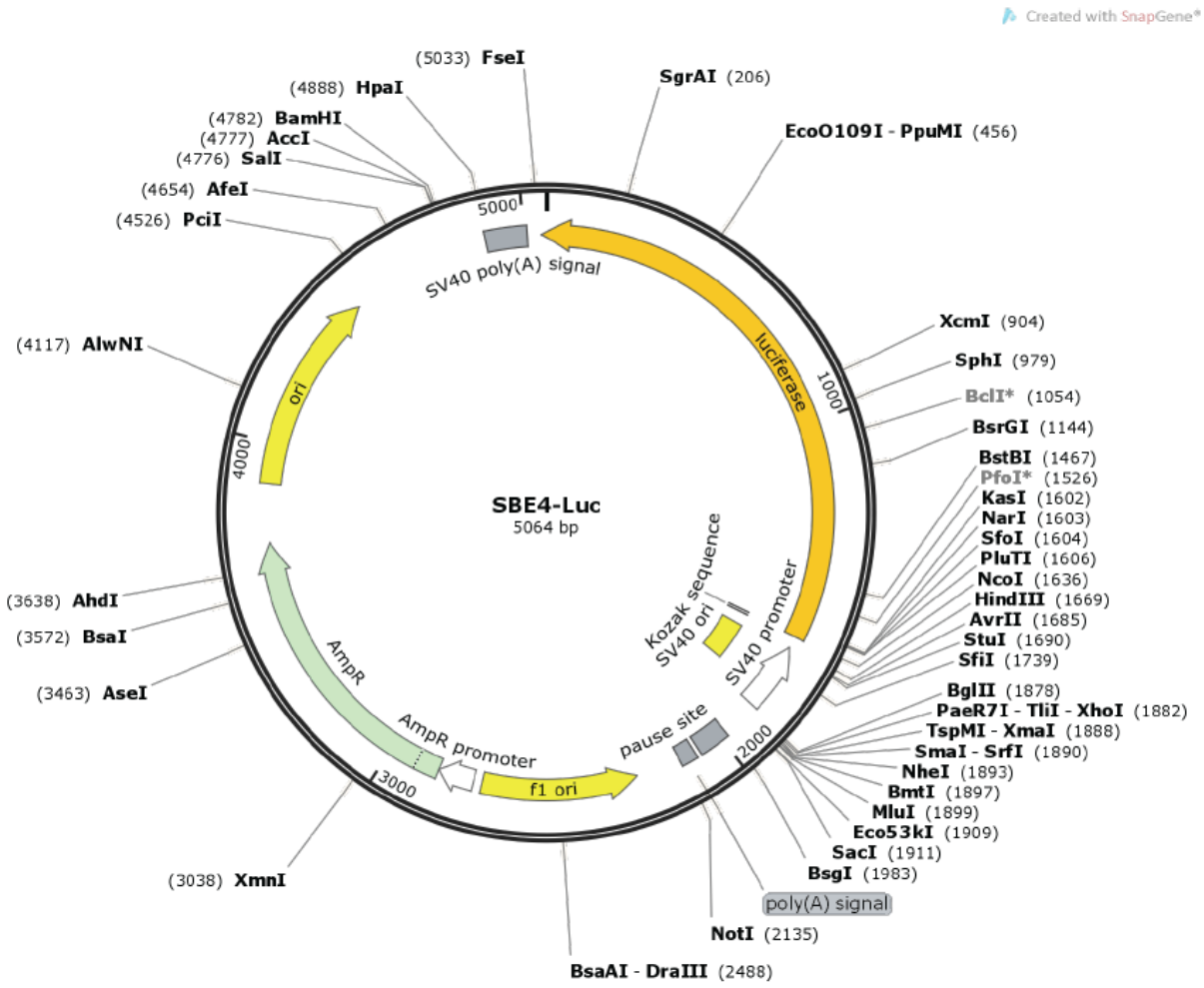

8.2 Supplementary figures

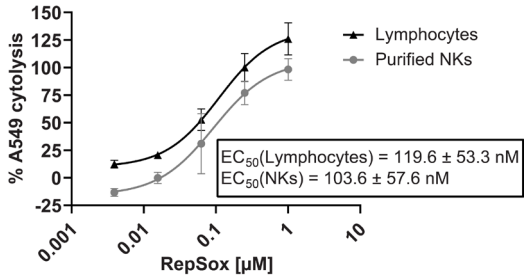

Figure S1: RepSox boosts NK cell cytotoxicity. Determination of the cytolysis rate of RepSox *via* the NK cell-mediated cancer cell cytolysis assay using lymphocytes or purified (mean values ± SD, n=3).

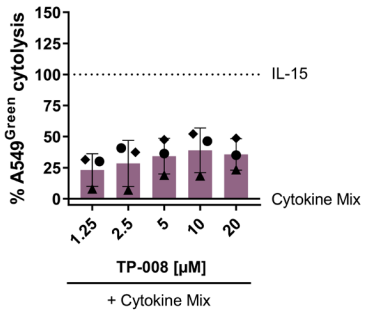

Figure S2: TP-008 enhances NK cell cytotoxicity. NK cell-mediated cancer cell cytolysis assay using TP-008-treated lymphocytes (mean values ± SD, n=3).

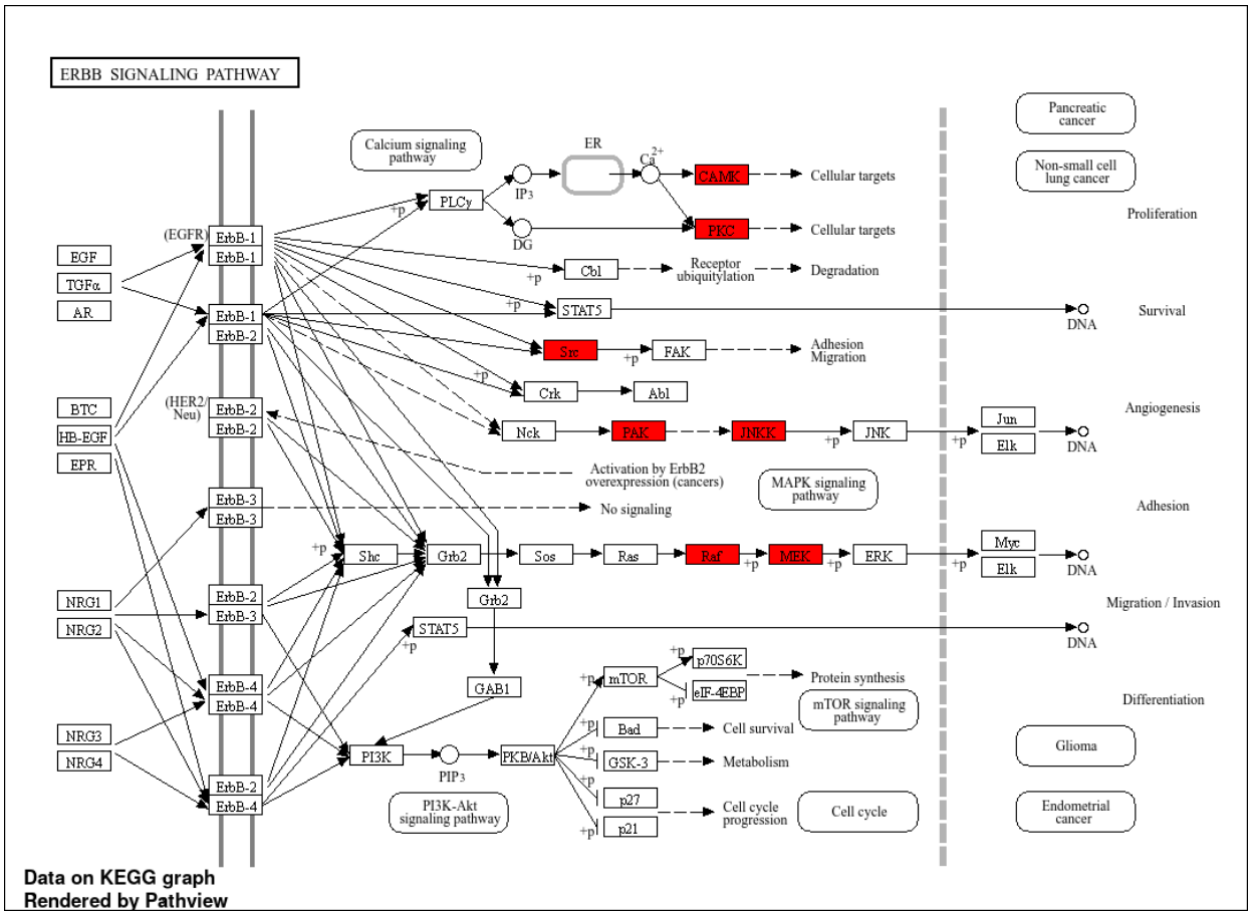

Figure S3: KEGG diagram representing enriched genes upon Deltacovalin treatment. Analysis was performed using the ShinyGO gene set enrichment tool.

CURRICULUM VITAE

CURRICULUM VITAE

10. PUBLICATION LIST

A. Christoforow, J. Wilke, **A. Binici**, A. Pahl, C. Ostermann, S. Sievers, H. Waldmann, "*Design, Synthesis, and Phenotypic profiling of Pyrano-Furo-Pyridone Psuedo Natural Products*", Angew Chem Int Ed Engl., **2019**, 58(41), 14715-14723.

E.S. Reckzeh, G. Karageoris, M. Schwalfenberg, J. Ceballos, J. Nowacki, M.C.M. Stroet, **A. Binici**, L. Knauer, S. Brand, A. Choidas, C. Strohmann, S. Ziegler, H. Waldmann, "*Inhibition of Glucose Transporters and Glutaminase Synergistically Impairs Tumor Cell Growth*", Cell Chem Biol., **2019**, 26(9), 1214-1228.

A. Binici, E. Hennes*, S. Koska, J. Niemann, A. Reich, C. Pfaff, S. Sievers, A. S. Kahnt, D. Thomas, S. Ziegler, C. Watzl, H. Waldmann, "*Identification of small molecule-enhancers of NK cell tumoricidal activity via a tumor microenvironment-mimicking co-culture assay*", bioRxiv, 2024.09.04.611205, https://doi.org/10.1101/2024.09.04.611205 (2024).

Eidesstattliche Versicherung (Affidavit)

Binici, Aylin
Name, Vorname
(Surname, first name)

177891
Matrikel-Nr.
(Enrolment number)

Belehrung:

Wer vorsätzlich gegen eine die Täuschung über Prüfungsleistungen betreffende Regelung einer Hochschulprüfungsordnung verstößt, handelt ordnungswidrig. Die Ordnungswidrigkeit kann mit einer Geldbuße von bis zu 50.000,00 € geahndet werden. Zuständige Verwaltungsbehörde für die Verfolgung und Ahndung von Ordnungswidrigkeiten ist der Kanzler/die Kanzlerin der Technischen Universität Dortmund. Im Falle eines mehrfachen oder sonstigen schwerwiegenden Täuschungsversuches kann der Prüfling zudem exmatrikuliert werden, § 63 Abs. 5 Hochschulgesetz NRW.

Die Abgabe einer falschen Versicherung an Eides statt ist strafbar.

Wer vorsätzlich eine falsche Versicherung an Eides statt abgibt, kann mit einer Freiheitsstrafe bis zu drei Jahren oder mit Geldstrafe bestraft werden, § 156 StGB. Die fahrlässige Abgabe einer falschen Versicherung an Eides statt kann mit einer Freiheitsstrafe bis zu einem Jahr oder Geldstrafe bestraft werden, § 161 StGB.

Die oben stehende Belehrung habe ich zur Kenntnis genommen:

Official notification:

Any person who intentionally breaches any regulation of university examination regulations relating to deception in examination performance is acting improperly. This offence can be punished with a fine of up to EUR 50,000.00. The competent administrative authority for the pursuit and prosecution of offences of this type is the chancellor of the TU Dortmund University. In the case of multiple or other serious attempts at deception, the candidate can also be unenrolled, Section 63, paragraph 5 of the Universities Act of North Rhine-Westphalia.

The submission of a false affidavit is punishable.

Any person who intentionally submits a false affidavit can be punished with a prison sentence of up to three years or a fine, Section 156 of the Criminal Code. The negligent submission of a false affidavit can be punished with a prison sentence of up to one year or a fine, Section 161 of the Criminal Code.

I have taken note of the above official notification.

Ort, Datum
(Place, date)

Unterschrift
(Signature)

Titel der Dissertation:
(Title of the thesis):

Identification and characterization of small-molecule enhancers that promote cancer cell elimination

Ich versichere hiermit an Eides statt, dass ich die vorliegende Dissertation mit dem Titel selbstständig und ohne unzulässige fremde Hilfe angefertigt habe. Ich habe keine anderen als die angegebenen Quellen und Hilfsmittel benutzt sowie wörtliche und sinngemäße Zitate kenntlich gemacht.
Die Arbeit hat in gegenwärtiger oder in einer anderen Fassung weder der TU Dortmund noch einer anderen Hochschule im Zusammenhang mit einer staatlichen oder akademischen Prüfung vorgelegen.

I hereby swear that I have completed the present dissertation independently and without inadmissible external support. I have not used any sources or tools other than those indicated and have identified literal and analogous quotations.

The thesis in its current version or another version has not been presented to the TU Dortmund University or another university in connection with a state or academic examination.*

*Please be aware that solely the German version of the affidavit ("Eidesstattliche Versicherung") for the PhD thesis is the official and legally binding version.

Ort, Datum
(Place, date)

Unterschrift
(Signature)